Advanced Materials, Process, and Designs for Silicon Photonic Integration

by

Rong Sun

B.S. Polymers Science and Engineering

Nanjing University, 2000

M.S. Materials Science

Dalhousie University, 2004

Submitted to Department of Materials Science and Engineering in Partial Fulfillment of the Requirements for the Degree of

Doctor of Philosophy in Electronic, Photonic, and Magnetic Materials
at the
Massachusetts Institute of Technology

February 2009

Signature of Author: _____

Department of Materials Science and Engineering
November 3rd, 2008

Certified by: _____

Lionel C. Kimerling
Thomas Lord Professor of Materials Science and Engineering
Thesis Supervisor

Accepted by: _____

Christine Ortiz
Professor of Materials Science and Engineering
Chair, Departmental Committee on Graduate Students

(This page is intentionally left blank)

Advanced Materials, Process, and Designs for Silicon Photonic Integration

by

Rong Sun

Submitted to the Department of Materials Science and Engineering on November 3rd, 2008, in Partial Fulfillment of the Requirement for the Degree of Doctor of Philosophy in Electronic, Photonic, and Magnetic Materials.

ABSTRACT

The copper (Cu) interconnect has become the bottleneck for bandwidth scaling due to its increasing RC time constant with the decreasing gate line width. Currently, silicon based optical interconnect is widely pursued as the most promising technology to replace Cu in microprocessor chips. Silicon optical interconnect is based on integrated silicon nanophotonic technologies. It can leverage the large scale and low cost of CMOS technology and deliver higher bandwidth with no EMI and low heat dissipation. Passive photonic component, such as waveguides, couplers, filters, splitters, are the backbone of integrated photonic circuit. This thesis is dedicated to the development of low loss, high performance, high index contrast optical waveguides and couplers via materials, processes engineering, development, and device designs. We primarily focus on SOI single crystalline silicon (c-Si or SOI), PECVD amorphous silicon (a-Si:H, or simplified as a-Si), and PECVD silicon nitride (SiN_xH_y) based single mode channel waveguides.

We have previously identified that sidewall roughness scattering is the dominant loss mechanism for the TE mode in high index contrast single mode channel waveguides. In this thesis, we provide a comprehensive understanding of the roughness scattering and its positive correlations with (1) sidewall optical intensity; (2) sidewall RMS roughness; and (3) sidewall index contrast. Novel processes and designs, such as hard mask and chemical oxidation, are developed based on the above understanding. In single mode, 500 × 200 nm^2 c-Si channel waveguides, we have achieved world-record 2.7 dB/cm and 0.7 dB/cm transmission loss coefficients for the TE mode and the TM mode, respectively.

For deposited waveguides, bulk absorption loss is also important for both TE and TM modes.

For PECVD a-Si, we adapt hydrogen passivation to reduce dangling bond density. We also use a thin silicon nitride as the over cladding layer to help preserve H passivation and to reduce sidewall index contrast, acting as the graded index layer for a-Si waveguide core. We have accomplished the lowest reported loss coefficients in directly etched, single mode, 700 × 100 nm^2 a-Si channel waveguides of 2.7 dB/cm for the TE mode, comparable to c-Si waveguide with similar dimensions. For the first time, damascene process has also been demonstrated as a promising process for a-Si waveguide fabrication. We have achieved a record-low loss of 2.5 dB/cm in 600 × 100 cm^2 a-Si channel waveguides. Chemical-mechanical polishing (CMP) is the most critical step.

For PECVD SiN_xH_y, we have previously identified that the absorption loss is due to the resonant absorption caused by N-H vibration. In this thesis, three different low temperature

approaches have been developed and optimized to reduce NH concentration in as-deposited SiN_xH_y via (1) deposition chemistry; (2) post-deposition Ultraviolet light (UV) treatment; and (3) post-deposition, in-situ N_2/Ar plasma treatment. All three processes are compatible with CMOS back-end processes, such as a-Si process. While changing deposition chemistry is the simplest method to obtain low NH containing SiN_xH_y, it comes with high SiH concentration and may have undesirable properties. Experimentally, for UV treatment, the highest H removal percentage is ~ 60%; for plasma treatment, ~ 90%. UV treatment shows strong compositional dependence. The underlying mechanism of such dependence is identified and confirmed by Monte-Carlo modeling.

Low loss and spectrally broadband optical couplers are indispensable optical components in an integrated photonic circuit. A high performance coupler should be capable of overcoming the mode-size mismatch, mode-shape mismatch, mode-position mismatch, and polarization mismatch, bridging different optical devices with minimal coupling loss. In this thesis, we have demonstrated a fiber-to-waveguide coupler based on asymmetric graded index taper and monolithically integrated cylindrical lens. It is capable of transforming single mode light between single mode fiber and waveguides with minimal coupling loss of 0.45 dB between 1520 nm and 1630 nm. We have also demonstrated a vertical waveguide-to-waveguide coupler that is based on complementary inverse tapers. This design is tolerant of large refractive index mismatch between the two waveguides and also of any fabrication variation that would affect the effective indices of the two waveguides. We have achieved a minimal coupling loss of 0.25 dB per coupler and excellent broadband behavior is also demonstrated.

Slot waveguides are a newly developed class of waveguides with unique optical properties. Slot waveguides can achieve exceptional high optical field in nanometer sized low index regions. In this thesis, we have demonstrated low loss transmission of 6 dB/cm for the fundamental slot mode in horizontal slot waveguides at 1550 nm. The horizontal slot configuration removes the constraints of thin slot definition by lithography and allows an arbitrarily thin slot to be fabricated via deposition or oxidation. Because the resulting interface is much smoother than the etched interface, the transmission loss in horizontal slot waveguides is much lower than in vertical slot waveguides. We also demonstrated that multiple slot configurations result in higher optical confinement compared to single slot configurations with the same slot thickness. The low loss and high optical confinement in the low index slot region realized in horizontal slot waveguides promises many useful applications, such as Er-doped silicon-based light emitters. For integration of slot waveguides with conventional channel waveguides, we have designed and simulated mode couplers and polarization rotators for slot-slot, slot-channel waveguide mode transformations.

Athermal operation is important for realizing stable passive, WDM optical network on silicon. Athermal design of silicon waveguide systems uses advanced polymer cladding of large negative TO coefficient to provide compensation for the large positive TO coefficient in silicon. The reduced thermo-optic (TO) effect is experimentally demonstrated by reducing TO coefficient from 85 pm/K to 11 pm/K using polymer films.

Thesis Advisor: Lionel C. Kimerling
Title: Thomas Lord Professor of Material Science and Engineering

This thesis is a tribute to my Aunt Xiaozheng Sun (1960-2001)

谨以此论文纪念我的姑姑孙小珍 (1960-2001)

(This page is intentionally left blank)

Table of Contents

List of Figures

List of Tables

List of Abbreviations and Symbols Used

Chapter 1

R: Resistance

C: Capacitance

Chapter 2

θ: Incident angle

$\theta_{critical}$: Critical angle

n, n_R, n_H, n_L, n_o: Refractive indices

NA: Numerical aperture

$\boldsymbol{k}$: Wave vector

ω: Angular frequency

A: Amplitude

a: Half thickness of a slab layer

m: Integer, optical mode order

Chapter 3

$\boldsymbol{E}_z$: Electric vector field

$\boldsymbol{H}_y$: Magnetic vector field

ε_o: Electric permittivity of free space, ~ 8.854×10^{-12} F/m

μ_o: Magnetic permeability of free space, $4\pi \times 10^{-7}$ H/m

n: Time, $t = \Delta t \cdot n$

k: Distance $x = \Delta x \cdot k$.

Δt: Time step

Δx: Distance step

∇^2: Laplacian operator, $\nabla^2 = \frac{\partial^2}{\partial x^2} + \frac{\partial^2}{\partial y^2} + \frac{\partial^2}{\partial z^2}$

σ: Pulse width

c: Speed of light in vacuum, $3\text{x}10^8$ m/s

$\boldsymbol{\varphi}$: Slowly varying envelop term of electric field

n: Index of waveguide core

n_0: Index of waveguide cladding

a_k: Forward amplitude

b_k: Backward amplitude

S: Scattering matrix

β_k: Propagation constant

Chapter 4:

P_{out}: Optical power come out a system

P_{in}: Optical power come in a system

α: Sidewall roughness loss

σ: Sidewall roughness RMS value

$|E|^2$: Normalized optical intensity

n_{core}: Index of core material

$n_{cladding}$: Index of cladding material

ΔN : Electron concentration change in [cm^{-3}]

ΔP : Hole concentration change in [cm^{-3}]

Δn_e : Refractive index change due to ΔN

Δn_h : Refractive index change due to ΔP

$\Delta \alpha_e$: Absorption coefficient change due to ΔN in [cm^{-1}]

$\Delta \alpha_h$: Absorption coefficient change due to ΔP in [cm^{-1}]

Chapter 5:

α_t : Total insertion loss in [dB]

α_c : Total coupling loss in [dB]

α_t : Waveguide transmission loss coefficient in [dB/length]

L: Waveguide length

R: Reflectance

$n_{incident}$: Refractive index of the medium from which light enters or exits the waveguide n_{eff}: Effective refractive index of the waveguide

P_{max}, P_{min}: Transmitted power of the resonance peak and valley, respectively

F: Finesse of the resonant cavity

$\Delta\Phi$: FWHM bandwidth

$\delta\Phi$: Free space range

α: Round trip loss

a_1: Input power, normalized, $|a_1|^2 = 1$

a_2: Power in the ring considering round trip loss

b_1: Transmitted power

b_2: Power in the ring

t: Transmission coefficient

κ: Coupling coefficient

θ : Phase change per round trip in a resonator

ϕ_t : Phase change in coupling region

Q: Quality factor,

$\Delta\lambda_R$: Full width at half maximum (FWHM)

λ_R : Resonance wavelength

α_{TM}: TM-mode transmission loss

α_{side}: Loss from sidewall roughness scattering

α_{top}: Loss from top surface roughness scattering

α_{sub}: Loss from substrate leakage

α_{bulk}: Loss from bulk absorption

α: Bulk absorption loss coefficient

Γ: Confinement factor

IL: Insertion loss

a, b, c, d: four scalar transfer functions, elements of Jones Matrix

ω: Frequency

v_g: Group velocity

n_{eff}: Effective index

c_0: Speed of light in vacuum

λ: Wavelength

Chapter 6

R: Resolution

$\vec{F}$: Flux of oxidant

h: Gas-phase mass-transfer coefficient

C^*: Oxidant concentration in ambient

C_o: Oxidant concentration at the oxide surface

$\vec{n}_s$: Unit vector normal to the oxide surface, pointing at the oxide

D: Diffusivity of oxidant

C: Local concentration of oxidant in oxide

k_s: Surface reaction rate

C_i: Oxidant concentration at SiO_2/Si interface

$\vec{n}_i$: Unit vector normal to the interface pointing away from the oxide

GR: Growth rate of oxide, or the interface velocity relative to the oxide

N: Number of oxidant molecules needed to form 1 cm^3 of oxide

Chapter 7:

A_i: Peak area in FTIR spectrum (Absorbance)

σ_i: Absorption coefficient

t: Film thickness

n_R: Refractive index

Chapter 8

$<S>$: Time-averaged energy flux

ε_o: Permittivity of free space

n_g: Group indices

R: Radius of ring resonator

$\Delta\lambda_{3dB}$: 3dB wavelength

Chapter 10:

$n_{air:}$ Effective index of the air

w: Taper width at the outer flat facet

w_t: Taper tip width and also the waveguide width

L: Taper length

α_t : Waveguide loss coefficient,

Chapter 11

L: Coupling length

$n_{aSi:}$ Index of amorphous Si

n_{SOI}: Index of SOI

l_i: Unit length at w_i,

Γ_i^{aSi}: Confinement factor for a-Si at w_i

α_i^{SOI} : Sidewall scattering loss coefficients for SOI at w_i

α_i^{aSi} : Sidewall scattering loss coefficients for a-Si at w_i,

α_{bulk}^{aSi}: Bulk absorption coefficient for a-Si.

$\alpha(C)$: Measured total coupling loss

$\alpha(T)$: Simulated transmission loss

Chapter 13

n_c: index of core

n_{cl}: index of cladding material

T_g: glass transmission temperatures,

Acknowledgements

How should I begin? It is a dream come true!

My dad was a self-taught mechanical engineer. He grew up in the miserable era of the Great Proletarian Cultural Revolution and lost the opportunity to go to college. When I was a kid, he used to encourage me to study hard in school and say: "Being the best student in your class, you may have a chance to be admitted by MIT one day." MIT is a prestige university and world renowned for her science and technology innovations. It would be a life-time honor for me to go and study with the most brilliant people in the world. Being a student at MIT is truly a dream shared by the father and the son.

I was fortunate to meet and be assisted by many great people. Their wisdoms, guidance, and friendship made this long journey easier and quite enjoyable. First off, I would like to thank Prof. Mary Anne White and Prof. Jeff Dahn at Dalhousie University, Halifax, NS, Canada. They co-advised my Master's study in 2002-2004. They gave me a lot of freedom to explore interesting and important topics, such as thermo-electric materials and combinatorial materials science approaches, which were completed new to me coming from chemistry background; and they were always there when I stuck and needed help. I still remember Prof. Dahn's famous saying: "Walk first; Run later." In two years, they helped me transform from a chemist to a materials scientist and prepare myself for new challenges. With their recommendations, I was successfully accepted by my "dream school" – the Massachusetts Institute of Technology in the spring of 2004.

I joined Prof. Lionel ("Kim") Kimerling's group in January, 2005 and became a proud EMAT member. Kim is a world-pioneer, a true leader, and a visionary in silicon photonics. Kim's knowledge and insights in semiconductor and photonics, experience in industry and university, and arts in management and teaching is far more than what a Ph.D. student could ever learn from. Kim gave me great freedom to explore different projects in his mega-sized group without boundaries and he strongly encourages collaborations. He was always very supportive to me, making himself available to me, and helping me with internship and job hunting. Kim is always calm, assertive, and very kind to his students. He is the best advisor that I have ever met. I am grateful for everything that Kim has done for me. Four years passed quickly. Under Kim's guidance, I have now grown up to be a more mature person in both scientific and persona life. Thank you very much, Kim! The learning from you will benefit me for the rest of my life.

Here in EMAT, I had many very gifted people to work with, I had many interested projects to work on, and I had endless resources that I could ever need. Kim has the ability to identify the potentials of the students and put them where not only they are interested, but also they are the most fit for the tasks. The result is that every student is highly self-motivated because they love what they do. EMAT also has a good atmosphere for collaborations. I don't know if anyone has realized this: E-M-A-T has every element to make a T-E-A-M! During my time in EMAT, I directly worked with more than 30 group members and other colleagues in other groups and there are 48 coauthors listed on all my publications here at MIT. Without the help from many great researchers, it would take me much longer to accomplish my thesis work, if it were still possible by me alone.

United around Kim, there are many incredibly talented people to whom I want to thank. Our Principal Research Scientist Dr. Jurgen Michel is essentially my co-advisor for my Ph.D. study. He is very savvy and creative. Thank you very much, Jurgen, for all your directions and advices to me, for reading all my manuscripts and conference

proceedings, for being one of my thesis committee members! Mr. Mark Beals is the associated director of the Microphotonic Center. He managed many large projects for Kim and we worked together on the EPIC project and MURI project. Mark is very knowledgeable in our field and he is also an expert of PECVD. He never hesitates to share his knowledge with me on PECVD and everything else. The past few years was a great time working with you and fighting with you. Thank you very much, Mark! I would also like to thank Dr. Anu Aguwal and Dr. Anat Eshed for helping me with many of my manuscripts and thesis proof readings. They gave me numerous encouragements when I was worried. For other group members I have worked with, I would like to thanks Dr. Jifeng Liu, Dr. Ning-ning Feng, Dr. Ching-yin Hong, Dr. Daniel Sparacin, Dr. Victor Nguyen, Dr. Mike Stolfi, Dr. Winnie Ye, Juejun Hu, Xiaochen Sun, Kevin McComber, Sarah Bernardis etc. Thank you all for your knowledge and assistance. I truly enjoyed the discussions, works, and fun we had together. The papers we have together are the best souvenirs for the good old days! Dr. Xiaoman Duan is extremely kind to me. I loved the flowers you sent me after my final thesis presentation! I am deeply grateful for your caring and endless support to me. Thank you Xiaoman! For other EMAT members who I have shared life with, I would like to extend my thanks to you all. They are Dr. Sajan Saini, Dr. Jaehyung Yi, Dr. Donghwan Ann, Dr. Samerkhae Jongthammanurak, Dr. Lirong Zeng, Dr. David Danielson, Dr. Wojciech Giziewicz, Jianfei Wang, Jing Cheng (Thank you for everything! P.S. I love you!).

I would like to give my special thanks to Dr. Doug Gill and Dr. Mahmoud Rasras, and Dr. Sanjay Patel at Bell Labs (Lucent Technologies) for hosting me in the fall 2005. I learned a lot about waveguide measurements using LUNA OVA from you guys on that day trip! I appreciate it! Also, many thanks to Dr. Mihaela Balseanu, Dr. Li-Qun Xia, and Dr. Hichem M'saad at Applied Materials for hosting my summer internship in 2006. I have learned so much about PECVD from AMAT. I had a great time that summer! At MIT MTL, there are many great staff members who helped me with fabrications. I would like to thank Vicky Diadiuk, Bernard Alamariu, Paul Tierney, Eric Lim, Robert Bicchieri, Kurt Broderick, Donal Jamieson, Krisofor Payer, and Paudely Zamora for their supports which are essential for completion of part of the thesis work.

Lastly, I would like to thank my family and friends for their never-ending supports and encouragements throughout my life. Specially, I want to thank my mom and dad. I hope I can always make them happy and proud of me like this moment! Also, to my Grandpa, Grandma in Wuxi, Uncle Gao and Aunt Yu in Nanjing, your loves are oxygen to me!

All of you made my dream come true. I do wish you all can share the happiness and excitement I am experiencing right now. To my Aunt Xiaozheng Sun, if you could hear me from the heaven, you made me strong and taught me the meaning of life. This thesis is a tribute to you!

I am ready for a new journey and a new dream!

1.1. Challenges and opportunities in information technologies

The advance of modern electronic industry has totally revolutionalized the way human beings are living and thinking. Moore's law has been governing the scaling of computer chip for more than 40 years since Dr. Gordon E. Moore introduced it in 1965 [1]. It states that the number of integrated transistors on a silicon (Si) chip will be doubled every 18 months. Looking ahead as we are now at 45 nm technology node at the end of 2008, the trend of scaling of electronic transistor may go on for another decade before it meets the fundamental limit for the physical size of the device.

However, around 2002, people started to realize that while the number of the transistors was still increasing steadily, the realized performance was not improving as fast. The difference between the expected performance based on transistor numbers and the realized performance creates the so-called "Moore's gap" as shown in Figure 1.1.

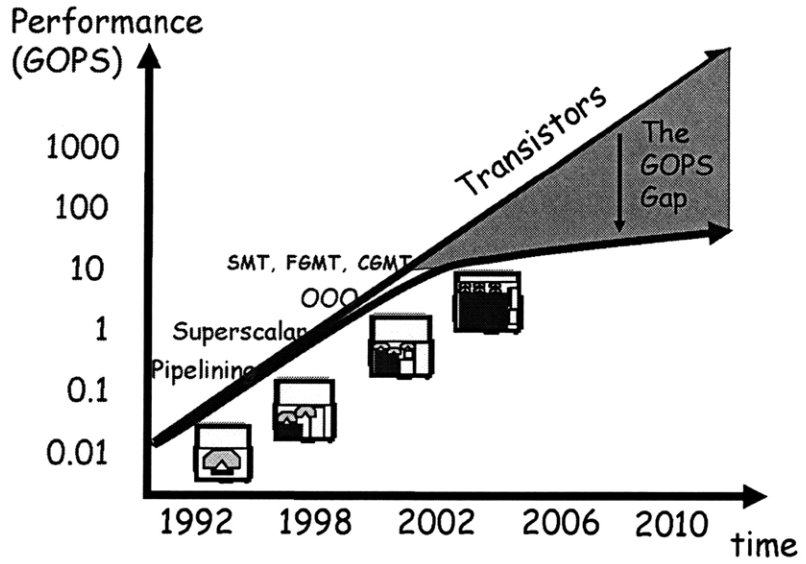

Figure 1.1. The "Moore's Gap" By Agarwal, MIT. GOPS: Giga Operations Per Second.

The fundamental cause for this "Moore's gap" is because the RC time constant for the Cu

interconnects currently used in transistors increases rapidly as the gate length decreases as shown in Figure 1.2. The RC delay of Cu interconnects has become the bottleneck for further bandwidth improvement. As the most recent development, Intel has terminated its plan for 4 GHz Pentium® 4 CPU in 2004, indicating the end of the campaign in bandwidth scaling of CPUs.

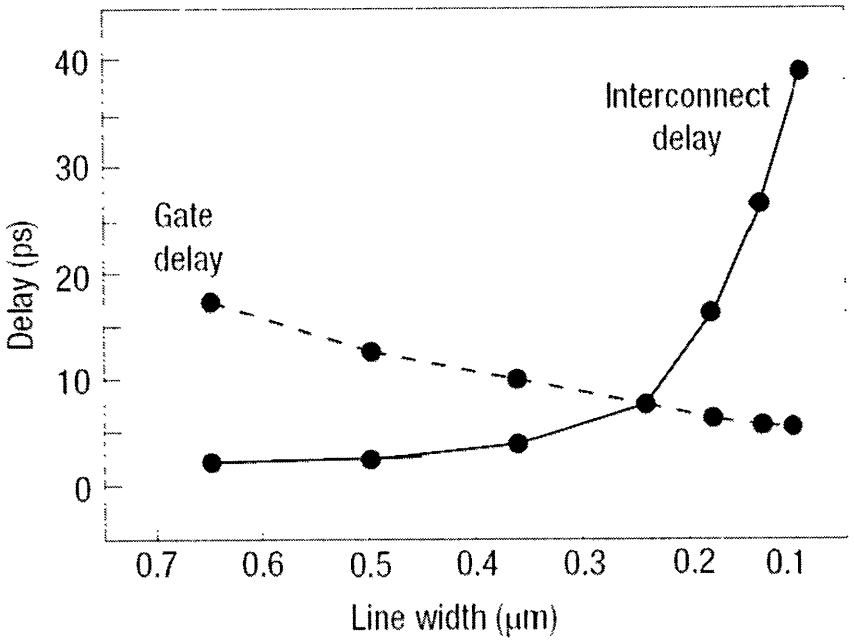

Figure 1.2. Interconnect delay due to the Cu RC time constant as a function of the gate line width (Figure taken from Ref. 2).

Information technologies will certainly not cease to evolve. Optical interconnect technology which uses photons as information carriers instead of electrons is believed promise to keep delivering higher bandwidths after Moore's law.

Optics and photonics are well established disciplinesl. The optical fiber system has been around for more than 20 years. Figure 1.3 is the chronological plot of the long haul telecommunication bandwidth of a single line, being that a Cu wire, a coaxial cable, or an optical fiber. Since the early 1980's, the introduction of optical fiber systems has brought us a tremendous improvement in bandwidth. The most important of all, the fiber optics technology is also scalable. Today, the bandwidth is already in terabit per second (Tbps). In retrospect, we discover that the

entry point for optical fiber systems was ~ 10 Mbps·km.

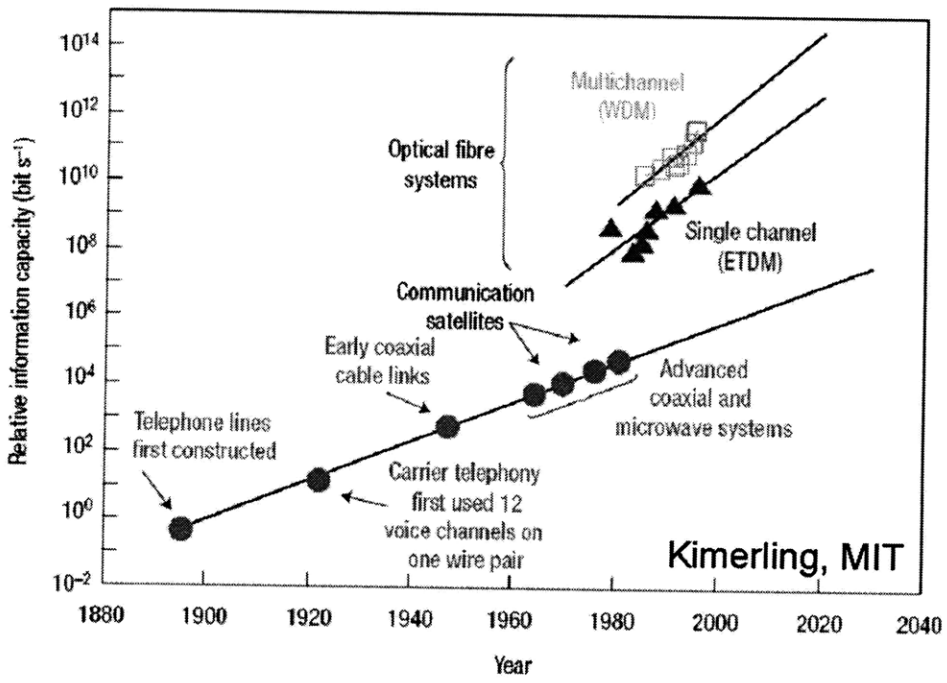

Figure 1.3. The chronological plot of the transmission bandwidth (bps) of a single line (Figure taken from Ref. 2).

If we can realize optical interconnect on a much smaller scale, e.g. on a single silicon chip, we can have the following benefits that electrons cannot be achieved with electrons:

- High data bandwidth
- No heat dissipation
- No electromagnetic interference (EMI)
- Leveraging CMOS technologies for silicon photonics

Silicon provides an ideal platform for high index contrast, chip level photonics integration. Silicon photonics based electronic-photonic convergence can leverage the large scale and low cost of CMOS technologies and has been widely recognized as a promising path. According to Kimerling et al., the economic entry point for silicon-based optical interconnects on silicon chip is 1 Tbps·cm which is equivalent to 10 Mbps·km [2].

Compared to electronic transistors, silicon photonics is still in its infancy. To demonstrate

the potential and to help the advancement of silicon photonics, the Defense Advanced Research Projects Agency (DARPA) created the Electronic-Photonic Integrated Circuits (EPIC) programs.

The MIT EPIC chip is designed to be a high-speed, optical RF channalizer as shown in Figure 1.4. Within a single silicon chip, a broadband RF signal (300 MHz to 2.2 GHz) is first brought on chip, modulated into optical signals, and split into different channels. In each channel, the optical signals are filtered, detected, and output digitally via transimpedance amplifiers (TIA). The whole system is essentially a high-speed analog-to-digital converter (ADC). As shown in Figure 1.5, current photonic devices are designed to be integrated with electronic transistors at pre-metal dielectric level using the Front-End of Line (FEOL) processes, this is because we can access to high quality single crystalline silicon and germanium for high performance photonic devices. In the future, researchers envision integrating photonics at interconnect level (BEOL) using polycrystalline and amorphous materials for both passive and active photonic devices where we can have more design space and flexibility for integration.

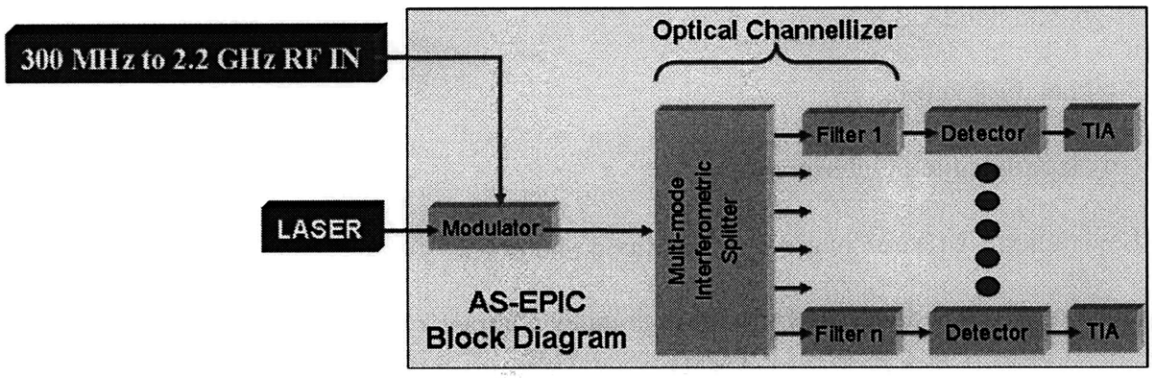

Figure 1.4. Block diagram of an integrated optical RF channalizer (Figure taken from Ref. 3)

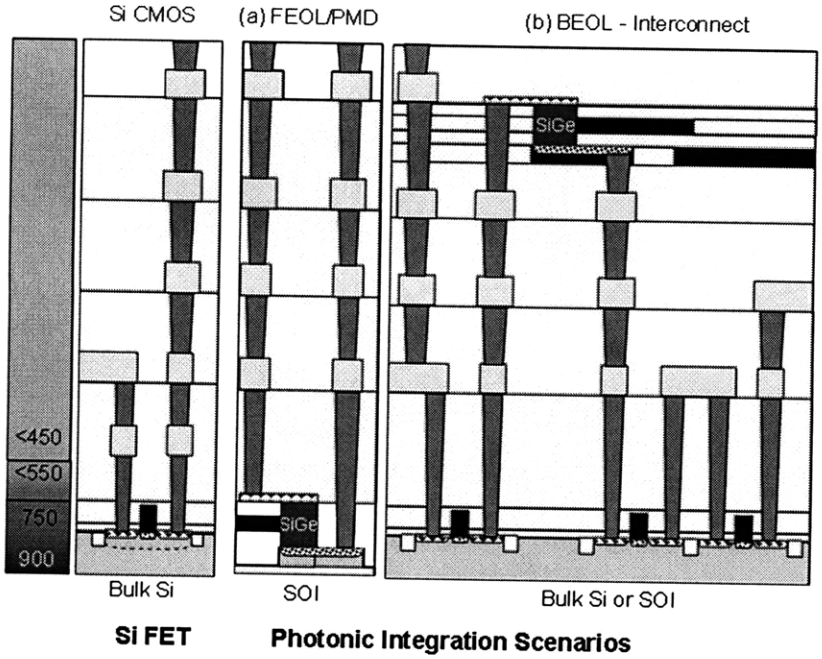

Figure 1.5. Current and future electronic-photonic integration schemes

Within the program, we have successfully established an open-architecture optical component library consisting of passive devices, such as low loss, high index contrast, silicon-based waveguides, couplers, MMI's, tunable filters; and active devices, such as high performance germanium-based (Ge) photodetectors as shown in Figure 1.6(a), GeSi EA modulators as shown in Figure 1.6(b), and Si EO modulators [4,5,6,7]. We have also demonstrated 3D photonic integration using high level deposited waveguides, such as amorphous silicon, as shown in Figure 1.7. Other indispensable silicon photonic devices, such as Si-based lasers, are currently under development at MIT as well as Stanford University, University of California, Santa Barbara, and Intel Corporation etc.

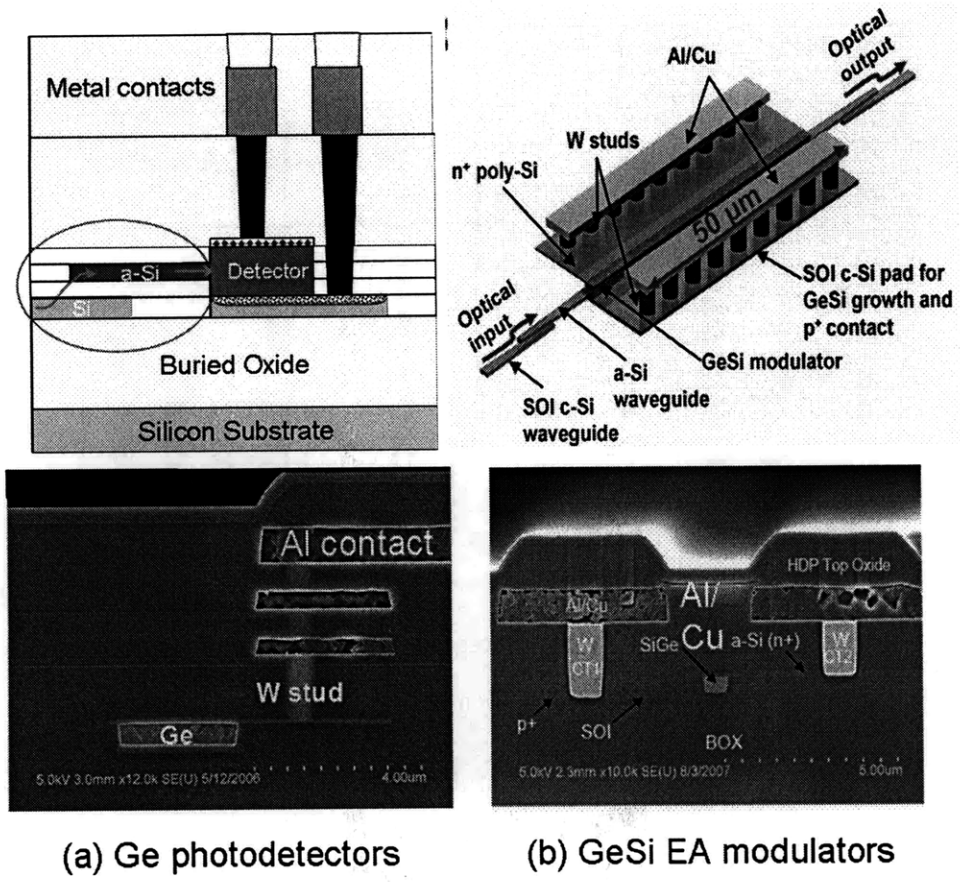

Figure 1.6. (a) waveguide-integrated Ge photodetector in a butt-coupled scheme; (b) Waveguide-integrated GeSi EA modulator in a butt-coupled scheme.

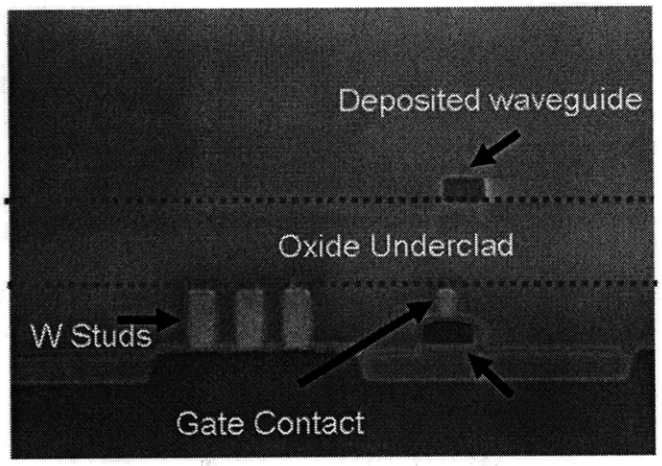

Figure 1.7. 3D photonic integration using deposited waveguides for high level optical routing.

1.2. Challenges in high index contrast (HIC) passivate photonic devices

This thesis focuses on low loss, high index contrast (HIC), silicon waveguide-based

passive photonic devices, such as waveguides, couplers, and filters. Waveguide's optical loss is the measure of the attenuation when light travels in waveguides. It is strongly dependent on waveguide materials, processes, and particularly the refractive index contrast (Δn).

1.2.1. Low loss and HIC optical waveguides

An optical fiber consist of Ge-doped SiO_2 core with un-doped SiO_2 cladding has Δn of 0.02. Its typical transmission loss is ~0.1 dB/km around 1550 nm. Chemical vapor deposition (CVD) developed in 1970's enabled high quality, low impurity containing optical fiber performs that allow extremely low materials absorption at 1310 nm and 1550 nm, the telecommunication wavelengths. The pulling process also results in defect-free, atomic flat fiber surface due to surface tension, thus minimizing the optical scattering loss.

A planar, HIC waveguide consist of silicon core (Si, n = 3.50) with silicon dioxide (SiO_2, n = 1.46) cladding has Δn of ~2. Currently, the optical transmission loss of a single mode channel Si/SiO_2 waveguide is about 1-10 dB/cm around 1550 nm, orders of magnitude higher than in an optical fiber. The typical planar waveguide fabrication utilizes current CMOS technology and involves photolithography and etching of high index silicon which gives rise to severe sidewall striation and roughness. Beside roughness scattering loss in HIC waveguides, for deposited waveguide materials, such as amorphous silicon (a-Si, n = 3.2 ~ 3.7), bulk absorption is another dominant loss mechanism. The typical loss in a single mode, PECVD a-Si waveguide is greater than 10 dB/cm.

For applications like an integrated optical delay line chip which normally have about 10 m long coiled single mode silicon waveguides and two fiber-to-waveguide couplers. The total insertion loss should be less than 3 dB. This requires that the waveguide loss to be on the order of

1 dB/10m or 0.001 dB/cm. Novel and CMOS-compatible processes are yet to be developed to achieve such low loss optical waveguides.

High optical loss not only means short signal transport distance or the necessity for optical amplifier which adds additional cost and complexity to the system, but also has huge impact on the performance of any waveguide-based devices, such as couplers and filters.

For example, the filter in Figure 1.8 is a 4th-order tunable optical filter designed by Bell Labs, Lucent Technologies [4]. It consists of two cascading Mach-Zehnder interferometers (MZI) with 4 integrated ring resonators. Without any waveguide loss, the ideal filter response characteristics consist of a flat-top like pass band, fast roll-off at the edge of the pass band, and the largest extinction ratio as shown in Figure 1.9. The increase in waveguide transmission loss will cause power imbalance in both arms of the MZI device, results in rounding of the pass band, degrading the filter performance in terms of bandwidth as well as extinction ratio. Realizing low loss in the constituent waveguides is the key to reduce the total insertion loss of the system and to obtain high performance filters and couplers.

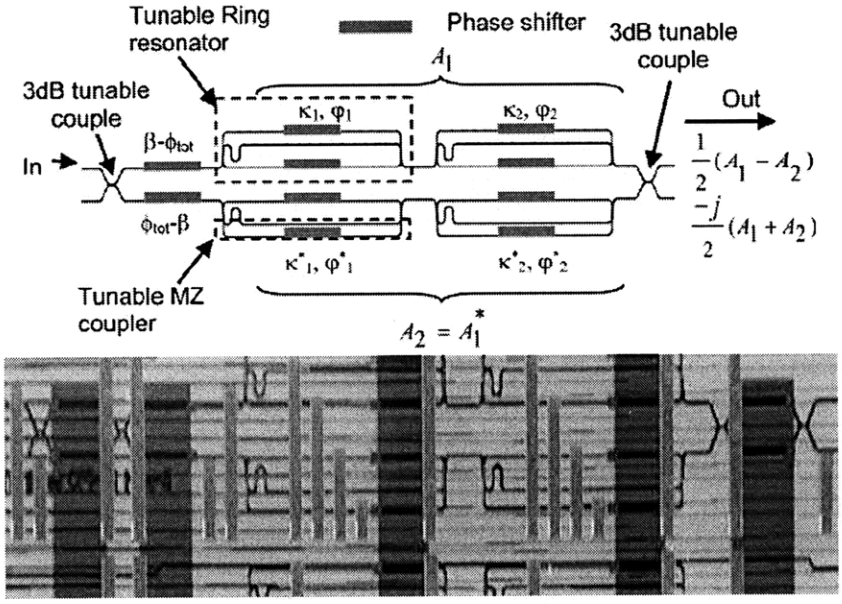

Figure 1.8. A 4th-order optical tunable filter based on Mach-Zehnder interferometer; the bottom image is the snap shot of the photo mask design (Figure adapted from Ref. 4).

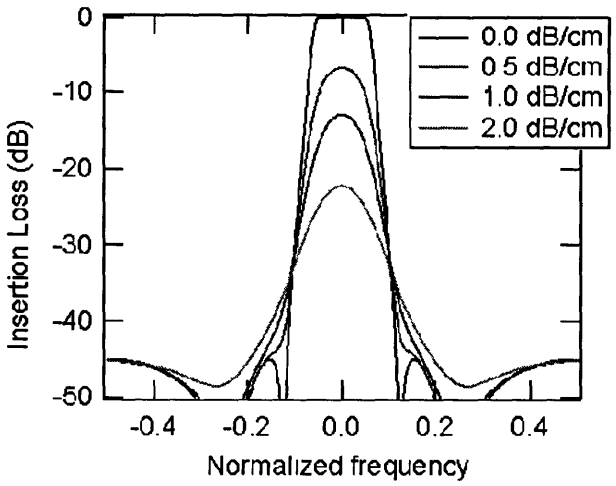

Figure 1.9. The simulated filter response for various waveguide transmission losses (Figure taken from Ref. 4).

1.2.2. Low loss and HIC optical waveguide couplers

Optical couplers are indispensable components in realizing photonic integration. Single chip integration not only can reduce assembling and packaging costs significantly, but also allowing high performance photonic devices, such as waveguide-integrated Ge-based photodetectors. For many discrete photonic devices on silicon, direct coupling among them will usually result in high and undesirable coupling loss, such as direct coupling between a single mode optical fiber and a single mode HIC optical waveguide due to large mode-size mismatch; sometimes, it is also impossible to couple two devices that are not on the same plane, for example, directly coupling between a SOI waveguide and Ge photodetector that is grown on the same SOI layer due to the height mismatch. High performance optical couplers need to overcome mode-size mismatch, mode-shape mismatch, mode-position mismatch, and polarization mismatch and achieve high efficiency mode transformation in a compact, low loss structures with good tolerance against fabrication variations.

In this thesis, high performance fiber-to-waveguide couplers, waveguide-to-waveguide vertical couplers, and couplers that can transform complex non-Gaussian modes with Gaussian

modes are sought.

1.2.3. Highly confined and low index guiding slot waveguides

Conventional optical waveguide guiding mechanisms are either based on total internal reflection in high index guiding waveguides or "total internal reflection"-like external interference effect in low index guiding waveguides, such as photonic crystal bandgap structures and anti-resonance reflecting optical waveguides. Those waveguide core dimensions are normally on the order of half the guided wavelength ($\lambda/2$). Confining optical modes in a much smaller dimension and particularly in low index materials can only be realized in slot waveguides. Slot waveguide consists on low index layers sandwiched by high index layers. This unique property of slot waveguides is believed to be ideal for electrically-pumped, Erbium (Er) based light emitters and lasers integrated on silicon platform. However, because the potential gain coefficient that can be realized in such system is small, reducing the cavity optical loss is very critical to realize net gain and eventually lasing.

In this thesis, different configuration of slot waveguide is proposed and relatively low loss optical transmission in slot waveguides is demonstrated. This validates and opens the possibilities for slot waveguide based silicon light emission applications.

1.2.4. Athermal electronic-photonic integrated circuits

Heat generation during operation in electronic chips is already so big a problem that it prevents clock frequency to be further scaled according to the roadmap. What's worse is that photonic devices are even more sensitive to temperature fluctuation due to the fact that refractive index is strongly dependent on temperature, as known as the thermo-optic (TO) effect. In an

electronic-photonic integrated circuit, heat generated by electronic transistor is dependent on the computation load and is not constant. Photonic devices, such as filters and modulators will require constant temperature control to stabilize the working wavelength, which adds extra costs and consumes more energy. For ultra-large scale integration of photonic devices, such as optical interconnect application in multi-core processors, tuning each individual filter up to tens of thousands at the same time is near impossible. Passive temperature compensation scheme is a must.

Silicon based photonic materials normally have positive TO coefficients while most of the polymeric materials have negative TO coefficients. In this thesis, we have proposed athermal operation based on TO compensation and demonstrated reduced temperature sensitivity using polymer cladding, proving polymer claddings is a viable path toward all passive athermal photonic circuits.

1.3. The layout of this thesis

In Chapters 2-5, we will review the waveguide fundamentals, the simulation methods that are used in this thesis work, the causes for optical transmission loss in waveguides, and the measurement methodologies. In Chapters 6-9, we will focus on the materials and processes development for low loss optical waveguides. In Chapters 10-12, we will go over the optical couplers and polarization rotators that are designed and demonstrated for realizing photonic integration. In Chapter 13, the temperature dependence of optical devices is discussed and athermal designs based on using negative TO coefficient polymers are suggested and demonstrated. Chapter 14 summarizes the thesis and gives some future directions.

(This page is intentionally left blank)

Chapter 2. Planar optical waveguides

This chapter is intended to introduce basic waveguide concepts and terminologies related to the research presented this thesis. Theese include waveguide materials, waveguide forms, and waveguide modes etc. Slot waveguides are a newly developed class of waveguides that has received significant attention and promise many applications in the future. The fundamentals of the slot waveguides will be explained in this chapter. The formulation mentioned in the following context is to help the follow of illustration. The detailed theories about optical waveguides, such as light propagation, dispersion, and coupling can be found in Ref. 8.

2.1. Silicon-based waveguide materials and refractive indices

As we have discussed in Chapter 1, silicon photonics is very attractive because it can leverage the large scale and low cost of CMOS technologies. CMOS compatibility is very important when we choose the waveguide materials.

According to Snell's law, light can be guided in high refractive index medium using the principle of total internal reflection (TIR) where the refractive light vanishes at the interface as shown in Figure 2.1. This corresponds to the condition that the incident angle of the light can not exceed the critical angle, $\theta \le \theta_1 = \sin^{-1}\sqrt{n_H^2 - n_L^2} \equiv \theta_{critical}$. This also defines the acceptance angle of the waveguide, or the numerical aperture (NA), $NA = \theta_{critical} \approx n_H \sqrt{\frac{2(n_H - n_L)}{n_H}}$. As a result, the refractive indices are also important parameters of the materials.

The common CMOS compatible waveguide materials and their corresponding refractive indices, n_R, are summarized in Table 2.1. The refractive indices quoted are all at 1550 nm.

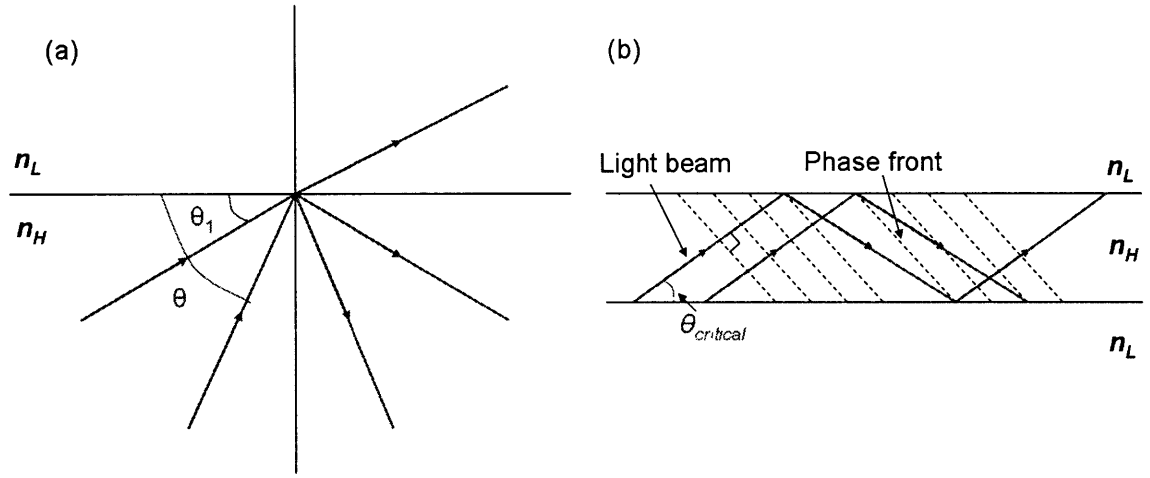

Figure 2.1. (a) Reflection at a dielectric interface where $n_H > n_L$; Total internal refractive in a slab.

Table 2.1. Summary of the waveguide materials and their refractive indices

Common waveguide materials	n_R	Comments
Single crystalline silicon	3.5	Readily available from SOI wafers
Poly-/amorphous silicon	3.2 ~ 3.8	Largely depending on processes
LPCVD silicon nitride	2.0	Stoichiometric
VTR silicon nitride	~ 2.2	Silicon rich
PECVD silicon nitride	1.8 ~ 2.2	Largely depending on processes
PECVD silicon oxynitride	1.5 ~ 1.7	Largely depending on processes
Thermal silicon dioxide	1.45	Often used as waveguide cladding layer
Polymer, e.g. PI, PMMA	1.4 ~ 1.5	CMOS back-end compatible, cladding layer

2.2. Optical waveguide forms

There are many optical waveguide forms suitable for different applications. For high index guiding waveguides that operate under TIR principle, four designs are commonly used:

- Slab waveguides where a high index slab layer is sandwiched by two low index layers;
- Strip-loaded waveguide where a strip of high index layer is placed on top of a low index slab layer to provide lateral optical confinement in the low index slab;
- Ridge waveguides where the high index layer is partially etched to create two index contrast sidewall interfaces to provide lateral optical confinement;

- Channel waveguides where the two sidewalls of the high index layer are completely etched. Sometimes, also called "strip waveguides".

These designs are presented in Figure 2.2. Channel waveguides, or sometimes called strip waveguides, are able to offer the highest optical confinement in the most compact size. This thesis focuses exclusively on the channel waveguide form.

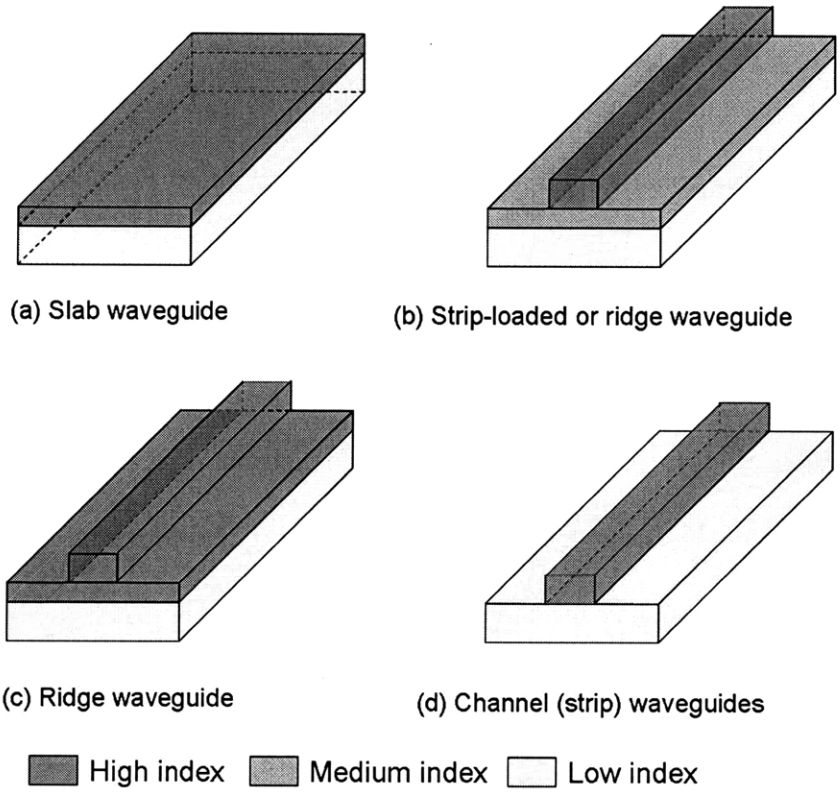

Figure 2.2. Optical waveguide forms based on high index guiding principle.

There are also low index guiding waveguides, such as Photonic Bandgap-based waveguides (PBG waveguides) and Anti-resonant reflecting optical waveguides (ARROW waveguides). They are based on the external inference effect that creates TIR-like guiding mechanism.

2.3. Optical modes

The plane wave can be described as

$$u(r,t) = A\exp\left(i(k\cdot r - \omega\cdot t)\right) \tag{2.1}$$

where $\boldsymbol{k}$ is the wave vector, ω is the angular frequency, and A is the amplitude. $Ae^{ik\cdot r}$ is also called the complex amplitude where $\boldsymbol{k}\cdot\boldsymbol{r}$ is the phase of the plane wave. The propagating wave has all matched phase for constructive interference inside the waveguide. This means the phase difference is always the integral numbers of 2π. For example, in a slab waveguide as in Figure 2.2(b), the phase-matching condition for a specific propagation angle, θ, is

$$\tan\left(kn_H a\sin\theta - \frac{m\pi}{2}\right) = \sqrt{\frac{2(n_H^2 - n_L^2)}{2n_H\sin^2\theta} - 1} \tag{2.2}$$

where a is the half thickness of the slab. Notice that the allowed propagation angles are discretized and are called "optical modes". At $m = 0$, the optical field distribution that satisfies Equation 2.2 is called the fundamental mode. For $m \geq 1$, they are called the higher order modes.

Analytical methods, such as the Marcatili's method [9], the Kumar's method [10], and the effective index method [11], can solve three-dimensional waveguides, e.g. rectangular waveguides with different aspect ratio, and ridge waveguides. For more complicated waveguide structures with arbitrary index profile, numerical methods should be used, such as finite element method and finite difference method.

Commercial software packages such as RSoft's latest FemSIM, Photon Design's FIMMWave, and Apollo Photonic Suite are great tools to obtain optical modes when designing waveguides. Figure 2.3 is an example of using FIMMWave to obtain all the guided TE modes (optical intensity and electric field profiles) in a 1000 nm (w) × 200 nm (h) silicon channel waveguide (n = 3.5) cladded with SiO_2 (n = 1.45). The waveguide is found to support three TE

modes. Their effective indices for modes of m = 0, 1, 2 are 2.70, 2.37, and 1.76, respectively. Figure 2.4 summarizes all guided TM modes within the same waveguides. Only two TM modes are found. The effective indices for modes of m = 0 and 1 are 1.82 and 1.56, respectively.

The fundamental modes in channel waveguides have the highest confinement factors among all guided modes. They are capable of having low loss optical transmission and doing sharp turns, ideal for applications in compact photonic integrated circuits. The details about transmission loss and bending performance will be discussed in 0. This thesis focuses primarily on designs, processes, and integration for single mode HIC channel waveguides.

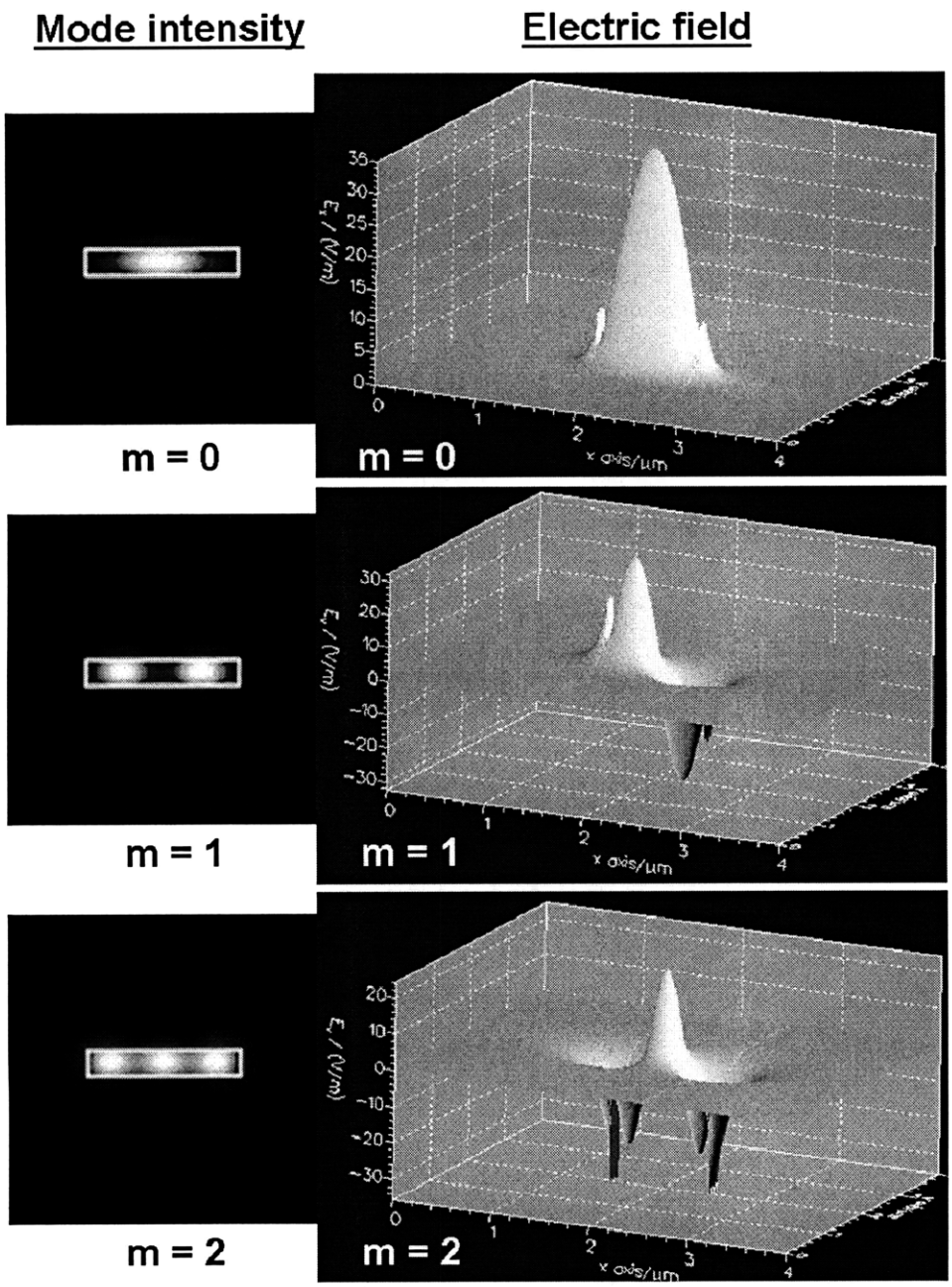

Figure 2.3. All guided TE-polarization modes of a 1000 nm × 200 nm Si waveguides. (left) optical intensity and (right) electric field distribution. m = 0 is the fundamental mode; m = 1 and 2 are the 2nd-order and 3rd-order modes. Simulation is done using FIMMWave.

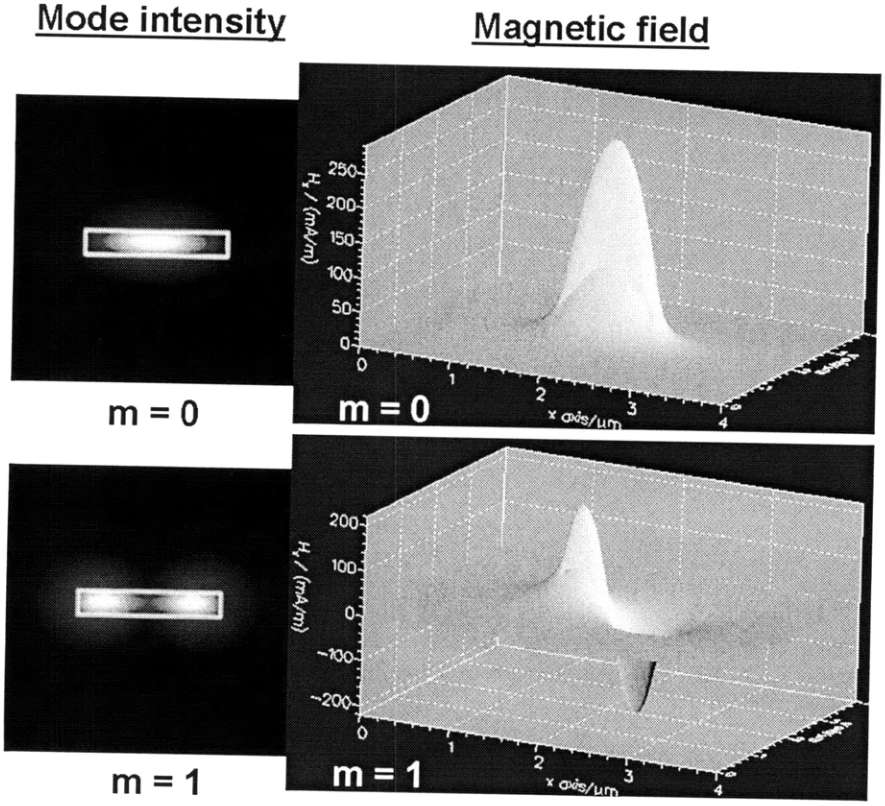

Figure 2.4. All guided TM-polarization modes of a 1000 nm × 200 nm Si waveguides. In this case, only two modes are supported. $m = 0$ is the fundamental mode and $m = 1$ is the 2nd-order mode. Simulations are done using FIMMWave.

2.4. Summary

In this chapter, we have introduced the fundamentals about optical waveguides, especially silicon-based CMOS compatible waveguides. Different waveguide forms and the concept of optical modes are briefly discussed with simple examples. These terminologies will occur multiple times in throughout this thesis. Low loss optical transmission in single mode, HIC channel waveguide is the focus of this thesis work.

(This page is intentionally left blank)

Chapter 3. Review of the simulation methods used in this thesis

In this chapter, the simulation methods used in this thesis work will be briefly reviewed. The commercial software packages are FullWave and BeamProp from RSoft; FIMMWave and FIMMProp from Photon Design; and Apollo Photonic Suite from Apollo. They are based on Finite-Difference Time-Domain method (FDTD), the Finite Difference Beam Propagation Method (FD-BPM), Eigenmode Expansion method (EME), and Finite Element Method (FEM). Because the detailed improvement and implement of each method are mathematically intense, only the fundamentals of the three methods will be reviewed and compared.

The above four methods can be categorized conveniently into two categories: time-domain and frequency-domain approaches.

In time-domain, FDTD solve Maxwell's equations directly and has no inherent accuracy limit. It can offer the wide band information when a time pulse is used in the simulation. It is very versatile and robust. The only drawback is that it is extremely time and memory consuming.

Frequency domain approaches can only simulate one particular wavelength each time. The most fundamental one is the FEM mode solver. It gives the eigenmodes in an infinite long waveguide structure. These modes can be used for EME and BPM. BPM is one more step approximation from the mode solver. It requires the structure in paraxial direction is slow varying, such as taper structures, and solves the slow-varying envelope of the field, taking advantage of the large propagation steps in slow-varying structure. If the structure in paraxial direction is more step-like, such as couplers and gratings, EME is more suitable given that the complete mode set can be obtained. Normally a complete mode set can be obtained in 2D structures, so this approach can be a good approach for 2D simulation. In 3D, it is very difficult to calculate multiple modes

especially when leaky and radiation modes are present. Sometimes, in order to save computation time and power, one will have to use truncated mode set instead of the complete mode set; however, this give rises to numerical errors.

3.1. Finite-Difference Time-Domain method (FDTD)

A complete description of the FDTD method can be found in Ref. 12. Basically, the time-dependent Maxwell's curl equations govern the behavior of electromagnetic field (EMF). In free space,

$$\frac{\partial E_z}{\partial t} = \frac{1}{\varepsilon_o}\frac{\partial H_y}{\partial x} \tag{3.1}$$

$$\frac{\partial H_y}{\partial t} = \frac{1}{\mu_o}\frac{\partial E_z}{\partial x} \tag{3.2}$$

where $\boldsymbol{E_z}$ and $\boldsymbol{H_y}$ are electric and magnetic vector field, respectively; ε_o is the electric permittivity of free space, ~ 8.854×10^{-12} F/m; and μ_o is the magnetic permeability of free space, $4\pi \times 10^{-7}$ H/m.

Instead of solving the equation rigorously, the derivatives are approximated using the "finite-difference" (FD) approximations. As shown in Figure 3.1, the derivative, $f'(x_o)$, is approximated by $f(x_o+\Delta x/2)$ and $f(x_o-\Delta x/2)$:

$$f'(x_o) = \frac{df(x_o)}{dx} = \frac{f(x_0 + \Delta x/2) - f(x_0 - \Delta x/2)}{\Delta x} \tag{3.3}$$

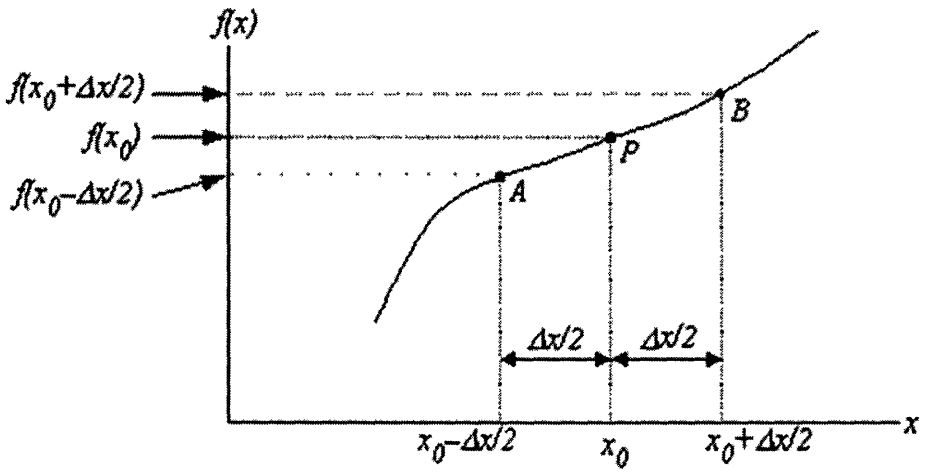

Figure 3.1. Illustration of the finite difference approximation of the derivative $f'(x_o)$ in terms of $f(x_o+\Delta x/2)$ and $f(x_o-\Delta x/2)$.

Then, Equations 3.1 and 3.2 can be expressed as:

$$\frac{E_z^{n+1/2}(k)-E_z^{n-1/2}(k)}{\Delta t}=\frac{1}{\varepsilon_o}\frac{H_y^n(k+1/2)-H_y^n(k-1/2)}{\Delta x} \tag{3.4}$$

$$\frac{H_y^{n+1}(k+1/2)-H_y^n(k+1/2)}{\Delta t}=-\frac{1}{\mu_o}\frac{E_z^{n+1/2}(k+1)-E_z^{n+1/2}(k)}{\Delta x} \tag{3.5}$$

where n actually means the time, $t=\Delta t\cdot n$ and k actually means the distance $x=\Delta x\cdot k$. For lossy media and high order dimension problems, the corresponding Ampere's law and Faraday's law should be used.

The grid point setup for 3D simulation is commonly known as the Yee lattice with an origin at (i, j, k) as shown in Figure 3.2 [13]. In space, every ***E*** field is located 1/2 cell width from the origin in the direction of its orientation; every ***H*** field is offset 1/2 cell. In time, the calculations of ***E*** and ***H*** are also interleaved. At a particular time step, all the ***E*** components are calculated and stored using the precious ***H*** data; then all ***H*** components are recalculated using the stored ***E*** data; and the cycle starts again for all ***E*** components using the newly computed ***H*** data.

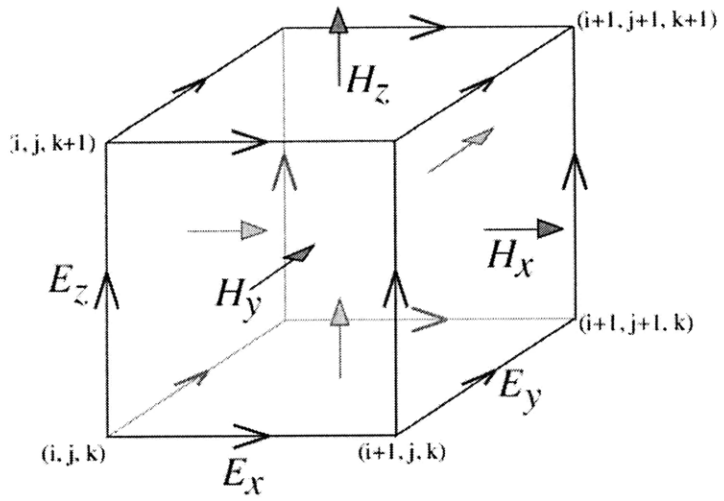

Figure 3.2. The electric and magnetic field vectors in a cubic unit cell of the Yee lattice. (Courtesy of Steven G. Johnson)

Absorbing boundary conditions are required to eliminate unwanted reflections at open boundaries. Those reflections sometimes cause numerical errors in simulations. One of the most used method is the Perfectly Matched Layer (PML) introduced by Berenger [14]. PML can be viewed as a specially designed absorbing material with "fictitious" electric permittivity and magnetic permeability. In a PML, any incident waves from a non-PML medium will be completely absorbed and thus has no reflection at the interface.

The space grid size is chosen such that the EMF does not change significantly. For example, the maximum grid size in each direction, Δx, Δy, and Δz, should be no greater than 1/20 of the wavelength [12]. This also determines the maximum time step, Δt, that can be used. In a homogeneous medium, $\Delta t < \frac{1}{c}\sqrt{(\Delta x)^2 + (\Delta y)^2 + (\Delta z)^2}$ e.g. $\Delta t = \frac{\Delta x}{c\sqrt{3}}$ or $\Delta t = \frac{\Delta x}{2c}$ [12]. As the discretizations in both space and time approach zero, the solutions of each field component becomes exact. As the result, FDTD method has no inherent accuracy limit. On the other hand, the way the N^{th} grid (N-dimension) is setup in the entire computation space, the discretizations, and

the propagation in time step result in extremely long computation time and large computation memory consumption, making it very difficult to simulate large structure/distance.

The frequency domain calculation can be obtained in one simulation using a broadband Gaussian source, $f = \exp\left[-\frac{(t-t_o)^2}{\sigma^2}\right]$. The range of frequency content is determined by the pulse width, σ. This is particularly useful for simulations on resonators, directional coupler, and Mach-Zehnder interferometers where the exact resonance response is not known. Its time domain nature also gives the evolution of the EMF in the system. A flow chart of FDTD analysis is shown in Figure 3.3.

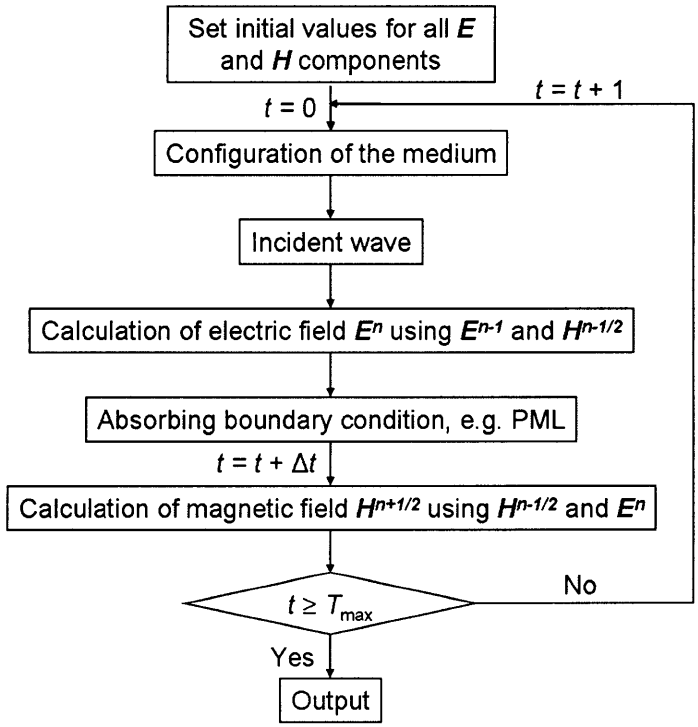

Figure 3.3. The flow chart of FDTD simulation (Adapted from Ref. 15).

3.2. Finite-element mode solver (FEM)

The waveguide analyses and derivations based on solving the homogeneous core planar waveguides will have difficulties in solving inhomogeneous waveguides with arbitrary index

profiles, such as the graded index planar waveguides. Directly solving the corresponding Helmholtz Equations is extremely difficult if not impossible. The finite-element method (FEM) is a numerical technique that can provide approximated solutions to those partial differential equations (PDE). The common methods include the Variational formulation, the discretization, and the choice of a basis set. Although FEM is intended to solve complicated waveguide structures, it can be used to analyze homogeneous planar waveguides as well. For polarization dependent mode problems, several vectorial FEM have been developed [16,17,18], but it is found that scalar wave solutions (the Helmholtz Equation with respect to x and y directions) can have sufficient accuracy [19]. The scalar wave equation is not solved directly. Instead, the solutions are obtained using Variational functional of the electric field. In addition, if the structure has symmetry, then the computation domain can be reduced according to the order of the symmetry.

First, the computation domain is discretized into small triangular grids. The boundaries should be placed far away from the waveguide core so the EMF amplitude becomes nil at the boundaries. The electric field in each region is approximated by a linear function of x and y and connected at the nodal point. The form of the Variational functional is rewritten accordingly. In the end, a global N^{th}-order linear simultaneous equation can be constructed with each element representing the contribution of each electric field component. Solving the global matrix using numerical calculation libraries such as Jacobi's method gives the eigenvalue for the electric field distribution. The detailed discussion can be found in Ref. 15.

3.3. Beam Propagation Method (BPM)

The beam propagation method (BPM) is an approximation technique used to solve the Helmholtz equation for light propagation in slowly varying optical waveguides. The detailed formalisms and derivation can be found in Ref. 15. The most important equations are selected and

represented as follows.

The scalar wave equation, or the Helmholtz equation, can be expressed in 3D as

$$\left(\nabla^2 + k^2 n^2\right)E = 0 \tag{3.6}$$

where ∇^2 is the Laplacian operator, $\nabla^2 = \frac{\partial^2}{\partial x^2} + \frac{\partial^2}{\partial y^2} + \frac{\partial^2}{\partial z^2}$; k is the wave number, $k = \omega / c_o$; and n is the refractive index of the core.

One important assumption of the BPM is that the electric field, $\boldsymbol{E}$, can be separated into the axially slowly varying envelop term of φ and the rapidly varying term of exp(-*jknz*) as $E = \varphi \exp(-jknz)$. Also, when light is assumed to be weakly guided, it is approximated that $(n^2 - n_o^2) \approx 2n_o(n - n_o)$. As the result, Equation 3.6 can be rewritten as

$$\nabla^2 \varphi - j2kn_o \frac{\partial \varphi}{\partial z} + k^2 (n^2 - n_o^2)\varphi = 0 \tag{3.7}$$

$$\frac{\partial \varphi}{\partial z} = -j \frac{1}{2kn_o} \nabla^2 \varphi - jk(n - n_o)\varphi \tag{3.8}$$

where $\nabla^2 = \frac{\partial^2}{\partial x^2} + \frac{\partial^2}{\partial y^2}$ and n_o is the refractive index of cladding layer. The elimination of the term $\frac{\partial^2 \varphi}{\partial z^2}$ is known as the paraxial approximation, $\frac{\partial^2 \varphi}{\partial z^2} << 2kn_o \left|\frac{\partial \varphi}{\partial z}\right|$, meaning the propagation is restricted to a narrow range of angles along the *z* axis. The first term on the right hand side in Equation 3.8 describes the free-space light propagation in the medium of n_o; the second term shows the influence of the medium of *n*. However, this separation of two effects is only valid for small distance along the *z* axis based on the slowly varying approximation.

The numerical solution of BPM can be obtained using the finite difference approach, e.g. the Crank-Nicholson scheme [20]. One can obtain the following:

$$\varphi_{i-1}^{m} + q_i^m \varphi_i^m + \varphi_{i+1}^m \equiv d_i^m \tag{3.9}$$

where i and m are grid points along x- and z- directions, respectively ($i = 0 \sim N$; $m = 0 \sim M$); and

$$q_i^m = -2 + k^2(\Delta x)^2\left[\left(n_i^{m+1/2}\right)^2 - n_o^2\right] + j\frac{4kn_o(\Delta x)^2}{\Delta z} - j2kn_o(\Delta x)^2\alpha_i^{m+1/2}.$$

One common boundary condition for FD-BPM is the transparent boundary condition (TBC) [21,22]. In this method, the electric field at the boundary, i = N, is assumed to be the plane wave with certain amplitude and direction: $\varphi = C\exp(-jkx)$ where C and k are complex numbers. The basic idea is to let the electric field at the boundary (radiation) freely escape the computational domain.

Later improvements over the FD-BPM include the vectorial BPM that can solve the transverse electric and magnetic fields independently [23], the bi-directional BPM that handle the simultaneous propagation along the negative z axis (e.g. reflections at interfaces) [24], and the wide-angle BPM that can remove the paraxiality assumption and allow a cone of ± 90° from the z axis [25].

For ultra high index contrast optical waveguides (Δn > 0.5) in 3D, the polarization coupling always exists so the polarization states are hybrid. Although the 3D full vectorial BPM is found to be very unstable for such applications, if we assume the coupling is weak enough to be negligible, then the two polarizations can be treated independently using a semi-vector BPM. This method is robust for planar waveguides with Δn up to 2.0, e.g. Si/SiO_2 waveguides, and it has been used extensively in this thesis.

3.4. Eigenmode Expansion Method (EME)

The Eigenmode Expansion Method can be used to solve long, slowly varying structures efficiently and provide the rigorous solution of the Maxwell's Equations. The comprehensive

description of EME method can be found in Ref. 26. The following derivations follow Ref. 27 closely.

In a z-invariant structure, e.g. an optical waveguide with uniform refractive index in the z direction, the time harmonic ($\exp(i\omega t)$) eigensolution of the Maxwell's Equations has the form of $E(x,y,z,t) = \varphi_m(x,y)\exp(i\beta_m z)$, where φ_m is the eigenfunction and β_m is the eigenvalue. There are a finite number of guided modes, leaky modes, and an infinite number of radiation modes. Together, they form a complete basis set for the solution of the Maxwell's equations:

$$E(x,y,z) = \sum_{k=1}^{M}(a_k e^{i\beta_k z} + b_k e^{-i\beta_k z})E_k(x,y) \tag{3.10}$$

$$H(x,y,z) = \sum_{k=1}^{M}(a_k e^{i\beta_k z} - b_k e^{-i\beta_k z})H_k(x,y) \tag{3.11}$$

where a_k and b_k are the forward and backward amplitude; and β_k is the propagation constant, $\beta_k = \frac{2\pi n_{eff}}{\lambda}$. These two equations are an exact solution of the Maxwell's Equation. They describe both the forward and the backward propagating modes, meaning EME algorithm is readily bi-directional. All the modes of ***E(x,y)*** and ***H(x,y)*** are orthogonal to each other.

Take the electric field as an example. Using the scattering-matrix theme, a waveguide joint is shown in Figure 3.4. The boundary conditions for the electric field determine that the tangential electric field must be continuous: $E_t^I = E_t^{II}$, or

$$\sum_{k=1}^{N}(a_k^I e^{i\beta_k z} - a_k^{II} e^{-i\beta_k z})E_k^a(x,y) = \sum_{k=1}^{N}(b_k^I e^{i\beta_k z} - b_k^{II} e^{-i\beta_k z})E_k^b(x,y) \tag{3.12}$$

Together with the orthogonality condition, one can show that

$$\begin{pmatrix} a^{II} \\ b^{I} \end{pmatrix} = S\begin{pmatrix} a^{I} \\ b^{II} \end{pmatrix}, \text{ where} \tag{3.13}$$

$$S = \begin{pmatrix} e^{i\beta_1 z} & 0 & 0 & \cdots \\ 0 & e^{i\beta_2 z} & 0 & \cdots \\ 0 & 0 & e^{i\beta_3 z} & \cdots \\ \vdots & \vdots & \vdots & \ddots \end{pmatrix} \tag{3.14}$$

where S is the scattering matrix, the S-matrix, for the joint. S can be solved easily using the computed eigenmodes. With the use of the complete basis set of eigenmodes for the S-matrix, one can obtain the exact solution for the Maxwell's Equation. However, in practice, a truncated S-matrix is used and this results in numerical errors.

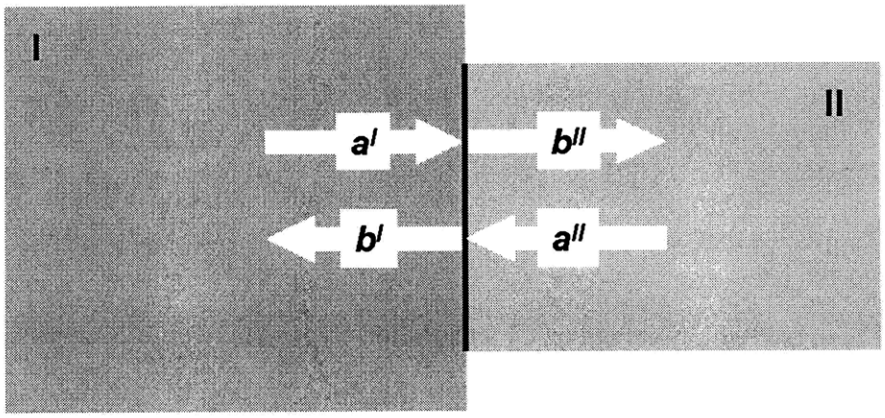

Figure 3.4. Mode coefficients at a joint in waveguides I and II in an S-theme.

For boundary conditions for EME method, the TBC is used at the input and output interfaces of the computation domain. PML is used inside the computation domain to obtain the complete basis set for the eigenmodes.

Using full vectorial EME, both TE and TM polarization can be simultaneously calculated by the S-matrix. EME is also capable of doing wide-angle simulation by using more corresponding modes. On the other hand, the accuracy of EME depends on finding the correct basis set of eigenmodes. For large cross-section structures which can support many guided modes and leaky modes, the computation time scales on the order of N^3 in terms of optical resolution [27].

3.5. Summary

In this chapter, we have briefly reviewed 4 different numerical methods that have been applied in this thesis work. The photonic simulation suites that are based on these methods generally offer a very convenient CAD tool to generate waveguide structures and mesh/grid setup. Although each tool is easy to use, the operator must have good understandings in order to pick the best method to his/her best advantage.

(This page is intentionally left blank)

Chapter 4. Optical waveguide transmission loss

Optical waveguide transmission loss is commonly defined in decibels (dB) per unit length, e.g. dB/cm where dB is given by the common logarithm of the relative power ratio.

$$dB = 10\log\left(\frac{P_{out}}{P_{in}}\right) \tag{4.1}$$

The presence of optical loss not only provides unwanted signal attenuation while traveling inside the waveguides, but also affects the performance of many waveguide-based optical devices, such as filters and couplers. Compared to optical fused silica fibers which only has a fraction of dB per kilometer, high transmission loss associated with silicon-based waveguides is due to the high index contrast in these waveguides and their planar geometry. This chapter is dedicated to understand various loss mechanisms and to provide information to assist in reduction or even elimination of waveguide loss.

4.1. Optical loss mechanisms in channel waveguides

Optical waveguide transmission loss is strongly dependent on waveguide fabrication processes. Silicon-based planar optical waveguides can be fabricated with a minimal 8-step process flow. Generally, starting with a silicon substrate, a SiO_2 layer is first deposited on the front side or thermally grown on both sides of the substrate. SiO_2 has a low refractive index of 1.46 and can provide optical insulation between high index contrast waveguides and the silicon substrate (n = 3.5). Then, various waveguide core materials are deposited on top of the under cladding layer. Using silicon-on-insulator substrate, one can access to crystalline silicon as waveguide core material directly. There are several techniques for pattern transfer: photolithography provides high-throughput, high consistency, and standardized platform; electron-beam lithography has also

been widely used in academic environments because it has the relative low maintenance cost and does not require making physical photomask; molding techniques, used to fabricate plastic optical waveguides, have been adapted to fabricate silicon waveguide [28]. The photoresist patterned waveguide layer is etched into either ridge or channel waveguides. Finally, after the photoresist is stripped and the wafer is cleaned, another low index top cladding layer is deposited to protect the waveguide devices. The process flow is illustrated in Figure 4.1.

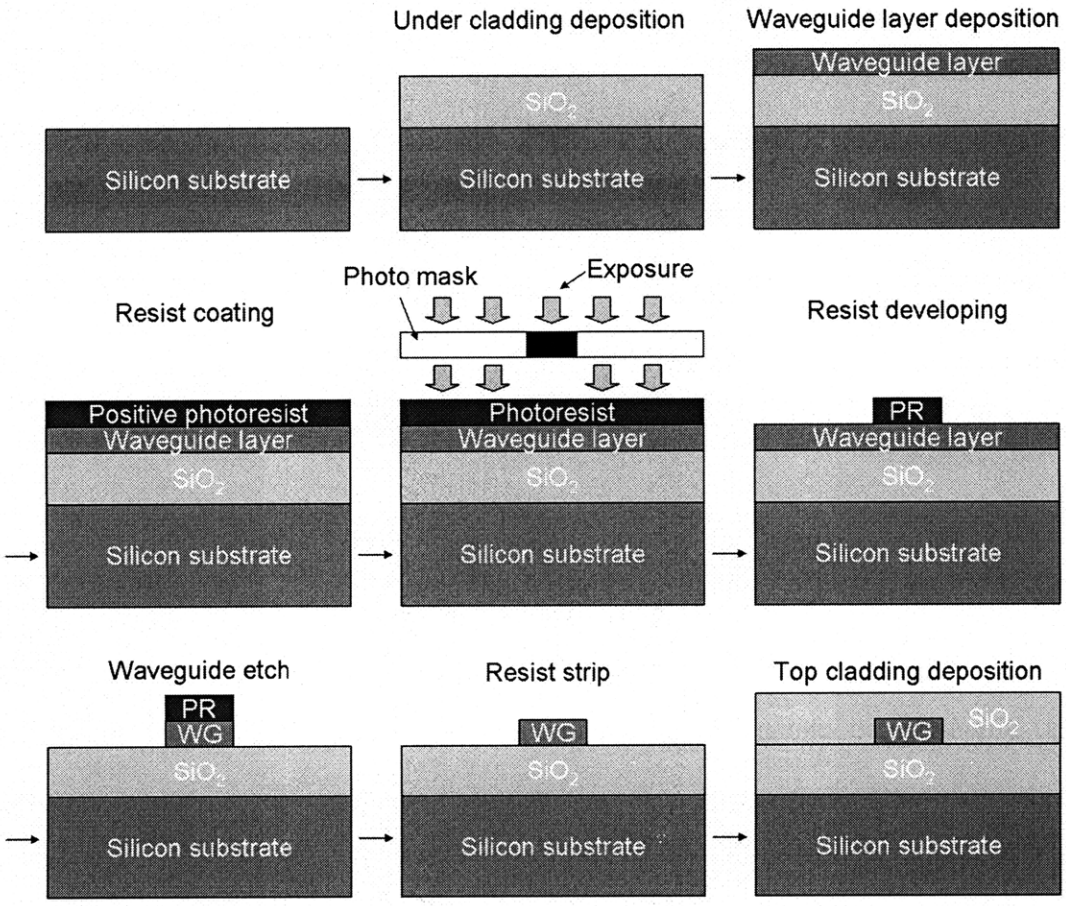

Figure 4.1. Schematic representation of channel waveguide fabrication process steps. Note that positive photoresist is used in this example.

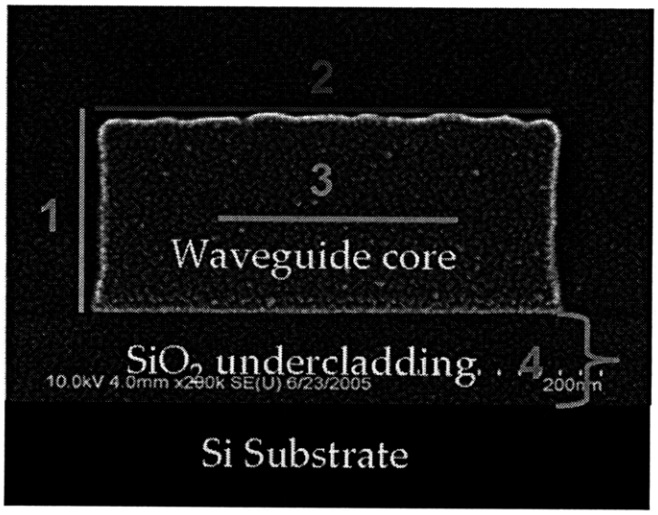

Figure 4.2. Illustration of the dominant waveguide transmission sources using a cross-sectional SEM image of a deposited a-Si waveguide.

Figure 4.2 is an illustration of the four dominant waveguide transmission loss mechanisms that we can identified in an optical waveguide. They are:

1. Side-wall roughness scattering;
2. Top surface roughness scattering;
3. Material absorption (including surface states or free carrier absorption);
4. Substrate leakage.

Other waveguide loss sources that are listed above but will be important in many cases are:

5. Waveguide bend loss (radiation loss);
6. Waveguide corner imperfection;
7. Trapped Air voids at waveguide sidewall during top cladding deposition;
8. Any other fabricated caused effective index variation that may lead to reflection or scattering.

The top surface roughness can be reduced using chemical-mechanical polishing (CMP). In the following context, transmission loss due to sidewall roughness scattering, material bulk absorption, bending, and substrate leakage will be discussed in details.

4.2. Sidewall roughness scattering loss

Waveguide sidewall roughness often presents as vertical line striations. It originates from the line edge roughness (LER) in photoresist during the photoresist exposure and develop steps and this LER in photoresist is transferred to underlying waveguide during dry etch. LER is primarily caused by the standing wave effect and aggressive develop process. The light intensity variation along the direction perpendicular to the photoresist surface creates unevenly exposed interface, which makes critical dimension control difficult and creates line edge roughness. Prebake and postbake processes can reduce this effect to some extent. Because aggressive develop dissolves the bulk polymer more than that at the interface, it also creates "scum" (residue photoresist) along the photoresist/substrate interface. LER is also affected by the exposure dose, the absorbance of the photoresist, and the glass transition of the photoresist. Sequentially, anisotropic dry etch turns LER in photoresist into sidewall line striation. One example of as-etched SOI silicon waveguide is shown in Figure 4.3 where vertical line striations are clearly visible.

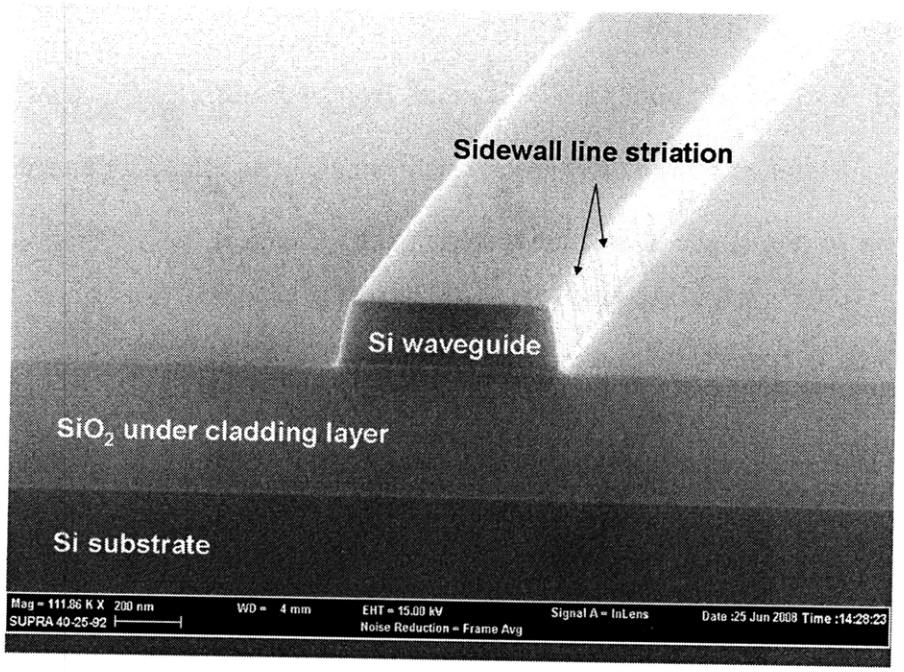

Figure 4.3. An example of as-fabricated SOI waveguide. The sidewall line striations are clearly visible.

There are several theories which provide mathematical description of sidewall roughness scattering, including the most recent 3D volume current method (VCM) [29,30,31,32]. According to VCM, a small index perturbation inside a waveguide, in our case at the waveguide sidewall, is an induced polarization current source and acts as the radiation source from the waveguide. Basically, the sidewall roughness loss (α) has a positive correlation with (1) Sidewall roughness RMS value (σ) where α is proportional to σ^2. (2) Sidewall optical intensity. The sidewall roughness scattering affects mostly the TE mode in a rectangular HIC waveguide. The boundary condition on the electric field states that there is no discontinuity in the transverse component of the electric field across an interface, or $n_1 \cdot E_{\parallel,1} = n_2 \cdot E_{\parallel,2}$. The index difference between waveguide core and cladding layer determines that there is discontinuity in the electric-field at the interface. α is proportional to the normalized optical intensity, $|E|^2$. (3) Index contrast at sidewall interface. α is proportional to $\left(n_{core}^2 - n_{cladding}^2\right)$. The comprehensive understanding about sidewall roughness scattering provides paths to reduce this effect by design and process optimizations.

4.3. Materials bulk absorption loss

Material bulk absorption can be caused by many different mechanisms, such as band-to-band transition and free carrier absorption in single-crystalline semiconductors, dangling bond absorption in non-single-crystalline materials, and chemical bond vibration absorption in dielectric materials.

Many optical devices operate based on band-to-band transition, or bandgap absorption, such as diode laser, photodetector, and electro-absorption modulators. Single-crystalline silicon has an indirect bandgap of 1.1 eV. It is transparent to light with wavelength larger than 1.2 μm, which is ideal for operations around 1550 nm.

Unlike in single-crystalline silicon where every Si atom is tetrahedrally bonded with four nearest neighbor silicon atoms in an ordered lattice, amorphous silicon does not have long range ordered structures. Distortion of Si-Si bond angle and length creates band tails into the bandgap. In this case, the bandgap of amorphous silicon is described as the mobility gap and is smaller than 1.1 eV. In addition, the unpaired electronics, or the dangling bonds, form mid-gap states in the mobility gap as shown in Figure 4.4. An incoming photon with wavelength of 1550 nm or 0.8 eV can either excite a ground-state electron to one of these dangling bond states or an electron at these states to the conduction band, and gets absorbed.

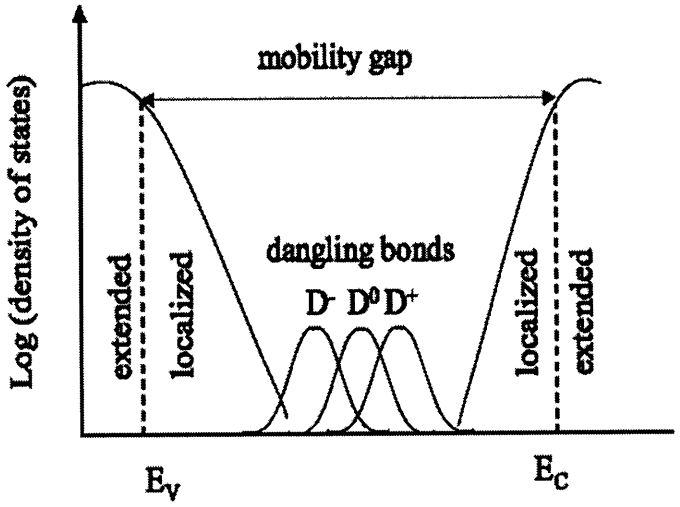

Figure 4.4. The schematic band diagram of amorphous silicon. The band edge extended into the bandgap caused by localized states in a-Si. Dangling bonds form mid-gap states in the mobility gap to cause absorption of photons with energies less than the normal bandgap energy.

Semiconductor surface where lattice structure is terminated abruptly will have dangling bonds if not well passivated. These surface states will contribute to absorption loss in a similar way as bulk dangling bonds. Waveguide top cladding layer, e.g. SiO_2, can provide passivation to some extent to reduce the surface state density.

In large bandgap materials and dielectric materials bond vibration absorption can introduce loss around 1550 nm. For example, PECVD silicon nitride uses silence (SiH_4) and ammonia (NH_3) as precursors. Smith et al. studied the plasma chemistry of PECVD silicon nitride and discovered that in the gas phase, clusters called amino-silane molecules are first formed and then condense onto the substrate [33]. Different amino-silance clusters react to form Si-N network and evolve NH_3 molecules back to the gas phase. This process is shown in Figure 4.5.

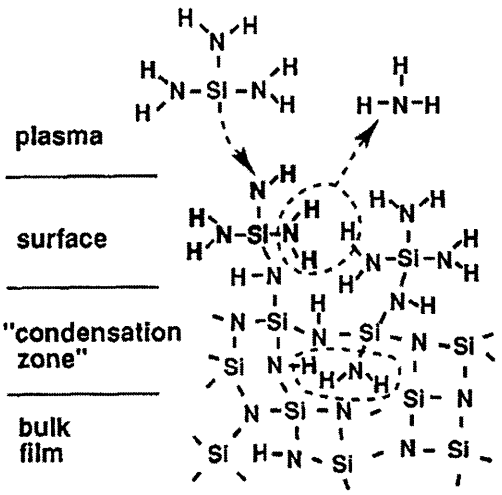

Figure 4.5. The condensation process of PECVD silicon nitride. (Figure taken from Ref. 33)

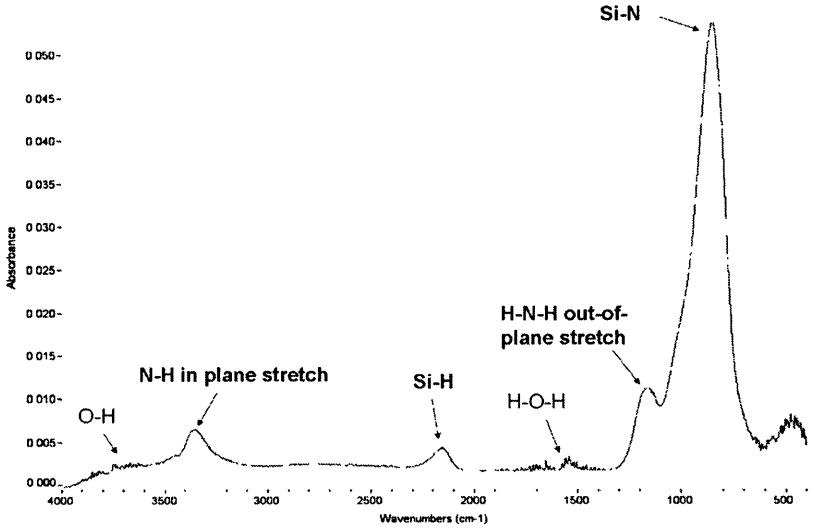

Figure 4.6. Example of FTIR spectrum of as-deposited PECVD SiN_xH_y, plotted in absorbance versus wavenumbers.

As-deposited PECVD silicon nitride inevitably contains a high concentration of hydrogen in the forms of SiH and NH bonds and is best described as SiN_xH_y. Figure 4.6 is an FTIR spectrum of as-deposited PECVD SiN_xH_y thin film. The characteristic peaks

- N-H in-plane vibration mode around 3450 cm^{-1}
- Si-H in-plane vibration mode around 2150 cm^{-1}
- H-N-H out-of-plane vibration mode around 1200 cm^{-1}
- Si-N in-plane vibration mode around 800 cm^{-1}

One of the high-order vibration modes of NH has resonance absorption centered at 1510 nm. Although this absorption is too weak to be detected in FTIR at 6600 cm^{-1}, it clearly shows up in the transmission spectrum of a PECVD SiN_xH_y waveguide as in Figure 4.7. Normally, waveguide transmission loss has only very small wavelength dependence due to refractive index dispersion resulting in changes in waveguide confinement factor. This rapid rising in waveguide insertion loss is clearly due to SiN_xH_y material bulk absorption. The fact that this is not observed in PECVD a-Si waveguide which contains a high concentration of SiH bonds confirms that this is due to the resonant absorption of NH bonds.

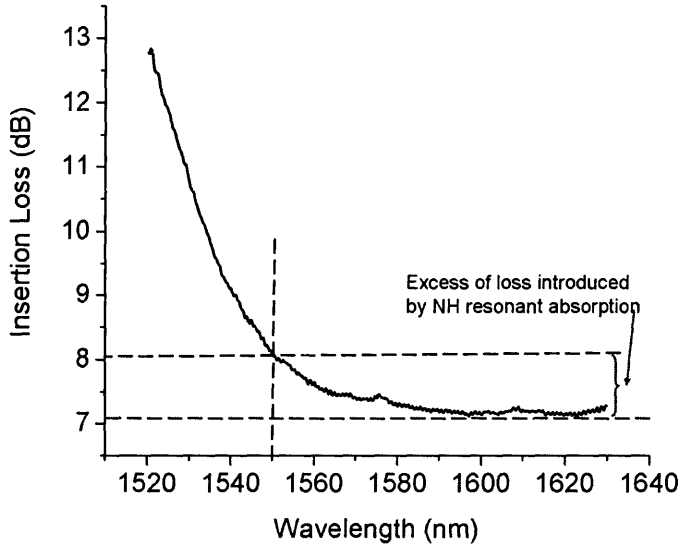

Figure 4.7. A PECVD SiN_xH_y waveguide transmission spectrum.

Free carrier absorption is essentially intra-band absorption and it occurs when a photon excites an electron in the conduction band, or a hole in the valence band, to a higher energy level within the same sets of bands. Free carrier absorption occurs when waveguide material is not intrinsic, meaning it is either doped intentionally or has impurities. Free carriers can also be injected into waveguides. The change in waveguide refractive index and absorption coefficient in silicon can be calculated using [34,35,36]:

$$\Delta n = \Delta n_e + \Delta n_h = -\left[8.8\times10^{-22}\cdot\Delta N + 8.5\times10^{-18}\cdot(\Delta P)^{0.8}\right] \quad (4.2)$$

$$\Delta\alpha = \Delta\alpha_e + \Delta\alpha_h = 8.5\times10^{-18}\cdot\Delta N + 6.0\times10^{-18}\cdot\Delta P \quad (4.3)$$

where ΔN is the electron concentration change, [cm^{-3}]; ΔP is the hole concentration change, [cm^{-3}]; Δn_e is the refractive index change due to ΔN; Δn_h is the refractive index change due to ΔP; $\Delta\alpha_e$, [cm^{-1}], is the absorption coefficient change due to ΔN; and $\Delta\alpha_h$, [cm^{-1}], is the absorption coefficient change due to ΔP. Coefficients 8.5×10^{-18} and 6.0×10^{-18}, [cm^2], are also called the absorption cross sections for electron and hole, respectively.

4.4. Substrate leakage

Substrate leakage happens when the low index undercladding layer is too thin to provide sufficient optical insulation between the high index Si substrate. This can be prevented easily with a careful designed substrate separation as shown in the example in Figure 4.8. For a 0.5 × 0.2 μm^2 Si waveguide, in order to have less than 10^{-3} dB/cm substrate leakage loss, the TE mode requires the undercladding SiO_2 layer to be at least 1.5 μm; and for the TM mode, 2.7 μm [37]. For most of our devices, the undercladding SiO_2 layer is chosen to be 3 μm.

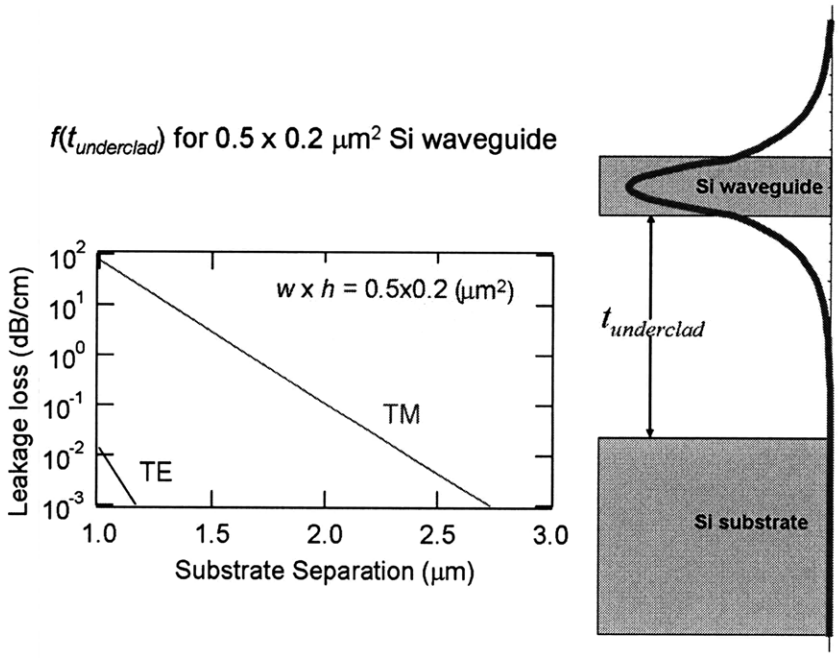

Figure 4.8. The leakage loss vs. substrate separation. The radiation loss into the substrate for TM mode will cause great loss for substrate separation distance less than 3 μm (Figure adapted from Ref. 37)

4.5. Bend loss

Bend loss is very important to consider when designing ring resonators, arrayed waveguide filter, and spiral-shaped optical delay line. It determines how compact the photonic circuit can be when the refractive indices of waveguides are given.

Gambling et al. showed that the fundamental mode in a bent waveguide is shifted slightly toward the outer rim of the bend due to conversion to higher order modes [38]. As the result of this shift in optical intensity inside the waveguide, the evanescent field outside the waveguide is enhanced; and when waveguide transform back to straight the elongated evanescent tail can not be fully reconfined and becomes radiative loss. Analytical models developed by Marcatili and Marcuse can be used to obtain curvature loss but are limited to low index, weakly guided waveguide with large bend radius. Various numerical methods have also been used to design and analyze waveguide bends, such as the eigenmode expansion [39], the method of lines [40], the

finite difference method [41], the variational method [42], the matrix method [43], the Wentzel–Kramers–Brillouin analysis [44], the beam propagation method [45,46], and a full-vectorial finite-element method [47]. Today, using commercially available photonic design tool kits, designing an arbitrary bend becomes straightforward. However, design should take into account the real waveguide transmission loss because beside the radiative loss, the shifted optical fundamental mode will increase the optical intensity at the sidewall, thus enhancing the sidewall roughness scattering loss as we discussed in previous section.

4.6. Summary

In this chapter, we have discussed the dominant loss mechanisms in high index contrast, single mode channel waveguides. For TE mode, sidewall roughness scattering loss is the dominant loss source. Due to the high index contrast in silicon waveguides, this effect is amplified orders of magnitude higher than in an optical silica fiber. For both TE and TM modes, bulk absorption loss in deposited waveguides is also very important. Bend loss is dependent on both the optical confinement and field orientation. Substrate leakage loss is the crosstalk between the waveguide and the substrate. Both bend loss and substrate leakage loss are largely dependent on structure and can be minimized with careful design.

Chapter 5. Optical waveguide insertion loss measurement

As we discussed in Chapter 1, waveguide transmission loss contributes to the attenuation of optical signal when it travels inside a waveguide. While the optical signal is transported and routed on chip, firstly it has to be coupled from optical fiber to on-chip. Generally, the combination of waveguide transmission loss and fiber-to-waveguide coupling loss is called the insertion loss which represents the total attenuation of the system, [dB]:

$$\alpha_t = \alpha_c + \alpha_t \cdot L \tag{5.1}$$

where α_t is the total insertion loss, [dB]; α_c is the total coupling loss, [dB]; α_t is the waveguide transmission loss coefficient, [dB/length]; and L is the waveguide length, [length].

The waveguide transmission loss coefficient, α_t, can be accurately measured by the following four techniques with improved accuracy.

1. Fabry-Perot resonance technique
2. "Paperclip" method
3. Ring resonator resonance technique
4. Ring resonator based "paperclip" method

5.1. Fabry-Perot resonance technique

A common method to measure optical waveguide is to launch signal from optical fiber into waveguide from the input port on one edge of the chip and pick up the output signal from the output port on the other edge. In order to reduce scattering during fiber-to-waveguide coupling, chip edges where waveguides are exposed are either polished or cleaved to obtain smooth facets prior to measurement. This creates a resonance cavity along the waveguide between the two highly

reflective facets and it is called Fabry-Perot cavity. Each facet has a positive finite reflectance, given by Fresnel equations, assuming normal incidence at parallel waveguide facets:

$$R = \left(\frac{n_{incident} - n_{eff}}{n_{incident} + n_{eff}} \right)^2 \tag{5.2}$$

where R is the reflectance; $n_{incident}$ is the refractive index of the medium from which light enters or exits the waveguide; and n_{eff} is the effective refractive index of the waveguide.

Each set of cavity length and effective index has a characteristic resonance feature created by interference effect due to the phase difference for different path length. The constructive interference satisfies

$$L = m \cdot \frac{\lambda}{n_{eff}} \tag{5.3}$$

where L is the length of the waveguide; m is an integer number and represents the order of the resonance or the number of round-trip that light has traveled in between the two facets; and λ is the resonance wavelength in vacuum. Figure 5.1 is an example of tuning resonance periodicity using the thermo-optic effect by thermal heating [48]. The waveguide loss can be calculated from

$$\alpha_t = \frac{1}{L} \ln \left(R \cdot \frac{1 + \sqrt{\frac{P_{min}}{P_{max}}}}{1 - \sqrt{\frac{P_{min}}{P_{max}}}} \right) \tag{5.4}$$

$$\alpha_t = \frac{1}{L} \ln \left(R \cdot \frac{\cos\left(\frac{\pi}{F}\right)}{1 - \sin\left(\frac{\pi}{F}\right)} \right) \tag{5.5}$$

where P_{max} and P_{min} are the transmitted power of the resonance peak and valley, respectively, as denoted in Figure 5.1; R is the reflectance of the waveguide facet; and F is the finesse of the resonant cavity, $F = \frac{\delta\Phi}{\Delta\Phi}$.

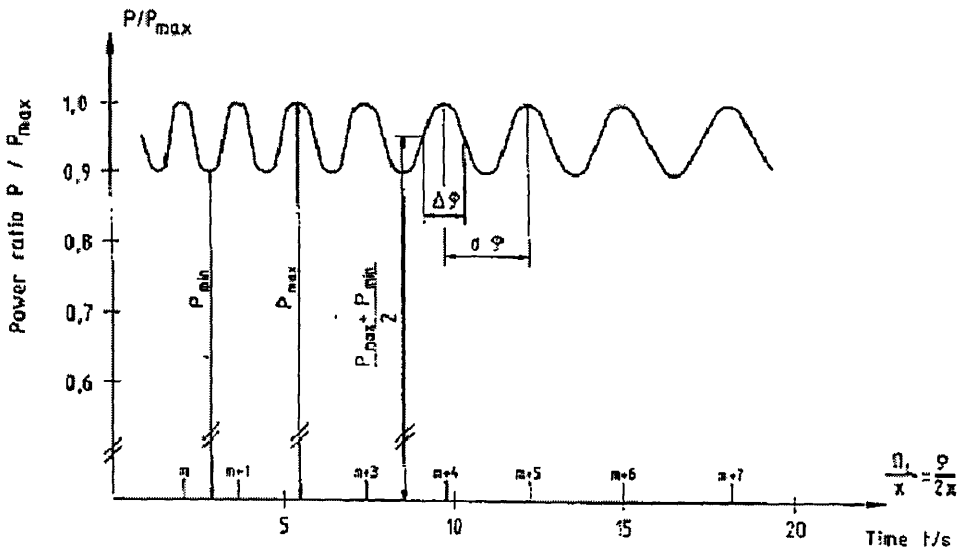

Figure 5.1. The normalized transmitted power versus heating time and phase shift for a $LiNbO_3$ waveguide. $\Delta\Phi$ is the FWHM bandwidth and $\delta\Phi$ is free space range (Figure taken from Ref. 48)

The drawback of the Fabry-Perot resonance technique is that the actual reflectance, *R*, always deviates from ideal case due to tilted facet, roughness, and tilted incident angle. For HIC waveguides, 3D-FDTD method must be used to simulate the effective index for calculation. Nevertheless, it can give quick waveguide loss estimation by just measuring one waveguide.

5.2. "Paperclip" method

From Equation 5.1, we know that the total insertion loss is dependent on waveguide length. If we keep the coupling loss constant then the total insertion will become a linear function of waveguide length with the slope being the waveguide transmission loss as shown here.

$$\alpha_t = \frac{\Delta\alpha_t}{\Delta L} \tag{5.6}$$

The "paperclip" method, sometimes called the "cutback" method, is based on this principle [49]. Figure 5.2 is a schematic representation of how a simple "paperclip" testing chip can be designed and an example of transmission loss coefficient measurement. In Figure 5.2(a), the waveguide length varies from *L1* to *L5* with *L5* being the longest. The two parallel chip edges are

also the waveguide facets for fiber coupling measurement. The benefit of having such design is that all waveguide facets can be prepared at once, either by polishing or by cleaving, to ensure similar coupling condition. The usage of automatic fiber-to-waveguide alignment station can also provide optimal coupling each time with high consistency. Bends are inevitable in this design. The bend angle can be arbitrary but can not introduce significant bend loss comparable to waveguide transmission loss. In some occasions when waveguide transmission loss coefficient is low and much longer waveguides are needed to provide large enough differentiation between waveguides, multiple bends and different numbers of bends can be used provided that the total bend loss should empirically be at least two orders of magnitude lower than the total waveguide transmission loss, $\alpha_t \cdot L$.

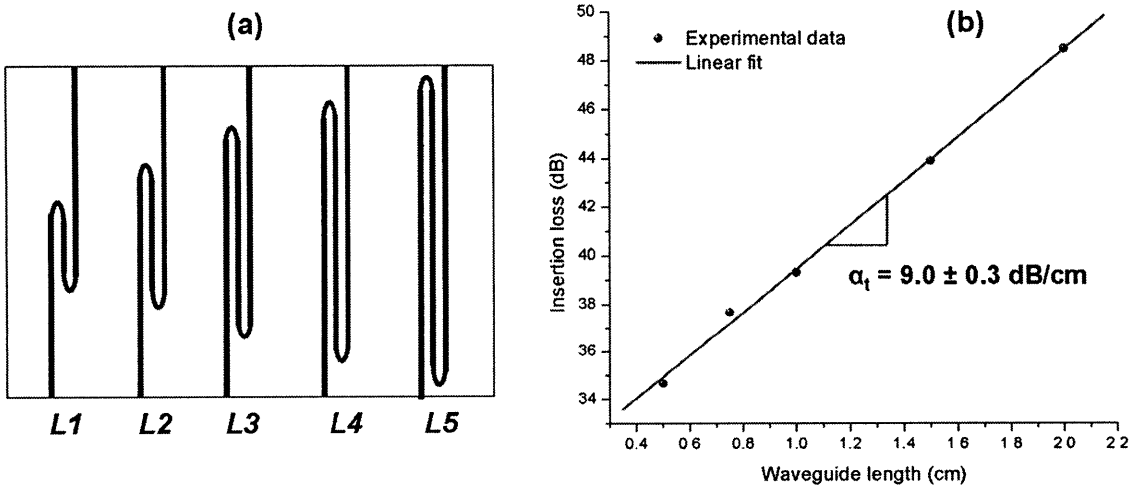

Figure 5.2. Example of a "paperclip" testing chip for waveguide transmission loss measurement. The transmission loss coefficient at 1550 nm is derived from the linear fit of 5 insertion loss values for 5 waveguides with length of 0.5, 0.75, 1.0, 1.5, and 2.0 cm.

Transmission loss coefficient (dB/cm) is the slope of the linear fit of a transmission (dB) versus waveguide length (cm) plot as shown in Figure 5.2(b). For each individual waveguide measurement, in order to calculate the transmission loss coefficient, one needs to substrate the system loss and coupling loss from the total transmission loss. Accurate, direct measurement of

system loss and coupling loss is difficult and they vary from time to time. The "paperclip" method is very accurate given the fact that random variation can be eliminated by the linear fit. However, this method requires fabricating a dedicated testing structure; both sample preparation and measurements are very time-consuming.

5.3. Ring resonator resonance technique

Ring resonators (or racetrack resonators) are not only important photonic devices for filter and modulator applications, but also useful to derive waveguide transmission loss coefficient.

A typical first-order ring resonator device has one bus waveguide, or through port, coupled with the ring, sometimes, there is a second bus waveguide to drop the resonance wavelength, or drop port as shown in Figure 5.3.

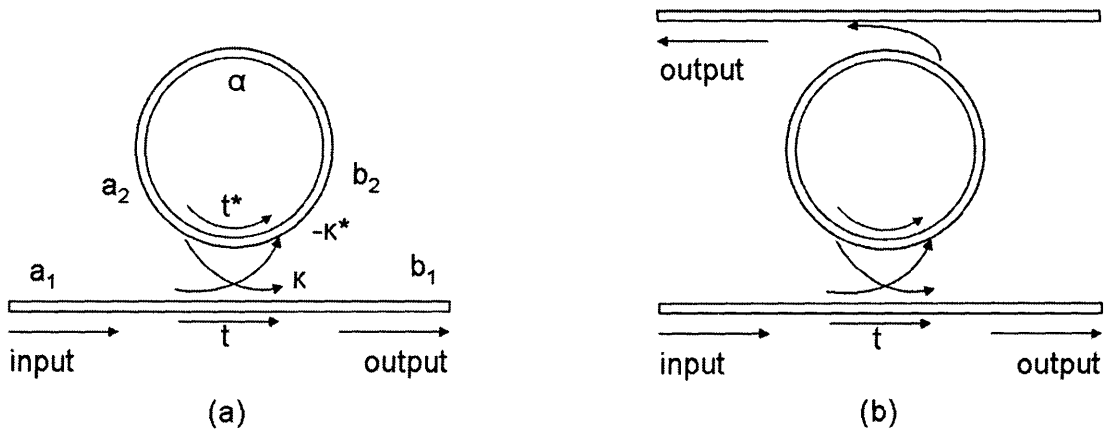

Figure 5.3. Schematics of (a) a ring resonator with only through port, and (b) a ring resonator with both through and drop ports

The following method and derivation closely follow Yariv's paper in Ref. 50. Yariv showed that the interaction of the ring resonator and the bus waveguide can be expressed by Equations 5.7 and 5.8 is the normalization condition. Equation 5.9 relates a_2 and b_2 with round trip loss α.

$$\begin{vmatrix} b_1 \\ b_2 \end{vmatrix} = \begin{vmatrix} t & \kappa \\ -\kappa^* & t^* \end{vmatrix} \begin{vmatrix} a_1 \\ a_2 \end{vmatrix} \tag{5.7}$$

$$\left|\kappa^2\right| + \left|t^2\right| = 1 \tag{5.8}$$

$$a_2 = \alpha \cdot e^{i\theta} b_2 \tag{5.9}$$

α: round trip loss. When bend loss is negligible, $\alpha = \alpha_t$

a_1: input power, normalized, $|a_1|^2 = 1$

a_2: power in the ring considering round trip loss

b_1: transmitted power

b_2: power in the ring

t: transmission coefficient

κ: coupling coefficient

From Equations 5.7 to 5.9, we can derive that

$$b_1 = \frac{-\alpha + te^{-i\theta}}{-\alpha t^* + e^{-i\theta}} \tag{5.10}$$

$$a_2 = \frac{-\alpha\kappa^*}{-\alpha t^* + e^{-i\theta}} \tag{5.11}$$

The total transmission power is

$$|b_1|^2 = \frac{\alpha^2 + |t|^2 - 2\alpha|t|\cos(\theta + \phi_t)}{1 + \alpha^2|t|^2 - 2\alpha|t|\cos(\theta + \phi_t)} \tag{5.12}$$

where $t = |t|\exp(i\phi_t)$; and total power in the ring resonator is

$$|a_2|^2 = \frac{\alpha^2\left(1 - |t|^2\right)}{1 + \alpha^2|t|^2 - 2\alpha|t|\cos(\theta + \phi_t)} \tag{5.13}$$

At resonance wavelength, $\theta + \phi_t = m \cdot 2\pi$, then the extinction ratio is

$$|b_1|^2 = \left(\frac{\alpha - |t|}{1 - \alpha|t|}\right)^2 \tag{5.14}$$

The extinction ratio is dependent on the round trip loss in the ring and the coupling strength between the bus waveguide and the ring.

Other important parameters for a ring resonator are the quality factor, Q, and the finesse, f. Q is defined as the ratio of the resonance wavelength to the full width at half maximum (FWHM), $\Delta\lambda_R$, of the resonance:

$$Q = \frac{\lambda_R}{\Delta\lambda_R} \tag{5.15}$$

And the finesse is defined as the ratio of the free spectrum range (FSR) to the FWHM:

$$f = \frac{FSR}{\Delta\lambda_R} \tag{5.16}$$

The Q factor can also be denoted in terms of $|b_1|^2$ at FWHM. Experimentally, the extinction ratio and the Q factor are derived from the Lorentzian fit of the resonance peak. We can obtain α_t and t by solving the above equations for the Q factor and the extinction ratio. Notice that we assume the round trip loss, $(\alpha_t \cdot L)$, is much greater than the bend loss of the ring resonator.

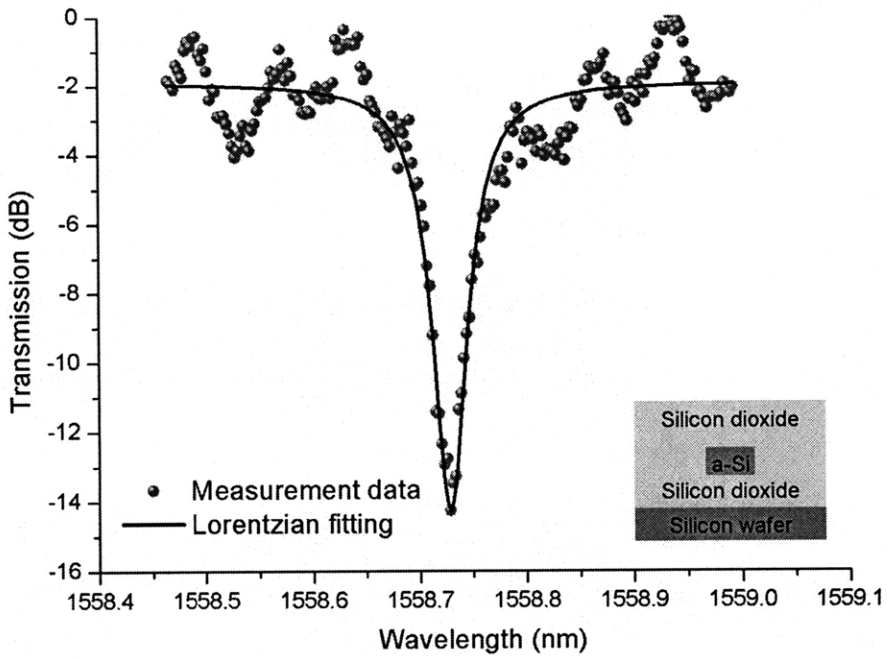

Figure 5.4. Example of a ring resonator resonance around 1558 nm (the red dots) and its Lorentzian fit (the black line). The large fringes are Fabry-Perot fringes caused by the bus waveguide flat facet as we discussed in Section 5.2.

Figure 5.4 is an example of applying this method to obtain waveguide transmission loss coefficient. The red dots are the measured resonance of a racetrack resonator around 1558 nm. The extinction ratio and Q factor are derived from the Lorentzian fit of the measured spectrum. The effective index of the waveguide is 2.1; bend radius is 50 μm; and the periphery of the resonator, L, is $(100\pi + 200)$ μm. The transmission loss coefficient is calculated to be 12.0 ± 1.8 dB/cm as listed in Table 5.1. We will revisit this example later.

Table 5.1. Important parameters and transmission loss coefficient of a racetrack resonator.

Resonance wavelength (nm)	**Extinction ratio (dB)**	**-3 dB bandwidth (pm)**	**Q factor**	**Loss (dB/cm)**
1558.146	12.3	69.4	22452	12.0 ± 1.8

This method is as simple as the Fabry-Perot resonance technique but more accurate because it involves only one measurement and the nature of coupling does not affect calculation. However, the two most important parameters, extinction ratio and Q, are derived under the

assumption that the resonance line shape is Lorentzian. For rings with a large Q factor, the resonant peak only consists of a few data points due to the resolution of the tunable laser that is used. The Lorentzian fit will have large uncertainty. Overall, the measurement uncertainty is estimated to be less than 15%.

5.4. Ring resonator based "paperclip" method

This method is based on the same principle in the previous section, but improves the accuracy of the single ring resonator resonance technique by measuring a series of ring resonators with different periphery length. This is similar to the "paperclip" method.

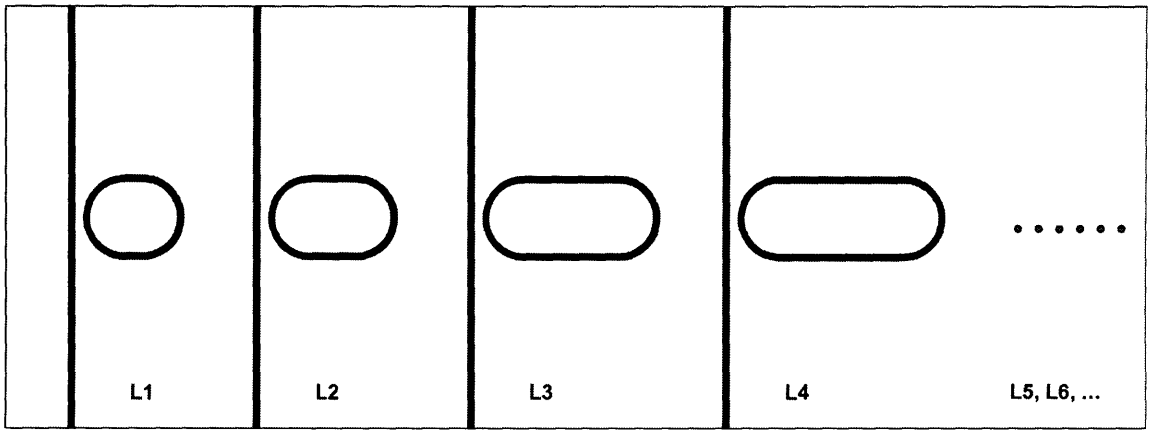

Figure 5.5. Schematic drawing of a waveguide transmission loss coefficient test chip. Different L's denote different racetrack periphery length.

Figure 5.5 is a schematic drawing of a test structure based on resonator "paperclip" design. The bus waveguide's length, width, bend radii, and the ring-bus coupling gaps are kept identical while the length of the straight racetrack part varies from device to device. Notice that the racetrack resonator is coupled with bus waveguide at bends, not at straight racetracks. This is to ensure the identical coupling condition for each racetrack resonator. For each individual resonator device, extinction ratio, Q, and round trip loss, $(\alpha \cdot L)$, can be calculated. Then using similar method as "paperclip" method, the transmission loss coefficient can be obtained with the best

accuracy compared to the above three methods. This method also requires that the bend loss is negligible compared to the round trip loss.

5.5. Deriving bulk absorption loss using TM-polarization

We know that for single crystalline silicon waveguides, the transmission loss of the TE-polarization is largely dependent on sidewall roughness scattering. Because c-Si has minimal bulk absorption loss, the measured TE-polarization transmission loss is in fact the sidewall roughness scattering loss (assume other loss sources are carefully eliminated already, such as substrate leakage loss and bend loss etc.). Comparing TE-mode loss coefficient one can readily compare different process conditions to find the one that gives the minimal sidewall roughness. Here we present a technique that can provide direct measurement of the bulk absorption loss coefficient using the TM-polarization for deposited waveguides.

The total TM-mode transmission loss of a deposited waveguide is

$$\alpha_{TM} = \alpha_{side} + \alpha_{top} + \alpha_{sub} + \alpha_{bulk} \tag{5.17}$$

where α_{TM} is the TM-mode transmission loss, α_{side} is the contribution of sidewall roughness scattering, α_{top} is the contribution of top surface roughness scattering, α_{sub} is the contribution of substrate leakage, and α_{bulk} is the contribution of bulk absorption.

Because the TM-mode is relatively insensitive to the sidewall roughness scattering, α_{side} can be ignored without introducing too much difference. We can also eliminate the top surface roughness loss and the substrate leakage loss using CMP process and a thick SiO_2 under cladding layer, then the terms α_{top} and α_{sub} can be left out of the equation. The total transmission loss of TM-mode is solely dependent on α_{bulk}. Furthermore, because the bulk absorption loss depends on the bulk absorption loss coefficient, α, a constant and a measure of the waveguide absorbing

strength; and the confinement factor, Γ, because only the optical power overlapping the absorbing waveguide will be affected, the equation can be rewritten as

$$\alpha_{TM} \approx \alpha_{bulk} = \alpha \cdot \Gamma \tag{5.18}$$

This technique involves measuring the TM-mode transmission loss of many waveguides with different widths. The derivative of α_{TM} with respect to waveguide width, w, is

$$\frac{\partial \alpha_{TM}}{\partial w} = \alpha \cdot \frac{\partial \Gamma}{\partial w} \tag{5.19}$$

where $\frac{\partial \Gamma}{\partial w}$ is the change rate of the confinement factor with respect to width.

The confinement factor can be calculated using photonic design tool kits, such as FIMMWave and Apollo. One example of the confinement factor for a-Si/SiO_2 (n = 3.64/1.46) channel waveguide is given in Figure 5.6. Within the interesting waveguide width range from 0.4 to 0.6 μm, the confinement factor can be approximated to have a linear dependence on waveguide width, thus $\frac{\partial \Gamma}{\partial w}$ becomes a constant as well.

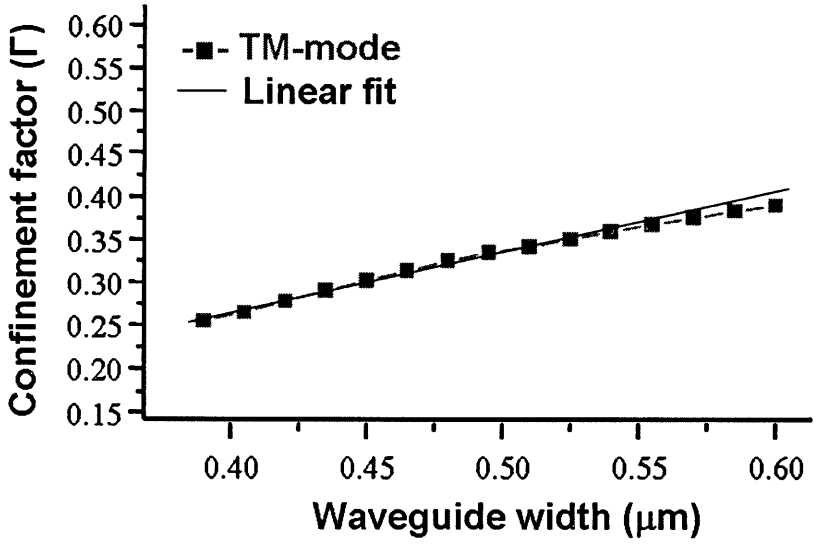

Figure 5.6. Confinement factor versus waveguide width for the TM-mode.

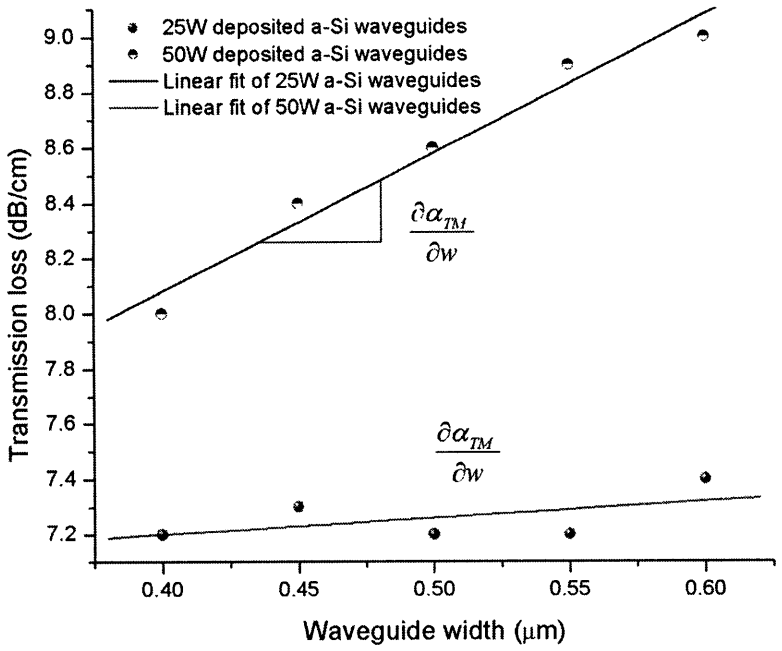

Figure 5.7. TM-mode transmission loss versus waveguide width. The $\frac{\partial \alpha_{TM}}{\partial w}$ is derived from the corresponding linear fit.

The measured TM-mode transmission loss as a function of waveguide width is plotted in Figure 5.7. Combining $\frac{\partial \alpha_{TM}}{\partial w}$ and $\frac{\partial \Gamma}{\partial w}$, the bulk absorption loss coefficient can be derived.

5.6. Waveguide measurement setup and techniques

Typical waveguide measurement setups use fiber-to-waveguide coupling techniques, being from the edge or from the top using special designed grating coupler [51]. Figure 5.8 is a schematic diagram of our measurement setup using an edge fiber-to-waveguide coupling scheme. It consists of a Newport Autoalign Station and LUNA Optical Vector Analyzer integrated with HP tunable laser.

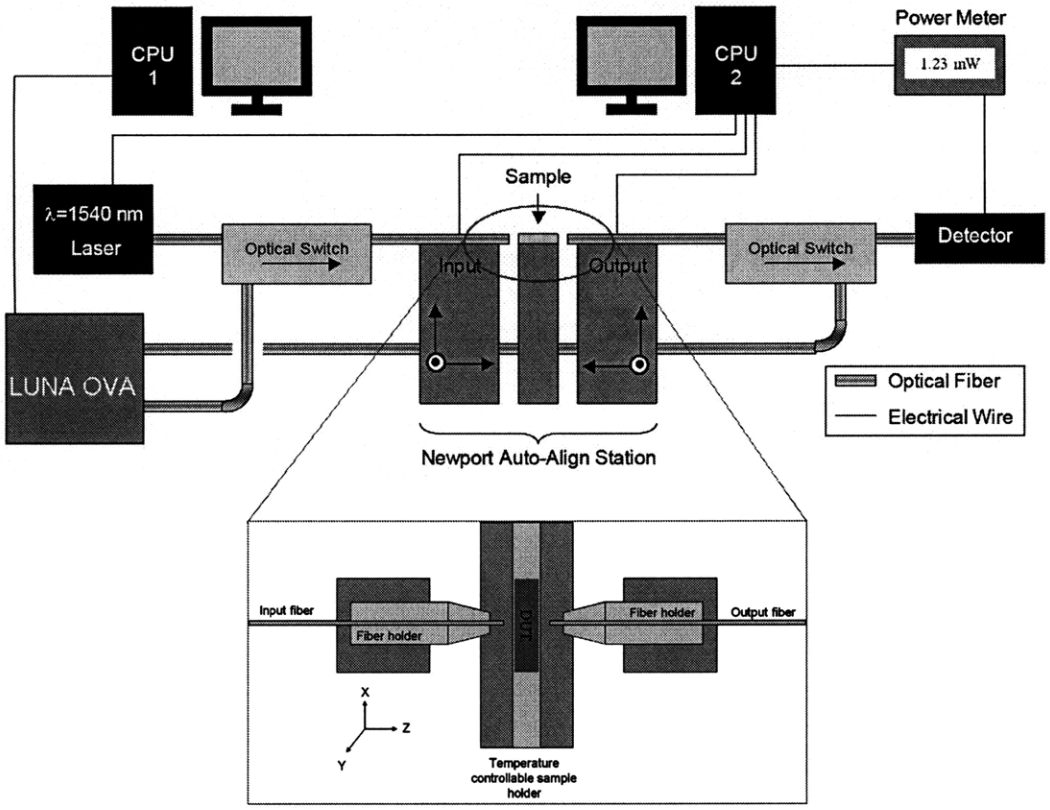

Figure 5.8. Schematic diagram of a Newport Autoalign station. The bottom is the top view of the sample stage and fiber holders where light is coupled from fiber to the device under test (DUT) (Courtesy of Dr. Daniel K. Sparacin).

A single wavelength alignment laser is first used to align the fiber-to-waveguide coupling, and then the optical path is switched to tunable laser and conduct wavelength sweep measurement. Details about our JDSU-SWS2000 system can be found in Ref. 37. The latest upgrade to the system is the addition of the LUNA Optical Vector Analyzer (OVA) system. Integrated with 2 Agilent tunable lasers, LUNA OVA is capable of measuring, not exclusively, (1) insertion loss, (2) polarization dependent loss, (3) group delay, (4) chromatic dispersion, optical phase, and (5) polarization mode dispersion as a function of wavelength in the range of 1470 nm ~ 1630 nm within 1 minute. For comparison, using the JDSU-SWS2000 system takes up to 3 minutes for the same wavelength scan. Both methods operate under the principle of the Jones Matrix method [52]. A typical optical system supports both TE and TM polarizations. Each input polarization can

couple into either of the two output polarization modes. A 2-by-2 complex matrix can fully characterize the system, as called the Jones Matrix:

$$J(\omega)=\begin{bmatrix} a(\omega) & b(\omega) \\ c(\omega) & d(\omega) \end{bmatrix} \tag{5.20}$$

where a, b, c, and d are the four scalar transfer functions; and ω is the frequency. LUNA OVA can simultaneously measure all four elements of the Jones Matrix and calculate all 5 parameters listed above. For example, insertion loss, IL, is defined as

$$IL = -10\log\left(\frac{|a(\omega)|^2 + |b(\omega)|^2 + |c(\omega)|^2 + |d(\omega)|^2}{2}\right) \tag{5.21}$$

Using LUNA system to measure waveguide transmission is straightforward with the integrated control software. However, sometimes, we need to control polarization by external polarization controller. The algorithm used by LUNA OVA as well as JDSU-SWS system can only give 2 eigen values (min. and max.) of the Jones Matrix, but it can not differentiate when two polarizations crossover.

Figure 5.9 is an example of the transmission spectrum of the drop port of a silicon ring resonator filter. This ring is designed for TE mode operation and has a coupling gap of 170 nm. The red line, denoted as min. power by the software, is the TM mode transmission response of the drop port. It is expected to be flat across the measurement wavelength range. The black line, denoted as maximum power, is the TE mode transmission response of the drop port. It is expected to have resonance according to the transmission spectrum of the through port shown as the inset in Figure 5.9. The TE mode response crosses the TM mode at around -30 dB at three resonance wavelengths. The software mistakenly treats that part of the TE mode response that is smaller than the TM mode as the TM mode response and record accordingly. Without attention, if one uses the

TE mode data directly, he would see an unrealistic flat-top shaped response for the TE mode of a first-order filter. This TE-TM crossover problem also happens in other cases.

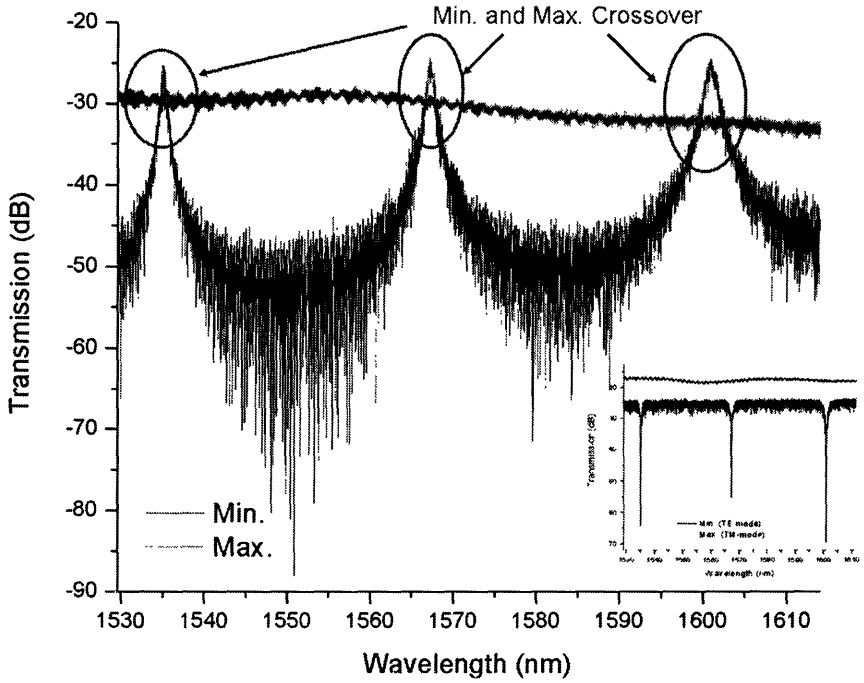

Figure 5.9. Transmission spectrum of a ring resonator's drop port. The red line is TM mode and has flat response; the black line is TE mode which has resonance response and crosses the TM mode response around -30 dB at three resonance wavelengths. The inset is the transmission spectrum of the through port of the same ring resonator.

We can solve this problem by filtering out the unwanted polarization in the output signal. In the above example, we are only interested in TE mode so we can block the TM mode by using an external polarization controller, e.g. HP 8169A Polarization Controller, as shown in Figure 5.10, before the photodetector.

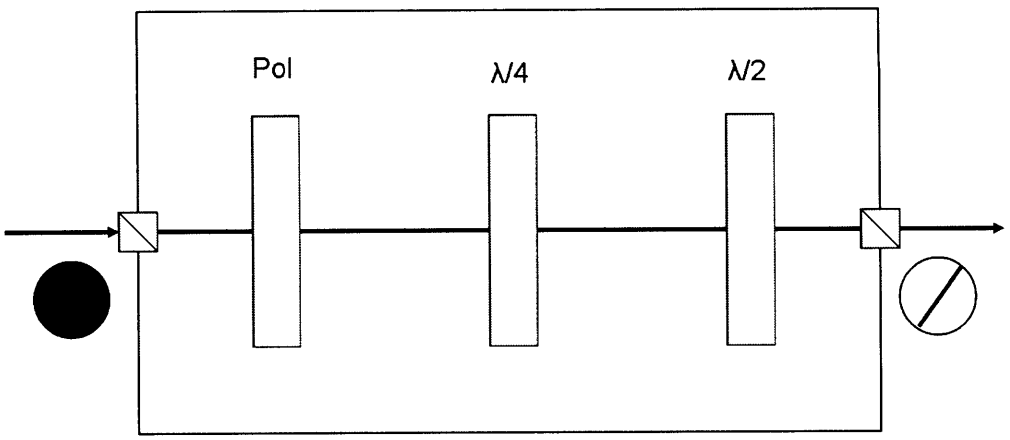

Figure 5.10. A schematic representation of a polarization controller. Incoming random polarized light, or unpolarized light becomes linear polarized at the output.

After the polarization is connected in the optical path and the DUT is aligned properly, the LUNA is set to do continual scan around one of the resonant wavelengths. To operate the polarization controller, linear polarizer, *Pol*, is first adjusted to obtain maximal transmission. Choose the "time domain amplitude" in the lower window in LUNA control software, there are two peaks in the time domain window. For a single mode silicon waveguide with rectangular cross section (width > height), the effective index of the TM polarization is smaller than the TE polarization, which means the TM polarization travels faster than the TE polarization in waveguide given $v_g = \frac{c_o}{n_{eff}}$ where c_o is the speed of light in vacuum. In time window, the TM polarization reaches the detector first and the peak of the TM polarization shows up earlier than the TE polarization as shown in Figure 5.11(a). By watching the time domain amplitude window while we adjust the half plate, λ/2, and the quarter plate, λ/4, we can minimize the peak corresponding to the TM polarization as shown in Figure 5.11(b). As the result, the output power entering the photodetector will contain mostly the TE polarization.

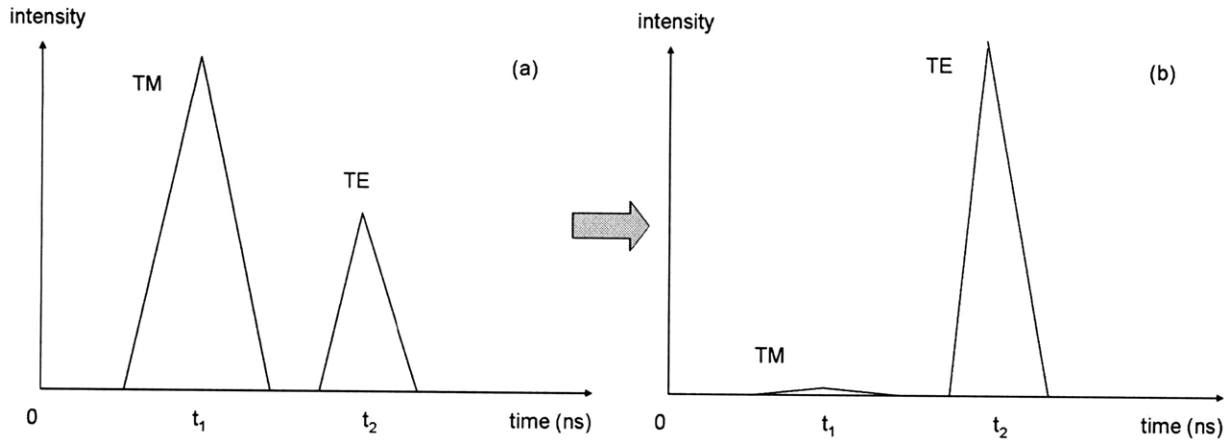

Figure 5.11.Schematic drawings of the time domain amplitude (a) before and (b) after polarization controlling. In this example, the TM polarization is stopped by polarization controller; only TE polarization is allowed to pass and enter the photodetector.

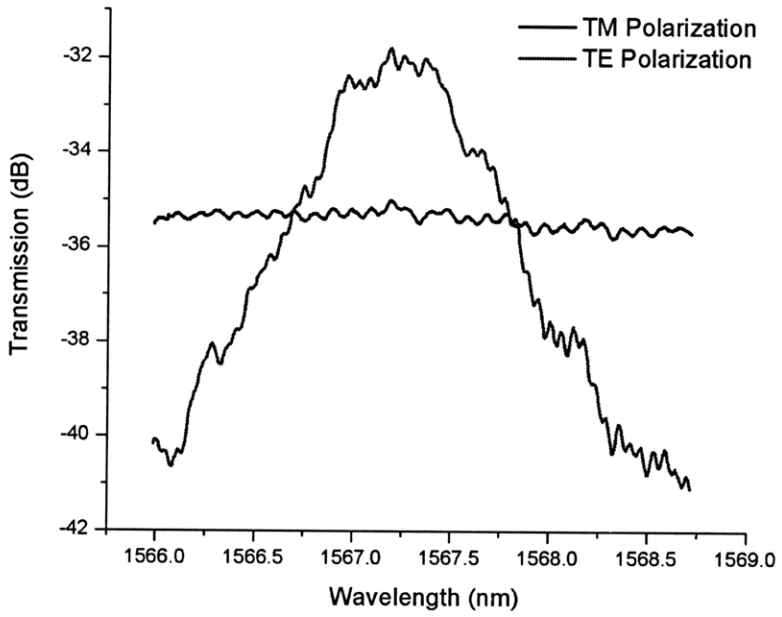

Figure 5.12. One of the drop port transmission spectra of the same ring resonator shown in Figure 5.9. This spectrum consists of two separate measurements in which only one polarization spectrum is obtained each time. Using polarization controlling, we can successfully solve the crossing problem using LUNA system.

Figure 5.12 shows one of the drop port resonant responses of the same ring resonator as shown in Figure 5.9, except polarization controller is used here to allow measurement on one polarization state each time so the figure consists of two separate measurements. Notice that the incorporation of polarization controller in the optical path introduces additional ~ 5 dB loss in total

transmission. Nevertheless, using polarization controlling method we can obtain the real response of any devices without worrying the issue of TE-TM crossing.

5.7. Summary

In this chapter, we have reviewed the various measurement methodologies that have been developed and used in this thesis work. The "paperclip" method is suitable for measuring waveguides with large transmission loss (> 5dB/cm) with relative large length difference in "paperclips"; for small transmission loss, resonator method and resonator based "paperclip" method are recommended. The polarization controlling measurement is also very important technique to overcome the TE/TM crossing problem caused by the Jone's matrix when measuring either straight waveguides or resonator devices when the transmission loss of either polarization has large wavelength dispersion.

Chapter 6. Process development for low loss silicon channel waveguides

As we have discussed in Chapter 1, the dominant optical transmission loss mechanism in single-crystalline silicon (c-Si) is sidewall roughness scattering; and in amorphous silicon (a-Si), the bulk absorption loss is another important loss source. In order to reduce sidewall roughness scattering loss, we can reduce the sidewall optical intensity, RMS roughness, and optical index contrast. For a-Si waveguides, H passivation is proven to be an effective method to reduce the dangling bond absorption. In this chapter, we will discuss new designs and new processes to improve c-Si and a-Si waveguide optical transparency.

6.1. Photolithography process optimization technologies

Because sidewall roughness, also known as sidewall line striation, is originated during photolithography step, we need to go back and re-examine the related photolithographic processes. This study is conducted in Integrated Circuits Laboratory (ICL) in Microsystems Technology Laboratories (MTL) at MIT. The key equipment is the 6 inch wafer stepper is Nikon NSR-2005i9. This i-line stepper has a designated wavelength, λ, of 365 nm and a variable numeric aperture (NA) of 0.6 ~ 0.66. According to $R = \lambda / NA$, this corresponds to resolution, R, of 550 nm ~ 600 nm. The average photon flux measured during experiments is calibrated to be ~ 420 mW/cm^2.

The photoresist (PR) used is MEGAPOSIT SPR-700 series from Rohm and Haas Company. Using coater track, wafers go through a vacuum HMDS (adhesion promoter) vapor prime oven, photoresist spin coater, and soft bake oven at 95 °C for 60 seconds. 1 μm thick photoresist is coated before entering stepper for exposure. During exposure, the exposed photoresist becomes dissolvable in developer and the unexposed part stays. The starting recipe for

post exposure bake (PEB) is at 115 °C for 30 seconds. PEB is necessary to eliminate standing wave effect (SW) as shown in Figure 6.1. The developer is MEGAPOSIT LDD-26W from Rohm and Haas Company. The starting recipe is 400 RPM constant spray for 37 seconds. A post develop hard bake (PDB) is set to be at 130 °C for 60 seconds.

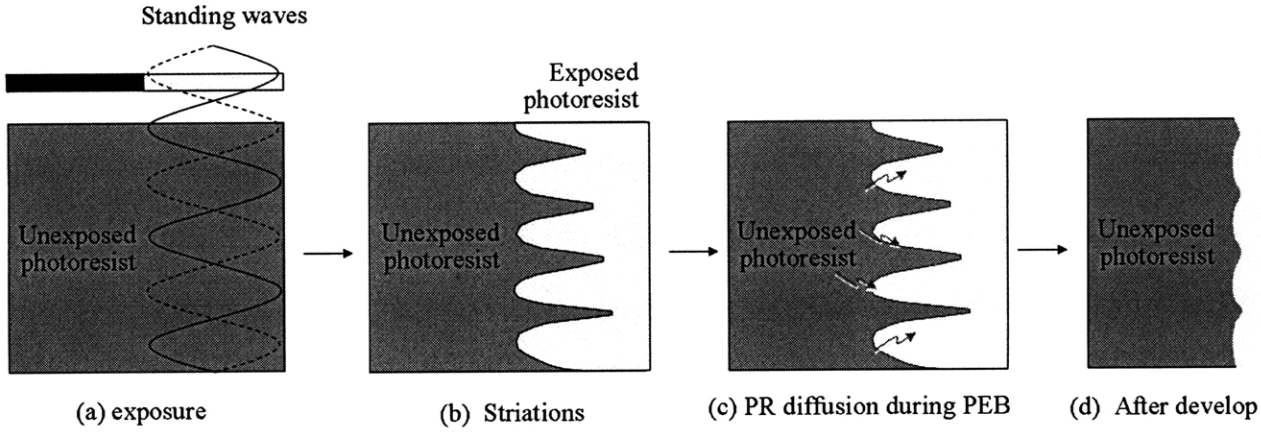

Figure 6.1. Schematic representation of standing wave effect in positive photoresist and post exposure bake (PEB) effect. Negative photoresist works in a similar way except the unexposed photoresist is dissolvable in developers.

First, PEB is optimized to be 120 °C and 60 second for improved SW effect at sidewall for both clear and dark field features as shown in examples in Figure 6.2 where 0.8 μm photoresist patterned on silicon substrate directly. The critical dimension (CD) control is studied with respect to exposure time for both clear field and dark field features. Figure 6.3 summaries the critical dimension change as a function of exposure time ranging between 120 ms and 180 ms for both clear and dark field features. It is found that 120 ms exposure, working with current develop recipe, gives the best CD control. This corresponds to photon energy of only 50.4 mJ/cm^2 for 0.8 μm thick photoresist. The feature dimension can be controlled within ± 30 nm after Reactive Ion Etch (RIE). Shorter exposure time will result in severe under exposure of photoresist.

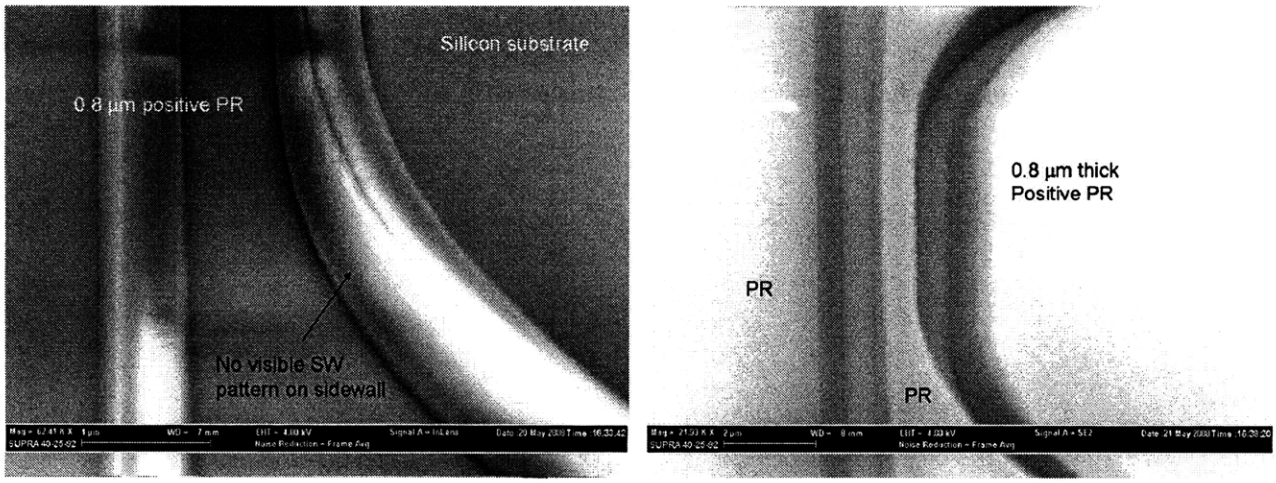

(a) Clear field (a) Dark field

Figure 6.2. SEM images of improved SW effect at sidewall in (a) clear field and (b) dark field. No striation pattern are visible on sidewalls.

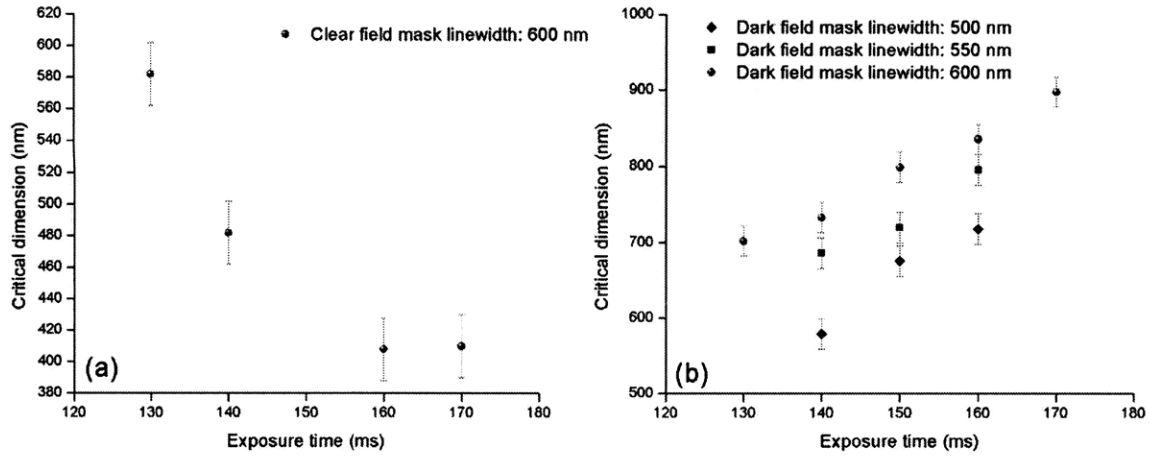

Figure 6.3. Critical dimension change vs. exposure time for both clear and dark field features.

The continuous spray develop recipe is an aggressive develop process that is optimized for high photospeed photoresist and manufacturing processes. However, in our study, the process results in scum and roughness in the developed photoresist. The formation of scum is due to the fact that aggressive developing process dissolves bulk photoresist more than at the substrate/photoresist interface. An SEM image of an as-developed photoresist is shown in Figure 6.4. Low normality developer (e.g. MICROPOSIT MF-26A or 24A developers) and less aggressive, static puddle resist develop method can be used to reduce both effects [53]. Due to the

equipment constraints, we can not fully implement these techniques in ICL. Alternative approaches are used and include a descum step prior to RIE and photoresist reflow at moderate temperatures.

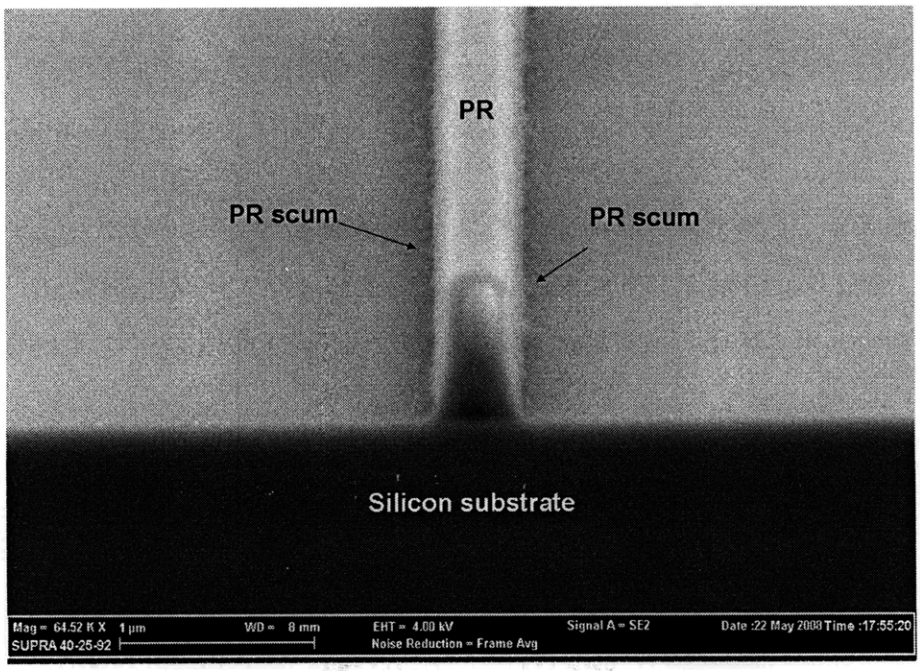

Figure 6.4. Photoresist scum formed at the PR/substrate interfaces due to aggressive develop process.

Photoresist scum on surface will be transferred into structure during etch step. The descum step is carried out in the RIE tool (Applied Materials, AME-P5000) instead of photoresist stripper (Asher). The reason is that the oxygen plasma descum in AME-P5000 is more anisotropic than in photoresist stripper. The descum step is set to 5 seconds and is found to have little effect on feature dimension. Due to the formation of thin oxide on silicon surface due to the O_2 descum step, a short oxide "break-through" etch step is inserted before the silicon etch. This step can remove up to 10 nm oxide. The improved etch result is compared to standard process as shown in Figure 6.5.

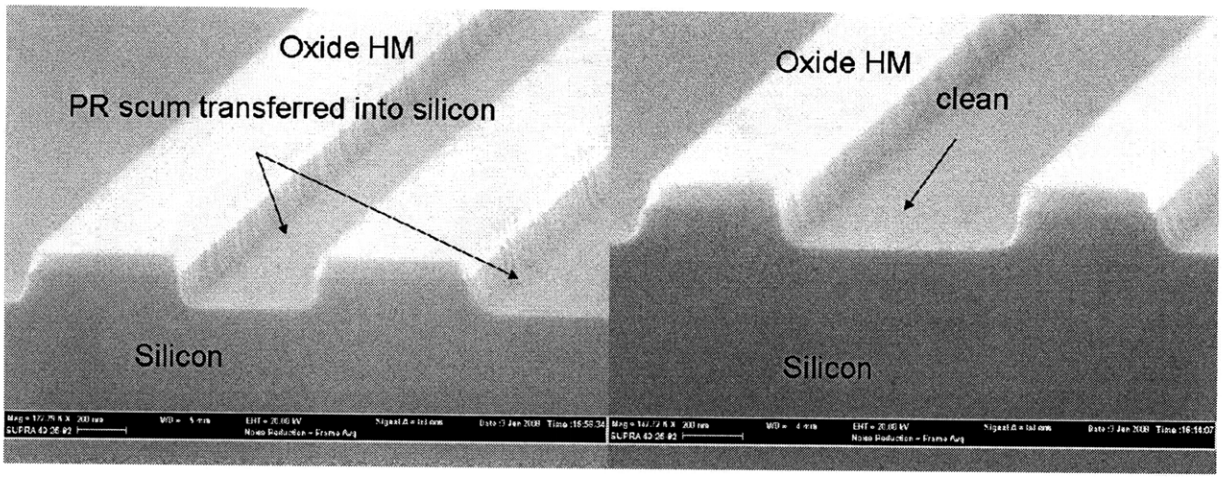

(a) Control process (b) With 5 sec descum in AME-P5000

Figure 6.5. Examples of descum effect on as-etch silicon structures using oxide hard mask. The oxide hard mask is defined using positive photoresist mask. Photoresist is removed (Asher) and wafer is cleaned (double Piranha cleaning) prior to SEM.

Photoresist reflow experiments are carried out at temperatures between 150 °C and 200 °C for 3 minutes. It has been found that for this particular photoresist, the bulk or large area always reflows before small features and edges. As a result, the clear field, isolated structures behave vastly different from the dark field structures.

Figure 6.6 is the SEM images of photoresist clear field structures reflowed at 4 different temperatures, including the standard 130 °C PDB. For isolated clear field structures, it is easily seen that the photoresist top surface starts to reflow immidiately at 150 °C, resulting in rounding of the top surface; the top half of the photoresist shows some degree of reflow. Unfortunately, the bottom half which is also the most important part in affecting the etch does not undergo significant shape changes. Especially there is no visible striation reduction along the photoresist/substrate interfaces. The standing wave pattern is somehow more noticeable at higher temperatures.

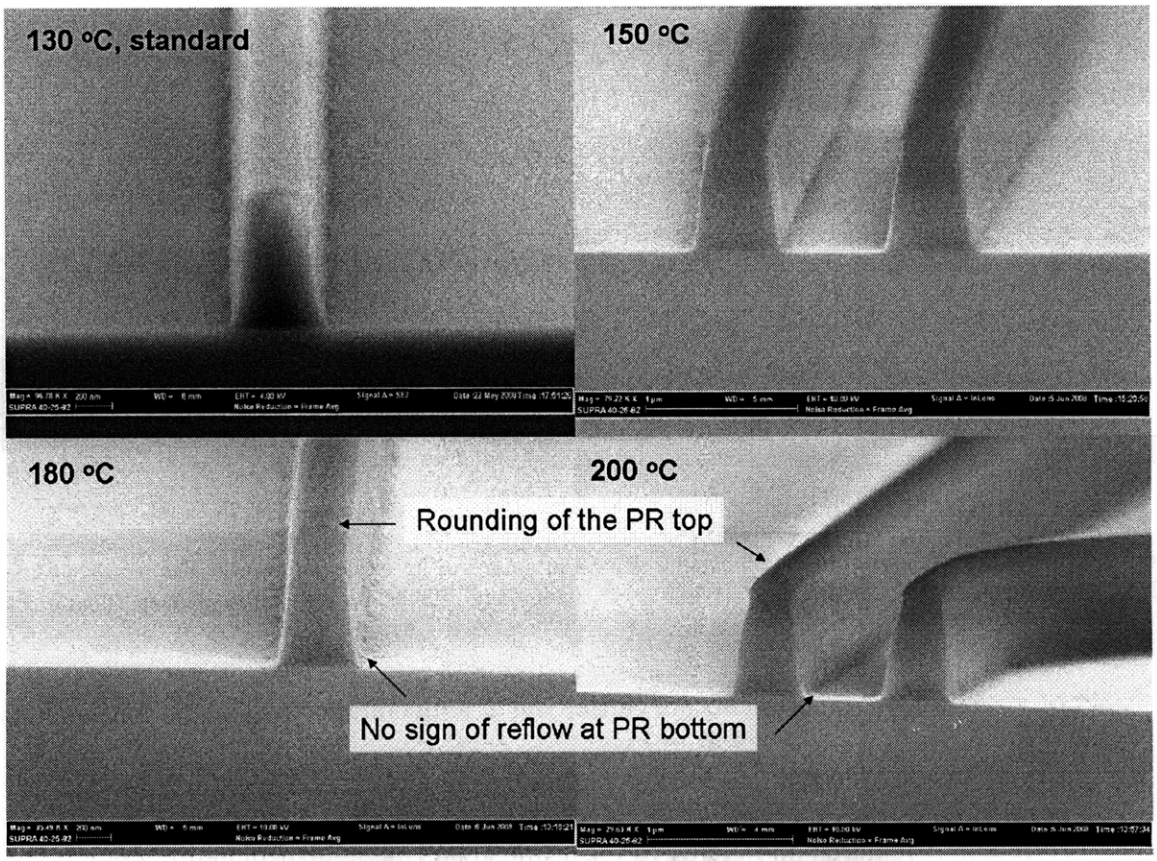

Figure 6.6. The SEM images of the photoresist clear field structures reflowed at different temperatures.

Figure 6.7 is the SEM images of photoresist dark field structures reflowed at temperatures from 150 °C to 200 °C, including the standard 130 °C PDB for comparison. Generally, the bulk photoresist is much easier to reflow compared to more isolated clear field structures. The photoresist sidewall angle changes from 60 ° to 33 ° after reflow. The photoresist/substrate interface does not retreat, possibly due to the strong adhesion of photoresist at substrate surface. Although this is good for CD control, the bottom half of the photoresist does not show significant signs of reflow.

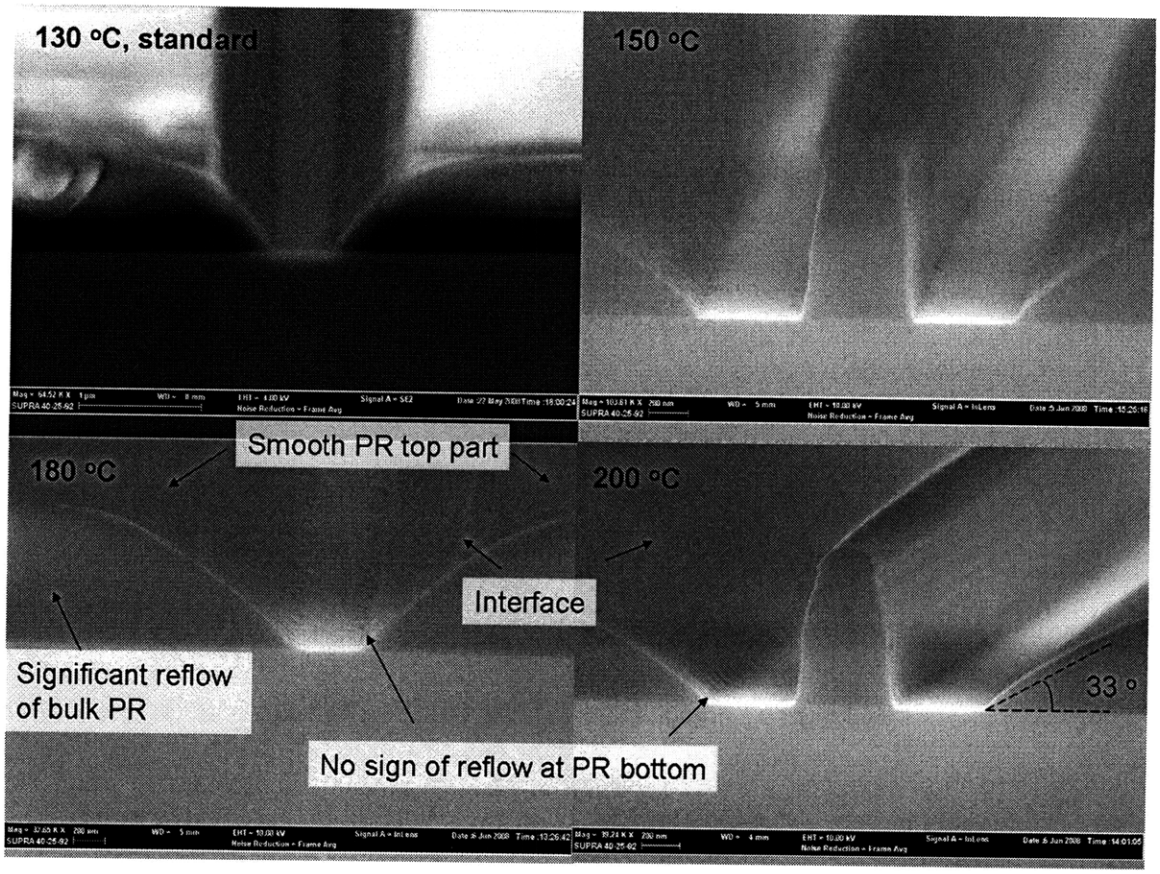

Figure 6.7. The SEM images of the photoresist dark field structures reflowed at different temperatures.

Because this particular photoresist, MEGAPOSIT SPR-700 series, can not be reflowed effectively on either silicon or silicon dioxide surface, Sidewall roughness reduction will be pursued using alternative approaches, such as hard mask and damascene process (for deposited waveguide only).

6.2. Hard mask vs. photoresist mask

In standard CMOS process, oxide, or sometimes oxide/nitride, hard mask is commonly used to reduce the LER of ploy-silicon gates. The photoresist mask process flow is already given in Figure 4.1. Figure 6.8 shows a modified process flow where oxide/nitride hard mask is used to define c-Si waveguides.

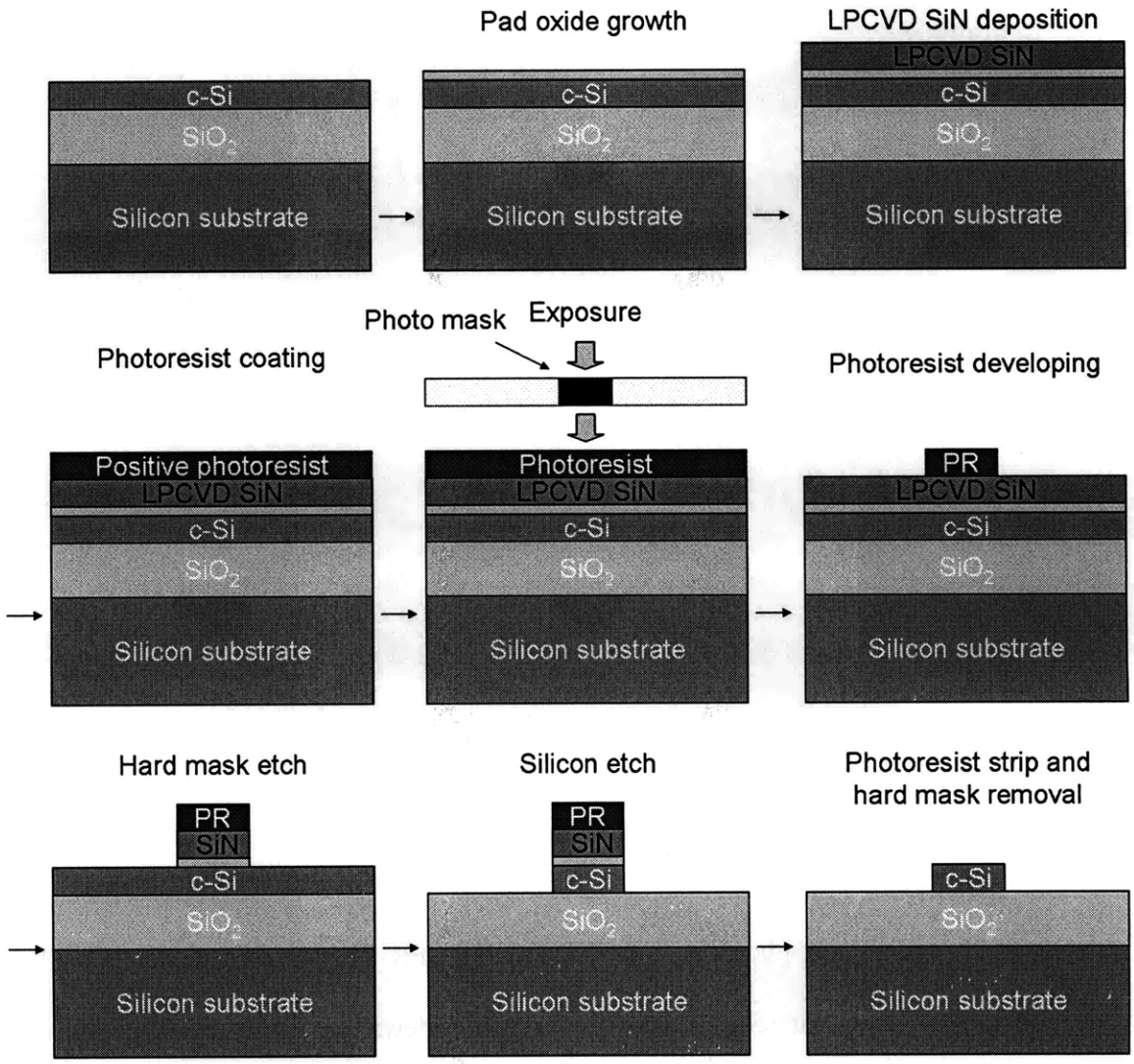

Figure 6.8. Example of the process flow for fabrication of c-Si waveguides using oxide/nitride hard mask. The last step of the process, which is not shown in this figure, is deposition of PECVD top cladding layer on fabricated optical waveguides.

For single-crystalline silicon waveguide (SOI waveguides), the hard mask used in our process consists of 90 Å thermal pad oxide layer and 1190 Å LPCVD silicon nitride layer which can also be used as ion-implantation mask and local oxidation of silicon (LOCOS) mask. The oxide/nitride mask etch uses CHF_3 and CF_4 chemistry; and silicon etch uses Cl_2 and HBr chemistry. The nitride layer can also be etched using SF_6 chemistry. From experimental results, we observed that the usage of hard mask can reduce 1/3 of the sidewall LER in silicon waveguides.

The reason for LER reduction is because the hard mask is resistant to degradation during the etch step by the reactive ion species. Regular photoresists are vulnerable to F and O radicals generated during the etch step which leads to photomask erosion at the sidewalls. The erosion is not uniform and creates additional sidewall striation. Photoresist selectivity relative to the silicon etch is typically low, e.g. ~3:1 or lower at higher powers and temperatures. Oxide or nitride selectivity relative to the silicon etch is much higher, e.g. ~10:1 up to ~100:1. With this selectivity, the hard mask can be thin which also helps with its own etch of the hard mask. A thin hard mask film can be etched with a photoresist film in a short period of time and thus not suffer significant erosion and sidewall degradation that is transferred into the etching hard mask.

The fabrication of SOI waveguides are done at BAE Systems' clean room facility in Manassas, VA. The waveguide measurements are conducted at MIT. The results will be presented later in 0.

For fabrication of amorphous silicon waveguides, PECVD oxide-only hard mask can be used because both thermal oxide and LPCVD nitride are not compatible with the a-Si process temperatures. The rest of the a-Si process flow is similar to SOI waveguides, except that we can insert a wet etch step on oxide hard mask using dilute HF (H_2O:HF, 50:1) to remove some sharp sidewall roughness. Unlike the dry/wet oxidation of c-Si, this process is generally isotropic and only effective to large RMS roughness.

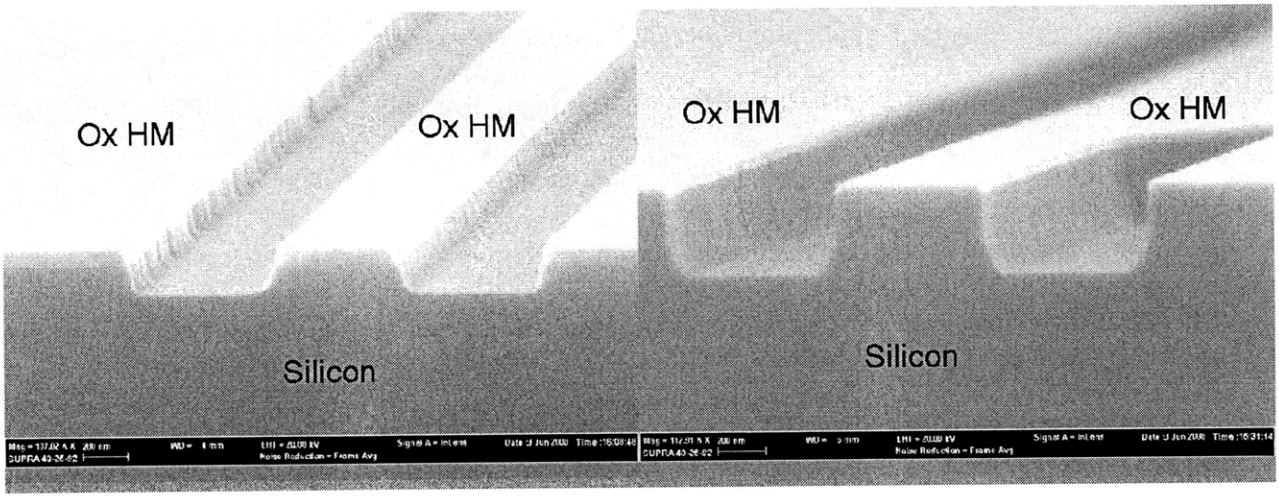

(a) Control process (b) Oxide HM with 1 min HF etch

Figure 6.9. (a) Control sample with standard processes. 1kÅ oxide HM as etched using photoresist mask, followed immediately by 30 seconds RIE silicon etch. Photoresist is removed before SEM. (b) After oxide HM is etched, photoresist is removed by double piranha; and then, the oxide is etched for 1 minute in diluted HF (50:1 H_2O:HF); the wafer is cleaned properly and finally etched for 30 seconds using the same silicon etch condition as in control sample. The scales are both 200 nm.

Figure 6.9 shows the comparison of a process split with and without 1 minute HF wet etch. Although the sidewall line striation can only be compared qualitatively using SEM with the same scale, we do see some extent of roughness reduction effect in sample (b). Other observations are:

- The wet etch rate for a-Si in freshly-made dilute HF solution is about 10 nm per minute. The waveguide dimension as well as the gap in between the waveguide will change accordingly.
- In sample (a), the presence of photoresist during silicon etch can help passivate the etched sidewall with the formed polymeric etch product, silicon etch is thus more anisotropic than in sample (b) where the photoresist is removed prior to silicon etch. The sidewall in sample (b) is curved inwards, indicating a more isotropic etch process.
- In AME-P1000, due to the presence of this polymeric intermediate etch product passivating the sidewall as well as the bottom silicon surfaces, the silicon etch rate in

sample (a) is much smaller than in sample (b). With the same 30 second etch, the silicon trench in sample (b) is ~ 3x deeper than in sample (a).

In this study, the effect of using oxide hard mask for amorphous silicon waveguide applications is proven. In addition, as we will discuss later, a thin, PECVD silicon nitride overcladding layer on a-Si waveguide has much larger loss reduction effect. The usage of oxide hard mask complicates the whole process flow because it is required to remove this oxide hard mask prior to the PECVD nitride deposition and treatment. This approach of using PECVD oxide hard mask for a-Si waveguides is not further pursued for waveguides fabricated at MIT, but hard mask has proven to be a better process than photoresist mask for fabrication of optical c-Si waveguides and is used as the standard process for c-Si waveguide fabrication.

6.3. Local oxidation (LOCOS) for c-Si waveguide fabrication: simulations

The abbreviation "LOCOS" stands for "Local Oxidation of Silicon" and was used to create the oxide insulation between single transistors. Using a mask consist of an oxygen diffusion barrier layer with local openings, e.g. CVD silicon nitride, oxygen (O_2) or water (H_2O) molecules diffuse into and react with Si to form SiO_2 through the openings at elevated temperatures (1000 ~ 1100 ^{o}C). Because the formed SiO_2 is about 2 times the volume of consumed Si, the edges of the nitride hard mask get pushed up due to the stress effect as shown in Figure 6.10.

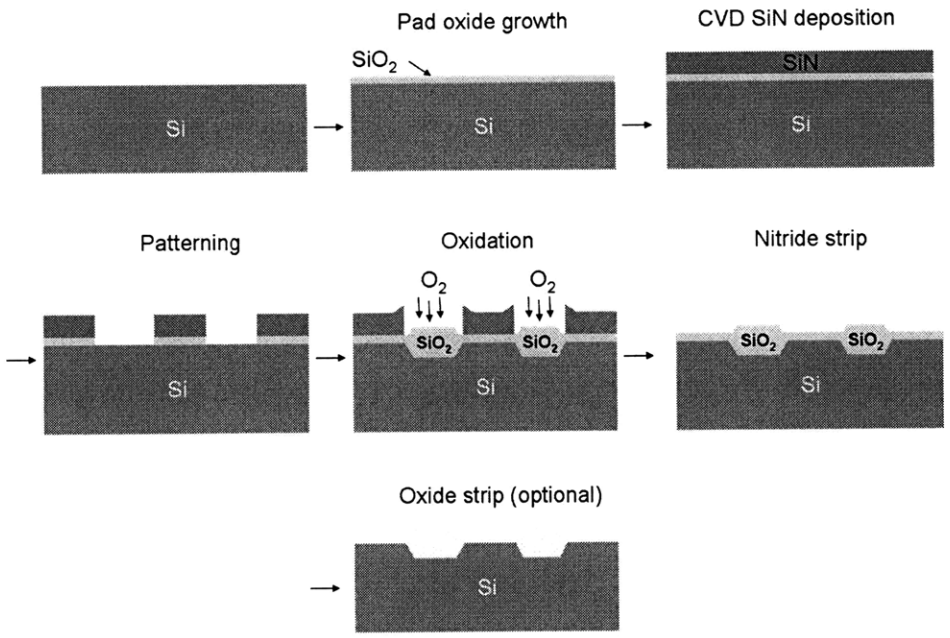

Figure 6.10. Example of LOCOS process flow. The waveguide sidewall definition can be done by oxidation. This substitutes directly etching of the waveguide sidewalls, avoiding striation-like sidewall roughness.

Most recently, LOCOS method has been adapted to fabricate low loss c-Si optical ridge waveguide on SOI substrate with TE-, TM- mode transmission losses below 1 dB/cm [54, 55]. At MIT, Dr. Yi has previously demonstrated c-Si channel waveguides and racetrack resonators fabricated by LOCOS process [56]. The prototype waveguides have 2.5 dB/cm transmission loss for the TE-mode at 1550 nm and the quality factors, Q, of the racetrack resonators range from 10^4 to 10^5. Limited by i-line stepper resolution, these racetrack resonators feature relative wide coupling gaps ranging from 500 nm to 700 nm between the bus waveguide and the racetrack waveguide. However, the oxidation in such narrow gap may not have a uniform oxidation rate as in isolated structures. This section is dedicated to study the pattern effect for fabrication of c-Si channel waveguides and resonators using LOCOS process.

The numerical simulation is based on the VISCOELA model in TSUPREM 4 software package. The oxidant first diffuse to the oxide surface, diffuse through oxide, and react with Si at the SiO_2/Si interface as shown in Figure 6.11.

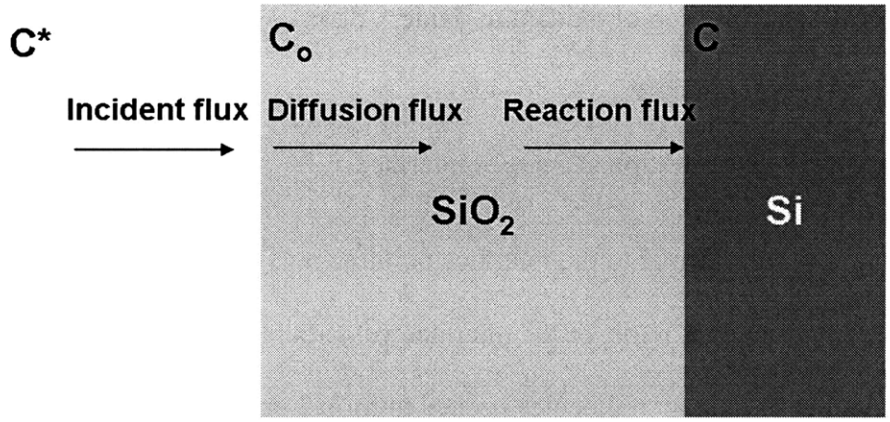

Figure 6.11. Schematic representation of oxidation of silicon.

According to Deal and Groove [57], the incident flux of the oxidant is

$$\vec{F} = h\left(C^* - C_o\right)\vec{n}_s \tag{6. 1}$$

The diffusion flux of the oxidant in the oxide is

$$\vec{F} = D\vec{\nabla}C \tag{6. 2}$$

The reaction flux of the oxidant at SiO_2/Si interface is

$$\vec{F} = k_s C_i \vec{n}_i \tag{6. 3}$$

In steady state, $\vec{\nabla}\cdot\vec{F} = 0$, the oxide growth rate is

$$GR = \frac{\vec{F}}{N} + r_o \tag{6. 4}$$

where

$\vec{F}$: the flux of oxidant

h: the gas-phase mass-transfer coefficient

C^*: the oxidant concentration in ambient

C_o: the oxidant concentration at the oxide surface

$\vec{n}_s$: the unit vector normal to the oxide surface, pointing at the oxide

D: the diffusivity of oxidant

C: the local concentration of oxidant in oxide

k_s: the surface reaction rate

C_i: the oxidant concentration at SiO_2/Si interface

$\vec{n}_i$: the unit vector normal to the interface pointing away from the oxide

GR: the growth rate of oxide, or the interface velocity relative to the oxide

N: the number of oxidant molecules needed to form 1 cm^3 of oxide

The VISCOELA model solves the above equations directly to obtain the growth rate at each point on the SiO_2/Si interface in two dimensions by considering different crystal orientation at the interface and their effect on oxidation rate. It also takes into account the shear stress effect during oxidation [58,59].

In our simulations, two masks are considered. The first one is the silicon nitride mask which has been used in experiments by Dr. Yi; the other one is the standard pad oxide + silicon nitride mask. The temperature is set to be 1000 ^oC.

For silicon nitride mask, we first examine the isolated structure, e.g. a semi-infinite nitride mask opening on a c-Si slab layer as shown in Figure 6.12. The c-Si thickness is 200 nm and the nitride thickness is 200 nm. The result of the simulation is shown in Figure 6.13. Generally, the lateral diffusion of oxidant under the nitride hard mask is limited. Because there is little oxide formed close to nitride/Si interface, the interface does not move after oxidation. However, sharp "bird beak" like corners occur at the top edges of silicon structures. These sharp corners are not desirable as they normally act as radiation centers when interacting with light, resulting in high optical scattering loss.

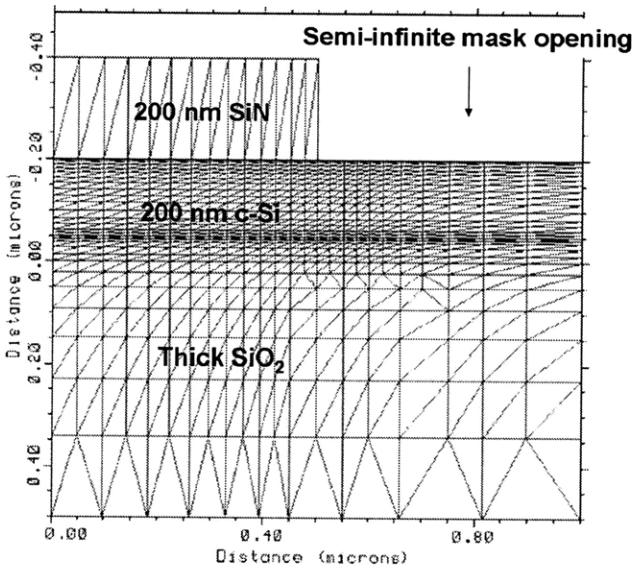

Figure 6.12. The screen snap-shot of the structure and simulation grid structure in TSUPREM 4.

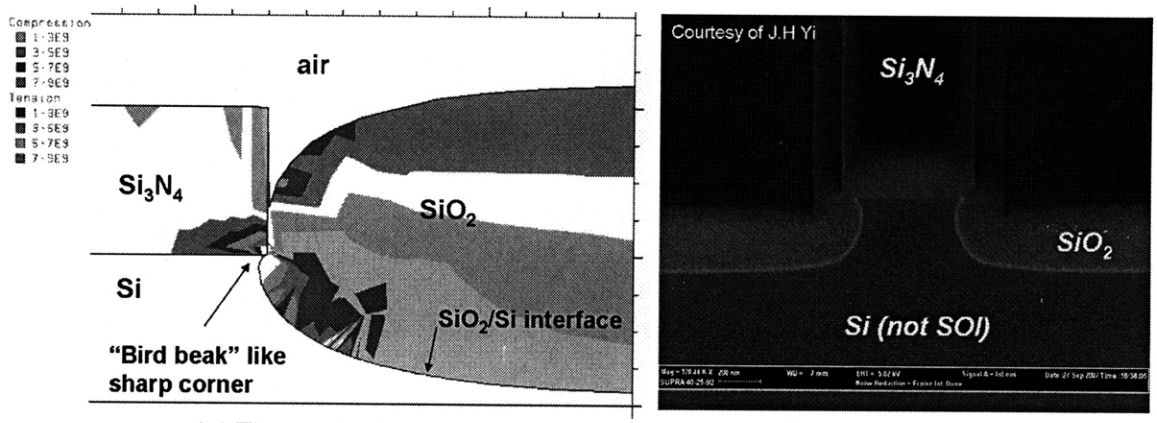

(a) The resulted contours of hydrostatic pressure

(b) An SEM image of waveguide cross section

Figure 6.13. (a) Simulation results of the contours of hydrostatic pressure after oxidation using nitride mask; (b) an SEM image of the fabricated waveguide using nitride hard mask.

The 2-dimensional SiO_2/Si interface movement as a function of oxidation time is plotted in Figure 6.14. It is found that it takes ~ 100 minutes to oxidize through 200 nm c-Si; a long tail with sharp corner is formed at the bottom of c-Si, denoted as the black dots in Figure 6.14. For longer oxidation times, c-Si is undercut due to the lateral diffusion of oxidant through under cladding oxide; as a result, the bottom SiO_2/Si interface becomes tilted and the bottom corners of c-Si are rounded.

Similarly, we can obtain the oxidation profiles through a nitride mask opening that is only 500 nm wide. The corresponding simulation results are plotted in Figure 6.15. We discover that it takes 160 minutes to oxide through the 200 nm thick c-Si with 500 nm wide mask opening. This indicates that the oxidation rate is dependent of the opening width. If we measure the height of the remaining c-Si at the end of each oxidation with different oxidation time as shown in Figure 6.16, we can see that for c-Si thicker than 100 nm, the oxidation rates will be different in the isolated regions and the more confined region, such as the coupling gap of a ring resonator and its bus waveguide or directional coupler.

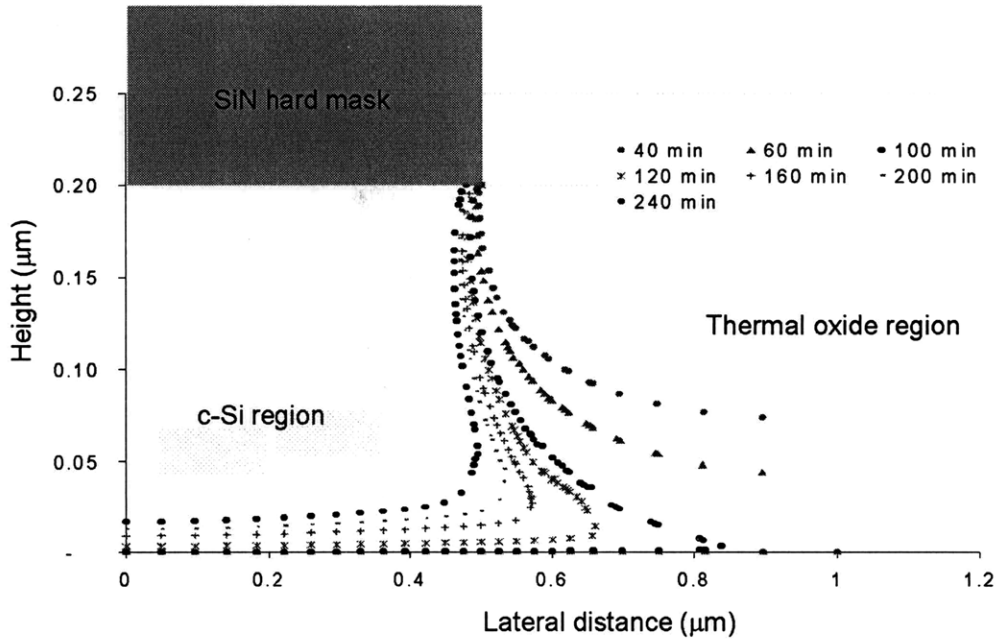

Figure 6.14. Simulated oxidation in semi-infinite mask opening. The scatter plots of the 2-dimensional SiO_2/Si interface movement as a function of oxidation time from 40 minutes to 240 minutes. The nitride hard mask is also shown as the reference position.

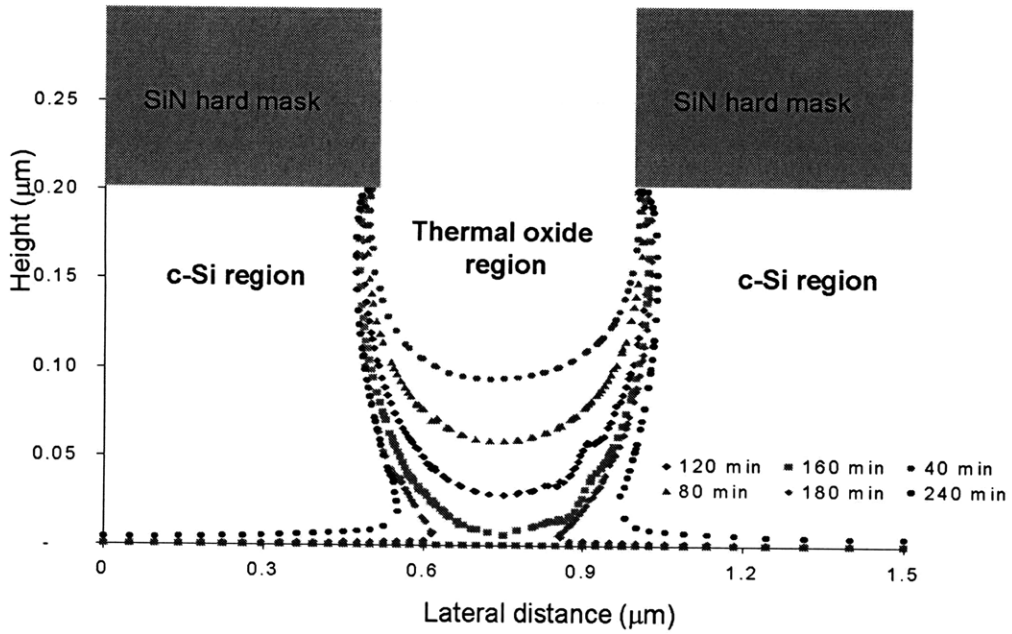

Figure 6.15. Simulated oxidation through finite mask opening of 500 nm. The scatter plots of the 2-dimensional SiO_2/Si interface movement as a function of oxidation time from 40 minutes to 240 minutes. The nitride hard mask is also shown as the reference position.

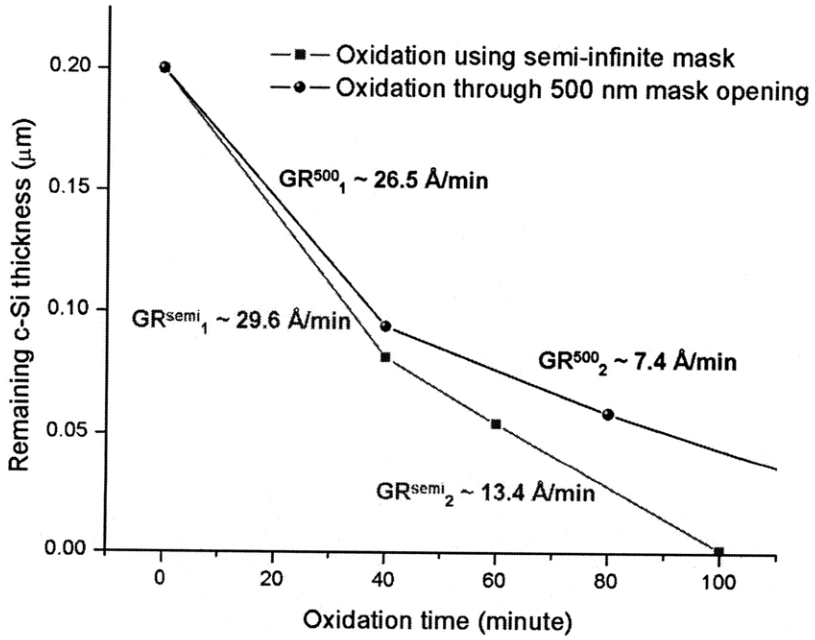

Figure 6.16. Comparison of simulated oxidation rate in semi-infinite and finite mask opening of 500 nm. The oxidation rate (growth rate, GR) becomes different after the first 100 nm c-Si oxidization. The oxidation in more confined is slower than in semi-infinite region.

To summarize the LOCOS process using nitride only hard mask, we observe the following in simulations:

- "Bird beak"-shaped sharp corners at top of the c-Si waveguides

- The top surface of the c-Si waveguide will not be oxidized
- The narrow window opening (e.g. 500 nm) will have a significant different oxidation rate than the semi-infinite opening for c-Si thicker than 100 nm. For ring resonators or directional couplers, the gap region and the regular waveguide region may have different geometries after oxidation
- For very long oxidation that removes silicon completely in the opening area, the silicon waveguide will be undercutting by oxide due to the lateral diffusion of oxidant through the under cladding oxide

The pattern effect is also studied in the case where the hard mask consists of pad oxide and silicon nitride. Example of the simulation structures for both semi-infinite and finite opening mask are given in Figure 6.17. The most significant difference from the nitride only hard mask is that using the pad oxide under the nitride will allow oxidant diffusion through this oxide layer and result in oxidation of c-Si top surface as shown in Figure 6.18. As the result, the "bird beak"-shaped sharp corner will not occur; also, the conversion from Si to SiO_2 result in ~ 2x volume increase in SiO_2 so that the nitride hard mask gets pushed up due to the stress in SiO_2.

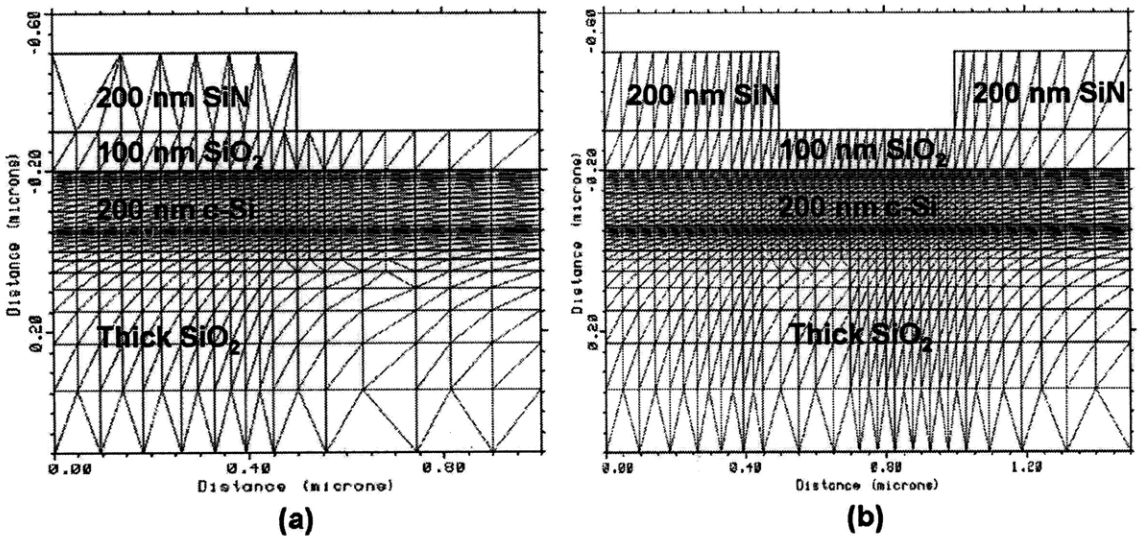

Figure 6.17. The screen snap-shots of the layered structures with (a) semi-infinite SiN hard mask; (b) finite-opening

SiN hard mask.

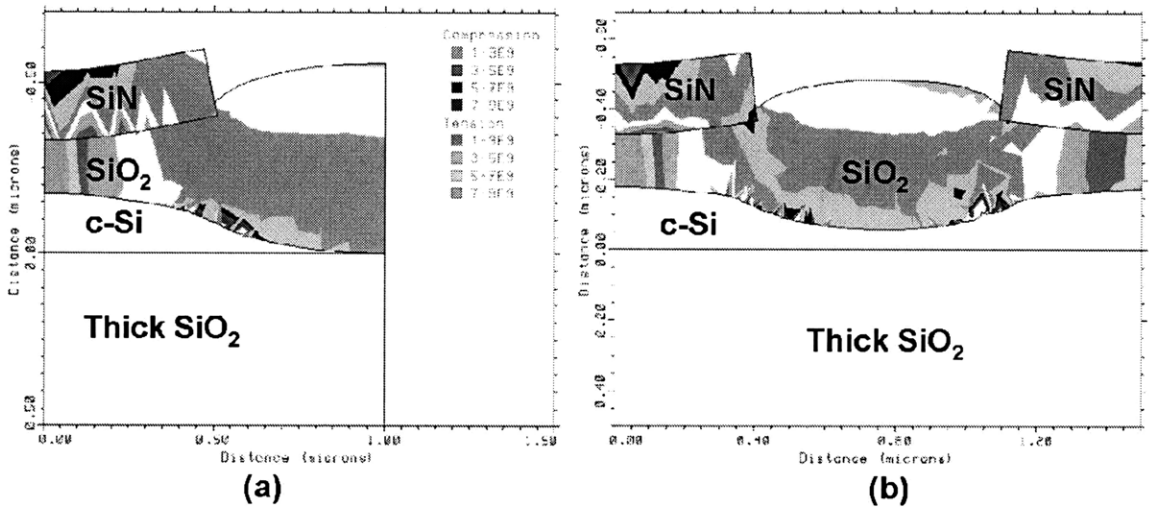

Figure 6.18. The contours of simulated hydrostatic pressure after oxidation using pad oxide and nitride mask in (a) semi-infinite mask opening and (b) finite mask opening.

The time series of three different oxidation processes are studied where semi-infinite mask, 500 nm wide mask opening, and 700 nm wide mask opening are used in oxidation simulation as shown in Figure 6.19. Similarly, the growth rates can be calculated as the slopes of the relatively linear portion of the remaining silicon thickness versus oxidation time plot as in Figure 6.20. We can see clearly that the three oxidation rates at lateral distance 0.8 μm are different due to different mask opening width. In order to achieve uniform oxidation and low pattern effect, it is found that the mask opening width has to be at least 700 nm for c-Si thicker than ~ 70 nm.

In conclusion, the usage of the LOCOS process for c-Si channel waveguide fabrication is examined theoretically using TSUPREM4. We have found that the pattern effect on oxide growth rates is significant for thick c-Si and narrow mask opening. Careful designs for waveguide geometry and oxidation condition are required in order to prevent this pattern effect.

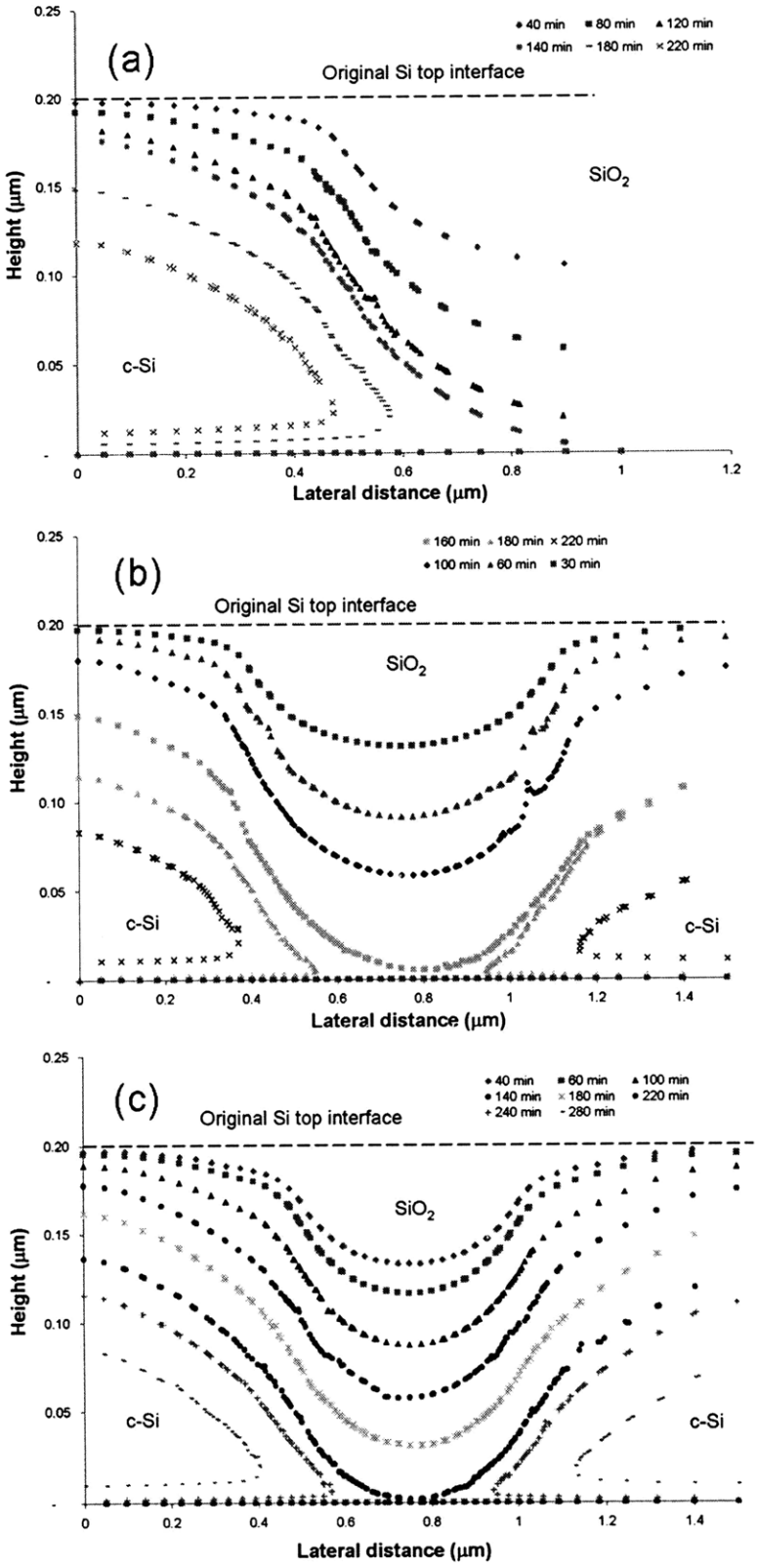

Figure 6.19. Simulated oxidation using pad oxide and nitride hard mask. The scatter plots of the 2-dimensional SiO_2/Si interface movement as a function of oxidation time. (a) semi-infinite mask opening; (b) 700 nm wide mask opening; and (c) 500 nm wide mask opening.

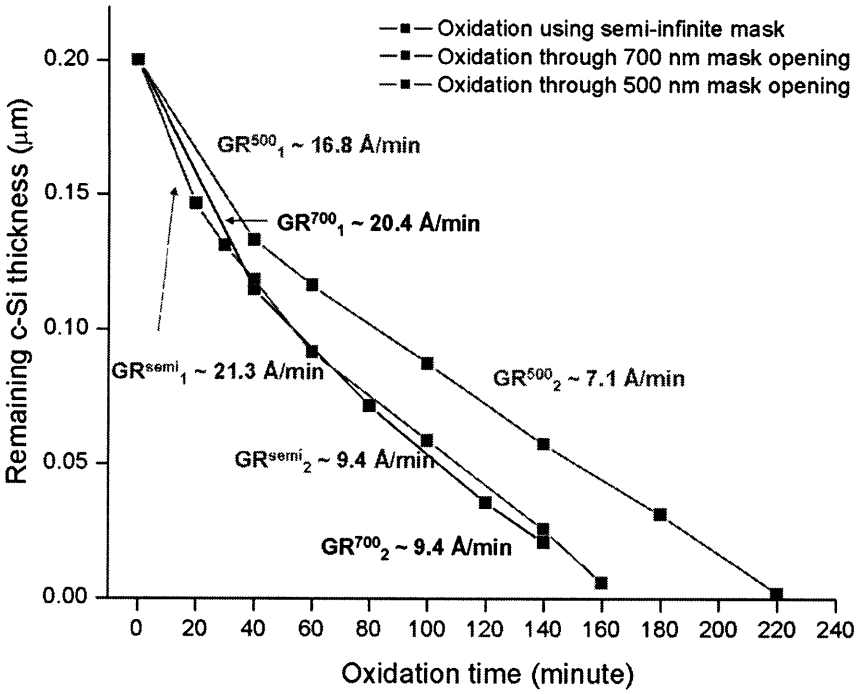

Figure 6.20. Comparison of simulated oxidation rates in semi-infinite and finite mask opening of 500 nm and 700 nm. The oxidation rate (or growth rate, GR) becomes different after the first 50 nm c-Si gets oxidized. The oxidation in more confined is considerably slower than in more open mask region.

6.4. Damascene process for deposited waveguides

Damascene process was first developed for copper interconnect technologies by IBM in 1990's [60]. Because there is no CMOS compatible process that can etch copper to define metal interconnects for transistors, the method of opening a trench, filling metal (copper) in the trench, and using chemical-mechanical polishing to remove excess copper outside the trench is developed, shown as an example from Intel in Figure 6.21. This technology has facilitated the adaptation of copper technologies and helped electronic industry to successfully follow the Moore's scaling law since it was introduced.

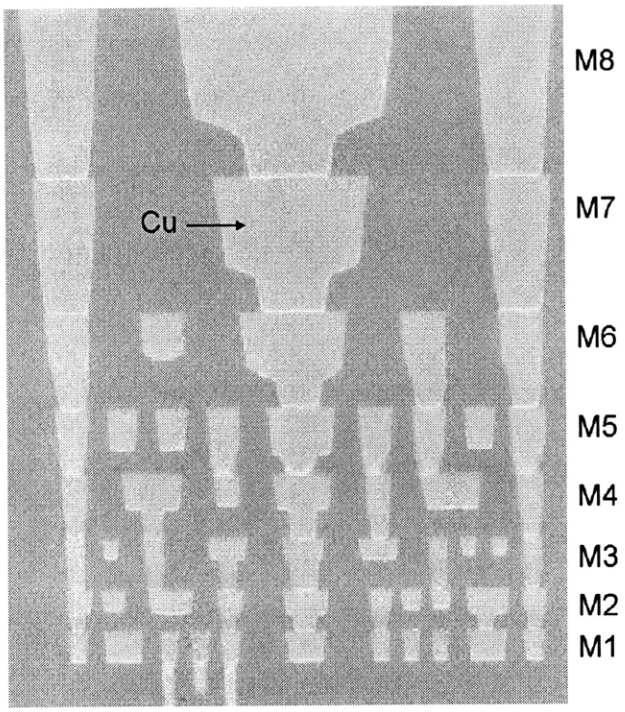

Figure 6.21. Example of advanced 8-layer copper interconnects from Intel (Figure adapted from Ref. 61)

Damascene process can also been applied for photonic device fabrications. The technology of the selective growth of germanium directly on silicon is one example of utilizing damascene-like approaches to fabricate high performance photodetectors and optical EA modulator devices [62]. Damascene process can also be used for fabrications of deposited waveguide fabrications, e.g. PECVD amorphous silicon waveguides. An example of the damascene process flow is depicted in Figure 6.22. Starting with a thermal oxide substrate with 2 ~ 3 μm thermal oxide, which can be either grown by wet oxidation or bought from vendors directly), a layer of positive photoresist is coated and patterned using dark field photo mask and developed; the oxide trench is opened up using RIE and then the remaining photoresist is cleaned; a layer of PECVD a-Si is deposited in the trenches and complete fills them; the excess of a-Si on surface is removed by CMP process and the residue chemical and debris are cleaned using double Piranha cleaning; and finally a layer of 2 ~ 3 μm PECVD SiO_2 is deposited as the top waveguide cladding layer.

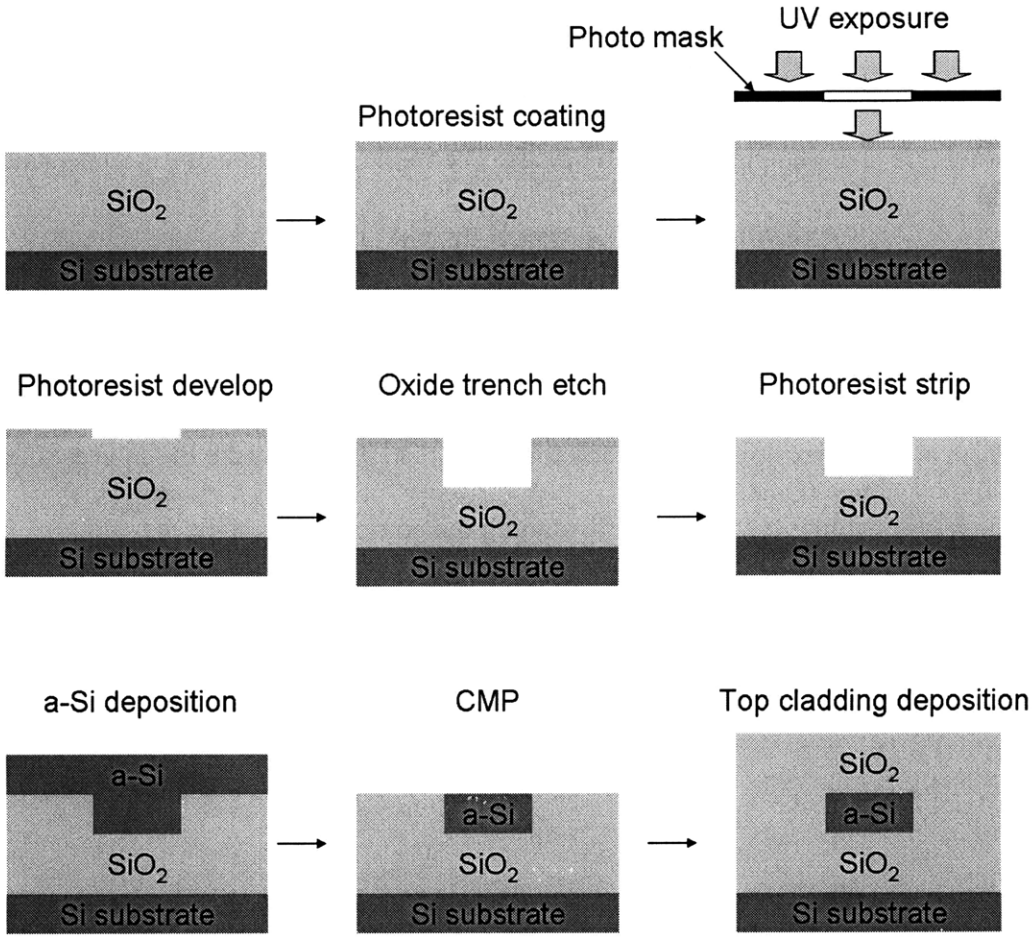

Figure 6.22. Process flow for a-Si waveguide fabrication using damascene process. In this example, positive photoresist and dark field photo mask are used.

Another advantage of using damascene process to fabricate a-Si waveguide is that some of the post-etch waveguide smoothing methods that are not compatible with a-Si process temperature can be applied to the oxide trench prior to a-Si deposition, such as high temperature annealing and thin LPCVD interlayer GRIN layer. The smooth sidewalls in oxide trench can translate into smooth sidewall a-Si waveguide if the trench is completely filled. Of course, one unique process associated with damascene process, the chemical-mechanical polishing (CMP), is the most critical for a-Si channel waveguide formation.

In experiments, the oxide trench is defined using positive photoresist with dark field photo mask. The positive photoresist works more consistently with our Nikon i-line stepper to achieve the smallest feature size than negative photoresist. The oxide etch chemistry is CHF_3 and CF_4.

Figure 6.23 shows a couple SEM images of the top view of an as-etched oxide trenches in a racetrack resonator configuration and the cross sectional view of the coupling region. The photoresist is then removed either by Asher and cleaned using Piranha recipe, or by double Piranha cleaning. From here, the oxide wafer is ready for the next step which is the PECVD a-Si deposition; or we can do a quick dilute HF treatment to smooth out some sharp roughness.

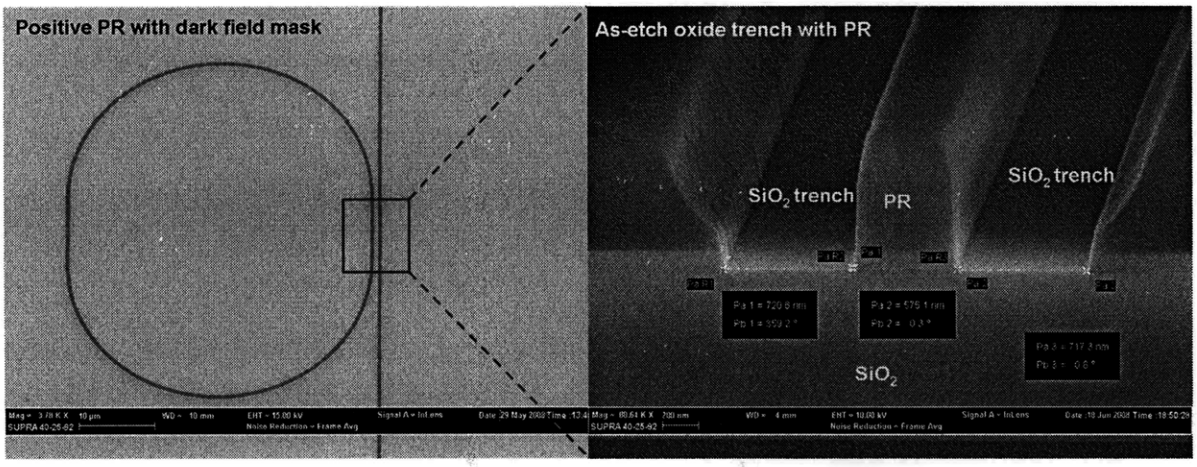

Figure 6.23. SEM images of the top view of an as-etched oxide trenches in a racetrack resonator configuration and the cross sectional view of the coupling region. The waveguide is designed to be 700 nm in width and the coupling gap is 600 nm. The trench depth is set to be 100 nm. The dimension is well controlled.

As mentioned in previous sections, diluted HF (50:1, H_2O: HF) can etch thermal oxide at a rate about 10 nm per minute. The roughness smoothing comes at the price of scarifying the precise dimension control. However, this deviation in dimension is not a concern for straight waveguides because these waveguides are generally wider than 500 nm. Such dimension change will not result in a large change in terms of confinement factor and bending performance. For resonator devices, any dimension deviation from design will result in resonance wavelength shift and changes in finesse. For these devices, we can make fresh HF solution to have relative constant etch rate of

thermal oxide; in design, we can adjust the dimension on photo mask according to the processes to compensate this deviation. Figure 6.24 is the comparison of the same oxide trench structures (the coupling region of a racetrack resonator device), as-etched and etched by diluted HF for 2 minutes. The measured dimensions on SEM images are not exact, but generally, the width of the coupling region is decreased and the oxide trenches are widened, depending on the HF concentration and treatment time.

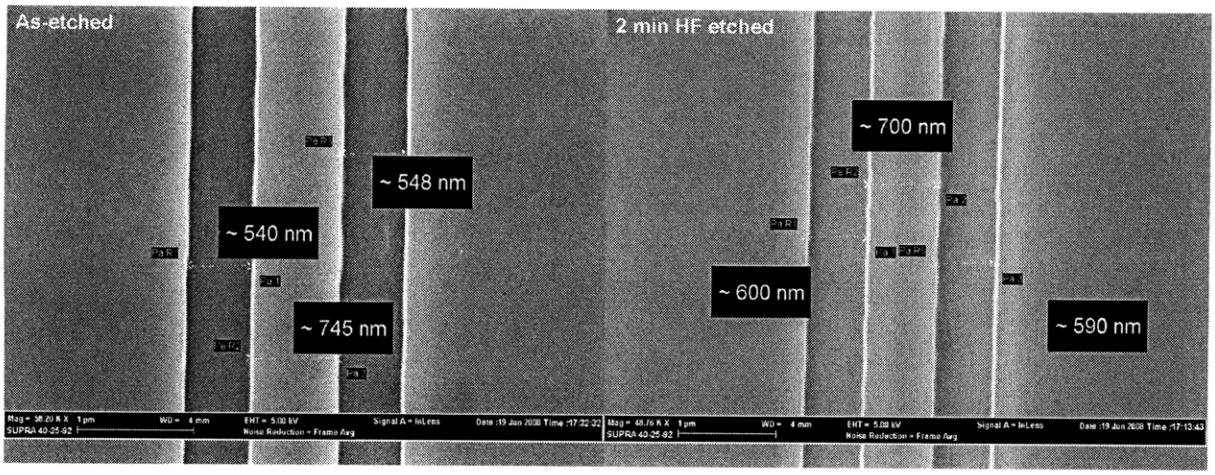

Figure 6.24. The top SEM images of the same oxide trenches, as-etched or undergone 2 minutes diluted HF treatment. Both oxide trenches are designed to be straight; the slightly wavy-shaped edges in the SEM images are due to small sample displacement caused by charging or vibration during multiple vertical scans.

These 1 μm deep trenches are filled with 3 μm PECVD a-Si using Applied Materials Centura 5300 DCVD. 2 μm extra a-Si is removed by CMP. The CMP step is outsourced with MTL approval to the Semiconductor Processing Company, Boston, MA. After double piranha cleaning, the wafers are examined by SEM. Examples of the waveguide cross-section SEM images are given in Figure 6.25. The measured a-Si thickness after CMP ranges from 84 Å to 99 Å from ~ 80° angled SEM images. Finally, 3 μm PECVD SiO_2 is deposited as the waveguides' top cladding layer. The waveguide performance will be discussed in the following chapters.

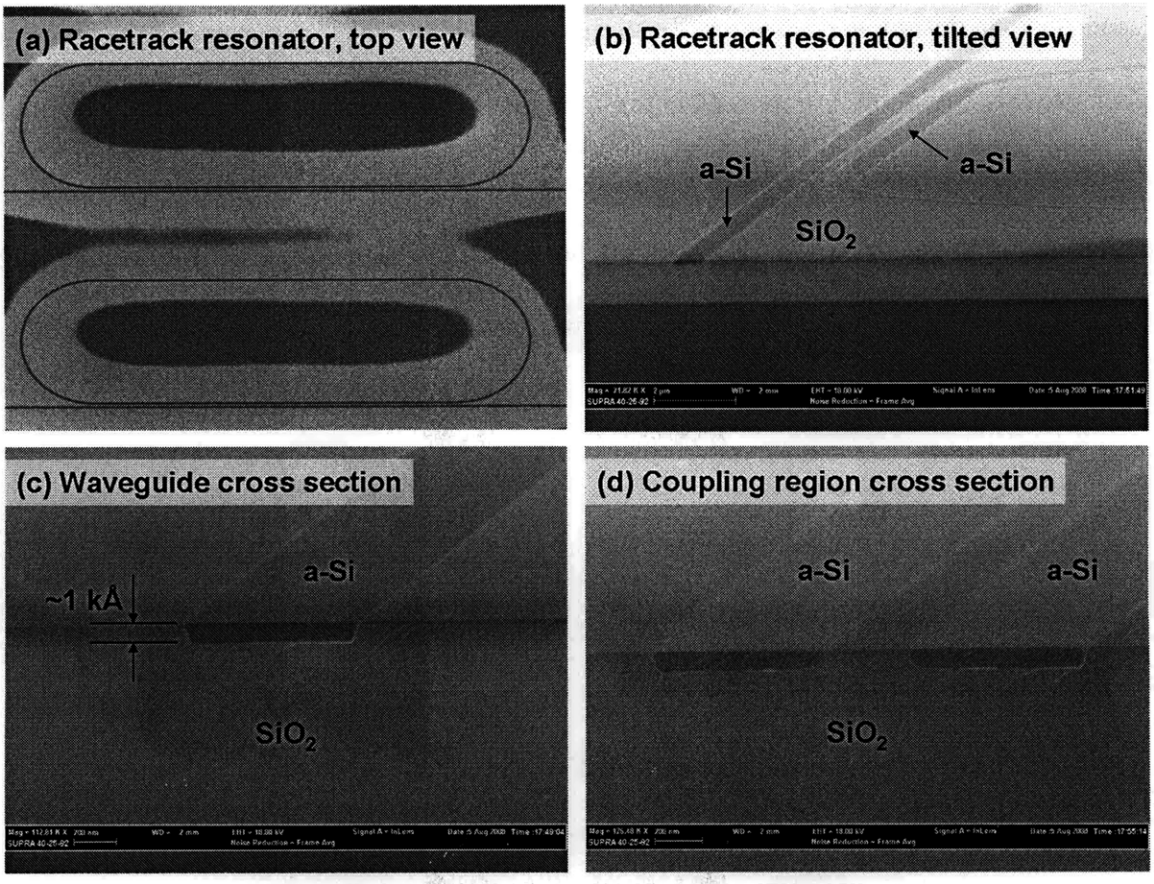

Figure 6.25. SEM images after CMP: (a) the top view, showing the uniform coupling spacing; (b) the tilted view of a racetrack resonator, showing the well controlled coupling region and the clean surface of SiO_2; (c) a cross sectional view of a bus waveguide, showing the a-Si thickness is well controlled during CMP; and (d) a cross sectional view of the racetrack coupling region.

6.5. Summary

In this chapter, we have discussed c-Si and a-Si waveguide process optimization. First, the general photolithography and the application of hard mask were discussed. For c-Si, local oxidation method is a promising technique to achieve line-striation free waveguide sidewalls. For a-Si waveguides, damascene process is particular interesting because the oxide trench smoothing can be done prior to a-Si deposition therefore it is not constrained by a-Si process temperature which is below 600 °C.

Chapter 7. Low temperature, low loss PECVD Silicon Nitride

Amorphous silicon nitride is an excellent dielectric material for photonic waveguide applications. Its large bandgap (~ 5 eV) ensures its transparency for wavelength up to UV-Vis range. Its refractive index ranges from 1.7 to 2.2, ideal for compact high index contrast integrated photonic circuit applications. This material's processing is also compatible with standard CMOS processes.

As we discussed in 0, for waveguide applications near the telecommunication wavelength of 1.55 um, the dominant transmission loss mechanism in PECVD SiN waveguide is the bulk absorption due to the broad NH resonant absorption centered around 1510 nm.

The Low Pressure CVD (LPCVD) silicon nitride contains minimal H and has excellent optical transparency around 1550 nm. It also has good step coverage due to its thermal process nature; very low wet etch rate in diluted HF; large break down voltage; and minimal leakage current. However, this furnace nitride are normally deposited at relatively high temperatures (e.g. 730, 760, or 825 ^{o}C) which is not readily compatible with a lot of the processes which requires lower temperatures, such as processes involve amorphous silicon, phase change memory, and NiSi contacts etc..

Plasma Enhanced CVD (PECVD) silicon nitride uses silane (SiH_4) and ammonia (NH_3) chemistry. Assisted by plasma in the gas phase, SiH_4 and NH_3 precursors dissociate and condense onto substrates, enabling low temperature deposition of silicon nitride below 600 C. The as-deposited thin film normally contains a large amount of H in the forms of SiH and NH, and is best described as SiN_xH_y. However, many techniques can also give us low NH containing silicon nitride, including:

1. High temperature annealing [63]
2. N_2/SiH_4 chemistry [64]
3. SiH rich chemistry
4. N_2/Ar plasma treatment
5. UV treatment

Table 7.1 qualitatively compares the above 5 methods in terms of thermal budget compatibility and film qualities. The first two methods have been studied in details by our two previous Ph.D. students. Here, only the last three methods will be discussed.

Table 7.1. Comparison of different techniques to obtain low loss PECVD silicon nitride

Technique	Pros	Cons
High temperature annealing	• Minimal H concentration • Good step coverage • Good stability	• High temperature processes (> 1000 °C)
N_2/SiH_4 chemistry	• Low temperature process • Relative low H concentration, e.g. 9.9% (compared to 18.3% using NH_3/SiH_4 chemistry) [64].	• Poor sidewall coverage
SiH rich recipe	• Low temperature process • Relative low NH concentration • High refractive index • Good step coverage	• Large leakage current • Small breakdown voltage • Poor stability
UV treatment	• Low temperature process • Low H concentration • Good step coverage • Small leakage current • Large breakdown voltage • Good stability	• Low throughput
Plasma treatment	• Low temperature process • Low H concentration • Good step coverage • Small leakage current • Large breakdown voltage • Good stability	• Extremely low throughput • Only applicable for ultra thin film applications (< 50 nm)

7.1. Low NH, SiH rich PECVD silicon nitride

The composition of PECVD SiN_xH_y films can be controlled directly during deposition. The NH and SiH bond concentration is largely dependent on NH_3, SiH_4 flow rates, RF powers, and deposition temperature etc. as all these listed parameters can effectively change the extent of dissociation for both NH_3 and SiH_4 molecules.

In the gas phase, for example, aminosilane radicals are formed as hydrogen atoms get stripped from the SiH and NH bonds. For a given RF powers, the SiH bonds are easier to break than the NH bonds. With high NH_3 flow rate at high RF power, the dominant intermediate radical clusters are the 3-aminosilane radicals.

$$SiH_4 + NH_3 \xrightarrow{plasma} \bullet SiH_2(NH_2) + H_2$$
$$\bullet SiH_2(NH_2) + NH_3 \xrightarrow{plasma} \bullet SiH(NH_2)_2 + H_2$$
$$\bullet SiH(NH_2)_2 + NH_3 \xrightarrow{plasma} \bullet Si(NH_2)_3 + H_2$$

By reducing NH_3 flow rate, the above three reactions are favored to move to the left hand side of the equations to form less NH_2 containing aminosilane radicals. As a result, the NH concentration is reduced. For example, when SiH_4 flow rate is 40 sccm, RF power is 75 W, with everything else fixed, reducing NH_3 flow rate from 900 to 100 sccm can reduce the NH/SiH ratio from 10 to 0.7 in the SiN_xH_y films deposited at 200 °C. More quantitatively, according to Rand's method [65], the absorption cross sections for SiH, NH, and SiN are 7.4×10^{-18}, 5.3×10^{-18}, and 2.1×10^{-18} cm^2, taken from Ref. 65 and 66. The concentration can be calculated using

$$[NH] = \frac{1.4 \times A_{NH}}{t \times \sigma_{NH}} \tag{7.1}$$

$$[SiH] = \frac{A_{SiH}}{t \times \sigma_{SiH}} \tag{7.2}$$

$$[H] = [NH] + [SiH] = \frac{1.4 \times A_{NH}}{t \times \sigma_{NH}} + \frac{A_{SiH}}{t \times \sigma_{SiH}} \tag{7.3}$$

where A_i is the peak area in FTIR spectrum (Absorbance); σ_i is the corresponding absorption coefficient; and t is the film thickness. The NH and SiH concentration at different NH_3 flow rate is plotted in Figure 7.1. The total H concentration also increases as NH_3 flow increases. Other important film parameters are summarized in Table 7.2.

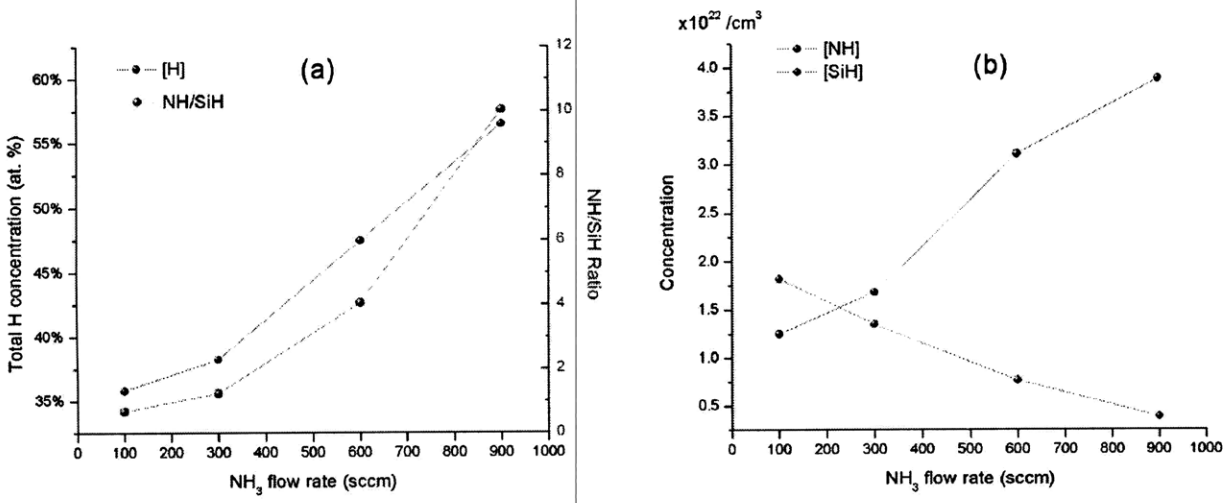

Figure 7.1. (a) the total H concentration and NH/SiH ratio as a function of NH_3 flow rate; (b) SiH and NH concentration (/cm^3) as a function of NH_3 flow rate, derived from their FTIR spectra using Rand's method.

Table 7.2. Summary of other film property variations as a function of NH_3 flow rate

NH_3 (sccm)	RF (W)	Uniformity (%)	Dep.Rate (Å/s)	RI	Stress (MPa)
900	75	0.49	9	1.6951	-154
600	75	0.59	8	1.7216	4
300	75	0.78	7	1.7594	131
100	75	1.01	9	1.7900	122

Increasing SiH_4 flow rate can achieve the same effect, obtaining low NH containing SiN_xH_y film as shown in Figure 7.2. The corresponding FTIR spectra are plotted together for

comparison in Figure 7.3. For both methods, low [NH] is always accompanied by high [SiH] and high total [H], which may not be desirable for the reasons listed in Table 7.1.

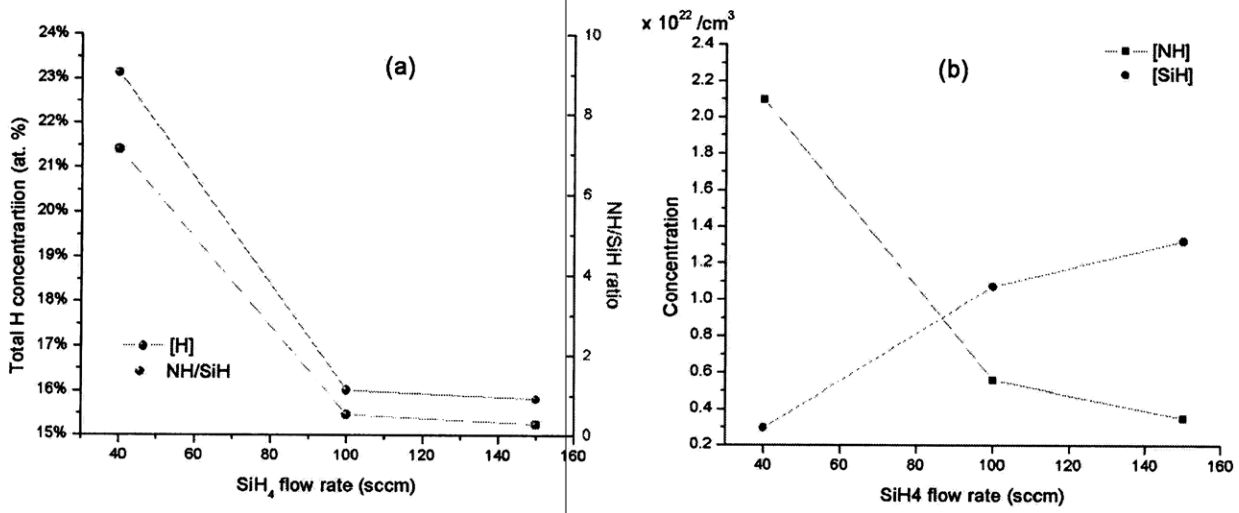

Figure 7.2. (a) the total H concentration and NH/SiH ratio as a function of SiH_4 flow rate; (b) SiH and NH concentration ($/cm^3$) as a function of SiH_4 flow rate, derived from their FTIR spectra using Rand's method.

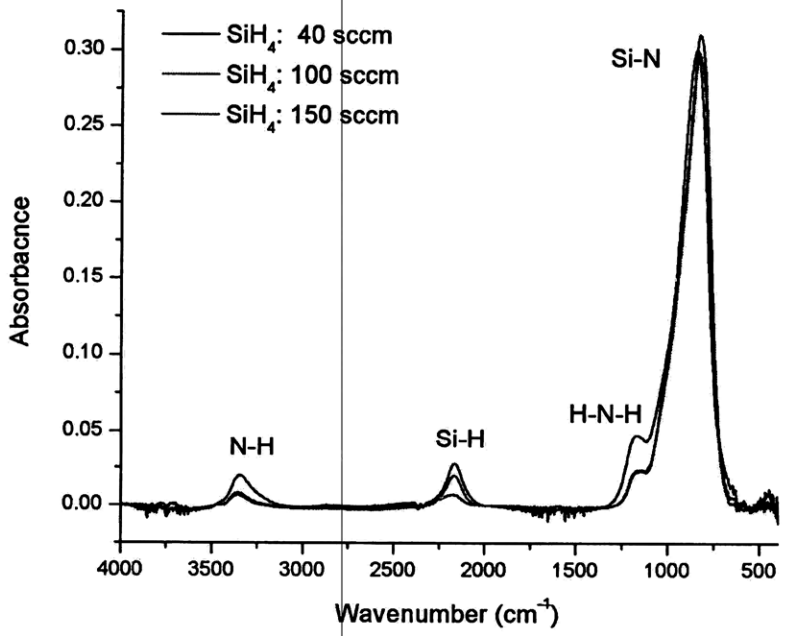

Figure 7.3. FTIR spectra of three samples deposited with different SiH_4 flow rates. The spectra are normalized with respected to their thickness.

Increasing the process temperature can also reduce the H content in PECVD SiN_xH_y films. Although the gas phase chemistry may not be affected by the substrate/heater temperature, assisted with more thermal energy, condensation reactions on the substrate are more likely to occur. Figure

7.4 is an example of two SiN_xH_y films deposited using the same recipe with 900 sccm NH_3 and 40 sccm SiH_4 but at two different temperatures of 200 and 400 °C.

In summary, changing the deposition conditions can effectively reduce the NH concentration in SiN_xH_y film. However, other film properties also change accordingly. Especially, the film will contain a high concentration of SiH bonds. Therefore, it is desirable to reduce NH and SiH concentration simultaneously.

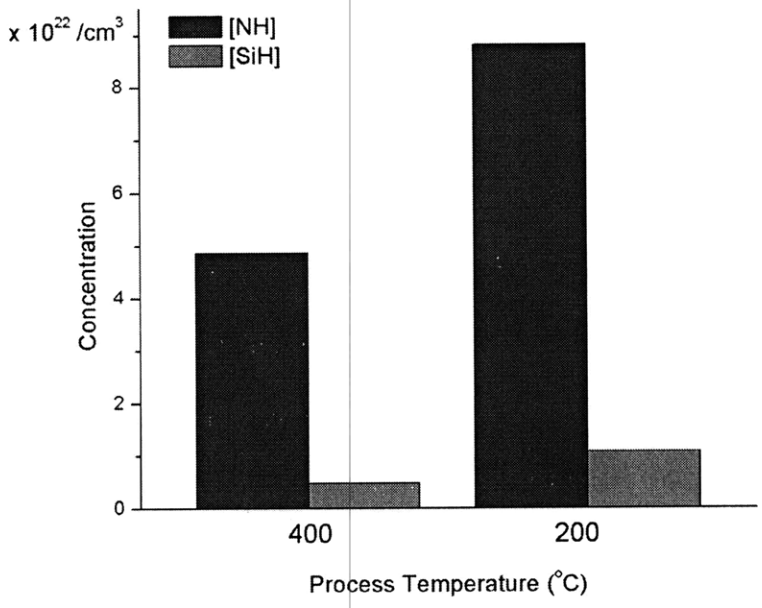

Figure 7.4. The difference for NH and SiH concentrations at 200 °C and 400 °C. Other process conditions are the same.

7.2. Post-deposition N_2/Ar plasma treatment

An alternative approach to get low NH concentration in SiN_xH_y films is to remove hydrogen from the film after it is deposited. An in-situ, post-deposition N_2/Ar plasma treatment is developed for this H removal purpose [67].

At the same process temperature as deposition, in N_2/Ar plasma, N_2 dissociates into •N radicals. Upon arrival at SiN_xH_y surface, they can penetrate the film into a small depth, react with the H atoms in the film, form and release NH_3 molecules back to the gas phase. As a result, both SiH and NH can be reduced as shown in Figure 7.5.

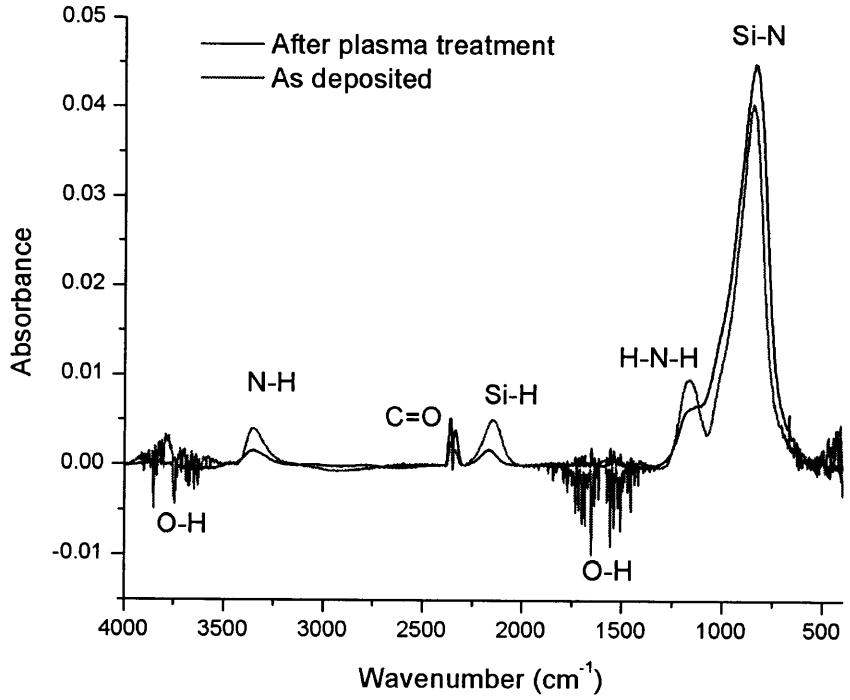

Figure 7.5. FTIR comparison of the same SiN_xH_y films before and after plasma treatment.

This effect of plasma treatment is strongly dependent on the film thickness because •N radical's penetration depth is extremely limited because the treatment is done in-situ in a deposition tool. In a deposition tool, the substrate is grounded, radicals in the gas phase could not response to the RF frequency (13.56 MHz, used in this case) due to its large mass. As a result, they can not accumulate enough kinetic energy; the reactions with H atoms are only skin-deep. In order to deposit a film thicker than a few nanometers, a cyclic deposition-treatment process has to be used. The schematic representation of such process is shown in Figure 7.6. During the deposition step, both NH_3 and SiH_4 gases are flowing and the RF power is 60 W. Upon plasma treatment, both NH_3 and SiH_4 are turned off. A large flow of Ar and N_2 are injected into the chamber; meanwhile the RF power is increased to 250 W.

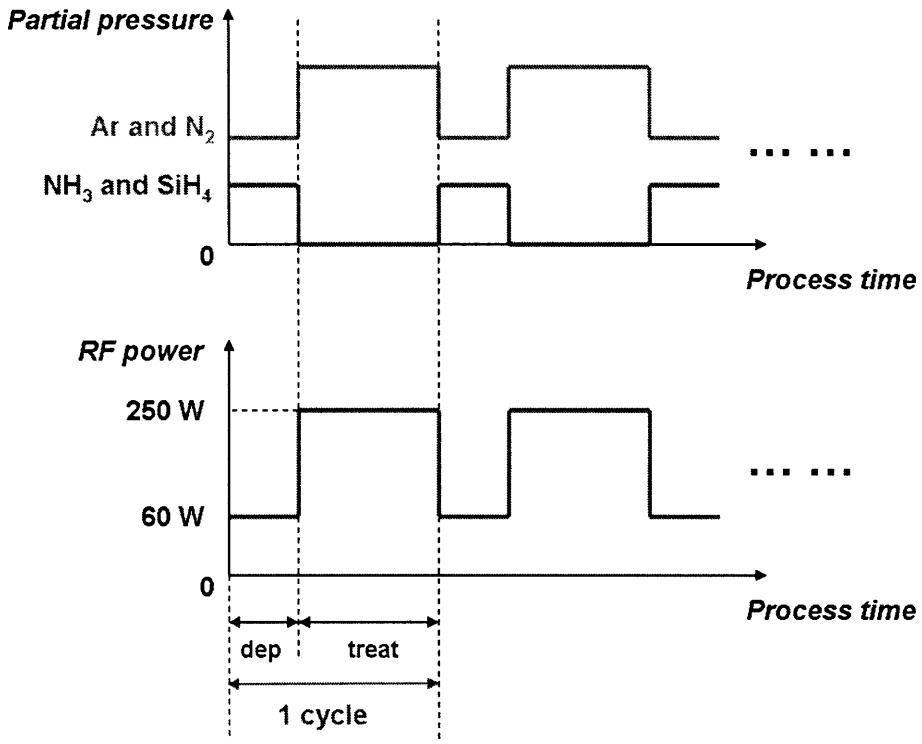

Figure 7.6. Schematic representation of the process flow for in-situ plasma treatment. One cycle is defined as one deposition and one following plasma treatment. The drawing is not to the scale.

Figure 7.7 shows the comparison for concentrations of [NH], [SiH], and total [H] in SiN_xH_y film after plasma treatment for 4 different processes/samples, where Sample 1 is without plasma treatment; Sample 2 yields 15 Å per cycle; Sample 3 yields 10 Å per cycle; and Sample 4 yields 5 Å per cycle. The reduction percentages and the film refractive indices are summarized in Table 7.3. The [NH] and [SiH] concentrations can be reduced from 5.3×10^{21} /cm^3 and 1.1×10^{22} /cm^3 in as-deposited Sample 1 to 1.1×10^{21} /cm^3 and 5.5×10^{20} /cm^3 in plasma treated Sample 4, respectively.

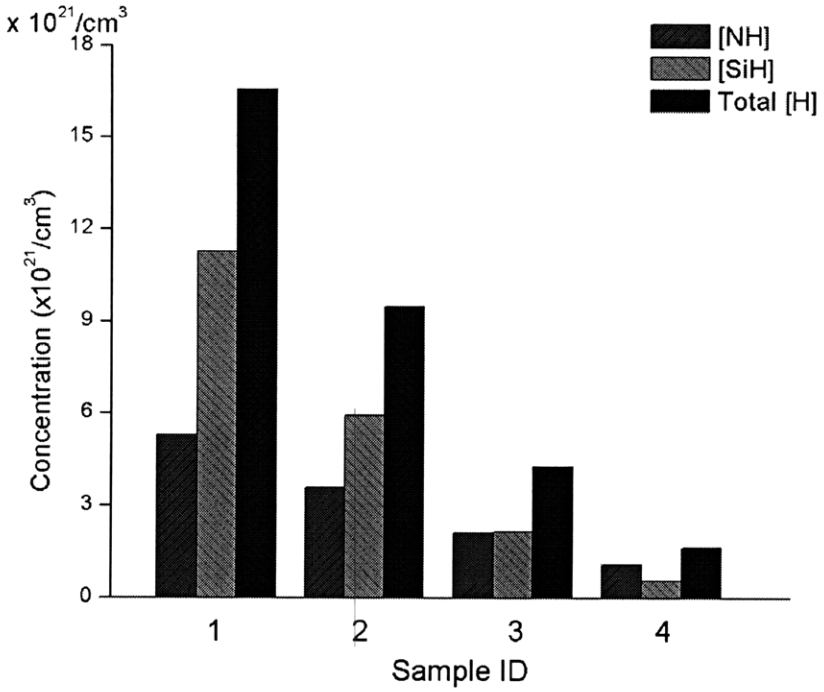

Figure 7.7. Concentrations of [NH], [SiH], and total [.H] after plasma treatment for different samples.

Table 7.3. Measured NH, SiH, and total H reduction percentages and film refractive indices as a function of layer thickness per treatment.

Sample ID	Thickness per treatment (Å)	Δ[NH] (%)	Δ[SiH] (%)	Δ[H] (%)	n_R
1	not applicable	0	0	0	2.089
2	15	-32.5	-47.5	-42.7	1.97
3	10	-59.9	-80.8	-74.1	1.917
4	5	-79.5	-95.1	-90.1	1.896

Although this method may be too slow to deposit films that are more than 100 nm thick, for some applications, such as a thin a-Si waveguide interlayer cladding layer, this approach can be very useful.

Beside film thickness, the H removal effect also depends on the plasma power and treatment time when SiN_xH_y films are thicker than the penetration depth of the •N radicals. Generally, high RF power and long treatment time can help to reach saturation more quickly as shown in Figure 7.8 in relative scales.

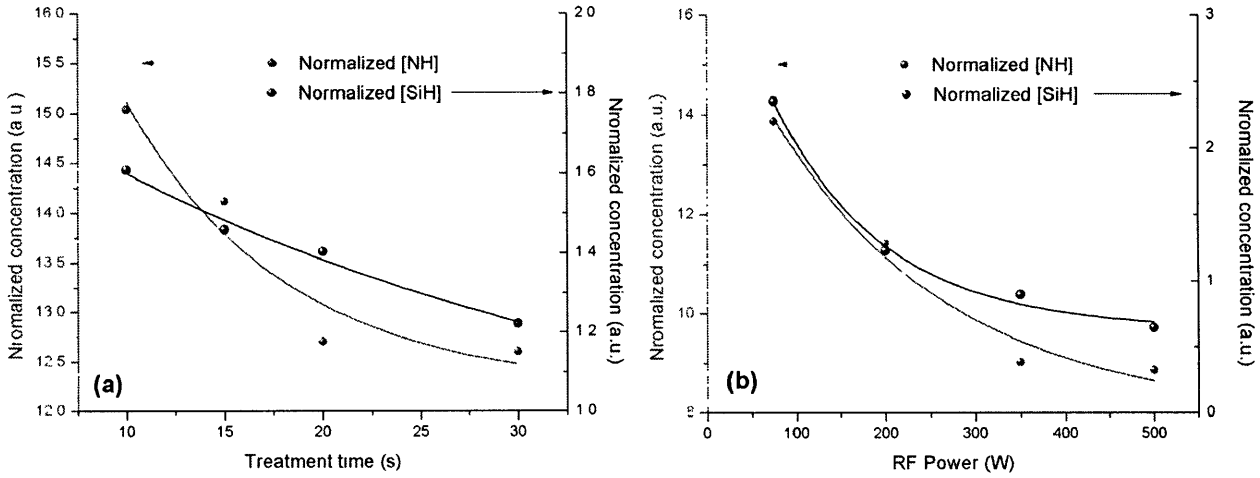

Figure 7.8. (a) Relative [NH] and [SiH] removal as a function of plasma treatment time at 150 W RF power; (b) Relative [NH] and [SiH] removal as a function of treatment RF power for 10 s treatment time. The dots represent the experimental results and the curves are exponential fits, showing how quickly the saturation is reached.

7.3. Post-deposition UV treatment: experimental and theoretical studies

7.3.1. Experimental studies of UV treatment effect on PECVD SiN_xH_y

Ultra-Violet (UV) illumination (λ = 200 ~ 400 nm) can induce chemical reactions that evolve hydrogen in SiN_xH_y film at temperatures below 500 °C. UV light refers to the photons with wavelength between 200 nm and 400 nm which corresponds to the photon energy between 6.4 eV and 3.2 eV. The bond energies for N-H and Si-H are 4.0 eV and 3.3 eV, respectively. Intuitively, a photon with wavelength shorter than 310 nm will have enough energy to disassociate both N-H and Si-H bonds. Using *Ab*-initio calculation and density functional theory (DFT) method, Zubkov *et al.* showed that UV illumination can induce bond weakening in N-H and Si-H by lowering the excited state energies of the N-H and Si-H bonds [68]. This method is shown experimentally to be effective for relative thick film (up to ~ 100 nm) comparing to plasma treatment. For thicker film, the evolved H_2 molecule out-diffusion becomes difficult. A hydrogen concentration gradient is expected to form and the film properties will become non-uniform.

There are three possible reactions among SiH and NH groups that can evolve H_2 during UV treatment as in Figure 7.9:

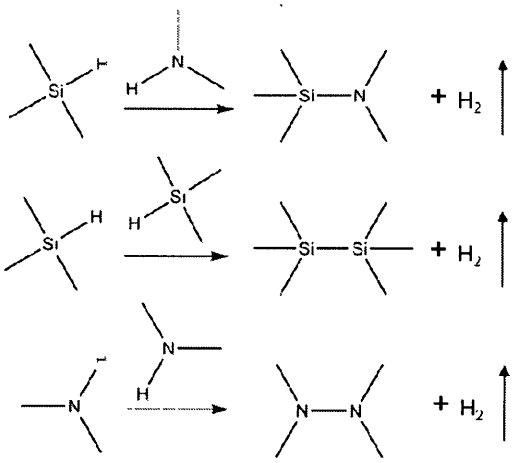

Figure 7.9. Reactions among SiH and NH groups in SiN_xH_y film.

According to chemical ordering theory, unlike bonds are preferred because of larger bond energies. In this case, SiH-NH reactions are dominant while SiH-SiH and NH-NH reactions are possible with reduced reaction constants at the same temperature [69]. Thus the total H removal must depend on the film composition as denoted as SiH/NH ratio.

The total H removal percentage as a function of SiH/NH ratio in PECVD a-SiN_xH_y film is studied experimentally and the results are plotted in Figure 7.10(a). These films are deposited at 400 °C and then UV-treated at 400 °C under high vacuum with identical conditions until saturation. Using FTIR, the total H removal is measured as the ratio of the total H concentrations in the film before and after UV treatment. The highest total H removal measured is about 60% for the film with SiH/NH ratio of 1. In regime 1, as the SiH/NH ratio increases to 1, H_2 evolution is increased as more N-H reacts with Si-H to form Si-N bonds; in regime 2, as the SiH/NH ratio increases beyond 1, the released H is trapped in Si-H bonds. The mechanism will be discussed later in this section. Figure 7.10(b) shows the FTIR spectra before and after UV treatment.

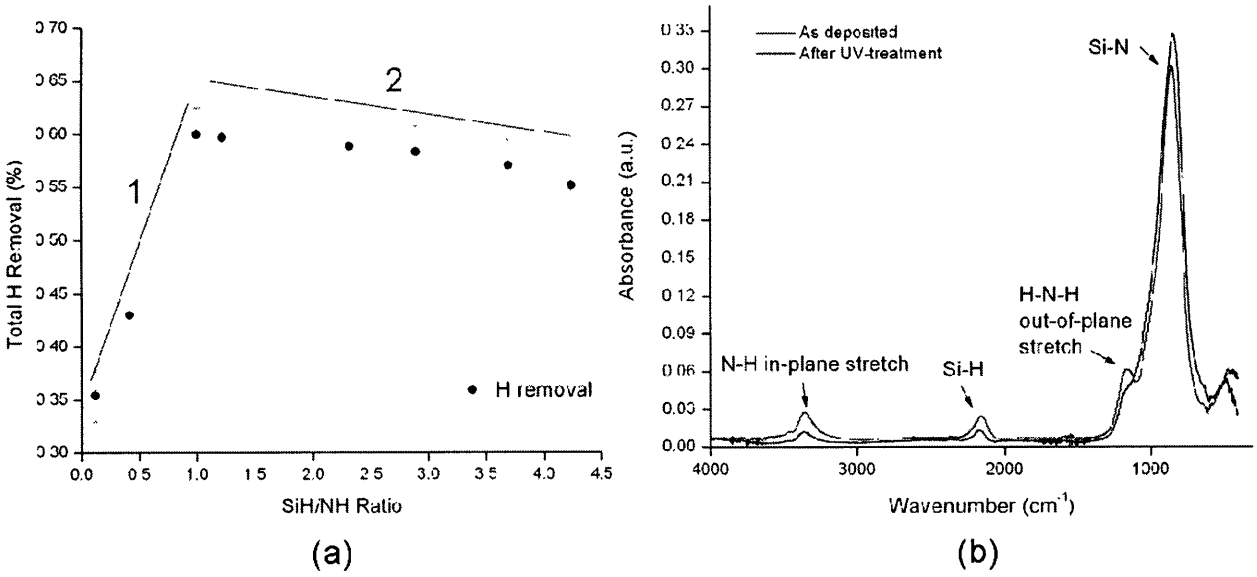

Figure 7.10. (a) The total H removal percentage in a UV-treated a-$Si_xN_yH_z$ film as a function of the as-deposited SiH/NH ratio. Different regimes highlighted by red lines have different underlying mechanisms to be explained later. (b) FTIR spectra of a-$Si_xN_yH_z$ film with SiH/NH ratio of 1 before and after UV-treatment (the latter is shifted down slightly for clearer view). Both FTIR spectra have been normalized with film thickness

7.3.2. Monte Carlo studies of UV treatment effect on PECVD SiN_xH_y

In order to explain the compositional dependence of UV treatment effect on PECVD SiN_xH_y and give predictions about the theoretical limits for total H removal percentage using UV treatment, a statistical Monte Carlo model is built to simulate the H_2 evolution processes.

Although SiN_xH_y does not have a real lattice as in crystalline materials, small clusters can be identified in short range [68]. We approximate the local chemical environment by using a 1D or 2D matrix with each lattice site representing a SiH or NH group. The size of the matrix is small compared to the number of atoms in the network (~10^{23}) but large enough to be statistically representative. Due to the size of the clusters, the average nearest neighbor coordination number of less than 4 is a reasonable estimation. Mathematically, they can be represented as in Figure 7.11.

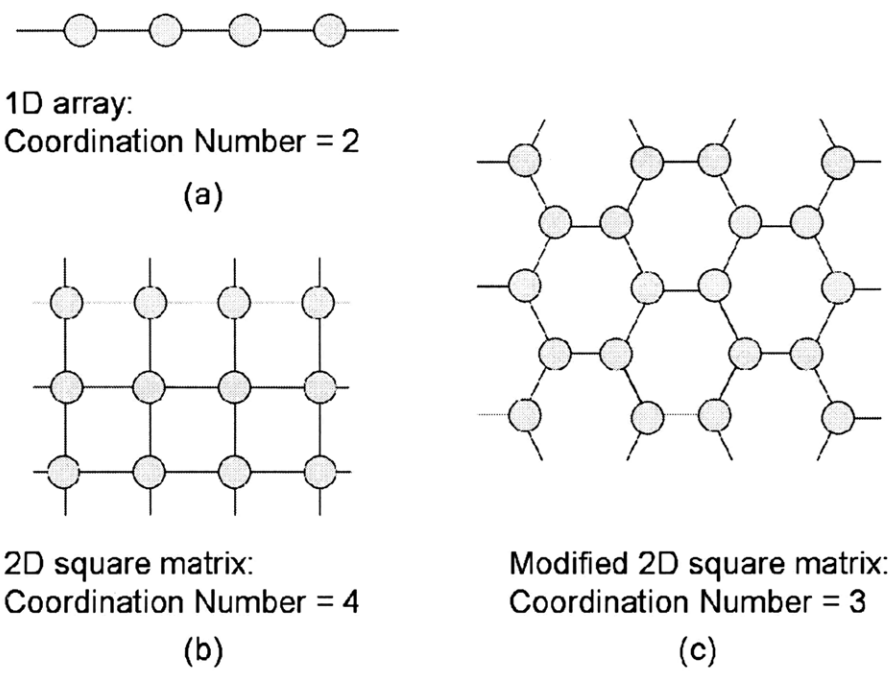

Figure 7.11. Schematic representations of mathematic models with different nearest neighbor coordination numbers. Black sticks represent possible bonding between the nearest neighbors and filled circles represent sites which can be occupied by either NH or SiH group.

We assume that SiH and NH groups, represented by "1" and "-1", are randomly distributed in our models. The numbers of SiH and NH groups are initialized according to the SiH/NH ratio. The total initial H concentration is the sum of the original numbers of SiH and NH groups in the matrix. A Monte Carlo algorithm is called to randomly select a lattice site (1 or -1) and search its nearest neighbors for counterparts to obtain "0" in a summation step, which corresponds to the evolution of one H_2 molecule. If there is more than one option in the nearest neighbors, a decision algorithm is called to randomly pick only one among many with the same success probability. This unique decision and the equal probability are guaranteed with a random number created by a uniform random number generator [70]. This random selection step is greater than 5 × (matrix size)^2, ensuring that less than 0.05% lattice sites would be unexamined which contributes to our simulation uncertainty. The remaining H is calculated as the sum of the remaining numbers of SiH and NH groups in the matrix. To obtain a statistic result, we used a large-size Monte Carlo

sampling step of at least 1000 times for one given matrix size and each time the matrix is uniquely re-initialized. The total H removal is then defined as one minus the average ratio of remaining H to original H. Figure 7.12 is a visualized representation of the H distribution in SiN_xH_y matrix before and after H removal simulation in which the SiH/NH ratio is 1 and the nearest neighbor coordination number of 4. Initially, the whole matrix is filled with SiH and NH (black and white pixels). After simulation, the area where H atoms are removed is represented by orange color. The matrix size in our simulations was carefully evaluated, for example, 2D square matrix is 1000 × 1000. Larger size matrices gave diminishing improvements but increased computation times exponentially as shown in Table 7.4.

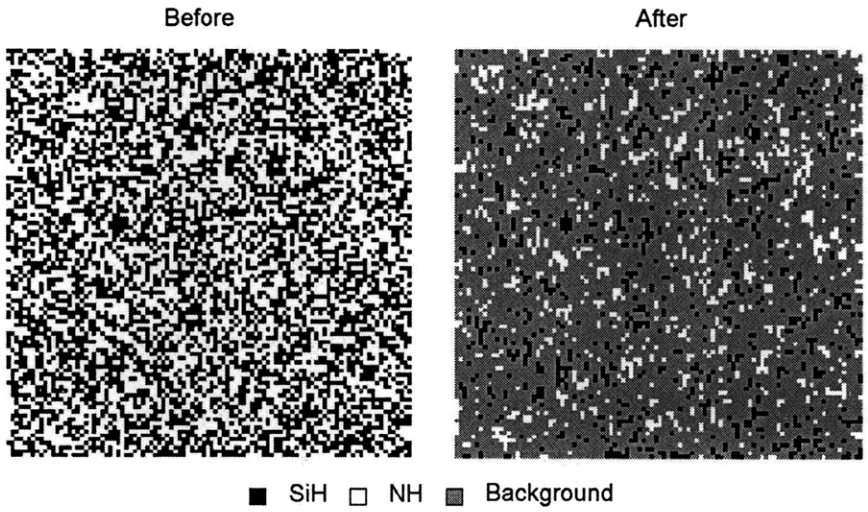

Figure 7.12. A visual representation of the H distribution in a-$Si_xN_yH_z$ matrix before and after H removal simulation. Before simulation, the matrix is fully filled with SiH and NH (black and white pixels); after, the orange colored area is the area where there is no H.

Table 7.4. The effect of matrix size and its effect on the simulation results: the total H removal percentage and computing times. The SiH/NH ratio is kept as 1 in these simulations for consistency. The computing time is the time to proceed 1000 times on a workstation with Pentium 4 3.2 GHz CPU and 1 GB RAM.

Matrix Size	1000 × 1000	5000 × 5000	10000 × 10000
Monte Carlo Sampling Steps	1000	500	100
Average total H Removal	0.7595	0.7604	0.7605
Standard Deviation	6.1329×10^{-4}	1.3616×10^{-4}	0.7059×10^{-4}
Computing Times	~ 40 minutes	~ 28 hours	~ 42 hours

The approach we take is to start with a simple mode where we only consider the preferred Si-N bond formation between two nearest neighbor SiH and NH groups.

Figure 7.13 shows the simulation results of the total H removal percentage versus SiH/NH ratio for different nearest neighbor coordination numbers. The highest H removals all occur at SiH/NH = 1, which is consistent with our experimental results. The total H removal decreases as the nearest neighbor coordination number decreases because fewer nearest neighbors result in lower probability for either SiH or NH to react with NH or SiH, respectively. At SiH/NH of 1, the theoretical total H removal ranging from 62% to 75% are higher than experimental results (60%). This is due to the following reasons. First, besides SiH and NH groups which are considered in our modeling, there are also SiH_2 and NH_2 groups in a real SiN_xH_y network. The presence of NH_2 is clearly shown by its H-N-H out-of-plane vibration at ~1100 cm^{-1} as shown in Figure 4.6. The presence of SiH_2 is also possible. However, due to the fact that its absorption peak around 860~890 cm^{-1} overlaps with the broad Si-N absorption peak, there is no direct evident of its presence in a SiN_xH_y FTIR spectrum [71]. The evolution of the second H in either SiH_2 or NH_2 groups leads to formation of a second bond with another NH or SiH, respectively. However, this process should have lower probability than the first H due to the reduced nearest neighbor coordination number. Incorporation of H rich groups in our simulation is simple, for example, we use "2" to represent the presence of NH_2 groups. Figure 7.14(a) is an example showing that increasing NH_2 concentration can reduce the total H removal percentage for films with overall SiH/NH =1. Figure 7.14(b) is the measured relative percentage of NH_2 in total N-H bonds at different as-deposited film compositions from FTIR spectra which indicates that a significant amount of N-H bonds are present as in NH_2 groups. Secondly, un-favored short range ordering, for example, silicon or nitrogen clustering may further reduce the probability for SiH-NH reaction, because reactions

among like groups are less likely than between SiH and NH groups due to the chemical bonding energy difference. This becomes more obvious in SiH-rich or NH-rich films with SiH/NH $\neq$ 1.

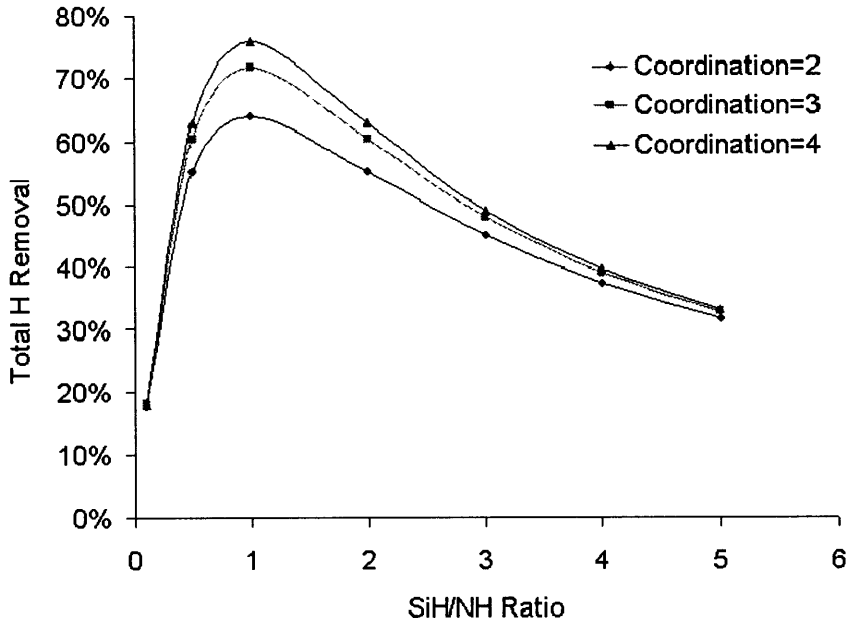

Figure 7.13. Simulation results on total H removals for different SiH/NH ratios considering only SiH-NH reactions. Different coordination numbers are considered to represent different local environment of SiH and NH groups.

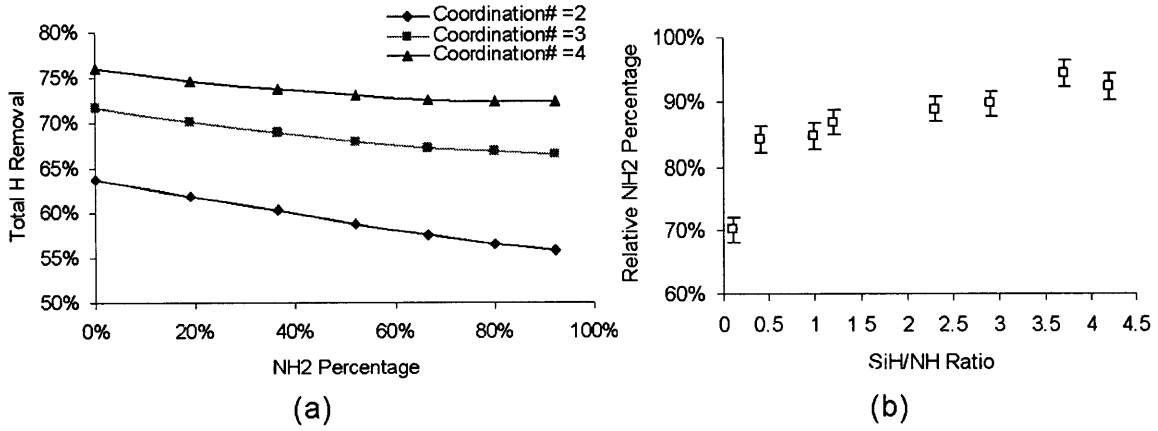

Figure 7.14. (a) An example of total H removal vs. NH_2 percentage as in total N-H bonds with overall SiH/NH =1; (b) Measured relative NH_2 percentages as in total N-H bonds at different film compositions.

We then allow SiH-SiH and NH-NH reactions with SiH-NH reactions at the same time and capture the reduced likelihood for SiH-SiH and NH-NH reactions by assigning each an arbitrary reaction constant, k ($0<k<1$), while setting SiH-NH reaction constant to 1. In the case that there is no unlike groups in nearest neighbor sites, a random number, r, is generated. Reactions among like

groups are only allowed when $r \leq k$ is satisfied. Then another random number is called to determine to which nearest neighbor site that the reaction occurs. For example, for coordination number of 4, Figure 7.15 summaries the simulation results on total H removal when we simultaneously consider SiH-NH reaction with reaction constant of 1; (a) NH-NH reaction (b) SiH-SiH reaction with reaction constants from 0 to 0.4, respectively. The experimental results are also plotted for comparison. From observing the slopes of the experimental results in the N-rich and Si-rich regimes, we can derive that at 400 °C the relative reaction constants for SiH-SiH and NH-NH reactions are approximately 0.2 and 0.1, respectively, while relative reaction constant for SiH-NH is 1 as shown below.

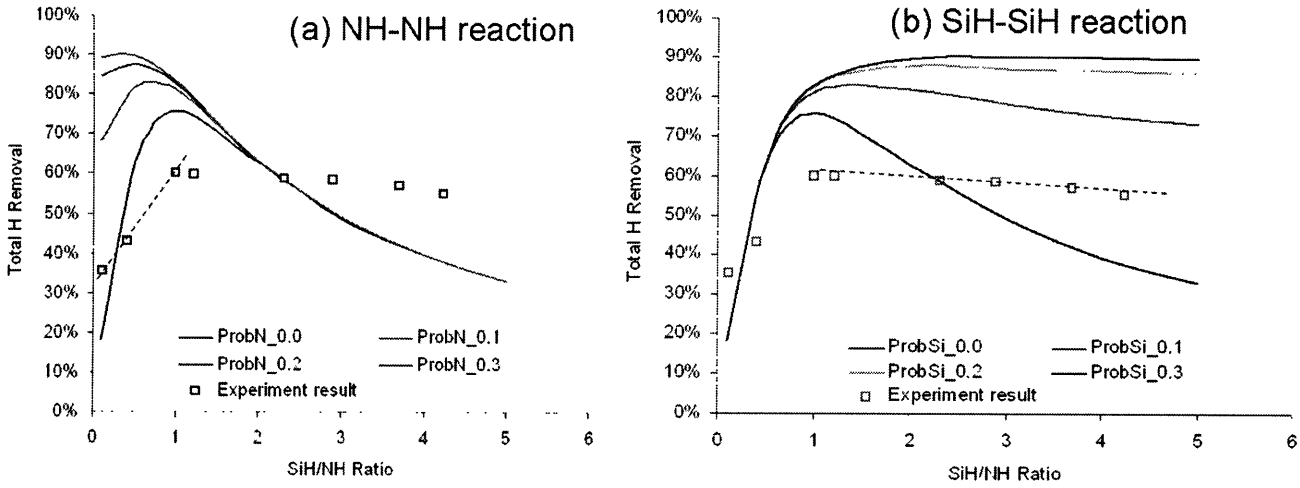

Figure 7.15. Simulation results on total H removals for different SiH/NH ratios for nearest neighbor coordination number of 4. The reaction constants for (a) NH-NH and (b) SiH-SiH reactions are 0 to 0.4.

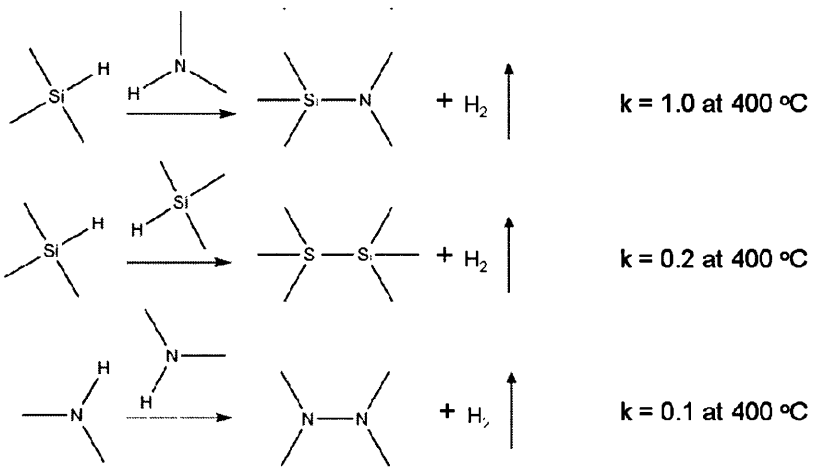

The Monte Carlo models are in good agreement with experiments and provide fundamental understanding of this process. The models suggest that the compositional dependency for H_2 evolution during UV treatment is due to the preferred SiH-NH reactions over SiH-SiH, NH-NH reactions with relative reaction constants derived to be 1, 0.2, and 0.1 at 400 °C, respectively. The total H removal percentage depends on the maximal availability of nearest neighbor SiH and NH groups which can be quantified by their coordination numbers. The maximal H removal percentage is also affected by the presence of hydrogen rich SiH_2 and NH_2 groups.

Nevertheless, for PECVD SiN_xH_y the tensile stress enhancement is naturally associated with H removal. Understanding the underlying mechanisms and finding new meanings to further increase the total H removal percentage can certainly improve the attractiveness of UV treatment process for many important applications.

7.4. Summary

In this chapter, we have discussed three different processes that can produce low NH containing PECVD SiN_xH_y film for optical application around 1550 nm. Changing the deposition conditions can yield low NH containing SiN_xH_y film but the film also contains high concentration

of SiH. The plasma and UV treatments are post deposition methods. They will not change some properties governed by the deposition chemistry, such as step coverage. After the films are deposited, the two processes can remove both SiH and NH from the film at temperatures compatible with a-Si processes. The plasma treatment is a slow process because in the deposition tool the reactions in which H atoms are removed almost only happen on surface. The UV treatment is more efficient when removing H from thicker films. However, it requires a dedicated chamber equipped with UV lamp, heating stage, and high vacuum.

(This page is intentionally left blank)

Chapter 8. Low loss horizontal slot waveguides

Slot waveguides are a newly developed class of waveguides that has received significant attention in recent years and promise many applications in recent years [72,73,74,75]. A slot waveguide consists of at least one narrow low index region sandwiched between high index regions as shown in Figure 8.1. Because of the refractive index discontinuity at the high index contrast sidewall, the boundary condition for transverse electric-field (E-field) in the horizontal direction determines that there is also a discontinuity in the E-field at the high index region sidewall interface. The E-field outside of the high index region decays exponentially as it moves away from the waveguide as we call the evanescent field. When two high index regions move close to each other within the decay length, $1/\gamma_l$, of the evanescent field, the E-field overlaps and gets enhanced. When the gap in between the two high index regions is much smaller than the E-field decay length, the optical field is strongly enhanced in the low index region nears the interfaces, also shown in Figure 8.1. This property of high confinement in low index medium is unique to slot waveguides and promises many important applications.

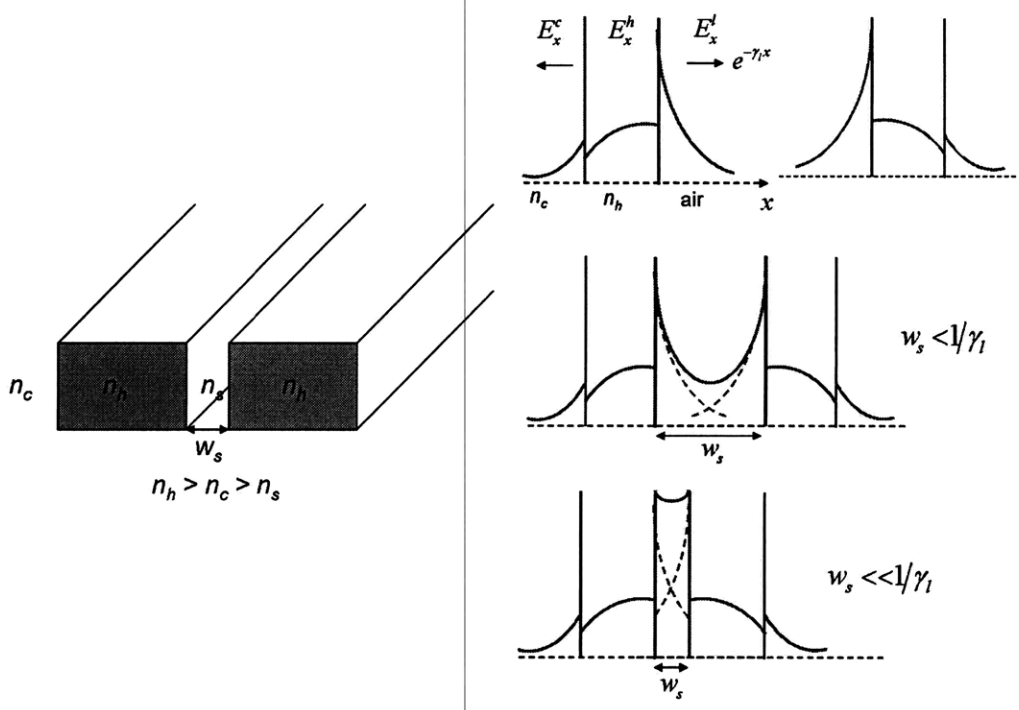

Figure 8.1.Slot waveguide guiding mechanism as shown in a vertical slot configuration

8.1. Low loss optical transmission at 1550 nm in horizontal slot waveguides

Normally, in a vertical slot configuration, thin slots are fabricated by etching in a very narrow opening into high index waveguides, e.g. silicon waveguides. However, high optical intensity at the sidewall interface results in high waveguide scattering loss due to sidewall roughness. The lowest loss reported in literatures in a vertical slot waveguide with a single slot of 70 nm is greater than 10 dB/cm for its fundamental quasi-TE slot mode in the horizontal direction [76].

On the other hand, a horizontal slot structure featured with a horizontal low index slot can be fabricated by layered deposition or thermal oxidation of silicon. The corresponding slot waveguide devices have virtually no fabrication constraints on slot thickness and location. Horizontal slot waveguide can have very low scattering loss due to small surface or interface roughness for the fundamental slot mode, the quasi-TE mode in the vertical direction. We have

also previously proposed multiple slot configurations in a horizontal slot waveguide to provide enhanced optical confinement in the low index slot region [77].

The experimental demonstration of low loss optical transmission at 1550 nm in horizontal slot waveguides are carried out using horizontal single and triple slot waveguides consisting of deposited amorphous silicon (a-Si, n = 3.50) and silicon dioxide (SiO_2, n = 1.46). On a 3 μm thermal oxide silicon wafer, we deposit amorphous silicon and silicon dioxide using Plasma Enhanced Chemical Vapor Deposition method (PECVD). To show differences in waveguide properties resulting solely from single slot or multiple slot configurations, we design waveguide geometries such that the overall waveguide height, total a-Si layer thickness, and total SiO_2 layer thickness are approximately the same for both single and triple slot waveguides. For the fabricated single slot waveguide, the stack has two 223 nm a-Si layers and one 55 nm SiO_2 layer. For the fabricated triple slot waveguide, the stack consists of two 152 nm a-Si outer layers, two 56 nm a-Si inner layers, and three 17 nm SiO_2 slot layers. All waveguides and ring resonators are 500 nm wide, patterned by E-Beam Lithography (EBL), and Reactive Ion Etch (RIE). No post-etch waveguide smoothing has been applied on these very early structures. Finally, 3 μm PECVD SiO_2 is deposited as the top cladding layer. The schematic structures as well as their normalized optical field ($|E|^2$) distributions are shown in Figure 8.2(a1, b1). The absolute value for the E field can be calculated with Poynting vector, $\langle S \rangle \sim \varepsilon_o cn|E|^2/2$, where $\langle S \rangle$ is the time-averaged energy flux, ε_o is the permittivity of free space, c is the free space speed of light, n is the refractive index, and E is the electric field. For example, for 1 mW transmitted optical power in our triple slot waveguides, the maximum E field in SiO_2 slot regions is about 2.5×10^8 V/m, one order of magnitude larger than in the Si regions. All the simulations were carried out using a numerical model solver based on finite-difference time-domain (FDTD) methods. The corresponding Scanning Electron

Microscope (SEM) images of the cross sections of the layered structures are also shown Figure 8.2(a2, b2). The deposited layered structures and each layer thickness are well controlled.

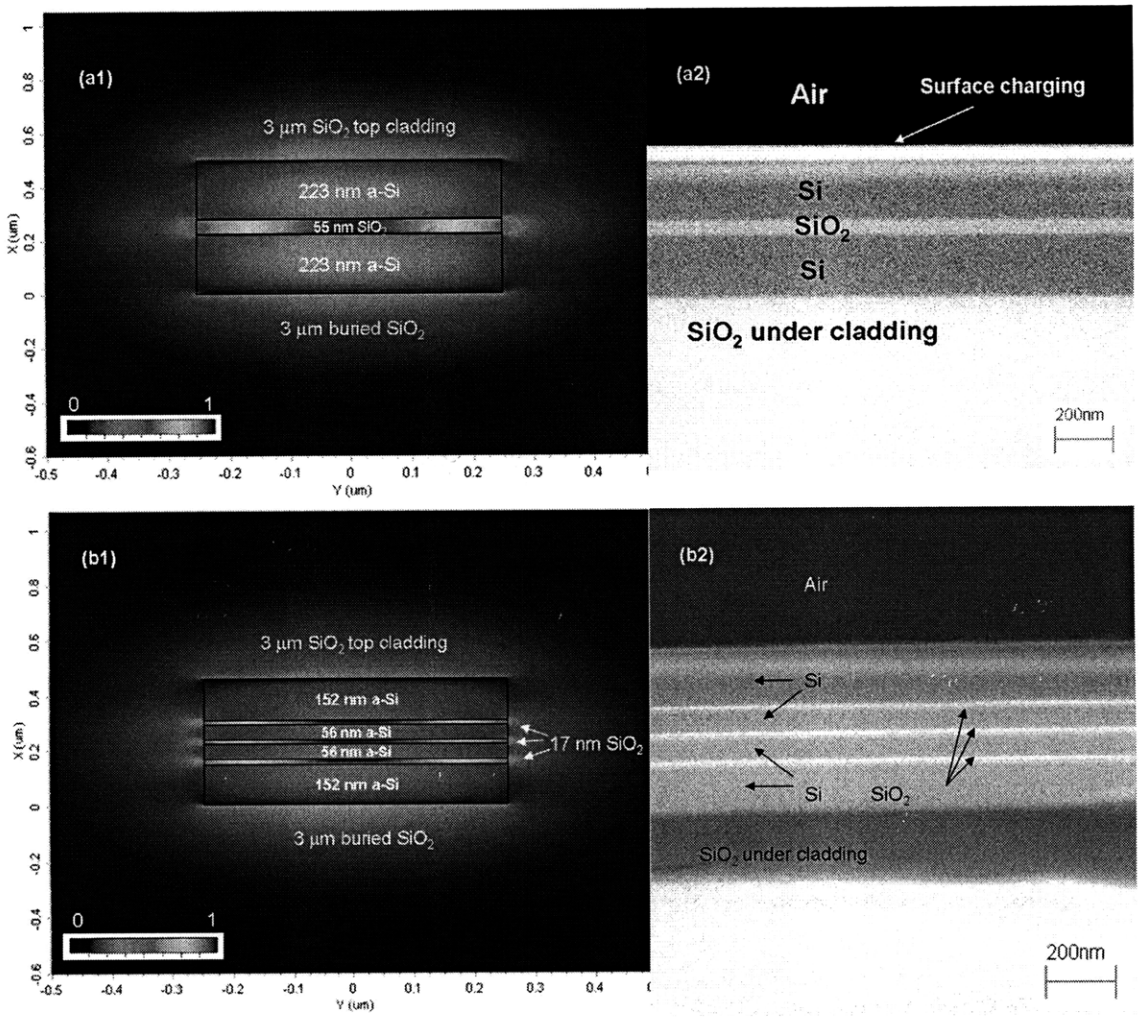

Figure 8.2.Schematic representation of the structures of a single (a1) and a triple slot waveguide (b1). The normalized optical field ($|E|^2$) distributions are simulated using a numerical mode solver based on finite-difference time-domain (FDTD) methods. Their corresponding cross-sectional SEM images to the right of the schematic drawings (a2) and (b2) show that the layered structures and each layer thickness are well controlled in fabrication.

We measured waveguide propagation loss using the cut-back method. As shown in Figure 8.3, at 1550 nm for the quasi-TE modes, the waveguide losses for single and triple slot waveguides are measured to be 6.3 ± 0.2 dB/cm and 7.0 ± 0.20 dB/cm, respectively. The relatively small difference in waveguide loss indicates that the addition of a-Si/SiO_2 interfaces in triple slot

waveguides does not introduce significant scattering loss under the same process conditions as the single slot waveguides. The horizontal single slot waveguide loss is much lower than that in a vertical slot waveguide with slot width of 50 nm (~11.6 ± 3.5 dB/cm) [76]. The excellent low loss performance for the quasi-TE modes of horizontal slot waveguides are due to (1) the fact that this quasi-TE mode is relatively insensitive to interface roughness at the etched waveguide sidewall; and (2) low interface roughness for deposited films (interfaces that are parallel to the substrate). For both deposited a-Si and SiO_2 layers, the surface roughness is less than 5 Å as measured by Atomic Force Microscopy (AFM). The dominant loss source in our a-Si/SiO_2 waveguide devices is the a-Si bulk absorption.

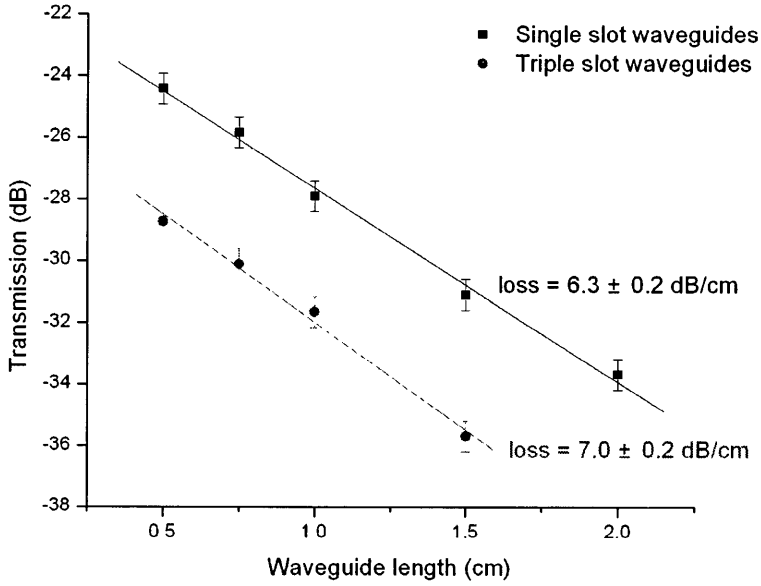

Figure 8.3. Single and triple slot waveguide losses: waveguide total insertion loss (dB) versus waveguide length (cm). The waveguide propagation loss in dB/cm is derived using the "paperclip" method.

The optical confinement factors in the SiO_2 slots, defined as the ratio of the optical power in the SiO_2 slot(s) and the total optical power, are calculated to be 36% and 56% for the single and triple slot waveguides, respectively. The confinement factors can be verified directly by measuring the thermo-optic coefficients of the slot ring resonator devices. For a silicon or SiO_2 waveguide, the refractive index increases as temperature increases, causing the ring resonator's resonant

wavelengths to shift to longer wavelength. But because the thermo-optic effect in SiO_2 is about ten times weaker than that in a-Si [78], the overall thermo-optic coefficient in an a-Si/SiO_2 slot waveguide is expected to be much smaller than in a regular a-Si waveguide with similar dimensions due to the high optical confinement in the SiO_2 slot region(s).

The fabricated single and triple slot ring resonators have the same ring-bus gaps of 250 nm and the same ring radii (R) of 10 μm. Figure 8.4(a) shows their spectra between 1535 nm and 1555 nm. Their free spectral ranges (FSR) and group indices (n_g) around 1550 nm are summarized in Table 8.1. The corresponding simulation results are included for comparison. Their theoretical values were calculated using Equations 8.1 and 8.2. The effective indices (n_{eff}) used in calculations were simulated directly using the mode solver. The on-resonance extinction is about 15 dB. Figure 8.4(b) shows the Lorentzian fitting on one of the resonance of the triple slot ring resonator. The -3dB bandwidth is 0.119 ± 0.008 nm. According to Equation 8.3, this corresponds to a quality factor (Q) of 13000 ± 1000 at around 1550 nm. The low Q factor is due to non-critical coupling conditions. Over all, the quality factors for single and triple slot ring resonators are estimated to be around 12500 ± 2500.

$$n_g = n_{eff}(\lambda) - \lambda \frac{dn_{eff}(\lambda)}{d\lambda} \tag{8.1}$$

$$FSR = \lambda_{m+1} - \lambda_m \approx \frac{\lambda^2}{n_g(\lambda) \cdot 2\pi R} \tag{8.2}$$

$$Q = \frac{\lambda}{\Delta\lambda_{-3dB}} \tag{8.3}$$

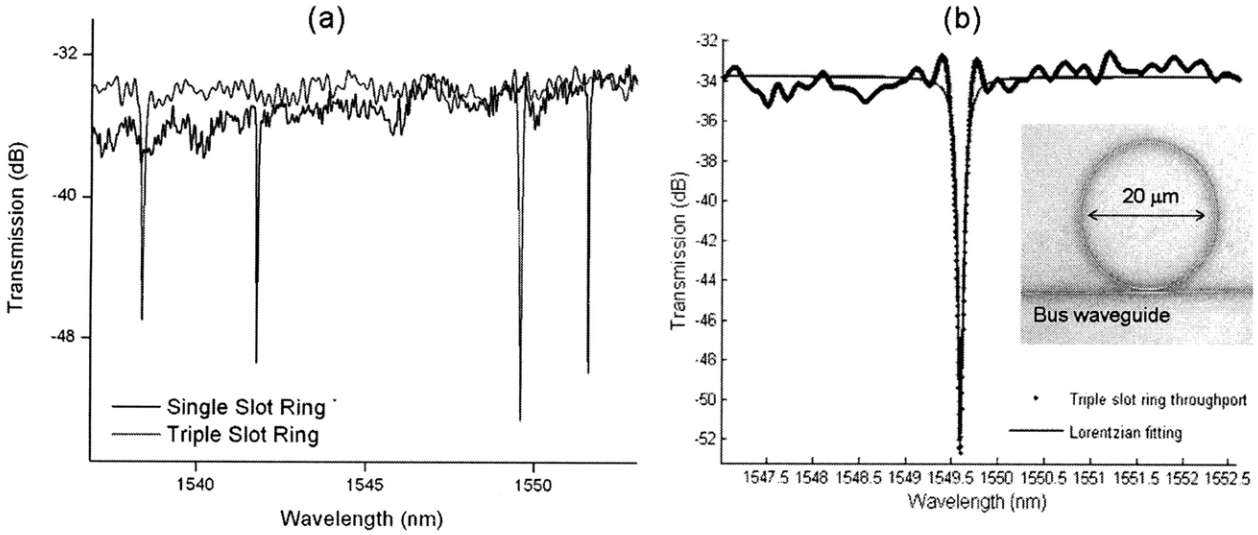

Figure 8.4. (a) Ring resonator spectra of a single and a triple slot waveguide. Both ring radii are 10 μm and bus-ring gaps are 250 nm; and (b) the Lorentzian fitting on triple slot ring resonator. Slot ring resonators are fabricated using e-beam lithography and reactive ion etches. Silicon etch uses Cl_2 and HBr chemistry; oxide etch uses CHF_3, CF_4 chemistry.

Table 8.1. Summary of the measured and simulated FSR and group index around 1550 nm of the single and triple slot ring resonators with 10 m radius.

	FSR		Group Index	
	Measured	Simulation	Measured	Simulation
Single Slot	9.8	9.4	3.902	4.055
Triple Slot	11.2	12.2	3.401	3.139

Figure 8.5 shows the thermo-optic coefficient measurement results of a single and a triple slot ring resonator. The tunable laser we used in experiments has a resolution of 2.5 pm. The measurement errors on the resonance wavelengths are minimal. The measured thermo-optic coefficient of the triple slot waveguide is 65.4 pm/°C, which is 12% lower than that of the single slot ring resonator, 74.6 pm/°C; their simulated thermo-optic coefficients are 64.6 pm/°C and 76.8

pm/°C, respectively, which correlates well with the measurement results. The difference in thermo-optic coefficient is due to the enhanced confinement in the low index SiO_2 slot region in the triple slot ring resonator. For comparison, the thermo-optic coefficients for the fundamental TM mode in a 500 nm tall, 500 nm wide, a-Si channel ring resonator is calculated to be 102.7 pm/°C. The overall low thermo-optic coefficients for the slot ring resonators confirm the optical concentration in low index SiO_2 slot region(s) in our slot waveguides devices. The lower thermo-optic coefficient in the triple slot ring resonator directly proves that multiple slot configuration provides greater optical confinement in low index slots compared to the single slot configuration.

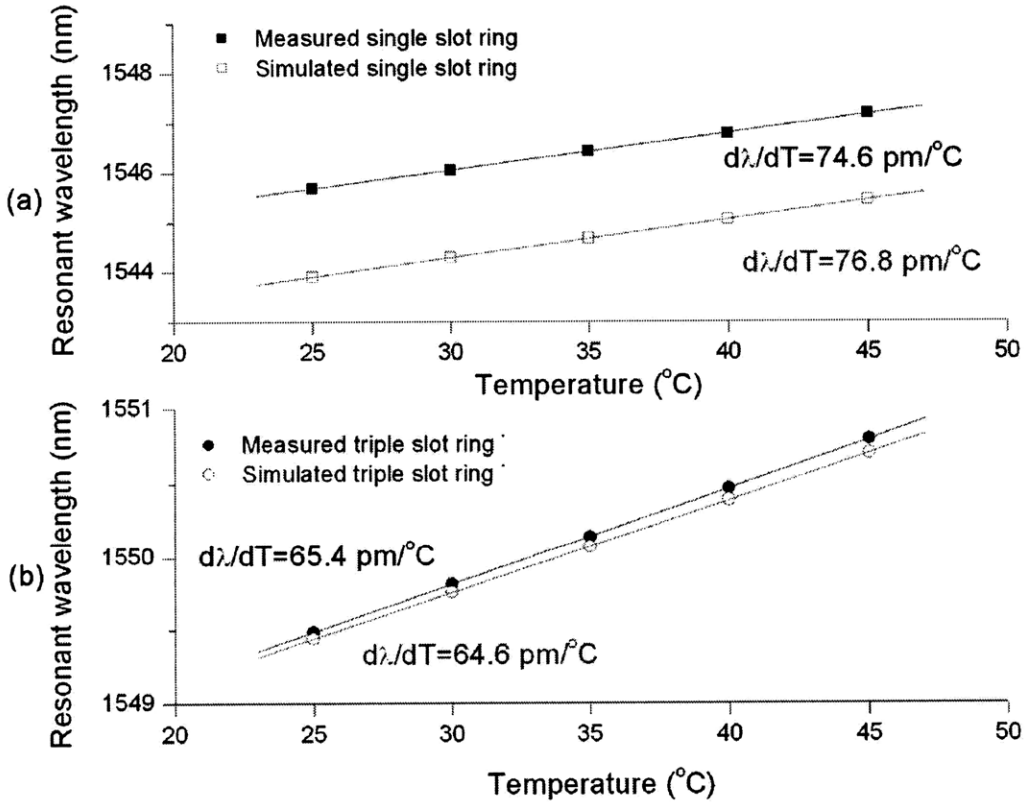

Figure 8.5. The measured and simulated thermo-optic coefficients for the quasi-TM modes of a single (a) and a triple (b) slot ring resonator. The simulations match well with the experimental results. The thermo-optic coefficient of the triple slot ring resonator is lower than that of the single slot ring resonator due to the improved confinement in the slot region. The difference between simulation and measurement is possibly due to ring radius and layer thickness variation

8.2. Summary

We have demonstrated experimentally optical transmission in horizontal a-Si/SiO_2 single and multiple slot waveguides and ring resonator devices. Low propagation loss has been achieved in these early devices. The thermo-optic coefficient measurements verify that the multiple slot configuration can further enhance optical confinement in the low index slot regions. With the low propagation loss for the fundamental slot mode and enhanced optical confinement realized in low index slot regions, horizontal slot waveguides with multiple slot configurations are very promising for applications such as dielectric gain media and non-linear optics.

(This page is intentionally left blank)

Chapter 9. Experimental results in low loss silicon waveguides

This chapter will summarize the experimental results from optical waveguides, including crystalline silicon and amorphous silicon waveguides, under different processing conditions.

9.1. Single crystalline silicon, single mode channel waveguides

The SOI c-Si channel waveguides work is associated with the DARPA sponsored EPIC program. All the fabrications were carried out in BAE Systems' clean room facilities. SOI wafers with 3 μm thick buried oxide and 200 nm thick c-Si are used for c-Si channel waveguides. Photolithography was done using Deep-UV stepper and positive photoresist. Process variation included (1) photoresist mask and (2) pad-oxide/silicon nitride hard mask. Waveguides were etched using poly silicon etch recipe with Cl_2 and HBr chemistry. Post-etch wet chemical treatment, e.g. 3 cycles of RCA SC1 clean (6:1:1, H_2O, H_2O_2, NH_4OH), and 10 seconds dip in diluted HF (50:1), has been proven to be able to reduce the sidewall roughness and was generally applied [37]. Finally the waveguides were cladded with another layer of 3 μm PECVD SiO_2. Under this baseline condition, the waveguide transmission loss values at 1550 nm measured by the "paperclip" method are summarized in Table 9.1. For the TE-mode, within the interesting width range, the transmission loss coefficient decreases as waveguide width increases as we expect the sidewall roughness scattering effect will decrease in wider waveguides. For the TM-mode, the transmission loss does not change for different width, indicating that the bulk absorption loss in c-Si is negligible.

Table 9.1 Transmission loss coefficients (dB/cm) at 1550 nm for the baseline c-Si waveguides using photoresist mask. "SL" stands for substrate leakage, meaning the loss is too high to be measurable due to loss caused by substrate leakage. The wafer ID is "SL1A-Wf 8-P".

	Polarization	Designed Waveguide Width (nm)				
		400	450	500	550	600
Loss (dB/cm)	TE mode	11.6 ± 0.4	8.2 ± 0.5	5.7 ± 0.4	4.6 ± 0.4	4.3 ± 0.6
	TM mode	SL	> 2	1.6 ± 0.4	1.7 ± 0.3	1.7 ± 0.3

The substrate leakage effect strongly affects the TM-mode and can be identified easily using TM-mode waveguide transmission spectrum. Figure 9.1 is an example of the TM mode loss profiles with respect to wavelength from the samples in Table 9.2. The significant increase in TM-mode waveguide transmission loss can only be explained by substrate leakage. Even with 3 μm thermal oxide under cladding layer, because, as wavelength increases, the confinement factor for the optical mode inside the c-Si waveguide actually decreases. This leads to longer evanescent tail outside the waveguide core, increasing the amount of optical power coupling with the Si substrate. The narrower the waveguide width, the smaller the confinement factor is. From the results, for 400 nm wide waveguides, the onset for substrate leakage occurs at the shortest wavelength as shown in Figure 9.1. Note that from SEM studies, some waveguides can be as large as 30 nm narrower than the designs due to over etch [37].

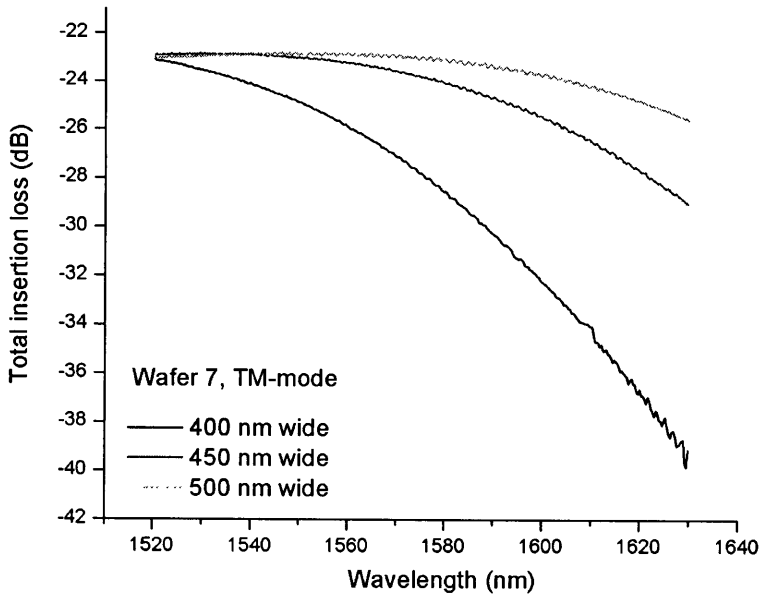

Figure 9.1. The total insertion loss spectra for three waveguides with different waveguide widths. The waveguide height is 200 nm. Total insertion loss includes measurement system loss, coupling loss, and waveguide transmission loss. The rapid increases in transmission losses at longer wavelengths are due to substrate leakage.

The pad-oxide/silicon nitride hard mask is adopted lately and the resulting waveguides show noticeable and consistent improvement in terms of the transmission loss. After the waveguide is etched and cleaned, a thin liner oxide is formed by dry oxidation process to improve the silicon interface quality. The hard mask is then removed by hot phosphoric acid etching of nitride or dry etch. The waveguides are again wet treated. Finally 3 μm PECVD is deposited as the waveguide top cladding layer. This process has become the standard process for the EPIC program. The typical loss values are summarized in Table 9.2. The waveguide heights are all 200 nm. The TM-mode performance, although relatively insensitive to sidewall roughness scattering compared to the TE-mode, is also improved significantly. Using hard mask processes, we have consistently achieved transmission loss less than 3 dB/cm for the TE-mode and less than 1 dB/cm for the TM-mode in 500 nm wide single mode c-Si waveguides.

Table 9.2. Transmission loss coefficients (dB/cm) at 1550 nm for the c-Si waveguides using hard mask process. The wafer ID for this process is "SuperNitContr-Wf1-789M".

ID	Sample	Polarization	Designed Waveguide Width (nm)			
			400	450	500	550
1	Control No nitride	TE mode	8.4 ± 0.3	4.9 ± 0.2	2.3 ± 0.2	2.0 ± 0.1
		TM mode	5.9 ± 1.4	2.2 ± 0.2	1.0 ± 0.1	0.8 ± 0.1

We have also studied the transmission loss of c-Si with the presence of a thin, LPCVD silicon nitride intercladding layer, because LPCVD silicon nitride (Si_3N_4) has excellent optical transparency, 100% sidewall step coverage, and its process temperatures at around 750 °C is compatible with c-Si waveguide processes. A total of 5 different processes are studied. The process conditions and their according loss values at 1550 nm are summarized in Table 9.3. According to Barwicz and Haus [32], an intercladding layer with intermediate refractive index can help reduce the sidewall roughness scattering effect, resulting in lower transmission loss for the TE-mode. Processes 1-3 have 20 Å, 50 Å, and 1000 Å thick nitride layers directly on c-Si sidewalls and top surface, respectively. Processes 4 and 5 insert a 20 Å liner oxide layer prior to nitride deposition and the nitride thickness varies from 10 Å to 20 Å. The purpose is to see which interface, thermal oxide/silicon or nitride/silicon, has better passivation on c-Si surface and to see which variation, the surface passivation or index contrast, would have more positive effect on the TE-mode loss reduction.

The TM-mode loss values remain relatively unaffected by the incorporation of the nitride layers. In order to compare these 5 processes as well as compare them with the baseline process more visually, the TE-mode data are re-plotted together as shown in Figure 9.2.

Table 9.3. Transmission loss coefficients (dB/cm) at 1550 nm for the c-Si waveguides in 5 different processes. LOX stands for liner oxide formation prior to Si_3N_4 and LTO depositions. LTO stands for low temperature oxide.

ID	Variation	Polarization	Designed Waveguide Width (nm)			
			400	450	500	550
2	20Å Si_3N_4	TE	8.9 ± 0.3	5.0 ± 0.3	3.2 ± 0.2	2.2 ± 0.2
		TM	6.6 ± 1.8	2.1 ± 0.4	1.1 ± 0.1	0.6 ± 0.1
3	50Å Si_3N_4	TE	8.3 ± 0.1	4.6 ± 0.2	2.9 ± 0.1	1.3 ± 0.1
		TM	3.3 ± 0.6	1.3 ± 0.2	0.8 ± 0.1	0.8 ± 0.1
4	100Å Si_3N_4	TE	8.2 ± 0.1	3.1 ± 0.2	2.7 ± 0.1	0.8 ± 0.4
		TM	2.1 ± 0.3	0.7 ± 0.1	0.7 ± 0.1	0.7 ± 0.1
5	20Å LOX 10Å Si_3N_4 100Å LTO	TE	8.5 ± 0.2	4.8 ± 0.2	2.7 ± 0.2	2.4 ± 0.2
		TM	9.1 ± 1.8	3.0 ± 0.5	0.9 ± 0.2	0.8 ± 0.1
6	20Å LOX 20Å Si_3N_4 100Å LTO	TE	8.7 ± 0.2	4.6 ± 0.2	2.8 ± 0.2	2.5 ± 0.1
		TM	5.4 ± 0.8	1.6 ± 0.2	1.0 ± 0.1	0.8 ± 0.1

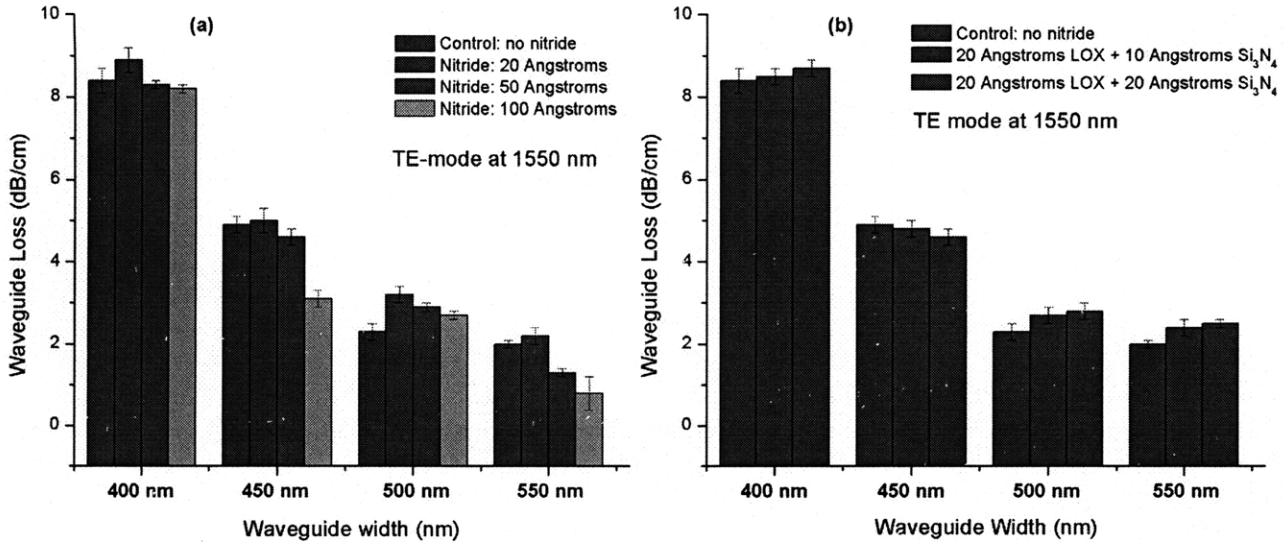

Figure 9.2. Column charts of waveguide loss vs. waveguide width for different intercladding layers for the TE-mode. (a) Nitride only processes; (b) LOX and nitride processes.

Unexpectedly, the initial incorporation of 20 Å nitride intercladding layer result in higher loss values for the TE-mode than the control samples without any nitride cladding (shown in Table 9.2). This could be caused by the change of interface from thermal oxide/silicon to nitride/silicon interface. Among the samples all with nitride intercladding layers, as nitride thickness increases,

waveguide loss consistently decreases, indicating a positive correlation between nitride thickness and sidewall roughness scattering reduction. The effective index change as a function of nitride thickness is examined using ring resonators. As an example, the resonance wavelengths for the same sized ring resonators with different nitride thickness are plotted in Figure 9.3(a). The resonance wavelength shifts to longer wavelength indicates an increase in effective index of the resonators which is confirmed by calculation as shown in Figure 9.3(b). However, even at 1.2% effective index change, e.g. from 2.5 to 2.525 for TE-mode, may not cause a significant optical power reduction by increased confinement factor along. We believe that the dominant effect here is the sidewall index contrast reduction.

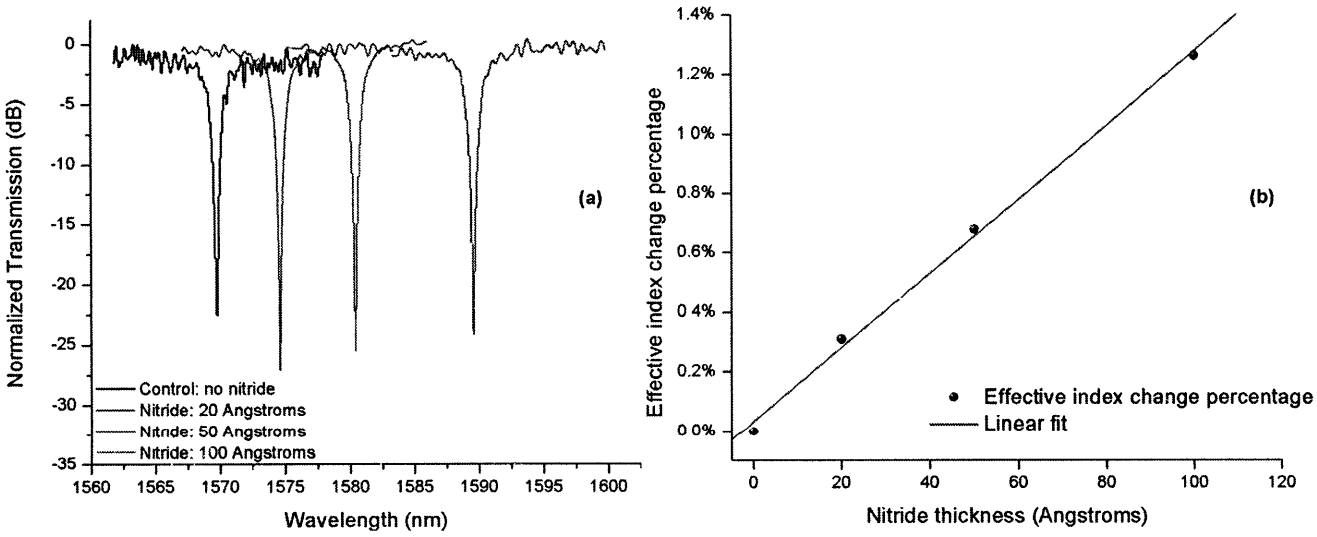

Figure 9.3. (a) Resonance wavelength shift as a function of nitride thickness; (b) the calculated effective index change percentage as a function of nitride thickness. The ring resonators have cross sections of 500 nm × 200 nm (W × H) and diameters of 6 μm. The coupling gap is 170 nm. The FSR is ~ 34 nm. The resonance peaks shown in (a) only span over 20 nm, meaning they are the same order resonance peaks.

For LOX/nitride intercladding splits, no consistent patterns have been observed at 1550 nm. One concern is that because at 1550 nm the optical confinement in c-Si waveguide core for both TE and TM modes is relatively high, the change in intercladding layers may not have significant impacts on scattering and surface-state related absorption at the interface. We extend our analyses to 1580 nm where the possibility for NH absorption in the nitride layer can also be eliminated even

though we know LPCVD nitride generally does not have such absorption. Moving from 1550 nm to 1580 nm, the changes for optical mode properties in a 500 nm × 200 nm ($w \times h$) c-Si channel waveguide are summarized in Table 9.4. We expect that the TM-mode waveguide loss will change noticeably because the confinement factor for the TM-mode reduces more than 10% at 1580 nm compared to at 1550 nm. The corresponding waveguide loss values for processes 1-6 are summarized in Table 9.5. Figure 9.4 shows that there are distinct patterns for both nitride and LOX/nitride intercladding layers. In both cases, it is believed that the incorporation of intercladding layers helps reduce the substrate leakage loss for the TM-mode. From Figure 9.1 we can see that even with 3 μm oxide under cladding layer, there is still significant loss increase at around 1580 nm. The nitride cladding helps increase the reduced effective index at 1580 nm compared to 1550 nm, reducing the substrate leakage effect at 1580 nm. Using nitride intercladding layer, we are able to achieve consistently less than 1 dB/cm transmission loss for the TM-mode operation. For the LOX/nitride intercladding processes, we can still see thicker nitride can reduce waveguide loss. Especially for two different intercladding layers with the same nitride thickness, the waveguide loss values are comparable. However, with limited data, we can not explain why 20 Å LOX/10 Å nitride intercladding layer results in higher loss than the control sample.

Table 9.4. The calculated effective index, confinement factor, Γ, and E-field at sidewall boundary at 1550 nm and 1580 nm.

Polarization	Wavelength	Optical Properties		
		n_{eff}	Γ	E-field at sidewall
TE-mode	1550 nm	2.395	0.723	26.236 (V/m)
	1580 nm	2.363	0.711	25.582 (V/m)
	Δ	**-1.34%**	**-1.66%**	**-2.50%**
TM-mode	1550 nm	1.673	0.290	
	1580 nm	1.648	0.259	
	Δ	**-1.49%**	**-10.69%**	

Table 9.5. Transmission loss coefficients (dB/cm) at 1580 nm for the c-Si waveguides in 6 different processes.

ID	Variation	Polarization	Designed Waveguide Width (nm)			
			400	450	500	550
1	Control No nitride	TE	8.0 ± 0.2	5.0 ± 0.1	2.8 ± 0.2	2.3 ± 0.1
		TM	14.4 ± 2.9	5.3 ± 0.9	2.0 ± 0.2	1.0 ± 0.2
2	20Å Si_3N_4	TE	8.7 ± 0.2	5.0 ± 0.2	2.4 ± 0.2	2.4 ± 0.2
		TM	12.0 ± 3.4	4.0 ± 1.0	1.4 ± 0.4	0.8 ± 0.1
3	50Å Si_3N_4	TE	7.6 ± 0.2	4.8 ± 0.2	2.6 ± 0.1	1.6 ± 0.2
		TM	6.0 ± 1.4	2.0 ± 0.4	0.8 ± 0.1	0.5 ± 0.1
4	100Å Si_3N_4	TE	7.8 ± 0.2	3.6 ± 0.2	2.7 ± 0.2	2.2 ± 0.2
		TM	3.6 ± 0.8	1.2 ± 0.1	0.7 ± 0.2	0.4 ± 0.1
5	20Å LOX 10Å Si_3N_4 100Å LTO	TE	7.8 ± 0.1	4.8 ± 0.2	2.9 ± 0.2	2.4 ± 0.2
		TM	15.6 ± 2.0	6.0 ± 1.0	2.0 ± 0.4	1.0 ± 0.3
6	20Å LOX 20Å Si_3N_4 100Å LTO	TE	8.3 ± 0.1	4.8 ± 0.2	2.8 ± 0.2	2.4 ± 0.2
		TM	10.1 ± 1.9	3.2 ± 0.5	1.4 ± 0.1	0.7 ± 0.1

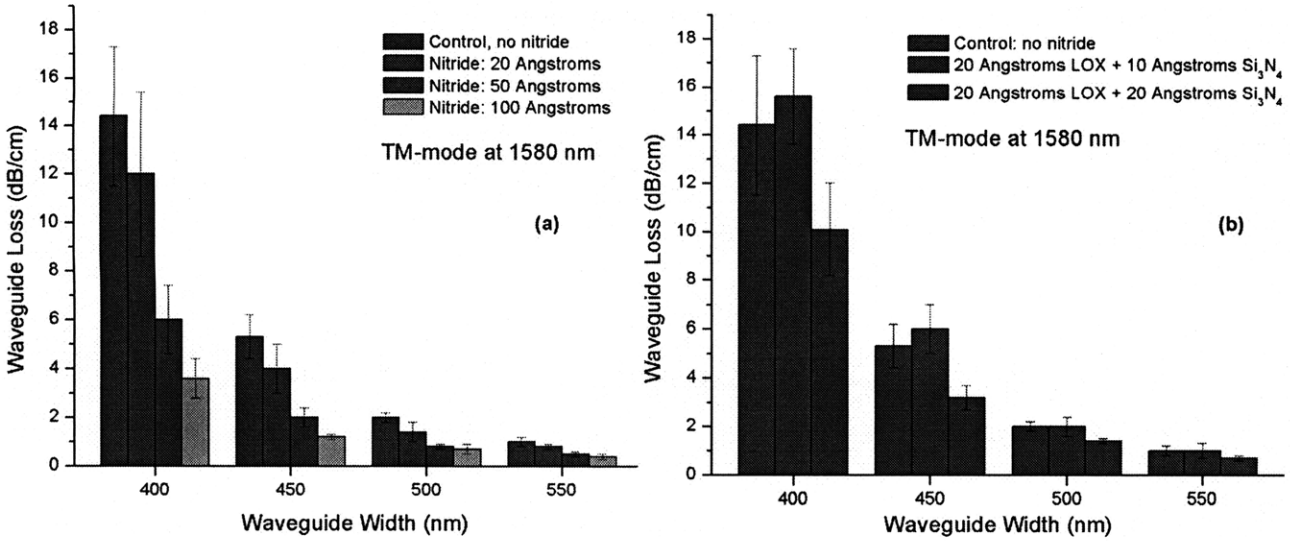

Figure 9.4. Column charts of the TM-mode waveguide loss vs. waveguide width for (a) nitride only intercladding layers and (b) LOX/ nitride intercladding layers

To summarize the thin nitride intercladding layer on c-Si channel waveguides study, we believe that the index grading effect is more significant when either the confinement factor is lower or the nitride thickness is thicker. We also discovered that 3 μm under cladding layer may not be sufficient for the TM-mode operation in longer wavelength even though previously we have shown that the theoretical substrate leakage should be lower than 10^{-3} dB/cm for 3 μm thick oxide.

The lowest losses we have achieved in single mode, c-Si channel waveguide are ~ 2.7 dB/cm for the TE-mode and ~ 0.7 dB/cm for the TM-mode in 500 nm × 200 nm waveguides with 100 Å nitride intercladding layer.

9.2. Amorphous silicon, single mode channel waveguides

In the EPIC program, parallel to c-Si waveguide work, we have also studied amorphous silicon (a-Si) waveguides. Our goal is also to realize low optical transmission in single mode, a-Si channel waveguides. This is achieved using

(1) H passivated a-Si waveguide material;

(2) PECVD silicon nitride intercladding layer with intermediate refractive index;

(3) Low optical loss PECVD silicon nitride.

The a-Si waveguide process is similar to SOI c-Si waveguides. Instead of using SOI wafers, a-Si (n = 3.64 at 1550 nm) is deposited on 3 μm thermal oxide wafers using PECVD at 350 ^{o}C in BAE Systems facilities. Because the as-deposited film has top surface roughness, lately we use CMP process to smooth the top a-Si surface. The deposited film is 400 nm thick and thinned down to 200 nm which is the waveguide thickness. Deep-UV lithography is used to define the waveguide structures using photoresist mask because pad-oxide/LPCVD nitride hard mask process temperature is not compatible with a-Si process. After poly etch, a-Si waveguides go through wet treatment to smooth out the sidewall roughness. Figure 9.5 shows two examples of the fabricated a-Si waveguide cross section. The sidewall angle is nearly 90^{o}. The top surface roughness problem has been addressed lately using CMP as the standard process. A 3 μm top oxide cladding layer is finally deposited at 400 ^{o}C (n = 1.46 at 1550 nm).

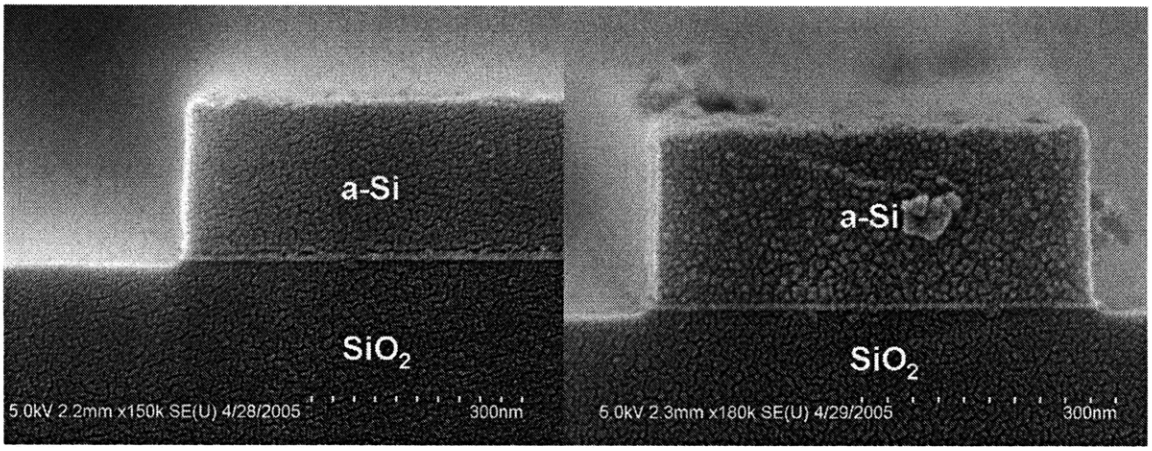

Figure 9.5. SEM images of the cross sections of the as-fabricated a-Si channel waveguides. The sidewall is nearly vertical. The texture on waveguide facets are due to sample preparation using Au coating.

Because hydrogenation is the key to low loss a-Si materials at 1550 nm, we first optimize the deposition power for PECVE process. The process condition variation and the waveguide loss values are summarized in Table 9.6. The bulk absorption coefficient is derived using the technique introduced in Chapter 5. The corresponding results are summarized in Table 9.7.

Table 9.6. Transmission loss coefficients (dB/cm) at 1550 nm for the a-Si waveguides using photoresist mask. The wafer ID's for these processes are "SL1A-Wf5-c3/b3", "SL1B-Wf7-h1/l6", and "SL1B-Wf6-h1/lb".

RF Power (W)	Polarization	Designed Waveguide Width (nm)				
		400	450	500	550	600
100	TE mode	22.6 ± 0.8	16.6 ± 1.1	14.2 ± 0.6	14.0 ± 0.3	13.9 ± 1.2
	TM mode	6.2 ± 0.4	7.8 ± 0.4	8.8 ± 0.5	9.8 ± 0.4	10.5 ± 0.7
50	TE mode	11.2 ± 1.1	8.6 ± 0.2	7.2 ± 0.5	8.4 ± 0.5	8.1 ± 0.3
	TM mode	7.6 ± 0.5	8.1 ± 0.4	8.2 ± 0.6	8.5 ± 0.5	8.6 ± 0.6
25	TE mode	9.4 ± 0.6	6.8 ± 0.4	6.8 ± 0.2	7.1 ± 0.1	6.9 ± 0.2
	TM mode	6.8 ± 0.6	7.0 ± 0.5	6.9 ± 0.4	7.0 ± 0.4	7.0 ± 0.4

Table 9.7 RF power and the resulting a-Si bulk absorption loss coefficients.

RF Power (W)	Bulk absorption loss coefficient (dB/cm)
100	15.2 ± 1.0
50	6.3 ± 1.0
25	0.6 ± 0.6

As we have discussed in 0, a thin silicon nitride intercladding layer can effectively reduce the a-Si waveguides' transmission loss by

(1) Acting as H diffusion barrier to prevent H from out diffusion, thus keeping the H passivation during later processes. This should work for both TE- and TM-modes; or

(2) Reducing the interface index contrast to reduce the sidewall roughness scattering effect for the TE-mode.

We have demonstrated this effect experimentally using the "paperclip" waveguide structures. Since 100 W a-Si is our initial baseline condition, the following data are obtained from a-Si waveguides using the same recipe. A 10 nm conformal PECVD nitride layer is deposited at 400 °C after a-Si waveguides are etched, cleaned, and wet treated. Finally, the 3 μm top oxide cladding is deposited. The results are summarized in Table 9.8. Compared to the standard 100 W a-Si waveguide loss listed in Table 9.6, the incorporation of such thin nitride intercladding layer reduces transmission loss by average 40% for the TE-mode and 27% for the TM-mode.

Table 9.8. Transmission loss coefficients (dB/cm) at 1550 nm for the a-Si waveguides using photoresist mask. Waveguides are over cladded by 10 nm thick PECVE silicon nitride. The wafer IDs for these processes are "SL1A-Wf15-i1/i3".

RF Power (W)	Polarization	Designed Waveguide Width (nm)				
		400	450	500	550	600
100	TE mode	11.1 ± 3.0	9.8 ± 0.4	8.6 ± 0.4	8.1 ± 0.4	9.7 ± 1.3
	TM mode	5.3 ± 1.1	5.8 ± 1.1	6.4 ± 0.6	6.4 ± 0.5	7.2 ± 0.3

We are aware that as-deposited PECVD silicon nitride has optical absorption at 1550 nm. By improving the nitride transparency, we could potentially achieve even lower loss in a-Si waveguides. The related process development for such a low loss nitride has been discussed in Chapter 7. The improved nitride contains only 10% of the original H in as-deposited nitride film.

We fabricate our new a-Si racetrack resonators in Microsystems Technology Laboratories (MTL) at MIT. Starting with a 6 inch silicon wafer with 1 μm thermal oxide undercladding layer, we deposited 100 nm PECVD hydrogenated a-Si thin film (n = 3.71). Because the deposition tool is different (Applied Materials Centura 5300 DCVD) from previous process in BAE Systems, the hydrogenated a-Si process is re-developed and the deposition power is optimized at 75 W. The as-deposited film has a refractive index of 3.71 at 1550 nm and the top surface roughness is measured to be less than 5 Å using Atomic force microscope (AFM), thus CMP step is not required. This film was patterned with I-line stepper (λ = 365 nm, NA = 0.6) using positive photoresist; and then etched using reactive ion etch method (RIE) with Cl_2 and HBr chemistry. Because we want to study the effectiveness of the nitride intercladding layer on sidewall roughness scattering reduction, we intentionally skipped the standard post-etch sidewall-smoothing wet treatments.

The waveguide has a cross-section of 700 nm × 100 nm ($w \times h$). The transmission loss coefficient is derived using resonance structure. The calculated effective indices are 2.06 and 1.47 for the fundamental TE- and TM-modes, respectively. The fundamental TE-mode has mode height of 1.2 μm and mode width of 1.5 μm; and for the fundamental TM-mode, they are 3.4 μm and 3.4 μm, respectively. To study the effect of the different silicon nitride intercladding layers, the wafer was broken into quarter-size pieces and the following experiments were performed:

Sample 1: Control, with no SiN_xH_y intercladding layer;

Sample 2: Deposited with 10 nm un-treated nitride intercladding layer (n = 2.089);

Sample 3: Deposited with 10 nm treated nitride intercladding layer (n = 1.896).

Different nitride deposition rates (Å per deposition-and-plasma-treatment cycle) were carefully calibrated prior to depositions. In the final step, all samples are cladded with 1 μm

PECVD SiO_2 as the top cladding layers. With 1 μm thick under cladding layer, the TM mode is lost due to substrate leakage. As a result, we obtain the resonator spectrum for TE mode only.

Racetrack resonator design helps enhance the optical coupling for large coupling gaps. In our case, the coupling gap is 600 nm and the coupling distance is 100 μm. The bend radius is 50 μm at which radiation loss due to bending is negligible. As a result, the round trip loss which determines the unloaded Q factor is dominated by waveguide transmission loss. A schematic representation of the racetrack resonator and an SEM image of the coupling region are shown in Figure 9.6. The waveguide cross section and the corresponding index profile are also shown.

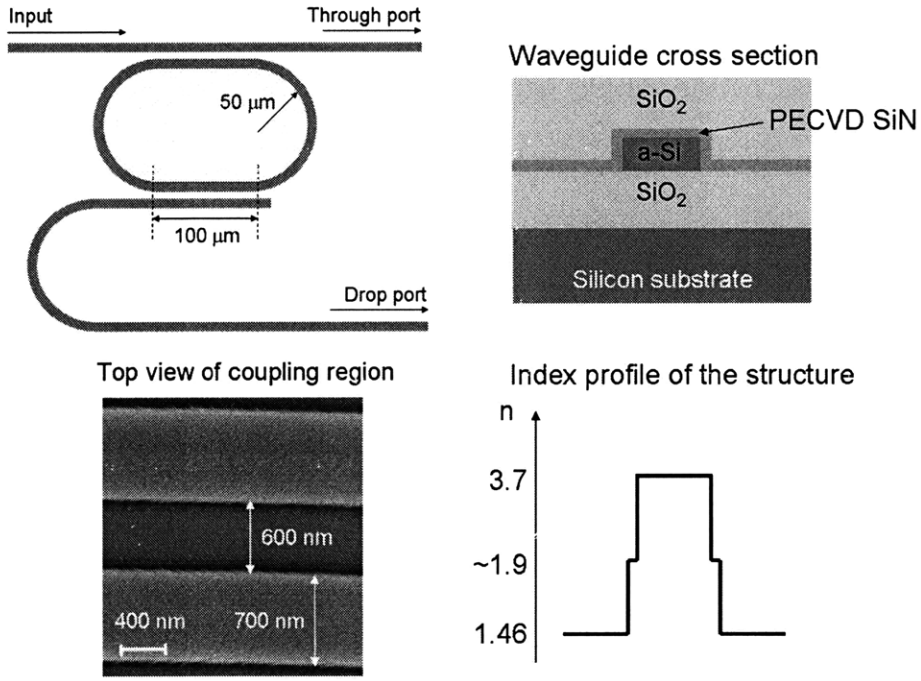

Figure 9.6. schematic representation of the racetrack resonator; the SEM image of the coupling region shows that the critical dimension is well controlled in fabrication; the waveguide cross section and its associated index profile are also given.

Waveguide transmission loss can be derived from the resonance spectrum of a first order resonator structure as we have discussed in Chapter 5. Figure 9.7(a) is an example of the resonant spectrum of one of the a-Si racetrack resonators. The FSR ranges from 1.35 nm to 1.36 nm as shown in the inset. Figure 9.7(b ~ c) highlights the three resonance spectra for Samples 1 ~ 3,

respectively. The extinction ratios and the -3dB bandwidths and Q factors are calculated from their Lorentzian fits. The fitting results and loss values are summarized in Table 9.9. We estimate that the uncertainty due to Lorentzian fitting and the real effective index deviation of the fabricated device from the design would result in ± 15% variation at most in the final waveguide transmission loss results. Incorporation of 10 nm as-deposited SiN_xH_y intercladding layer on the a-Si channel waveguides reduce the transmission loss from 12.0 ± 1.8 dB/cm (Sample 1) to 6.5 ± 0.9 dB/cm (Sample 2). These results are in good agreement with previous results derived using the "paperclip" method from straight waveguides in Table 9.6 and Table 9.8. The plasma treated nitride used in Sample 3 further reduces the loss to 2.7 ± 0.4 dB/cm.

Our current optimal PECVD SiN_xH_y still contains about 21.5% of the NH bonds compared to the as-deposited SiN_xH_y as shown in Figure 7.7. Comparing Samples 2 and 3, if we assume that the loss reduction of 3.8 dB/cm (0.876 cm^{-1}) is solely due to the NH reduction of 4.21×10^{21} cm^{-3} or 2.87×10^{16} cm^{-2}, then we can obtain the effective absorption cross section for NH resonance absorption at ~1560 nm to be 3.05×10^{-17} cm^2. This absorption cross section is expected to increase as wavelength approaches 1510 nm. We can derive that the same a-Si channel waveguide transmission loss coefficient can be further reduced by 0.4 dB/cm down to ~2.3 dB/cm at 1560 nm.

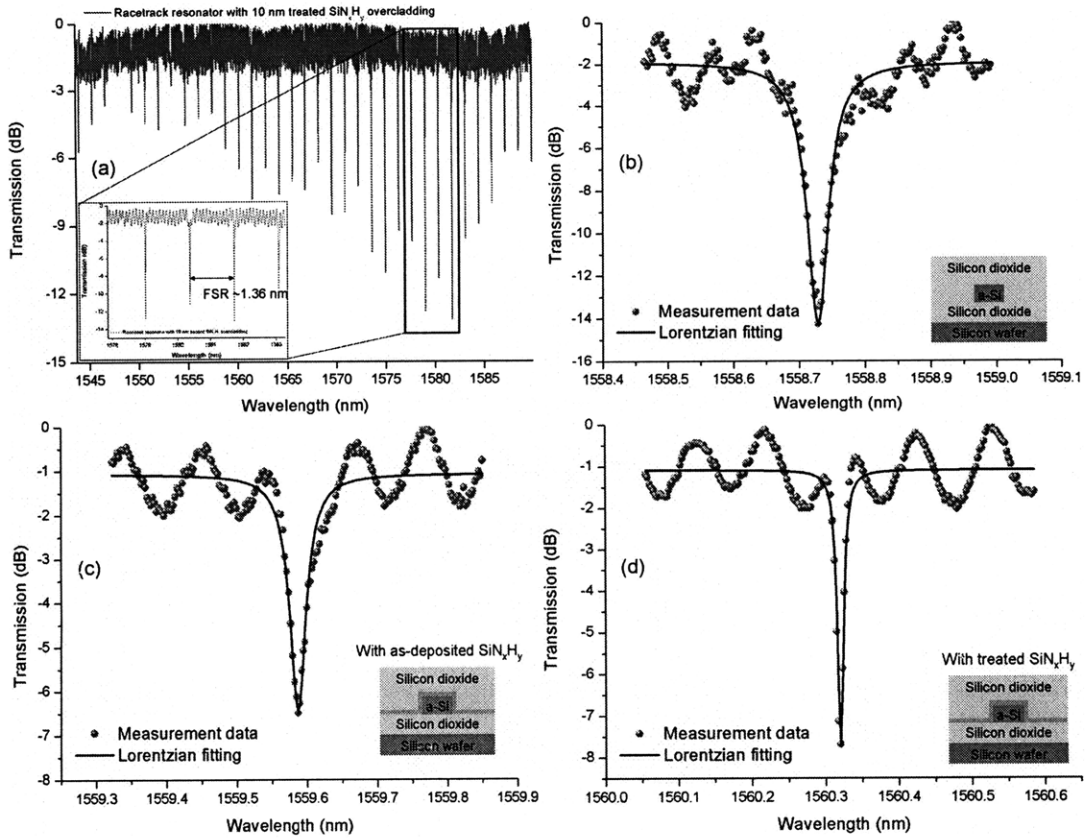

Figure 9.7. (a) The normalized resonance spectrum of an a-Si racetrack resonator with 10 nm nitride intercladding layer. (b-c) Three resonance spectra for Samples 1~3. The black lines are the corresponding Lorentzian fittings. The large periodic ripples are Fabry-Perot resonance from the waveguide input and output facets.

Table 9.9. The fitted data from Samples 1-3.

Sample	Resonance wavelength (nm)	Extinction ratio (dB)	-3 dB bandwidth (pm)	Q factor	Loss (dB/cm)
1	1558.146	12.3	69.4	22452	12.0 ± 1.8
2	1559.587	5.4	25.8	60449	6.5 ± 0.9
3	1560.319	6.9	11.0	141847	2.7 ± 0.4

9.3. Damascene processed single mode, a-Si channel waveguides

We have evaluated damascene processed a-Si channel waveguide samples in the form of racetrack resonators. There are two sets of samples: oxide trenches are as-etched (Wafer #2) and are treated with diluted HF (50:1 H_2O:HF) for 2 minutes (Wafer #3). The waveguide transmission losses are derived using the resonator method. Because the bend radii are all 50 μm, for the round trip loss, bend loss is negligible compared to transmission loss. The obtained round trip losses (dB)

are approximated to be transmission loss only and then converted to transmission loss coefficients (dB/cm) using the periphery lengths of the racetrack resonators.

The measured waveguide transmission loss (dB/cm) is summarized in Table 9.10. The 4 measured chips are taken from the outmost periphery of each wafer with the same radial distance to the center. Wafer #2 receives no HF treatment prior to a-Si deposition. Wafer #3 receives 2 minutes HF treatment after the oxide trenches are fabricated and prior to a-Si deposition. The resulting oxide trenches are ~ 50 nm wider than the mask width and the resonator-bus gaps are ~ 50 nm narrower accordingly. The inner chips on both wafers are found to be mostly ridge-shaped due to non-uniform CMP and those racetrack resonators are generally not working.

Table 9.10. Summary of the measured waveguide transmission loss in dB/cm (in red).

Sample ID		**Loss (dB/cm)**			**Comments**
		Waveguide width			
Wafer #	**Chip**	650 nm	600 nm	550 nm	
2	1	n/a	3.57 ± 0.58	7.49 ± 1.31	Oxide trenches received NO diluted HF treatment
2	2	n/a	2.46 ± 0.09	4.71 ± 0.53	
3	1	5.91 ± 0.80	6.71 ± 0.83	10.54 ± 0.87	Oxide trenches received 2 min diluted HF treatment
3	2	5.62 ± 0.66	6.15 ± 0.67	8.98 ± 1.20	

For a-Si waveguides fabricated directly by RIE and without nitride cladding layer in previous sections, e.g. 700 nm (w) × 100 nm (h), the loss coefficient is 12.0 ± 1.8 dB/cm. Our damascene processed a-Si waveguide devices have much lower transmission loss coefficients even though they are much narrower in width. In general, the transmission losses increase as waveguide widths decrease, indicating that sidewall roughness scattering is the dominant loss mechanism. Unexpectedly, the HF treated samples from Wafer #3 have higher loss than the as-fabricated ones from Wafer #2. The diluted HF solution (~ 10 nm/min for thermal oxide) should

be considered as aggressive isotropic etchant for surface treatment purpose. The 2 minute treatment time may be too long for roughness removal at trench sidewalls because the RMS roughness is normally less than 10 nm. The isotropic nature of HF etch has no selectivity to the capillarity effect caused by the roughness peaks and valleys, compared to the dry oxidation smoothing of SOI waveguide sidewalls.

Figure 9.8 shows some of the resonance spectra from the devices on Wafer #2. The resonance features have well spaced free spectrum range (FSR) and > 10 dB extinction ratio. The smaller fringes are the Fabry-Perot resonances due to the two flat waveguide facets.

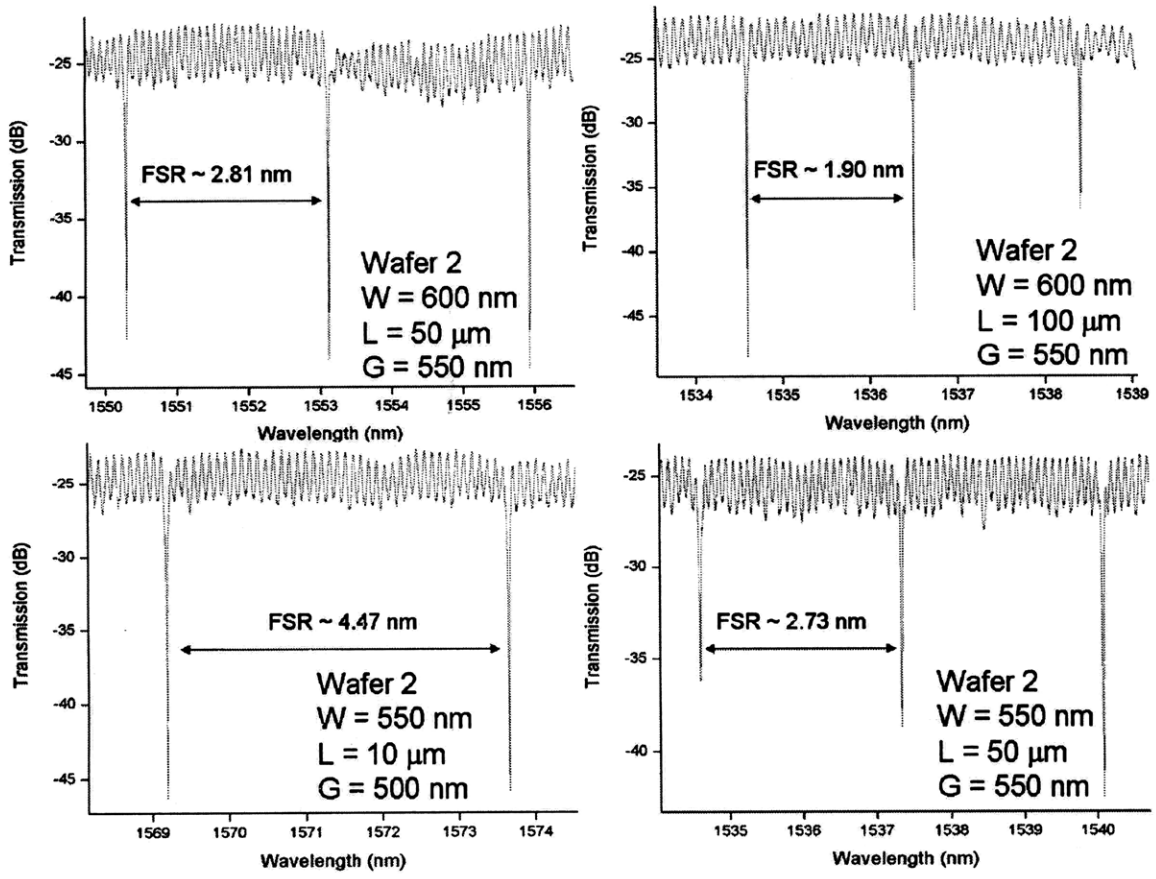

Figure 9.8. Examples of the resonance spectra from the racetrack resonator devices on Wafer #2. This is the first demonstration of racetrack resonators using damascene process.

Table 9.11 summarizes all the measured transmission losses from Wafer #2. For each waveguide width, the derived intra-chip losses from different resonators are relative consistent.

The inter-chip losses vary greatly with Chip 2 has generally lower losses than Chip 1. This is another sign of CMP non-uniformity: while the waveguide widths are similar in different chips, the actual waveguide heights may vary quite a lot.

Table 9.11. Summary of measured loss transmission loss at ~ 1550 nm for different devices from Wafer #2.

Chip ID	Width (nm)	n_{eff}	L (μm)	gap (nm)	Loss (dB/cm)
Chip 1	550	1.998	10	500	6.34
			50	550	8.44
			50	600	6.39
			50	650	8.79
	600	2.052	50	550	3.99
			50	600	3.9
			50	650	2.73
			100	600	3.65
Chip 2	550	1.998	50	550	4.97
			50	600	5.05
			50	650	4.1
	600	2.052	50	550	2.61
			50	600	2.36
			100	650	2.51
			100	600	2.35

Assuming that the sidewall roughness scattering effect is dominant in the transmission loss, we calculate the E-field strengths at the sidewall interface for different waveguide thickness as the result of non-uniform CMP. The E-field profiles are plotted in Figure 9.9. Because thinner channel waveguides have high E-field strengths at sidewall interface, it is likely that the higher transmission loss in Chip 1 of Wafer #2 is caused by over-CMP. Also, because ridge waveguide configuration has lower E-field at sidewall interface, Chip 2 of Wafer #2 is possible to contain ridge waveguides with very thin slab layer.

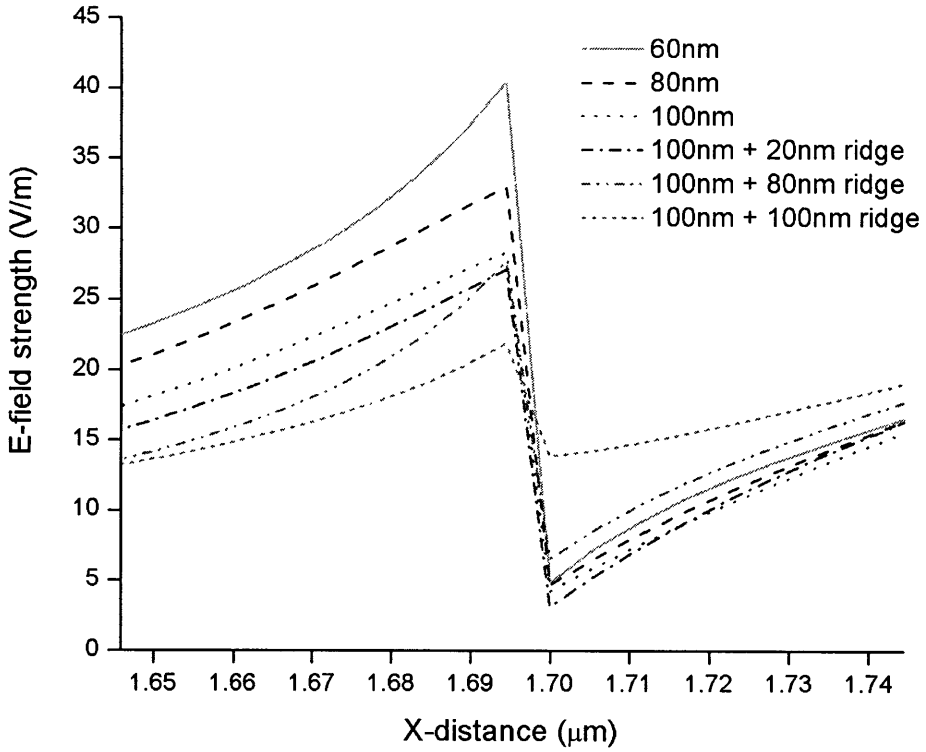

Figure 9.9. The theoretical E-field profiles for 6 different waveguide thicknesses. The waveguide sidewall is at 1.7 μm. Waveguide width is kept at 600 nm. The first 3 samples are channel waveguides with 60 nm, 80 nm, and 100 nm in height. "100 nm + 20 nm ridge" means that because CMP is not completely to the depth, there is 20 nm thick a-Si slab layer remaining and so forth, resulting in an "upside-down" ridge waveguide.

Similarly, Figure 9.10 plots the resonant spectra of devices from Wafer #3. The corresponding measurement results from the chips on Wafer #3 are summarized in Table 9.12. The variations among the two chips from Wafer #3 are smaller compared to Wafer #2, indicating that our current CMP is really on a case-by-case basis! More reliable and repeatable CMP is required in order for damascene process to be a robust alternative fabrication method for deposited waveguides.

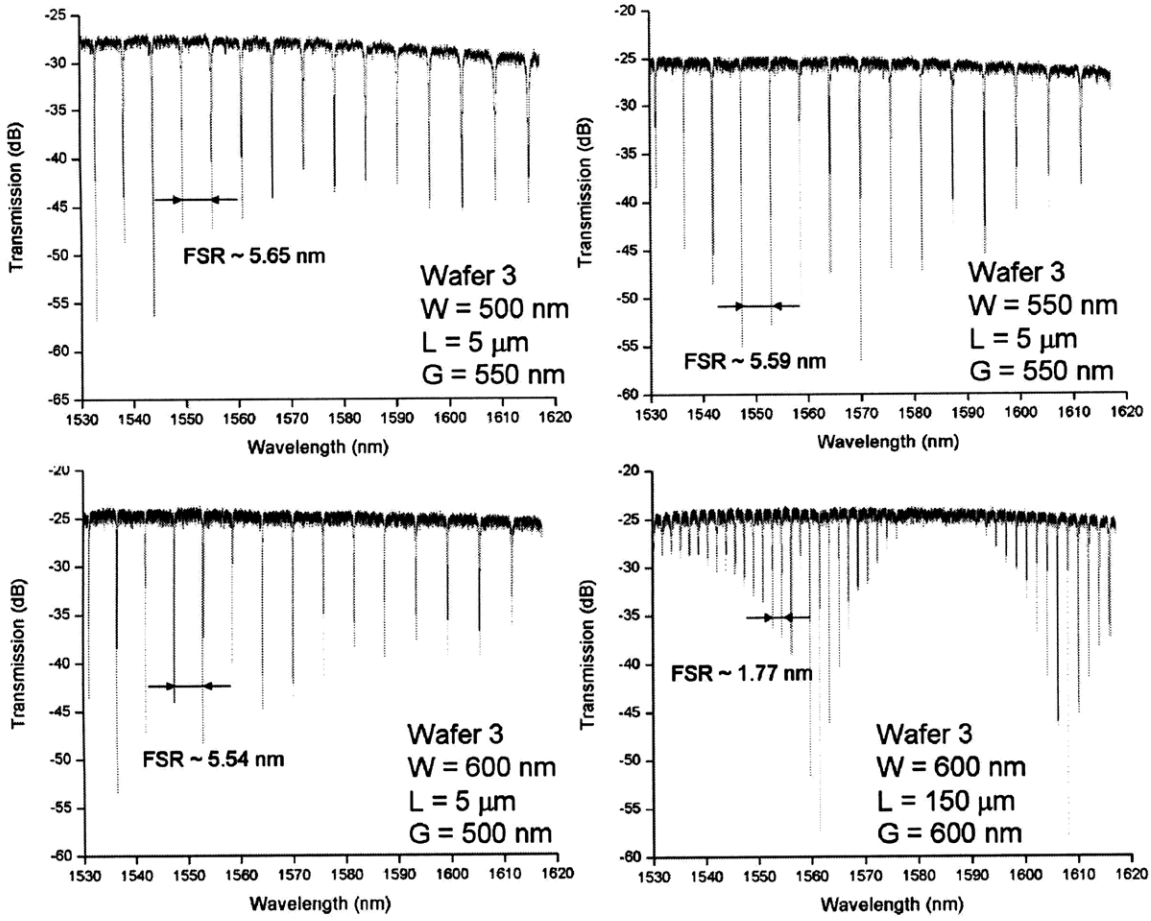

Figure 9.10. Resonant spectra from the racetrack resonator devices on Wafer #3. The variation in extinction ratio is caused by different coupling conditions. The extinction ratio is maximized at critical coupling condition where the power coupled into resonator is equal to the round trip loss of the resonator.

Table 9.12. Summary of measured loss transmission loss at ~ 1550 nm for different devices from Wafer #3.

Chip ID	Width (nm)	n_{eff}	L (μm)	gap (nm)	Loss (dB/cm)
Chip 1	550	1.998	5	500	11.86
			5	600	9.66
			10	600	11.07
			10	650	10.62
			10	700	9.43
			100	550	10.41
			100	600	10.08
	600	2.052	5	500	6.5
			5	550	7.65
			5	600	5.63
			10	600	7.44
			10	650	6.35
	650	2.096	5	450	6.56
			5	500	5.44
			10	600	5.01
			100	550	6.61
Chip 2	550	1.998	10	600	10.32
			10	650	7.99
			10	700	8.62
	600	2.052	5	450	6.9
			5	550	6.72
			10	550	5.44
			10	600	6.20
			10	650	5.51
	650	2.096	5	450	5.26
			5	500	5.26
			10	500	6.88
			10	550	6.27
			10	600	4.41
			10	650	5.51

9.4. Summary

We have demonstrated the low loss optical transmission in single mode, c-Si channel waveguides with minimal TE mode loss of 2.7 dB/cm and TM mode loss of 0.7 dB/cm, respectively. For single mode, a-Si channel waveguides, we have achieved the lowest transmission

loss of ~2.7 dB/cm for the TE-mode operation using H passivated a-Si and a thin, low loss PECVE nitride intercladding layer. We have also successfully demonstrated the damascene process for deposited waveguide fabrications. The resulting a-Si channel waveguide devices have much lower loss than those directly fabricated by RIE etch of a-Si. The diluted HF solution treatment does not reduce the transmission loss, possibly due to too aggressive and isotropic etch.

(This page is intentionally left blank)

Chapter 10. Lensed, asymmetric GRIN fiber-to-waveguide couplers

10.1. Overview

While optical signals can be routed and processed on an integrated photonic chip, they have to be transmitted from optical fiber to on-chip first and be coupled off the chip after process. Low loss, broadband fiber-to-waveguide couplers are indispensable I/O components in an integrated photonic system.

For HIC waveguide, low loss fiber-to-waveguide coupler design is always challenging. Direct coupling is very inefficient because of three major mismatches:

1. Mode size mismatch
2. Mode shape mismatch
3. Modal index mismatch

A regular single mode fiber (e.g. SMF-28) consists of a doped silica core, a silica cladding, and a protective polymer coating and has a mode field diameter (MFD) around 10 μm. Its effective index is 1.4681 at 1550 nm. For Gaussian-like mode, the MFD is defined as the diameter at which power is reduced to $1/e^2$ of the maximum power. Figure 10.1 is a schematic representation of the cross section of a SMF-28 fiber and its mode distribution.

On the other hand, a HIC planar silicon waveguide has much different mode size and mode shape. The MFD of a typical single mode silicon waveguide (500 nm wide, 200 nm tall) is 0.49 × 0.55 μm ($w \times h$) for its fundamental TE mode and 0.92 × 0.67 μm ($w \times h$) for its fundamental TM mode.

The rectangular-shaped waveguide also has high birefringence. The effective indices for the fundamental TE and TM modes are 2.395 and 1.673, respectively. Direct coupling from fiber

to waveguide through free space will cause severe loss due to reflection at the waveguide and fiber facets.

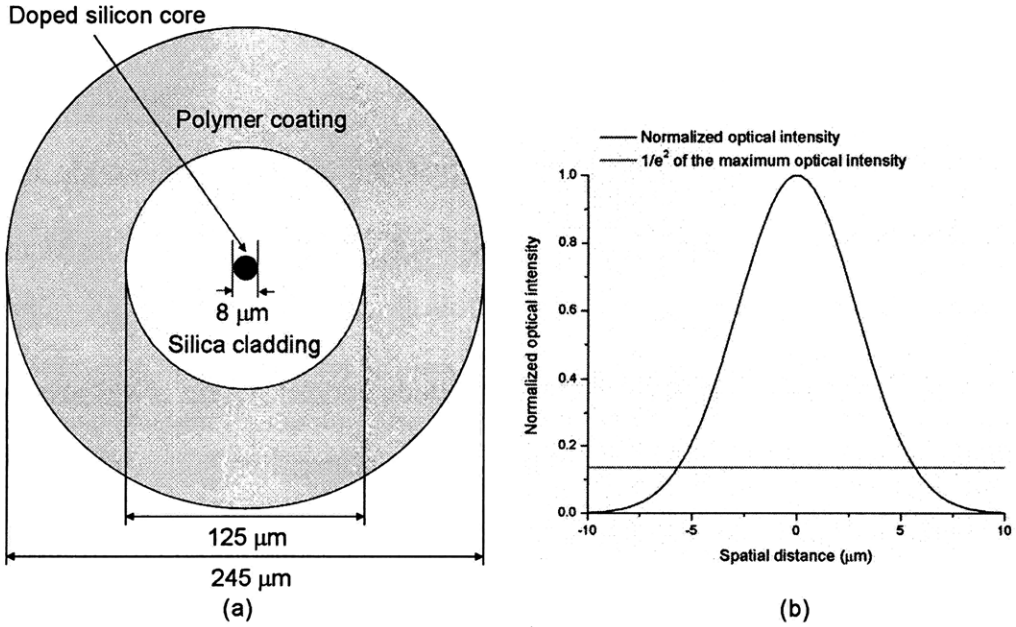

Figure 10.1. schematic representation of (a) a cross section view of a SMF-28 fiber and (b) its mode distribution. The black curve in (b) is a representation of the optical intensity distribution; the red line in (b) corresponds to $1/e^2$ of the maximum intensity. The locations where two curves intersect show the boundary of the MFD which is around 10 μm.

A number of methods have been developed to improve the fiber-to-waveguide coupling. For the optical fiber, lens tipped fibers and tapered fibers offer reduced MFD. For example, a typical lens tipped fiber has a MFD of 3 μm (Nanonics Imaging Ltd.); and for a tapered fiber, 1.7 μm (Nanonics Imaging Ltd.). The smaller MFD and non-flat fiber facet helps reduce the mode size mismatch as well as the reflection, improving coupling efficiency.

Index matching fluid (IMF) can also be used to reduce the reflection. IMF has various refractive indices ranging from 1.45-1.81 and normally wets both fiber and waveguide surfaces. They can effectively reduce the index contrast at fiber and waveguide facets compared to free space coupling ($n_{air} = 1$).

For waveguides, fiber-to-waveguide couplers can be used to increase the waveguide's MFD. The common ones are linear inverse taper couplers [79,80], parabolic inverse taper couplers

[81], normal 3D taper fabricated by grayscale lithography [82], grating based planar coupler [83], nonperiodic segmented waveguide coupler [84,85], and graded index based couplers [86,87]. The coupling loss can be reduced to be less than 1 dB per coupler.

Our design of a low loss fiber-to-waveguide coupler consists of an asymmetric taper made of 7 graded index layers with a monolithically integrated lens. Our prototype devices are made of silicon nitride and silicon oxynitride. A minimal loss of 0.45 dB per coupler is achieved when coupling a single mode SiO_xN_y waveguide with a MDF of 1.45 μm to a single mode fiber with MFD of 6.8 μm (Nufern980^{TM}). The averaged coupling loss is 0.4 dB between 1520 nm and 1620 nm.

10.2. Previous design of an asymmetric graded index taper coupler

Grade index (GRIN) structures are widely used in optical fiber application to reduce the modal dispersion caused by the different propagation velocities of the optical signals. Governed by the Snell's law, light is refracted toward the highest index core. A parabolic index step profile works the best in terms of providing confinement. The same idea can be utilized for a planar waveguide coupler.

Nguyen designed a coupler which has an asymmetric stepwise parabolic index profile to confine light vertically and a non-adiabatic taper structure to change the mode size in the horizontal direction as shown in Figure 10.2 where w is the taper width at the outer flat facet; w_t is the taper tip width and also the waveguide width (0.9 μm); and L is the taper length [88]. The GRIN structure is made of 7 layers of SiO_xN_y with refractive index increasing from the top layer to the bottom which is also the waveguide level. The layer thickness and index is carefully designed to form a stepwise parabolic index profile as shown in Figure 10.3(a). The single mode SiO_xN_y

waveguide has a cross section of 0.9 x 0.9 μm^2 with a MFD of 1.45 μm. 2D-FDTD simulation shows the efficient focusing effect of fiber mode to the waveguide mode as in Figure 10.3(b). The coupler length is designed to match the focal distance of the GRIN layers. The SiON waveguides and the GRIN coupler were deposited by plasma-enhanced chemical vapor deposition on 3 μm thermal SiO_2 on a silicon wafer. The refractive indices are tuned by changing deposition parameters (More details can be found in Ref. 88). The coupler structure is defined by a plasma etch using trifluoromethane chemistry. Because waveguide and coupler are fabricated in 2 separated steps, good alignment is critical. An example of the SEM image of the fabricated coupler is shown in Figure 10.4 [89].

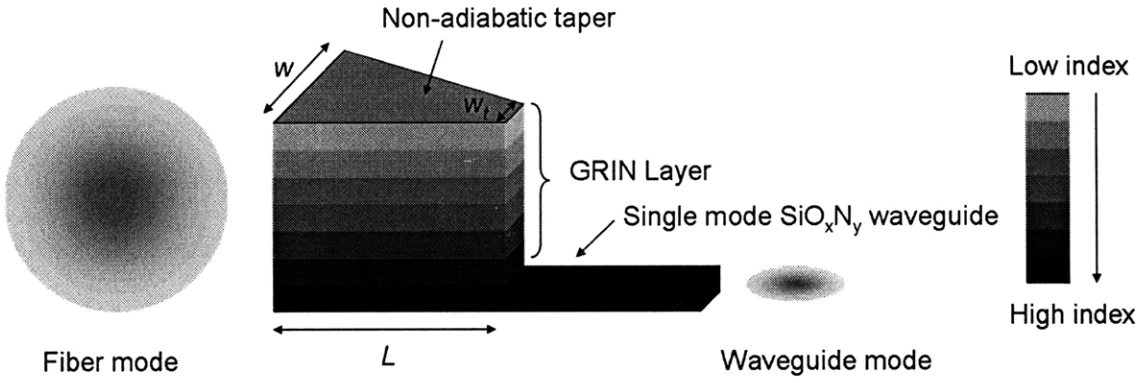

Figure 10.2. Schematic representation of a 7-layer GRIN coupler capable of transferring the fiber mode to waveguide mode and vice versa. The highest index layer is at the bottom which is also the waveguide level.

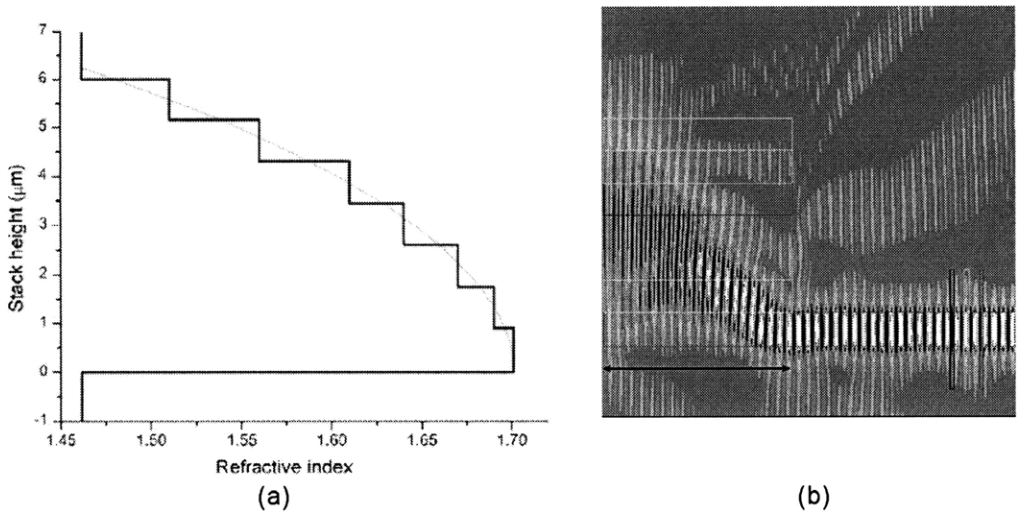

Figure 10.3. (a) The index profile for asymmetric GRIN layer stack with bottom and top cladding layers being SiO_2 (n = 1.46). The lighter curve is the ideal parabolic index profile; (b) 2D-FDTD simulation shows the optical focusing effect from fiber mode to waveguide mode (Figure taken from Ref. 88).

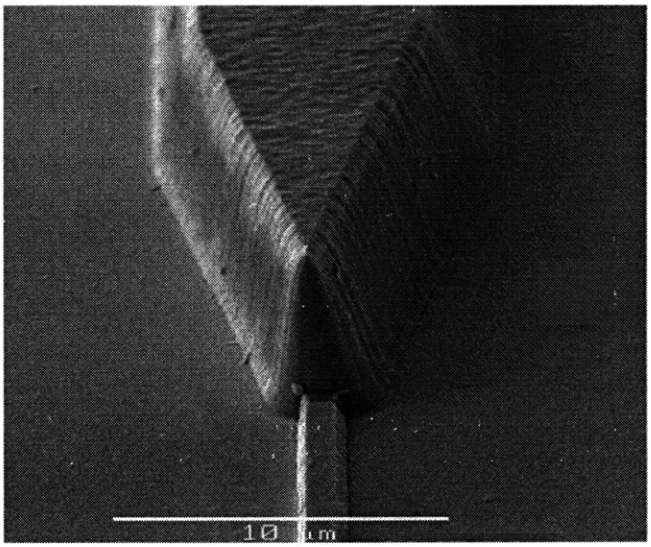

Figure 10.4. The SEM image of an uncladded coupler. The waveguide alignment with the coupler is well controlled (Figure taken from Ref. 89)

Nguyen studied the coupling efficient variation as a function of w and L and discovered that the lowest coupling loss is 2.2 dB per coupler in a 6 μm high, 20 μm long, and 8 μm wide coupler. In addition, from 1520 nm to 1620 nm, this coupler has a coupling loss ranging from 1.9 dB to 2.7 dB per coupler with minimal coupling loss at around 1540 nm.

10.3. Lensed, asymmetric graded index taper coupler

An improved design of the above fiber-to-waveguide coupler is proposed and demonstrated. The most significant change is the incorporation of a monolithically integrated lens at the couple facet. Because the focal distance of the GRIN layer determines the coupler length, L, and to keep the coupler footprint as small as possible, the taper structure has to be non-adiabatic. The lens structure can help light confinement in the horizontal direction in the taper structure, improving the coupling efficiency. The deposition and etch of the GRIN taper is as before. The incorporation of the lens does not increase the complexity of the process because the lens and the coupler structure are defined simultaneously in both photolithography and etch steps. The lens structure is shown as a scanning electron microscopy SEM image in Figure 10.5. Due to the improved plasma etching process, a less slanted sidewall of 94° is obtained. This requires only an index matching fluid with index of 1.4587 to obtain the maximal transmission, as opposed to the higher index matching fluid required to correct the slanted facet for the sloped sidewall in Ref. 89. At the end of the 6 μm deep lens formation etch, the silicon substrate beneath the coupler juts out and precludes efficient coupling between the coupler facets and fiber. An additional process step includes an anisotropic etch at this stage which removes 100 μm of the silicon substrate under the coupler and allows the optical fiber to be brought into close proximity of the input and output facets of the coupler. The effectiveness of the lens has been verified using finite-difference beam propagation code using the TE mode qualitatively.

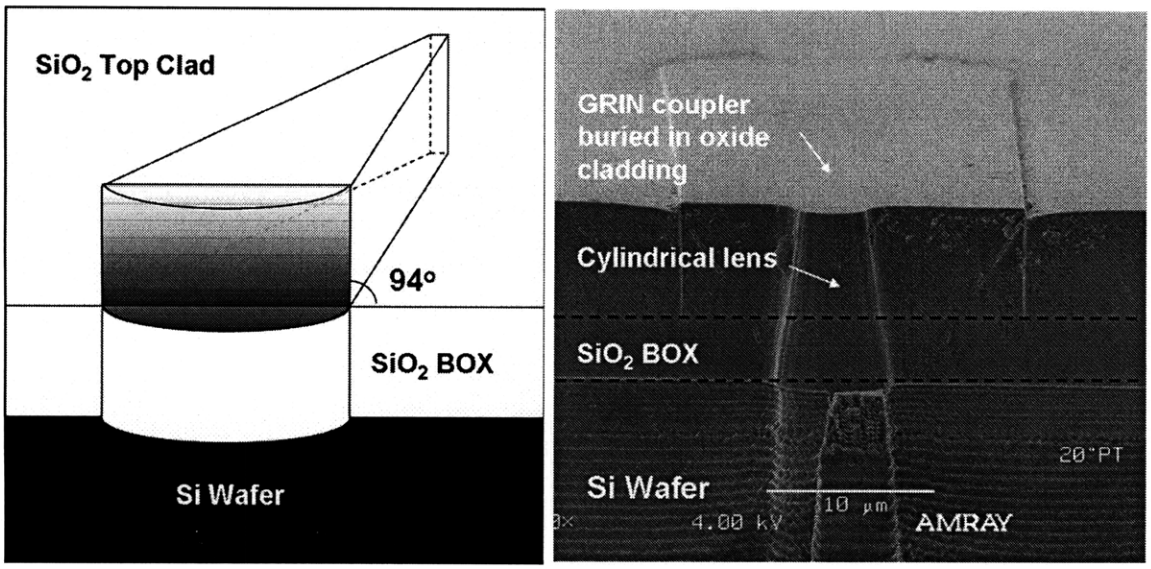

(a) (b)

Figure 10.5. (a) Schematic representation of the asymmetric GRIN lensed coupler and (b) cross-sectional SEM image. The etch profile has a slope of 94°. The coupler structure is buried in the oxide top cladding but the cylindrical lens can be seen clearly. The layered structure in the silicon wafer is due to the dry-etch process and is not the GRIN coupler itself.

The coupling loss per coupler was obtained by subtracting waveguide loss and system loss from the total propagation loss. First, the waveguide loss is evaluated from the SiO_xN_y waveguides using tapered Nanonics fibers for input and output to match the small MFD of the waveguides. The waveguide loss coefficient, α_t, is measured to be 4.13 ± 0.28 dB/cm at 1550 nm, slightly lower than the first run of 4.8 ± 0.50 dB/cm in Ref. 88. Then, the total insertion loss of the SiO_xN_y waveguides with the same length but with two GRIN couplers is measured using non-tapered Nufern fibers. Here, we use IMF with n = 1.4587 to eliminate the reflection loss at the facets of the coupler as well as the fiber. In both measurements, the Auto-Align station optimizes the coupling between the input and output facets and the fiber. The coupler's loss is calculated by subtracting waveguide loss from the total insertion loss. The detailed formulation is as follows:

$$\alpha_t \cdot L = \alpha_{insertion}(1) - 2\alpha_{coupling}^{nanonics} \tag{10.1}$$

$$\alpha_{coupling}^{nufern} = \alpha_{insertion}(2) - \alpha_t \cdot L \tag{10.2}$$

where

- $\alpha_{insertion}(1)$ is the total insertion loss measured from waveguides without couplers using tapered fiber (Nanonics fiber);
- $\alpha_{coupling}^{nanonics}$ is the fiber-to-waveguide coupling loss included in $\alpha_{insertion}(1)$; it is simulated to be 0.8 dB per coupler using FIMMWave.
- $\alpha_{insertion}(2)$ is the total insertion loss measured from waveguides with couplers using Non-tapered single mode fiber (Nufern fiber); and
- $\alpha_{coupling}^{nufern}$ is the fiber-to-waveguide coupling loss included in $\alpha_{insertion}(2)$.

First, expecting that the improved reactive ion etch may improve the flat-end coupler's performance we revisit the old design of flat-end couplers without lenses. The coupler's lengths are fixed at 20 μm. The couple widths vary from 4 to 14 μm. The coupling losses are collected and summarized in Figure 10.6. The lowest loss obtained is 0.9 dB per coupler for the TE polarization for the coupler with 7 μm wide flat-ended facet. From the optimized etching, there is 300% improvement over what was previously reported.

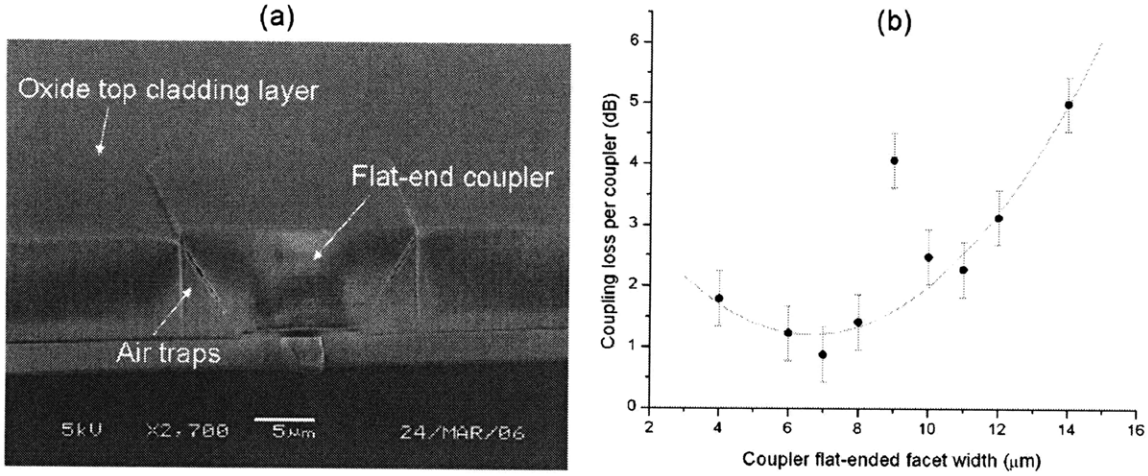

Figure 10.6. (a) An SEM image of the exposed facet with flat-end coupler. The waveguide and actual couplers are buried by oxide already, although the outline of the coupler is still visible; (b) the experimental results of the coupling loss with error bar. The red line is there to guide the eyes.

To test the effect with different lens radii, the chord lengths are kept constant and match the coupler outer flat facet width, *w*, which is fixed at 8 μm, so the lens structure can cover the entire facet. The couplers are also 20 μm long. The lens radii vary from 4 to 20 μm. A schematic drawing of the lens structure is shown in Figure 10.7(a). These lensed couplers perform better than flat-end couplers as expected. In Figure 10.7(b), we observed the lowest coupling loss of 0.45 dB for the TE polarization for a 9 μm radius lensed coupler. The polarization dependent losses of lensed couplers are averaged to be 0.2 dB. The lens provides 300% improvement over the 8 μm wide flat-ended coupler shown in Figure 10.6(b). Because the chord length is fixed at 8 μm, the curvature for large radius lens becomes very small and virtually it behaves like a flat-ended coupler. The abnormal behavior of a 9 μm wide flat-end coupler and a 7 μm radius lensed coupler is because of the remained lens obstruction that prevented the fiber tip from moving to the optimal coupling position; optimal coupling position could not be achieved, resulting in much high coupling losses.

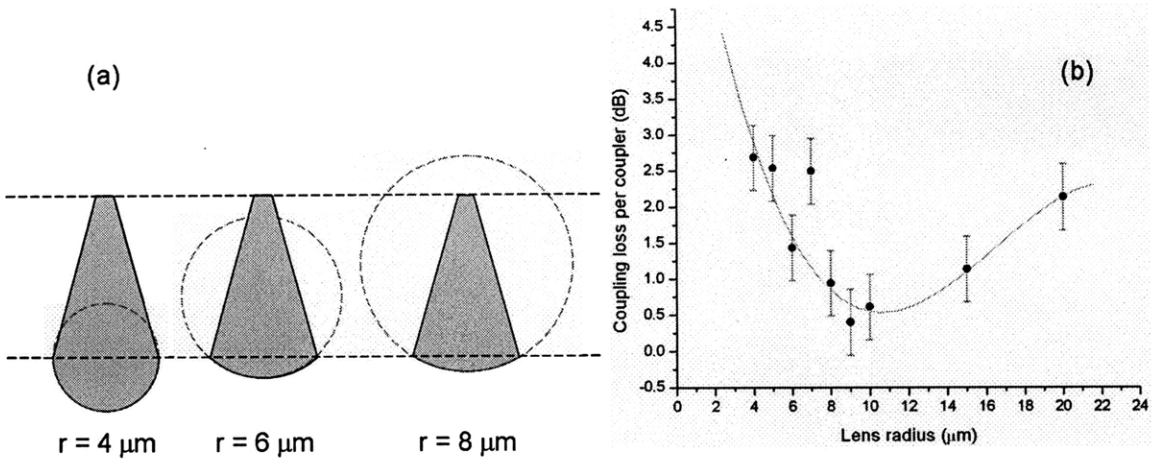

Figure 10.7. (a) Schematic drawings of the top view of the lensed couplers with different radii. The chord lengths are fixed at 8 μm while the radii change. (b) Measurement results of coupling loss vs coupler width for lensed asymmetric GRIN couplers with couple chord width of 8 μm. The red line is to guide the eyes.

The wavelength dependence is also studied in the wavelength range between 1520 nm and 1630 nm. The transmission spectra for the waveguides with/without couplers show strong absorption pattern according to PECVD SiO_xN_y as shown in Figure 10.8. As we discussed in Chapter 1, this is due to the NH resonance absorption centered around 1510 nm.

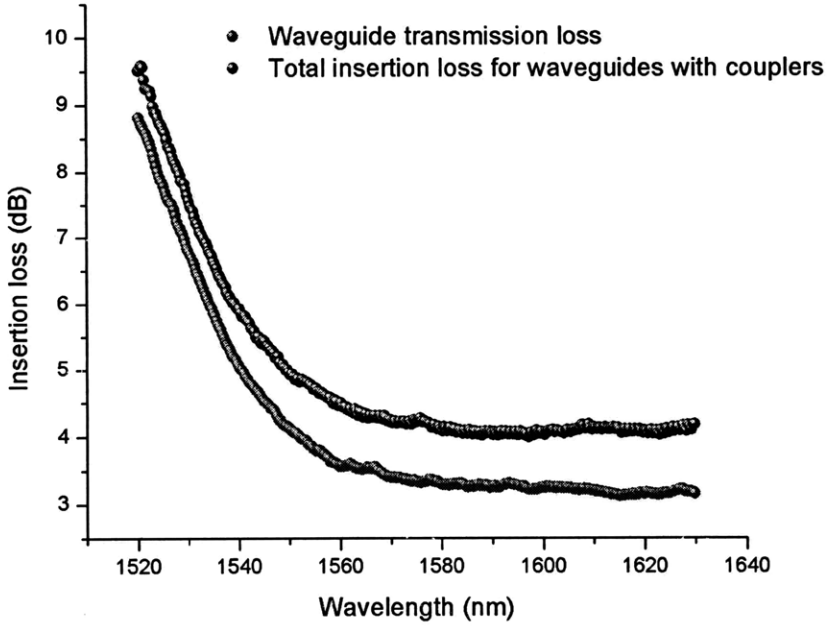

Figure 10.8. (red) Waveguide transmission loss spectrum; (blue) the total insertion loss of the same waveguide with two couplers at each end.

The coupling loss for each coupler is one-half of the loss difference in above two curves. The NH absorption effect from the waveguide is dominant because the two couplers are very short compared to the waveguide. The NH absorption inside the coupler is thus negligible. Figure 10.9 plots the coupling loss per coupler as a function of wavelength. The small fluctuation can be caused by the electronically driven Autoalign stage drifting during the time span of the measurement. The average coupling loss between 1520 and 1630 nm is 0.42 dB. The loss values are 500%–600% smaller than those in flat-end couplers.

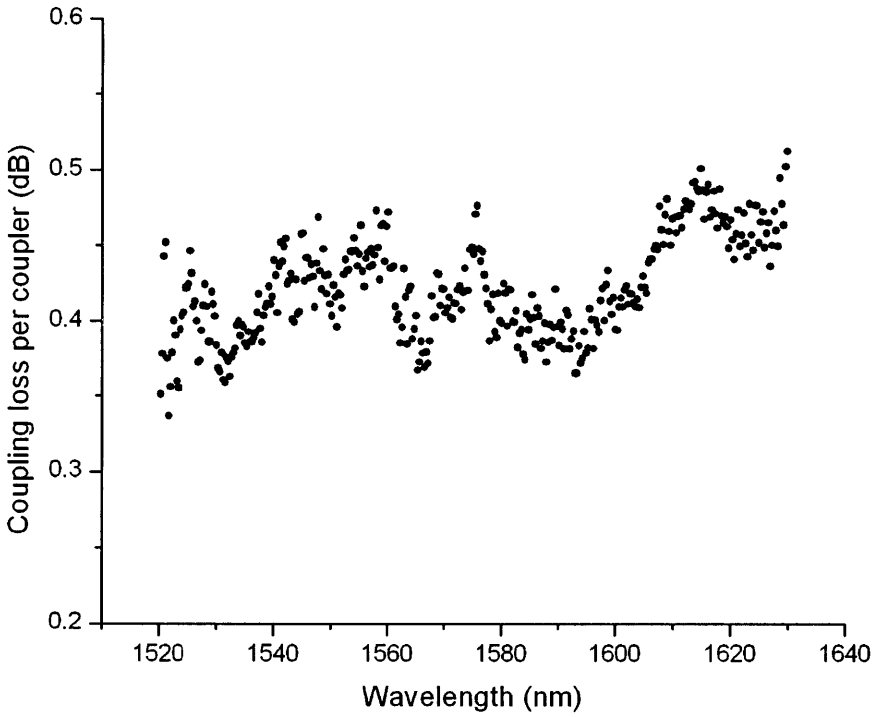

Figure 10.9. The measured coupling loss vs wavelength for a 20 μm long, 8 μm wide, and 9 μm radius lensed coupler.

10.4. Summary

In this chapter, we have designed a class of high performance fiber-to-waveguide couplers for high index contrast waveguides. The couplers consist of a GRIN layered structure in the vertical direction and a non-adiabatic taper for light confinement in the horizontal direction. The initial design is modified to incorporate a monolithic integrated lens at the flat coupler facet to help

light confinement in horizontal direction. The fabricated couplers based on the new design have shown a significant performance improvement in terms of loss values and broadband behavior. The lowest coupling loss obtained is 0.45 dB per coupler and the average coupling loss is 0.42 dB from 1520 to 1630 nm.

Chapter 11. Impedance matching vertical waveguide-to-waveguide couplers

11.1. Overview

A common approach for integration of photonic components utilizes a co-planar design with silicon-on-insulator (SOI) substrates. This limits the pattern density and creates restrictions for scaling. A 3D integration approach can significantly increase the device density on a single wafer. In order to efficiently route and transmit an optical signal among different levels of photonic devices, a low loss vertical waveguide-to-waveguide coupler is indispensable.

One application for vertical waveguide is to enable waveguide coupled germanium-based photodetectors and electro-absorption modulators as shown in Figure 11.1. For operations around 1550 nm, strain-engineered single crystalline germanium (Ge) will have the right bandgap and high carrier mobilities for high performance photodetectors and modulators [90,91,92]. High quality single crystalline Ge is epitaxially grown on single crystalline silicon (also is highly doped, serving as bottom contact) using a two-step growth technique with a 60nm thick, defective Ge buffer layer firstly grown on SOI at ~ 360 ^{o}C followed by a high quality Ge growth at ~730 ^{o}C and sequential annealing [92,93]. As a result, bulk Ge is not at the same level as SOI silicon. Directly coupling light from SOI waveguide is not feasible. In both scenarios, optical signal is routed from bottom SOI waveguide to top amorphous silicon waveguide through a vertical waveguide coupler, and then coupled into bulk Ge. A low loss, broadband SOI-to-a-Si vertical coupler is the key enabler for these applications.

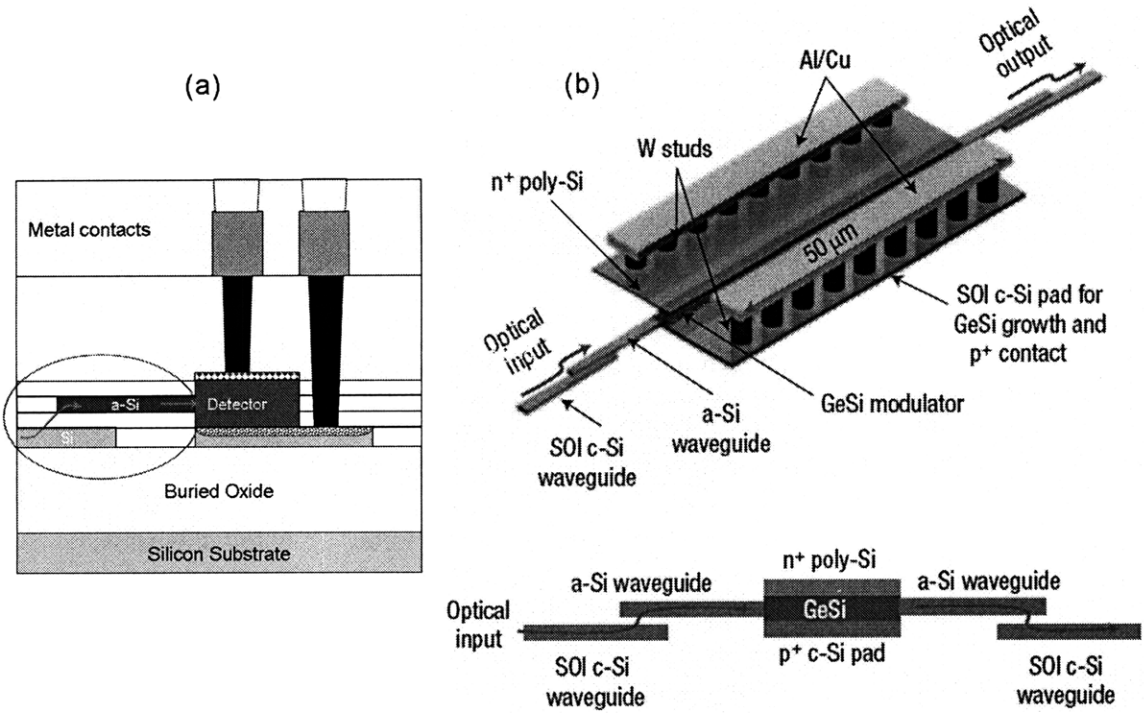

Figure 11.1. (a) a butt-coupled Ge photodetector; (b) a butt-coupled GeSi electro-absorption modulator. Both are enabled by using a vertical waveguide coupler to route optical signal from bottom SOI waveguide to top amorphous silicon waveguide.

11.2. Design and demonstration

11.2.1. Conventional vertical directional coupler design

The simplest design of a vertical waveguide coupler can be based on conventional directional coupler as shown in Figure 11.2. In our case, $w_1 = w_2 = 500$ nm; $h_1 = h_2 = h_3 = 200$ nm; and the coupling length, L, varies depending on refractive indices of the SOI and a-Si. The interlayer thickness of 200 nm was determined by the CMOS process flow that is used. The vertical coupling concept itself can be used for various interlayer thicknesses.

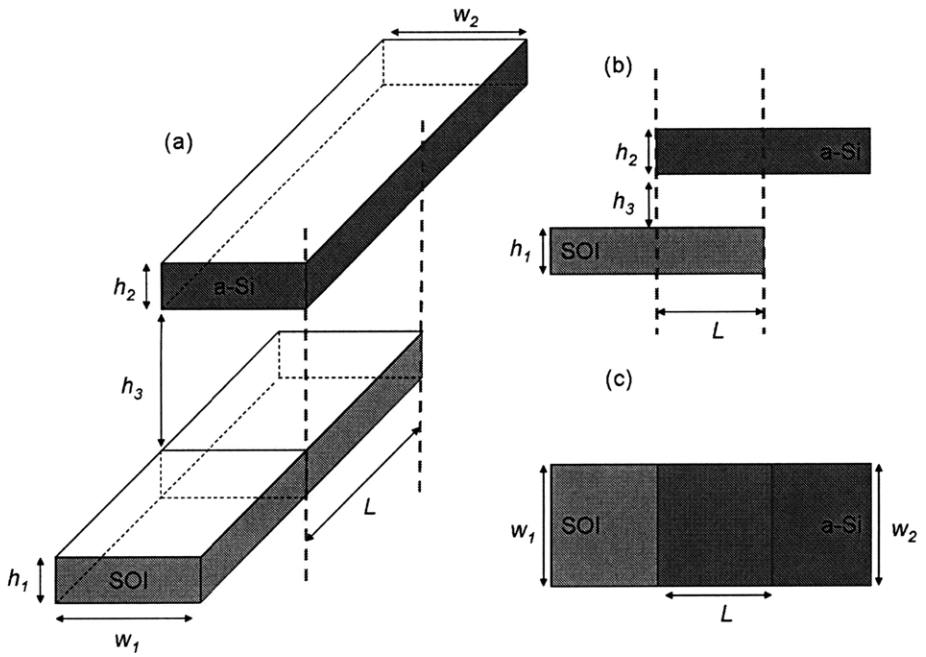

Figure 11.2. Schematic drawings of a vertical waveguide coupler based on conventional directional coupler design: (a) 3D view; (b) side view; and (c) top view.

A conventional directional coupler with two adjacent, parallel waveguides is well understood [94,95]. According to Saleh, 100% power transfer requires perfect optical impedance matching where the effective indices of the two waveguides are identical and the coupling length is exactly equal to the transfer distance at which 100% power transfer is complete. In our previous design, the refractive index of a-Si is assumed to be 3.5, equal to that of SOI. As a result, the optimal coupling length, L, is found to be 7 μm using BeamProp method. However, this design is not robust. The reasons are as follows.

First, for a vertical coupler consisting of two different waveguide materials, e.g. SOI crystalline Si (c-Si) and a-Si, index matching is difficult to achieve because the refractive index of a-Si depends greatly on deposition conditions and processes. Figure 11.3(a) shows the theoretical optimal coupling efficient as a function of a-Si refractive index. As a-Si index deviates from 3.5 which matches the SOI index, the maximal achievable coupling efficient decreases rapidly. Our a-Si refractive index is measured to be 3.64 in the final fabricated devices. This corresponds to a

maximal 56.5% coupling efficient. The a-Si index variation also changes the coupling length as shown in Figure 11.3(b). At n_{aSi} = 3.64, the optimal coupling length is 4.9 μm instead of 7 μm. Together, the 7 μm long coupling length based on n_{aSi} = 3.5 can only yield a coupling efficient of 36.8%, or 4.34 dB loss per coupler.

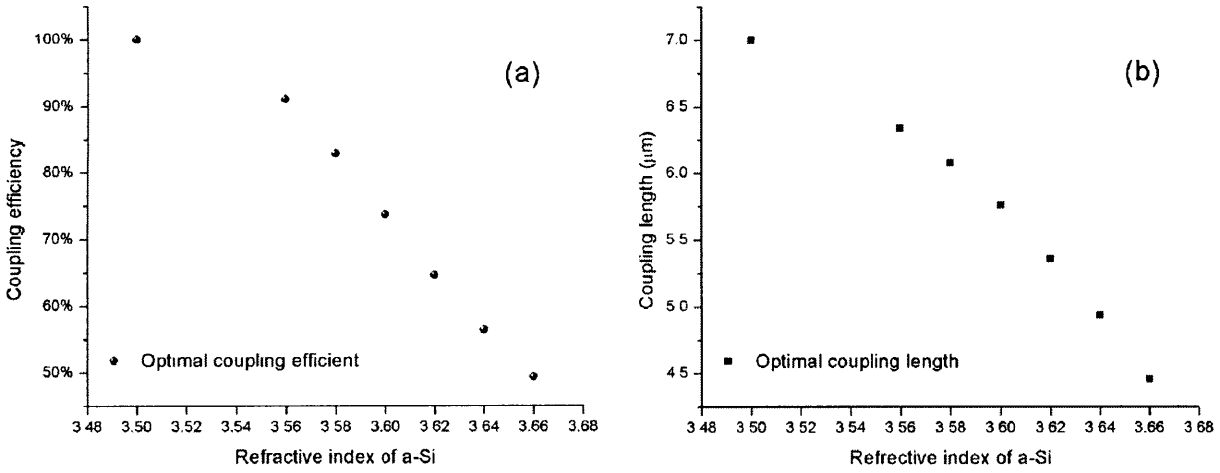

Figure 11.3. (a) Theoretical coupling efficient and (b) the corresponding coupling length as a function of a-Si refractive index in a vertical directional coupler. The refractive index of SOI is 3.5.

Secondly, fabrication of a vertical coupler requires multiple process steps that introduce variations in the dimensions of the waveguides at each level. These variations in waveguide dimension will cause a deviation in the effective index of the waveguide. An example is given in Figure 11.4 where n_{aSi} = 3.64 and n_{SOI} = 3.5. It shows that a-Si width variation can also change the maximal coupling efficient as well as the corresponding coupling distance.

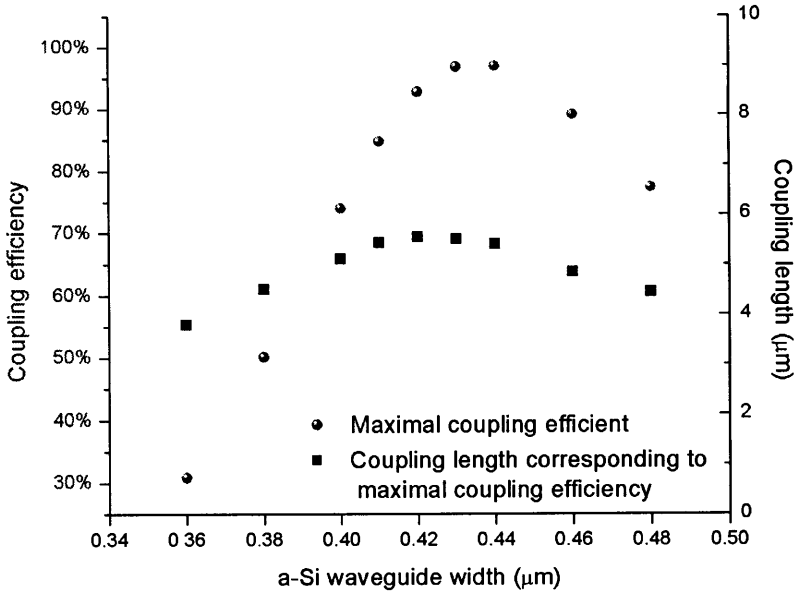

Figure 11.4. The theoretical maximal coupling efficiency and the corresponding coupling distance as a function of a-Si waveguide width. $n_{aSi} = 3.64$ and $n_{SOI} = 3.5$.

Last, waveguide misalignment changes the effective coupling gap between the two waveguides; and it can affect the coupling efficient and coupling length as well as shown in Figure 11.5.

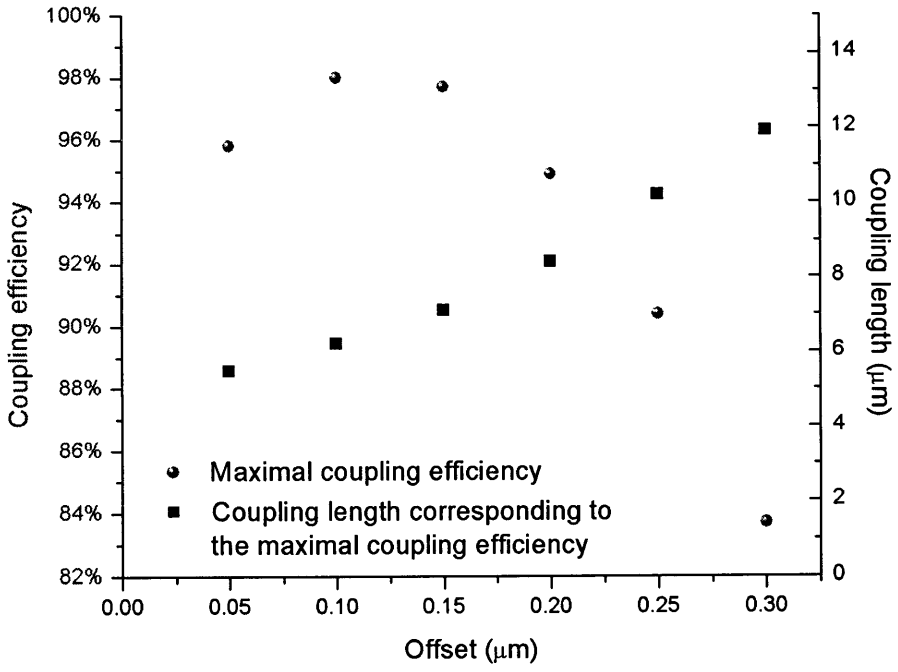

Figure 11.5. The theoretical maximal coupling efficiency and the corresponding coupling distance as a function of a-Si waveguide offset. $n_{aSi} = 3.64$ and $n_{SOI} = 3.5$.

In conclusion, the vertical coupler can not use conventional directional coupler design. A better design which can tolerate variations in materials and fabrication is needed.

11.2.2. Inverse taper vertical coupler design and demonstration

Our new vertical waveguide coupler design consists of two vertically overlapped inverse tapers extending from the respective waveguides. Figure 11.6 shows the structure of a vertical coupler in 3D, top and side views. Waveguides are also 500 nm wide and 200 nm tall designed for TE single mode operation at 1550 nm. The waveguide interlayer consists of 200 nm thick silicon dioxide.

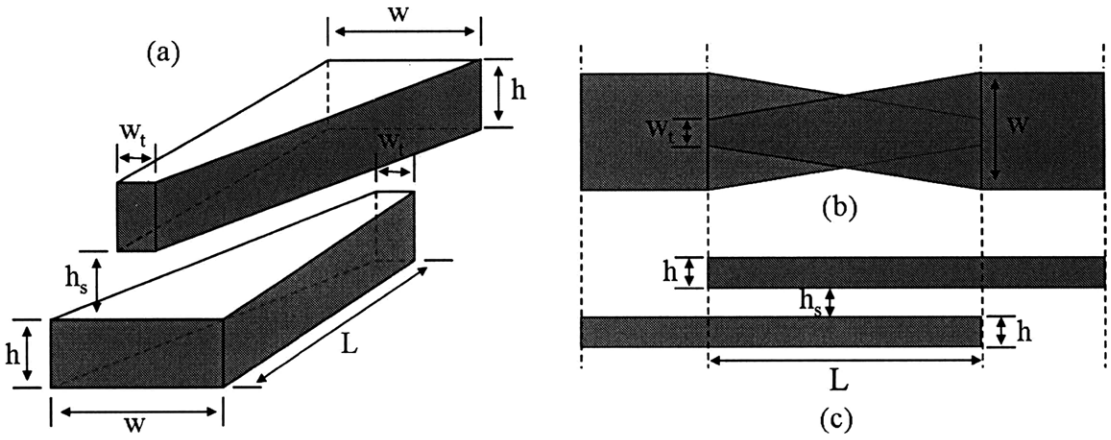

Figure 11.6. Schematic representation of an improved vertical coupler design: (a) 3D view; (b) top view; and (c) side view of the vertical coupler with finite tip width (w_t).

The inverse tapers have a shallow linear slope to ensure an adiabatic evolution of the optical mode. The linear taper is the simplest design for proof of concept although nonlinear tapers may provide a more optimized coupling performance. The top a-Si taper is designed to be central symmetric to the bottom SOI taper for simplicity.

This design is significantly improved compared to similar designs in the literature that use only one inverse taper with either a straight waveguide or a slab layer [96,97]. The effective index matching condition of this design is illustrated in Figure 11.7. The figure shows the effective

index profiles for top and bottom tapers as a function of waveguide width which is plotted along the top and bottom x-axes, respectively. The figure illustrates the impact on utilizing a single taper design compared to our dual taper design for the vertical coupler using a-Si with SOI. The index for SOI silicon is constant at 3.5, whereas the index for a-Si can range between 3.3 and 3.7. If only the SOI waveguide is tapered, an index match condition can not be met with a-Si index greater than 3.5. Alternatively, if the upper a-Si waveguide is tapered, a matching condition with SOI can not be found for a-Si index less than 3.5. Tapering both waveguides provides greater tolerance in the variation of a-Si material properties and guarantees optical impedance matching for the optical power to be efficiently transferred regardless of a-Si refractive indices.

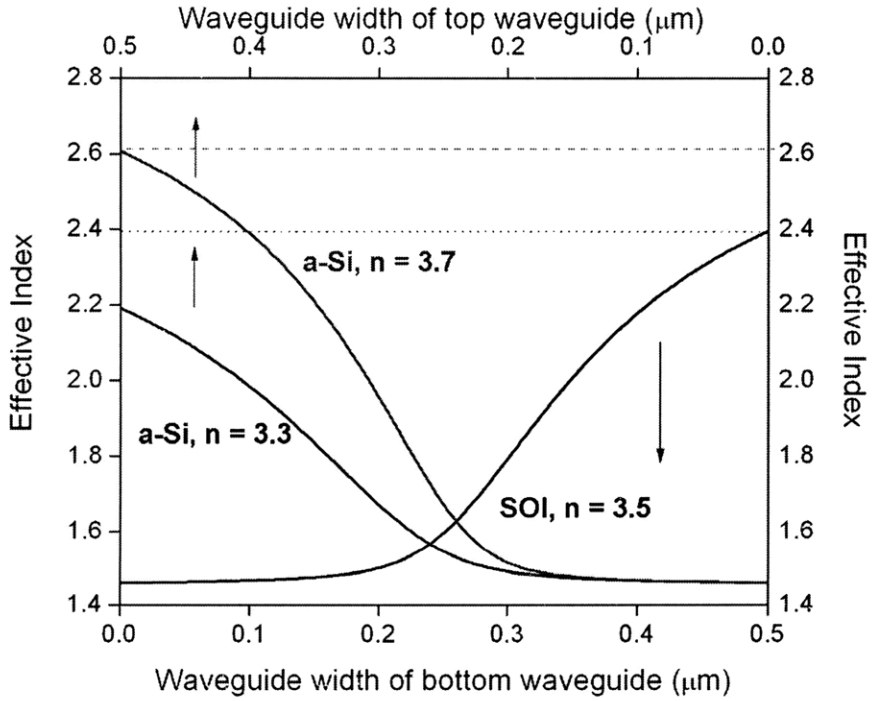

Figure 11.7. The effective index profiles in a vertical coupler of SOI and a-Si. The cross-over points indicate at which position optical impedance matching between SOI and a-Si waveguides is achieved. The horizontal dashed and dotted lines represent untapered a-Si and SOI waveguides, respectively.

The tolerance of this design on the a-Si index variation is examined using the eigen-mode expansion (EME) approach in FIMMPROP. Figure 11.8(a) shows a side view of the dynamic power transfer process inside the vertical couplers (L = 60 μm, w_t = 200 nm) for each a-Si index

condition. The dotted rectangles outline the area of the couplers. The dashed line highlights the location of the impedance matched condition where maximum power is transferred. As shown in Figure 11.8(b), the loss per coupler is consistently less than 0.14 dB for all a-Si index condition and corresponds to coupling efficiencies above 96%. Another important advantage of our vertical coupler design is that power oscillation can be effectively suppressed. Unlike the optical mode in a conventional directional coupler that oscillates sinusoidally between two waveguides, in our tapered vertical coupler there is little power coupled back once it is transferred to the other waveguide due to the fact that mode matching conditions for both waveguides are only satisfied at the coupling point.

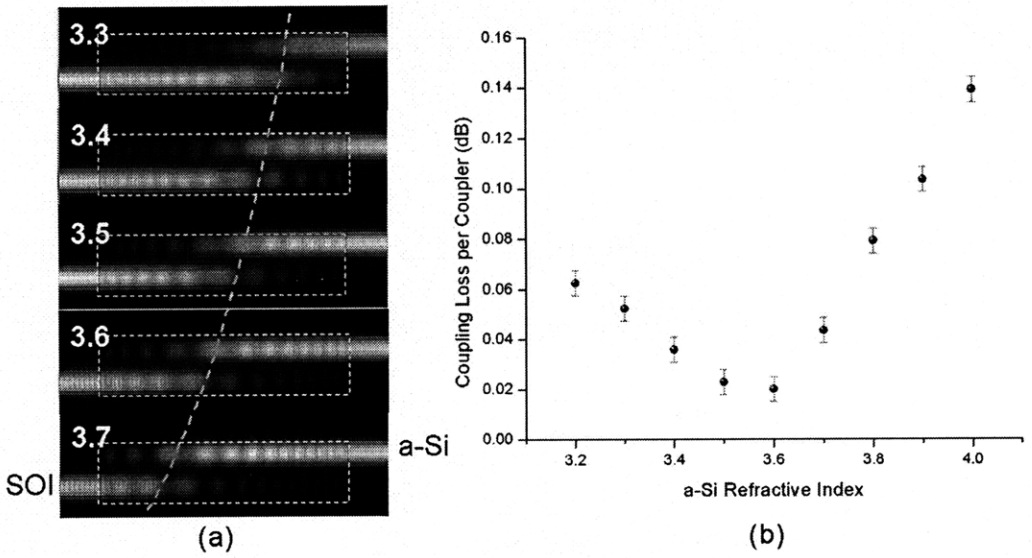

Figure 11.8. (a) Mode coupling inside a vertical coupler (L = 60 μm, w_t of 200 nm) with different a-Si refractive indices. White dotted rectangles highlight the cross section of the vertical coupler. (b) the corresponding coupling loss as a function of the a-Si refractive index. The SOI index is fixed at 3.5.

Although the mode matching condition between waveguides can always be satisfied in our vertical coupler, the total power transmission also depends on the coupler length and the tip width which defines the taper angle. Figure 11.9 summarizes the calculated coupling efficiencies as a function of coupler length for various tip widths using the same EME approach. In this analysis,

the index of refraction for a-Si is set to 3.6 and is consistent with the index obtained in our fabricated devices. For long vertical couplers with $L > 60$ μm, coupling efficiencies of more than 99.5% (or less than 0.02 dB coupling loss) can be achieved. In this case, a zero tip width design can be used without breaking the adiabatic condition along the taper. This is also very desirable since it eliminates abrupt index changes thus reducing light scattering when the optical mode travels from waveguide into coupler region. However, practical fabrication of tip widths less than 120 nm is very challenging using 193 nm photolithography. Vertical couplers less than 60 μm long are desired for reduced footprint, but they can not use zero tip width due to loss of adiabatic conditions. Coupling efficiency decreases as tip width decreases at constant coupler length as shown in Figure 11.9. A finite tip width reduces taper angle and helps mode evolution in the vertical coupler to stay lossless. For small refractive index differences in a c-Si/a-Si vertical coupler, high coupling efficiency can be obtained without tapering the coupler to zero width. For a given coupler length, a large tip width, or a small tapering angle, ensures the adiabatic mode evolution without causing significant reflection and scattering losses. In general, although a sufficient long coupler can ensure high coupling efficiency, more compact vertical couplers with $L > 30$ μm and $w_t \sim 200$ nm can also guarantee an adiabatic transition with high coupling efficiency.

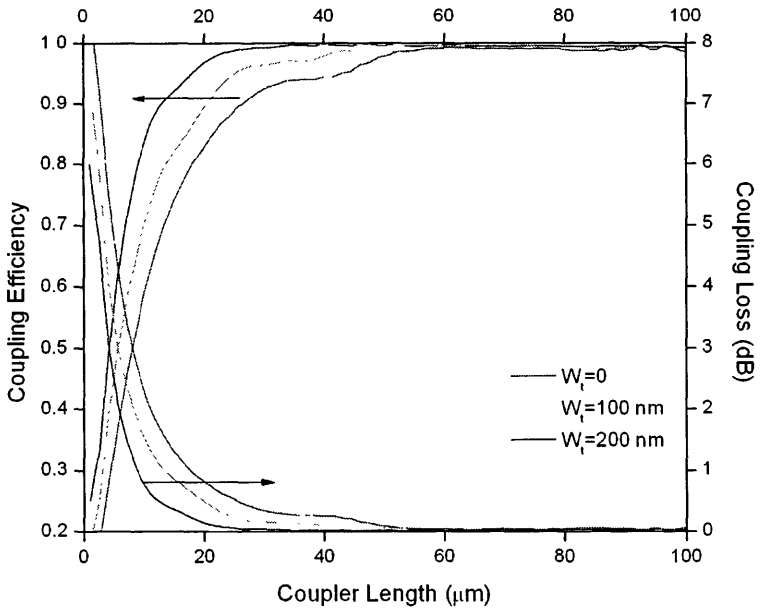

Figure 11.9. Coupling efficiency for various taper tip widths (wt) as a function of coupler length. The refractive index of the a-Si taper is fixed at 3.6.

Our test structures use finite tip widths of 200, 250, and 300 nm due to photolithography and other fabrication constraints. Coupler lengths were 30, 45, and 60 μm, resulting in 9 different coupler variations. The prototype devices were fabricated on 6 inch SOI substrates with 200 nm c-Si for the bottom waveguide and a 3 μm bottom oxide layer serving as the lower waveguide cladding. The bottom level SOI waveguide and the taper structures were defined using an ASML 5500/850 Deep UV Scanner and Applied Materials Centura silicon etcher. A 400 nm thick high-density plasma (HDP) PECVD SiO_2 interlayer was deposited and chemical-mechanically polished (CMP) to 200 nm. A 400 nm thick PECVD a-Si layer was deposited using an Applied Materials P5000 lamp heated PECVD chamber at 350 °C and CMP back to 200 nm forming the top waveguide material. The top a-Si waveguides were defined and fabricated with the same dimensions as the bottom SOI waveguides. Finally, another layer of 3 μm HDP PECVD SiO_2 was deposited as the waveguide top cladding (see Ref. 98 for more detail). An SEM image of the cross section of the vertical coupler is given in Figure 11.10.

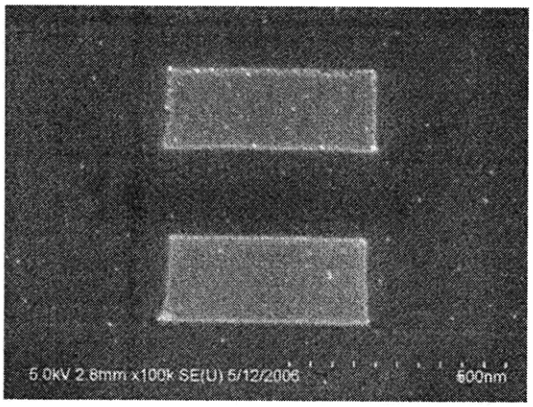

Figure 11.10. One cross-sectional SEM image of the vertical coupler. The bottom waveguide is SOI and the top waveguide is made of a-Si. The interlayer and cladding layers is SiO_2.

The loss values were derived using a design similar to the "paperclip" method. We designed a set of waveguides containing different numbers of cascading vertical couplers, while keeping the waveguide length constant. Under the same measurement conditions, the total coupling losses of these cascading vertical couplers are different and result in differences in their waveguide transmission. The vertical coupler loss can be derived from the slope of the linear fit for a transmission versus number of vertical couplers plot. The measurement results at 1550 nm are summarized in Table 11.1. The measurement uncertainty is mainly due to the fiber-to-waveguide coupling which we estimated to give an average 0.03 ~ 0.05 dB uncertainty to the coupling loss. Minimal coupling loss of ~ 0.20 ± 0.05 dB per coupler can be achieved with good consistency for 30 and 45 μm long devices. Although the simulations assumed total transparency in our waveguides and vertical couplers, the measured total coupling loss inevitably contains common waveguide transmission losses resulting from material bulk absorption and side wall roughness scattering. We measured different loss coefficients for test waveguides with different widths and expressed the loss coefficient as a function of width for both SOI and a-Si waveguides. We can alternatively derive the bulk absorption loss coefficient using the method described in Ref. 99. For example, for a 500 nm (w) × 200 nm (h) straight waveguide, the waveguide sidewall scattering loss

coefficients for both SOI and a-Si are measured to be 5.5 dB/cm for TE mode; the a-Si bulk absorption loss coefficient is measured to be 5.4 dB/cm [99].

We know that the sidewall roughness scattering loss coefficient is proportional to $|E|^2$ where E is the amplitude of electric-field at the sidewall interface. From E we can estimate the waveguide width dependence of the roughness scattering loss coefficient. Figure 11.11 is the simulated E-field amplitude at the outside of the sidewall interface as a function of waveguide width. Surprisingly, as waveguide width increases from 50 nm to 800 nm, the E-field amplitude first increases; reaches maximum around 300 nm; and decreases afterwards. This indicates that in an inverse taper with zero tip width, the change of taper transmission loss coefficients is not monotonic.

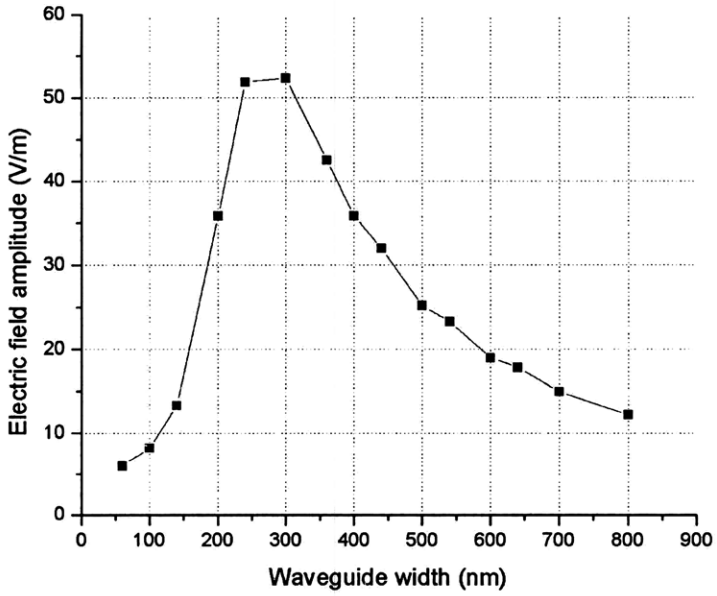

Figure 11.11. The simulated E-field amplitude at the outside of the sidewall interface as a function of waveguide width.

For inverse taper structures with tip width larger than 250 nm, based on Figure 11.10, we expect that as waveguide width decreases, side wall roughness scattering for TE mode will increase in both SOI and a-Si tapers, while bulk absorption loss will decrease in the a-Si taper

structure due to reduced confinement factor. The method we used to estimate these waveguide related losses is illustrated in Figure 11.12. Our previous simulations show our vertical couplers satisfy adiabatic conditions. Therefore reflection and scattering at the boundaries of each slice can be ignored. The measured total coupling loss and the calculated coupler transmission loss due to sidewall scattering and a-Si absorption are listed in Table 11.1 for comparison. From Table 11.1 it is clear that the small coupling loss contains a substantial contribution from waveguide transmission loss.

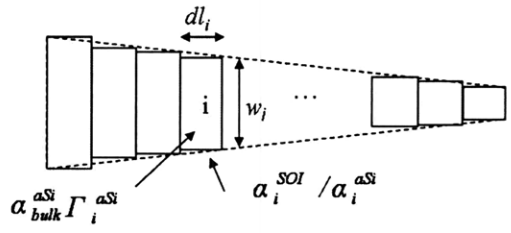

(a)

$$\textit{Total Waveguide Loss} = \textit{Scattering loss} + \textit{absorption loss}$$

$$= \underbrace{\int \alpha_i^{SOI} \cdot d\ell_i}_{\text{Sidewall scattering in SOI}} + \underbrace{\int \alpha_i^{aSi} \cdot d\ell_i}_{\text{Sidewall scattering in a-Si}} + \underbrace{\int \alpha_{bulk}^{aSi} \cdot \Gamma_i^{aSi} \cdot d\ell_i}_{\text{Bulk absorption in a-Si}}$$

(b)

Figure 11.12. (a) We estimate waveguide transmission loss by integrating sidewall roughness scattering and bulk absorption loss along taper structures; (b) corresponding mathematical formula, where l_i is the unit length at w_i, Γ_i^{aSi} is the confinement factor for a-Si at w_i, α_i^{SOI} and α_i^{aSi} are the sidewall scattering loss coefficients for SOI and a-Si at w_i, α_{bulk}^{aSi} is the bulk absorption coefficient for a-Si. While α_i and Γ_i is a function of w_i, α_{bulk} is constant for a-Si. Here, we assume SOI silicon does not have bulk absorption at 1550 nm, $\alpha_{bulk}^{SOI} = 0$.

Table 11.1. Measured total coupling loss, $\alpha(C)$, and simulated transmission loss, $\alpha(T)$, for the 9 different vertical couplers, e.g. α_{30} is the loss coefficient for 30 μm long coupler. The loss is given in dB.

L (μm) / w_t (nm)	Measured α_{30} (C)	Simulated α_{30} (T)	Measured α_{45} (C)	Simulated α_{45} (T)	Measured α_{60} (C)	Simulated α_{60} (T)
200	0.23 ± 0.05	0.10	0.29 ± 0.03	0.15	0.45 ± 0.06	0.22
250	0.24 ± 0.05	0.08	0.26 ± 0.03	0.12	0.39 ± 0.06	0.15
300	0.20 ± 0.05	0.07	0.21 ± 0.03	0.10	0.30 ± 0.06	0.13

The difference between measured total coupling loss and simulated transmission loss, $\alpha(C) - \alpha(T)$, captures the intrinsic coupling loss as well as the scattering loss at taper tips during entry and exit. Because Figure 11.8(b) suggests that the intrinsic coupling loss is very small, the majority of this difference must be related to taper tip scattering and other fabrication imperfection. Derived from our experiments, the following HIC vertical coupler design rules are evident:

1. Design trade-offs for taper length L.
    a. A taper has to be long enough to satisfy the adiabatic condition;
    b. A longer taper introduces higher transmission loss;
    c. A longer taper requires larger footprint.
2. Design trade-offs for tip width w_t.
    a. A small wt increases taper sidewall roughness scattering;
    b. A large wt increases the effective index discontinuity at the taper entries, thus increasing the scattering loss when the optical mode enters and exits vertical coupler.

11.2.3. Broadband performance: butt-coupled Ge photodetectors

The butt-coupled GeSi photodetectors are fabricated with integrated vertical couplers based on both the conventional vertical directional coupler and the inverse taper vertical coupler design. The rest processes are identical for both cases. The light couples from the SOI waveguide to the a-Si waveguide, and then reaches the GeSi photodetector. Figure 11.13 shows the two GeSi photodetector responsivity spectra. While the vertical directional coupler only offers efficient coupling at around 1520 nm, our inverse taper vertical coupler achieves high efficiency coupling in a much broader wavelength range of 1470-1570 nm, as manifested by the significantly

improved responsivity in a 100 nm-wide spectral range. Detailed discussion about the photodetector can be found in Ref. 98 and100.

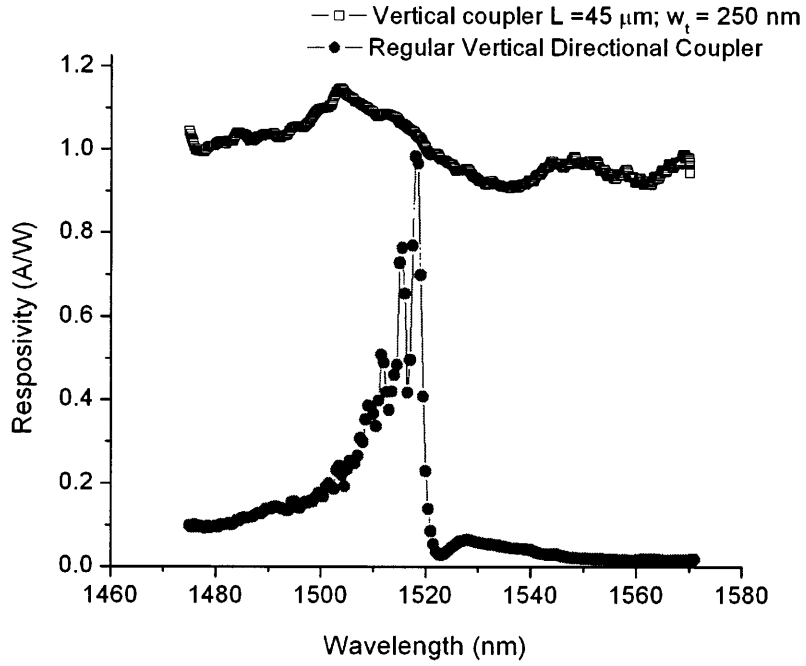

Figure 11.13. GeSi photodetector responsivity comparison showing improved broadband detection using the inverse taper vertical coupler design as oppose to regular vertical directional coupler design.

11.3. Summary

In this chapter, we have analyzed two vertical waveguide couplers based on conventional vertical directional coupler design and inverse taper vertical coupler design. For vertical coupler consists of two different waveguide materials, we have found that the inverse taper vertical coupler design can ensure optical impedance matching conditions and tolerant a wide range of design and fabrication variations. For small refractive index differences in the c-Si/a-Si vertical coupler, high coupling efficiency can be obtained using non-zero tip width inverse taper structures. For small coupler lengths, a large tip width can ensure adiabatic mode evolution without causing significant loss due to reflection and scattering. Experimentally, we have achieved consistently low coupling loss of 0.20 ± 0.05 dB in our prototype devices. Our vertical waveguide coupler has been

successfully adopted in device applications, and it is promising for future 3D photonic and electronic-photonic integration.

Chapter 12. Slot waveguide based couplers and polarization rotators

12.1. Overview

Being able to realize high optical confinement in ultra-thin low index slots, slot waveguide is unique and very promising for many applications as we have discussed in previous chapters. Horizontal slot waveguide configuration can enable low loss optical transmission in slot waveguides; however, it could still have higher loss than regular SOI channel waveguides. One way to utilize slot waveguide's unique properties and to avoid high optical insertion loss is to integrate slot waveguide structure only where its functionality is needed and to use low loss channel waveguides for global signal transporting and routing. In order to achieve low insertion loss, a low loss coupler between slot waveguide and channel waveguide is indispensable.

Direct butt-coupled slot waveguides with channel waveguides will result in high coupling loss because there are (1) effective index mismatch. Since a large portion of the optical field is concentrated inside the low-index slot regions, the effective index of the slot waveguide is much lower than the channel waveguide with high index core. Direction coupling will result in large reflection loss at the interfaces of two different waveguides. (2) Mode size mismatch. Slot waveguide modes, concentrated in low index slots, are normally smaller than channel waveguide modes. (3) Mode shape mismatch. Slot waveguide modes are very complicated and non-Gaussian-like, while channel waveguide modes resemble a Gaussian distribution of the confined optical power.

In the following chapter, two types of waveguide couplers are proposed to transform the optical power between vertical/horizontal slot waveguides and channel waveguides with minimal

theoretical coupling losses. In addition, a polarization rotator is also proposed to realize low loss transformation of the fundamental slot modes between the vertical and horizontal slot waveguides.

12.2. Vertical-slot-to-channel waveguide couplers

Low loss waveguide couplers based on complementary taper pairs are proposed to realize lossless optical power transfer between channel waveguides and vertical slot waveguides as illustrated in Figure 12.1.

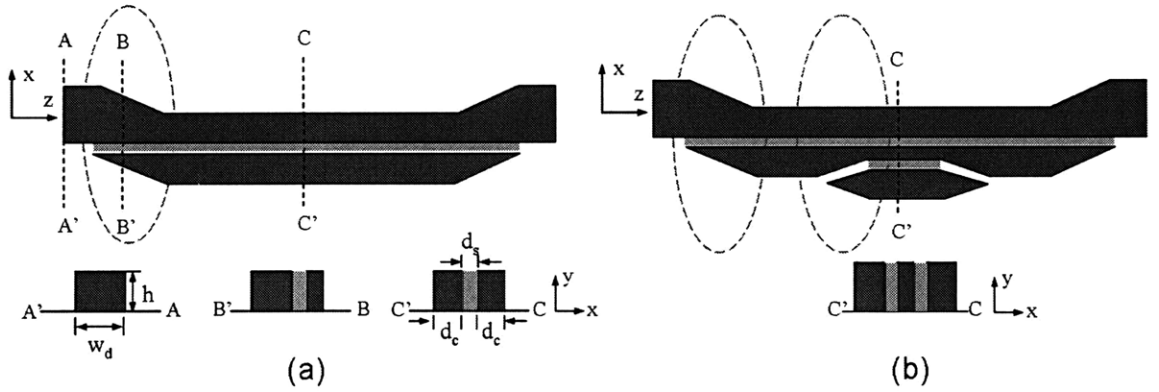

Figure 12.1. Schematics of the proposed (a) single- and (b) double-slot waveguide couplers. The dashed circles highlight the location of the couplers. (Drawing is not to the scale)

The complementary taper pair uses the push-pull scheme and adiabatically pushes the field out from the upper high-index region to the lower high-index region. To avoid perturbation of the optical field in the center of the waveguide where the field intensity is the strongest, thus avoiding high scattering loss, the proposed coupler enhances the evanescent tail of the original Gaussian-like mode and gradually transforms it to that of a slot waveguide. This adiabatic transforming process can be clearly observed through the field evolution demonstrated in Figure 12.2, where a strip silicon waveguide to single and double slot coupler has been simulated. The simulation is carried out by using a finite-difference beam propagation code [101]. The structure also demonstrates the inverse process of double to single slot and strip waveguide transforming. It is shown that the coupler proposed here is really reciprocal even for a multiple-slot coupler.

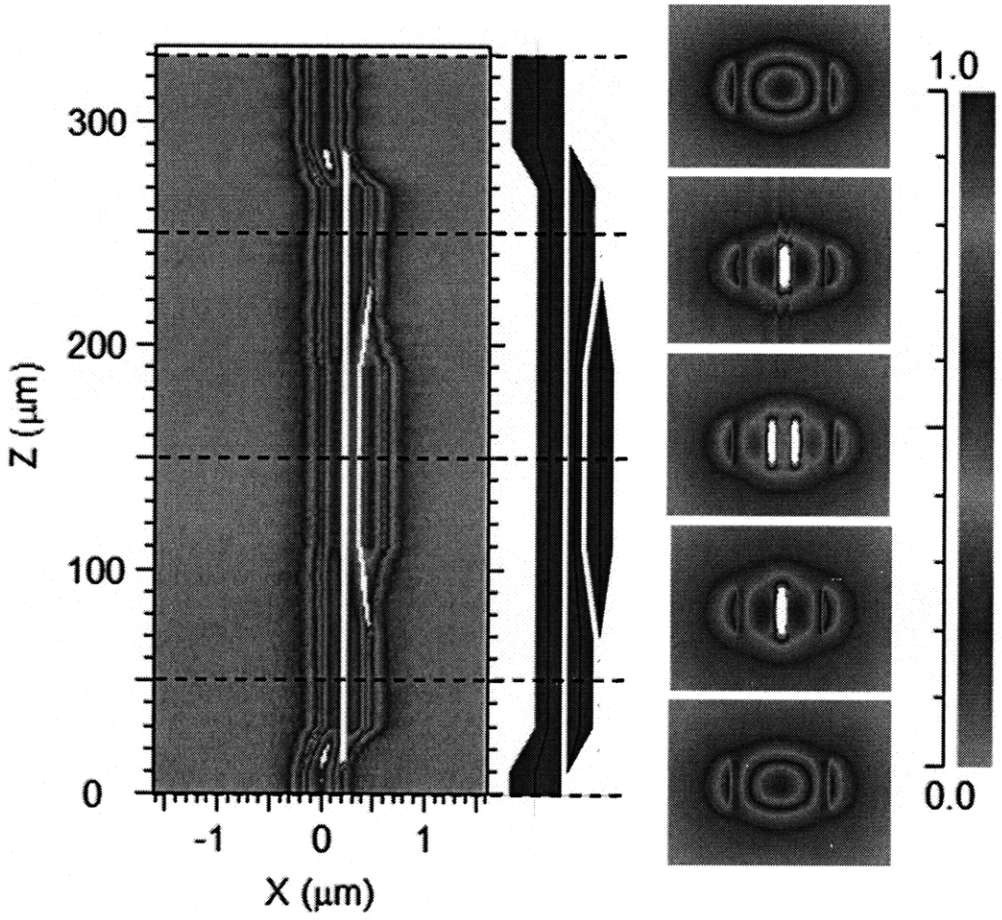

Figure 12.2. The Field evolution of a silicon waveguide to single and double slot waveguide coupler. The white slot represents the highest filed intensity in BeamProp software.

In reality, the coupler itself has loss due to waveguide transmission loss. However because the coupler does not require the phase matching condition as for the traditional directional coupler, this loss does not affect the coupling. In our simulation, we only consider the linear tapers with no waveguide loss.

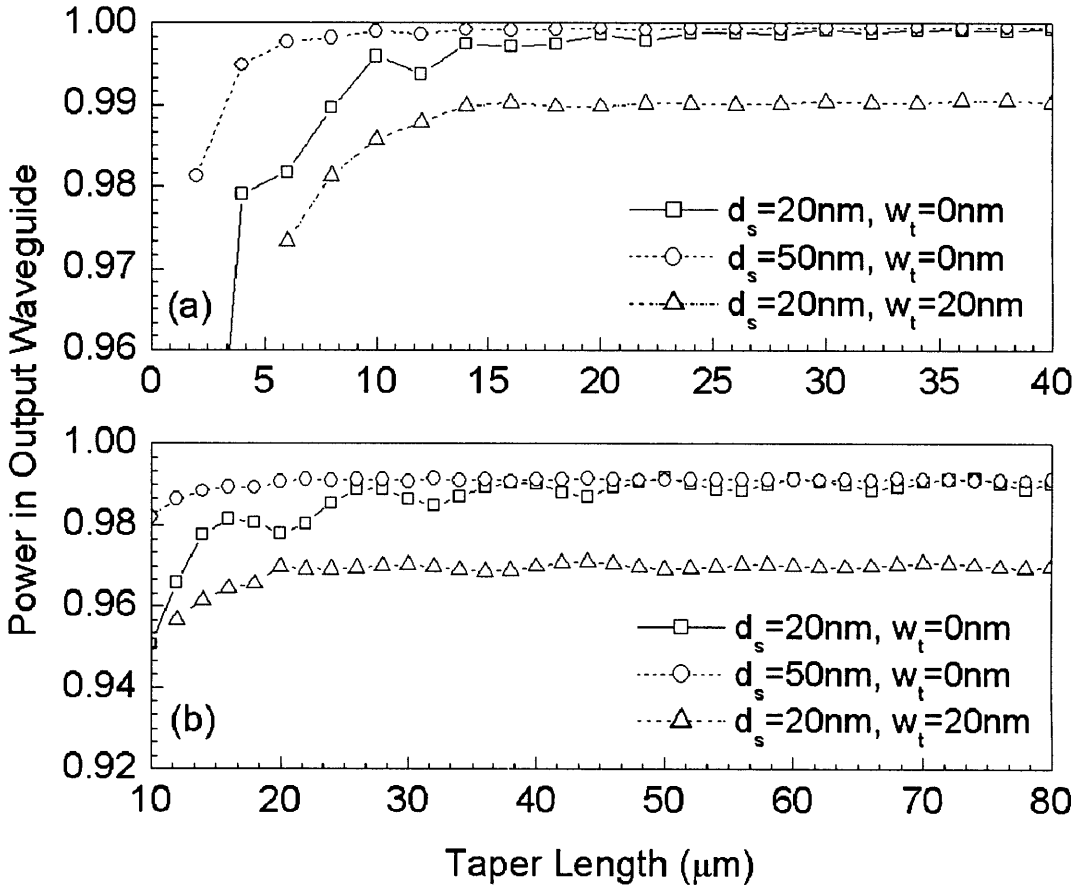

Figure 12.3. The taper designs for the (a) single- and (b) double-slot waveguide transformers with two different slot widths, d_s, of 50 nm and 20 nm, respectively.

In Figure 12.3, we show design examples of channel waveguide to single- and double-slot waveguide couplers both consist of Si and SiO_2 (n_{Si} = 3.50, n_{SiO2} = 1.46). The structures with channel-slot-channel waveguide coupler pairs shown in Figure 12.1 have been simulated. The total power after passing through the whole structure is shown as a function of taper length for two different slot widths d_s = 50 nm and 20 nm, respectively. It is found that for the single-slot coupler, a taper length of 20 μm and 40 μm will ensure more than 99.5% and 99.8%, respectively, of remaining power in the output silicon waveguide, which corresponding to less than 0.01 dB and 0.004 dB, respectively, of insertion losses for one-trip coupler (the structure involves one forward and one backward couplers). It also indicates that the smaller the slot width is, the less the

conversion loss will be. For double-slot coupler, two stages of complementary taper pairs are used to accomplish the transforming from single to double slot waveguides. Fixing the length of the first stage of tapers at 20 μm, it is found that with a taper length about 40 μm for the second stage of tapers, the total insertion loss for the one-trip coupler (silicon to double slot) is less than 0.02 dB. It is noticed that the insertion loss involving the slot waveguide with a 50 nm wide slot shows a little oscillation with short taper length. The mode mismatching causes the mode beating between the two slots and in turn leads to the field fluctuation in the output waveguide. This fluctuation diminishes when the taper length increases or when the slot width decreases to 20 nm. To study the sensitivity of the proposed waveguide couplers design, we also performed simulations considering the non-ideal tapers (with finite taper tip width w_t) due to limited fabrication resolution and the results are plotted in Figure 12.3. A non-zero taper tip width leads to a reduced transmission power due to the unwanted power scattering at the none-zero taper tips. According to our simulations, with a 20 nm taper tip width, the power transmissions for 20 nm wide optimized single- and double- slot waveguide couplers decrease slightly from 99.8% and 99% to 99% and 97%, respectively. With a finite taper tip width, the coupler generally requires a little longer taper in order to achieve a stable, high transforming efficiency. Our further study shows that, for a 50 nm wide slot-coupler even with a 50 nm taper tip width, 95% (0.025 dB) coupling efficiency can be achieved. The proposed waveguide couplers are readily to be fabricated by the state-of-the-art E-beam lithography [102].

In Figure 12.4, we show the wavelength dependence of a double slot waveguide coupler. In the simulation, we select the taper lengths for the first and the second stage tapers to be 20 and 40 μm, respectively. Over a 400 nm wide wavelength range, the insertion loss change per coupler is less than 0.02dB. The proposed coupler is weakly sensitive to wavelength.

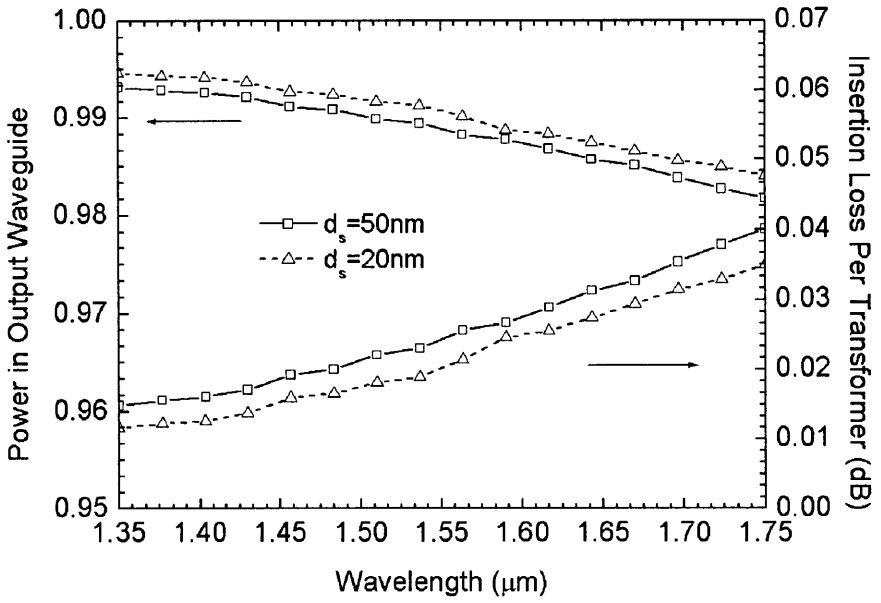

Figure 12.4. Simulated wavelength dependence of the optimal double slot waveguide transformer with two different slot widths, d_s, of 20 nm and 50 nm. The taper lengths for the first and the second stage tapers of this transformer are 20 and 40 μm, respectively.

12.3. Horizontal-slot-to-channel waveguide couplers

Single and multiple horizontal slot waveguides have been previously proposed and demonstrated to realize low loss optical transmission and enhance optical confinement. The horizontal slot waveguides are more favorable in applications where low optical loss and extremely thin slot layers are mandated, such as in an electrically pumped SiO_2:Er silicon light emitter [103]. A possible scenario using horizontal slot coupler is shown in Figure 12.5. Ideally, low loss transformation between the fundamental slot mode of the horizontal slot waveguide and the fundamental TE-mode of the channel waveguide is desired.

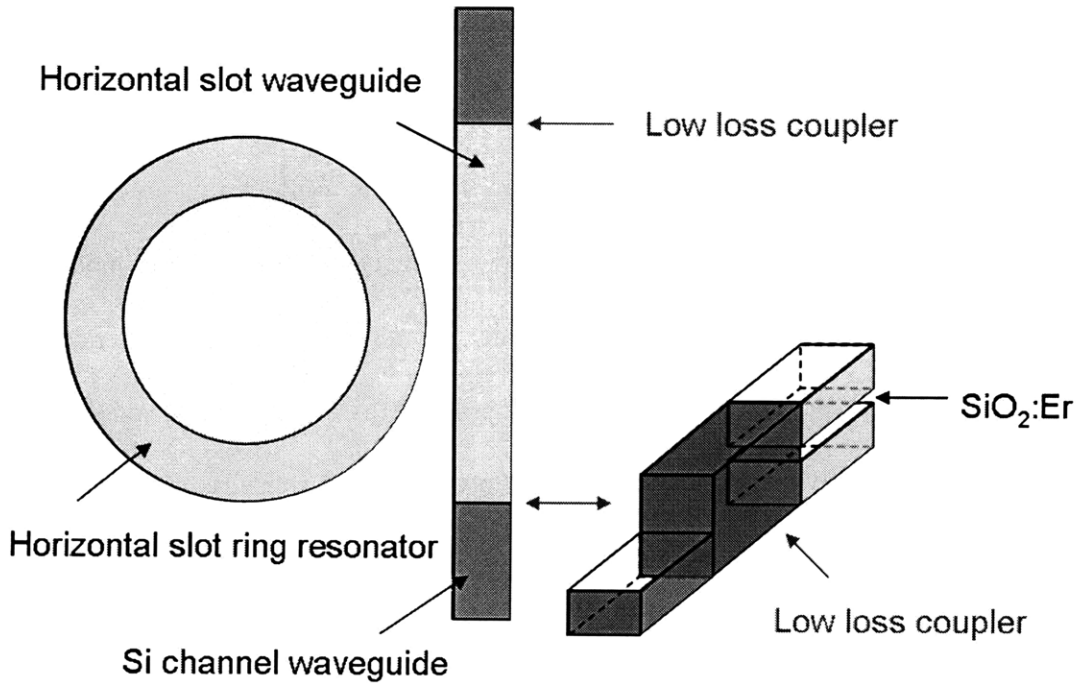

Figure 12.5. Schematics of a horizontal slot ring resonator with SiO_2: Er thin slot, coupled with silicon channel waveguides using a low loss horizontal-slot-to-channel waveguide coupler (denoted as the red "box" bridging the two types of waveguides) (drawing is not to the scale).

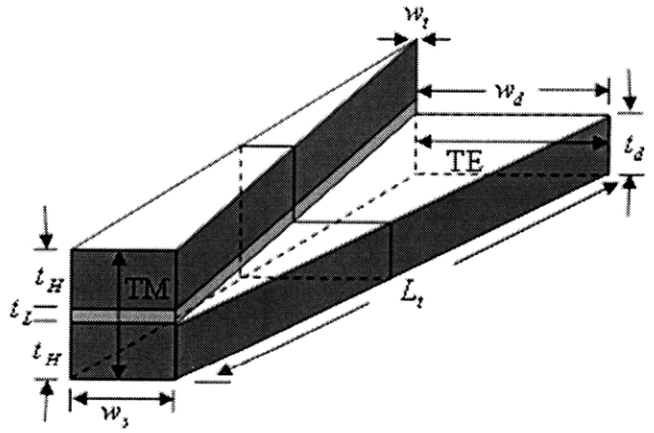

Figure 12.6. Schematics of a horizontal-slot-to-channel waveguide coupler (drawing is not to the scale).

Schematics of the proposed mode couplers are shown in Figure 12.6. It shows a mode-evolution-based mode coupler for a horizontal slot waveguide to a channel waveguide. A polarization rotator based on similar structure for channel waveguides has already been demonstrated [104]. The structural parameters are designed to be: $t_H = 200$ nm, $t_L = 20$ and 60

nm, $w_s = 230$ nm, $w_d = 330$ nm, $t_d = 200$ nm, $w_H = 200$ nm, and $w_L = 20$ and 60nm. The refractive indices of the high-index Si and low-index SiO_2 are $n_H = 3.50$ and $n_L = 1.46$, respectively, and the entire structure is cladded by the SiO_2. With the parameter settings, the fundamental mode of the horizontal slot waveguide is the quasi-TM mode with the non-Gaussian-like mode profile. The structure consists of one low-index SiO_2 thin layer vertically sandwiched by two high-index Si layers. The two top layers (Si + SiO_2 layers) and the one bottom Si layer are asymmetrically and oppositely tapered to gradually form a structural transition from a horizontal slotted waveguide to a strip waveguide as shown in Figure 12.6. The principle axis of the structure and the polarization states of the fundamental mode rotate in unison along the transition. The performance of the structure is analyzed through the eigenmode expansion (EME) approach. The EME approach has been used and demonstrated to be a very efficient and accurate approach for mode-evolution-based devices and can produce comparable results to the FDTD approach [104].

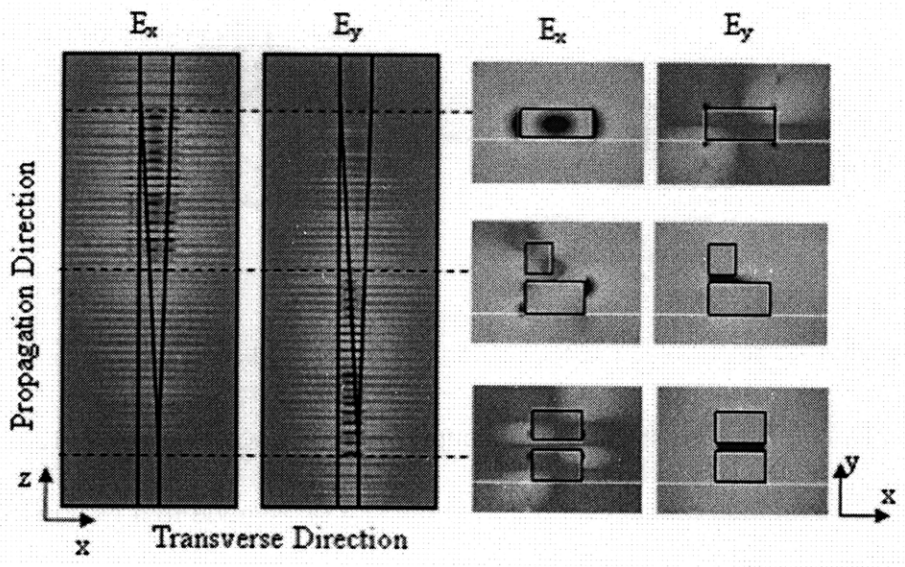

Figure 12.7. Field evolution of the horizontal-slot-to-channel waveguide couplers simulated using FIMMWave.

The modal field evolutions along the propagation axis of the structure are plotted in Figure 12.7. The structure is excited by the fundamental TE-polarized mode of the slot waveguide (shown in the cross-sectional view of the right panel). Gradually interacting with the structure, the E_y component of the mode quickly gets suppressed while the E_x component gets enhanced. With sufficiently long taper, a complete power transition from an E_y-dominant slotted waveguide mode to an E_x-dominant strip waveguide mode can be accomplished.

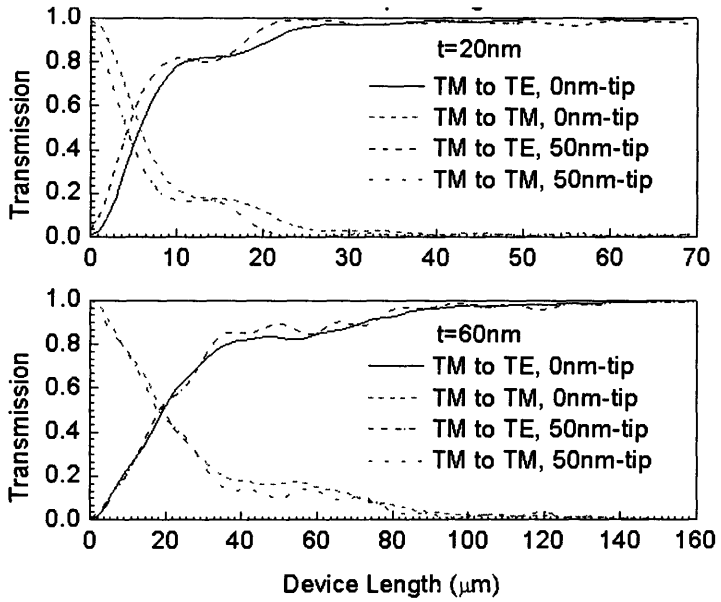

Figure 12.8. Simulated transmissions of the horizontal-slot-to-channel waveguide couplers with different slot thicknesses versus device length.

The power transmissions as a function of the device length are shown in Figure 12.8 for a wavelength of 1.55 μm. The results indicate that the power lost from the fundamental TE-polarized slot waveguide mode is directly transferred to the fundamental TE-polarized channel waveguide mode. For a horizontal slot waveguide with 20 nm thick SiO_2 slot layer, a complete polarization rotation can be achieved with a merely 50 μm long coupler. Longer coupling length is necessary for slot waveguides with much thicker slot layer, for example, it is found that a coupling length of 140 μm is required for $t_L = 60$ nm. To demonstrate the robustness of our design, we also

performed simulations considering non-ideal tapers with finite tip width $w_t = 50\,\text{nm}$ caused by the limited fabrication resolution. The results are also plotted in Figure 12.8. As expected, the power transmission exhibits some oscillations attributable to the weak resonance caused by the residual reflection at the non-ideal taper tip. It is interesting to find that with finite tip width, it is possible to accomplish polarization rotation with shorter device length. For instance, only 25 μm and 98 μm long devices are needed for structures with slot layer thicknesses of 20 nm and 60 nm, respectively, to ensure more than 99% power transformation.

12.4. Horizontal-to-vertical-slot waveguide polarization rotator

By cascading the two couplers shown in previous two sections, we can obtain a horizontal-to-vertical-slot waveguide polarization rotator as shown in Figure 12.9.

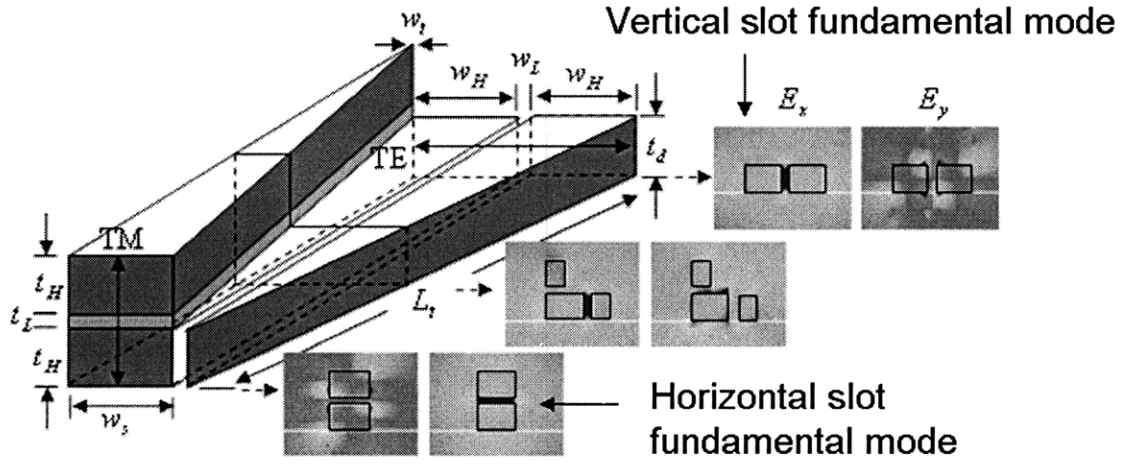

Figure 12.9. Schematics of the presented horizontal-to-vertical-slot waveguide polarization rotator and the mode profiles at various locations inside.

It is similar to the one shown in Figure 12.6 except that a low-index gap (slot) is cut along the propagation direction to form a vertically oriented slotted waveguide at the end. The cross-sectional views of the modal field evolution are plotted at different locations. They clearly illustrate the polarization state rotating process of the modal fields along the propagation direction.

The power transmissions for the structures with two slot thicknesses are plotted versus the device length in Figure 12.10.

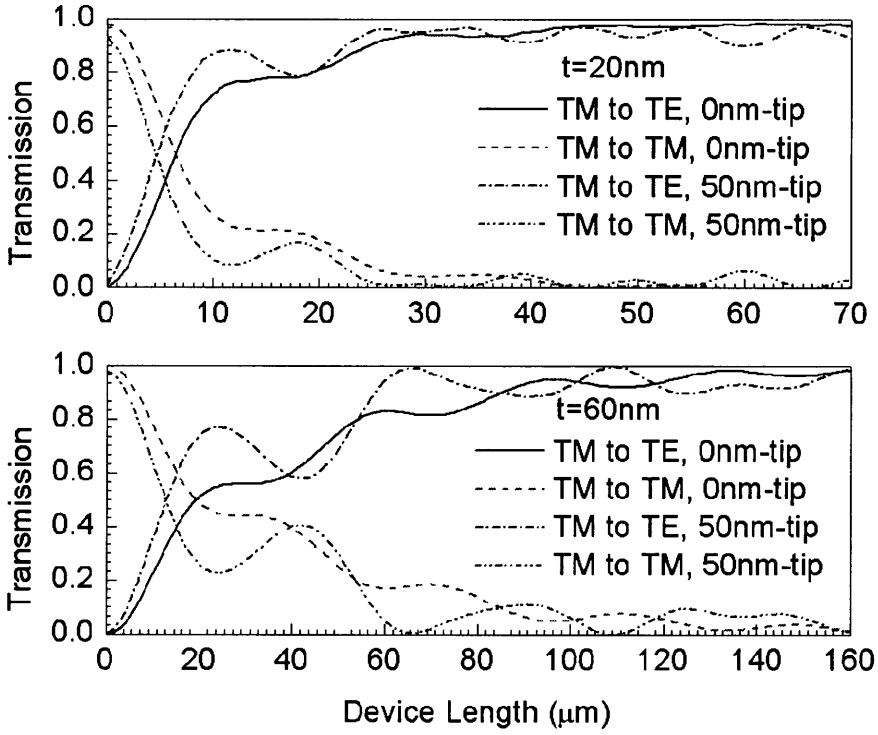

Figure 12.10. Simulated transmissions of the horizontal-to-vertical-slot waveguide polarization rotator with different slot thicknesses versus device length.

The device can realize a nearly perfect polarization rotation and transformation with a comparable device length to the slot-to-channel waveguide couplers discussed in previous two sections with minimal loss of 0.05 dB. The transmissions of the structure with the non-ideal taper exhibit much large oscillation due to the complexity of the structure. The oscillations tend to be smoothed out with the increase of device length. The internal resonance is so strong that it is possible to obtain a complete power transferring between the two polarized states with much shorter device length. With 50 nm taper tip width, the minimum device length can be as small as 32 μm and 65 μm for devices with slot layer thicknesses of 20 nm and 60 nm, respectively. Increasing the tip width can further decrease the minimum device length at the price of reducing bandwidth resulting from the stronger resonance. For a wideband application, longer device length is

preferable due to weakened resonance caused by the non-ideal taper tip. According to our simulation, the power transmissions for the devices with 60 μm and 140 μm long tapers with 20 nm and 60 nm thick slots, respectively, exhibit extremely flat response over a wavelength range of 1.45-1.65 μm.

12.5. Summary

In this chapter, two slot-to-channel waveguide couplers and horizontal-to-vertical slot waveguide polarization rotator are proposed and analyzed. The devices are designed to convert optical modes between channel waveguide and slot waveguide modes as well as the mode transforming between horizontal and vertical slotted waveguides. Numerical simulation results show that complete mode transformations and polarization rotations can be achieved within tens of micrometers with minimal loss. The designs are very robust and the devices perform very well even with non-zero taper tip width.

Chapter 13. Athermal waveguides

13.1. Overview

Thermo-optical (TO) effect describe the phenomenon that material's refractive index changes as temperature changes. This is caused by changes in both polarizability and density (expansion or contraction) due to temperature. For most semiconductors and dielectrics that are optical waveguide materials, the TO coefficients are positive, meaning their refractive indices increase as temperature increases. For resonators, MZI narrow band filters, directional couplers, and gratings, their resonant wavelengths shift to longer wavelengths as temperature increases. For the Dense Wavelength Division Multiplex (DWDM) applications, such as in Arrayed Waveguide Grating modules (AWG) where many channels are closely spaced, this may cause channel cross-talks. They require constant temperature control by integrating resistor heaters to ensure stability in the optical properties of the wavelengths being combined or split. Constant heating is not desired because the power required for tuning large scale integrated photonic with thousands of filter devices is prohibitive. For photonic-electronic integrated circuits, the heat dissipation from electronics can affect photonic devices as well and is very hard to compensate. Athermal devices are the key to realize low power consumption, temperature insensitive operations.

Early work on athermal, low index contrast systems, such as planar lightwave circuit (PLC), involves using polymers with negative TO coefficients [105] and thermo-elastic effect [106] to compensate for the positive TO coefficient of the devices. The typical TO coefficients, strain-optical coefficients, and thermal expansion coefficients (CTE) for common CMOS waveguide materials are summarized in Table 13.1.

Table 13.1. TO coefficients, strain-optic coefficients, and thermal expansion coefficients for CMOS compatible waveguide materials [105].

	TO coefficient (K^{-1})	Strain-optic coefficient	CTE (K^{-1})
SiO_2, SiN, SiON	10^{-5}	-0.4	$\sim 0.6 \times 10^{-6}$
c-Si and a-Si	$\sim 2 \times 10^{-4}$	> 0	$\sim 2.6 \times 10^{-6}$
Polymer (PMMA, PI)	$-10^{-4} \sim -4 \times 10^{-4}$	Not available	$\sim 6.8 \times 10^{-5}$

13.2. Athermal silicon channel waveguides

For high index contrast silicon waveguides, the strain effect is too weak to provide enough negative index compensation for the positive index change in Si waveguide core [107]. Due to the high optical confinement in Si waveguide core, regular polymers, such as PMMA and Polyimide, also do not have large enough negative TO coefficients to achieve athermal condition if used as the cladding layers. Polymer cladding layers with large negative TO coefficients, on the order of 10^{-3} K^{-1}, are needed.

Because Si waveguides are sitting at the SiO_2 undercladding layer, the polymer top cladding can only cover three sides of the Si waveguides. The resulting cross section of the waveguide device looks like in Figure 13.1.

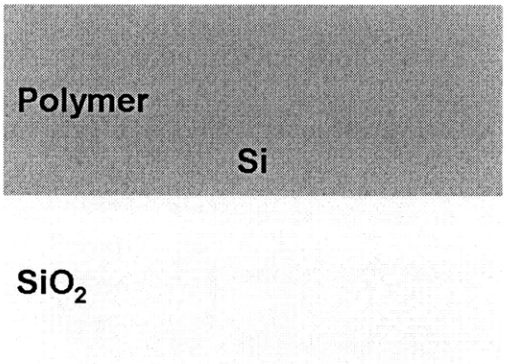

Figure 13.1. Schematic of the cross sectional of a Si waveguide core cladded with polymer

Athermal condition can be achieved because the confinement factor, Γ, of the c-Si waveguide core is not 100%. There is still optical power in the cladding layer. The overall effective index can be approximated using the power weighted indices of the waveguide core and cladding layer, n_c and n_{cl}. For waveguide configuration like in Figure 13.1, without knowing any

waveguide geometry, a generic empirical equation for the athermal condition has been derived as determined solely by n_c, n_{cl}, and Γ [108]:

$$\frac{dn_{cl}}{dT} - (A\frac{dn_c}{dT} + B)\Gamma^2 + (C\frac{dn_c}{dT} + D)\Gamma + E\frac{dn_c}{dT} + F = 0 \qquad (13.1)$$

where $A = -4.854065 \times 10^{1}$

$B = -2.169000 \times 10^{-5}$

$C = 5.206713 \times 10^{1}$

$D = 2.326577 \times 10^{-5}$

$E = -1.589253 \times 10^{1}$

$F = 4.575161 \times 10^{-6}$.

The right hand side of Equation 13.1 represents the overall effective index of the waveguide, $\frac{dn_{eff}}{dT}$ has no temperature dependence, thus equals to 0. Figure 13.2 summarizes the confinement factors that are required to achieve athermal condition, $\frac{dn_{eff}}{dT} = 0$, under different combinations of $\frac{dn_{cl}}{dT}$ and $\frac{dn_c}{dT}$. Any deviation above the lines results in positive $\frac{dn_{eff}}{dT}$; and below the lines, negative $\frac{dn_{eff}}{dT}$.

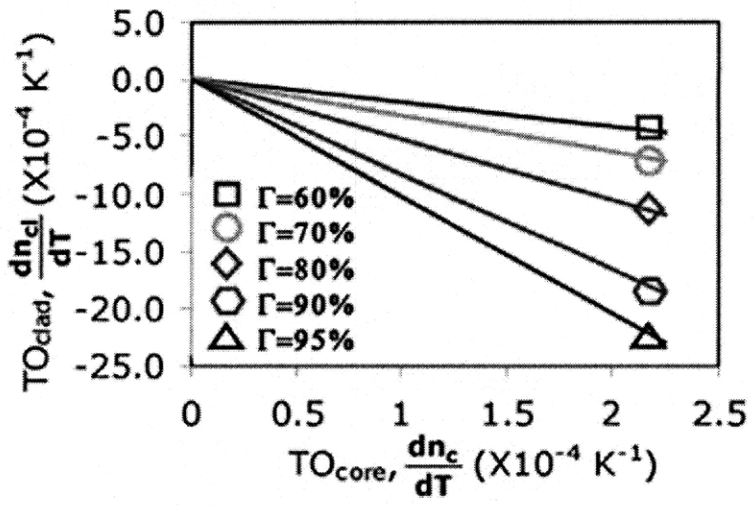

Figure 13.2. Athermal conditions for channel waveguides. The lines represent the exact confinement factors that are required to achieve athermal condition for different combinations of the TO coefficients of the cladding layer and the waveguide core. (Figure taken from Ref. 108)

For a single mode c-Si waveguide, the confinement factor for the TE-mode is ~ 80% and $\frac{dn_c}{dT}$ is ~ 2×10^{-4} K^{-1}. This means we need polymers with $\frac{dn_{cl}}{dT}$ of at least -10^{-3} K^{-1}. DuPont's polymers C1 and E1 are specially designed polymer with excellent transparency at 1550 nm and large negative TO coefficients, ideal for Si waveguide's athermal design. Figure 13.3 shows the refractive index change with respect to temperature for polymers C1 and E1. Their TO coefficients are also derived and summarized in Table 13.2. The measurements are done using ellipsometry with 632 nm laser. The assumption here is that the TO coefficients will not change significantly at 1550 nm.

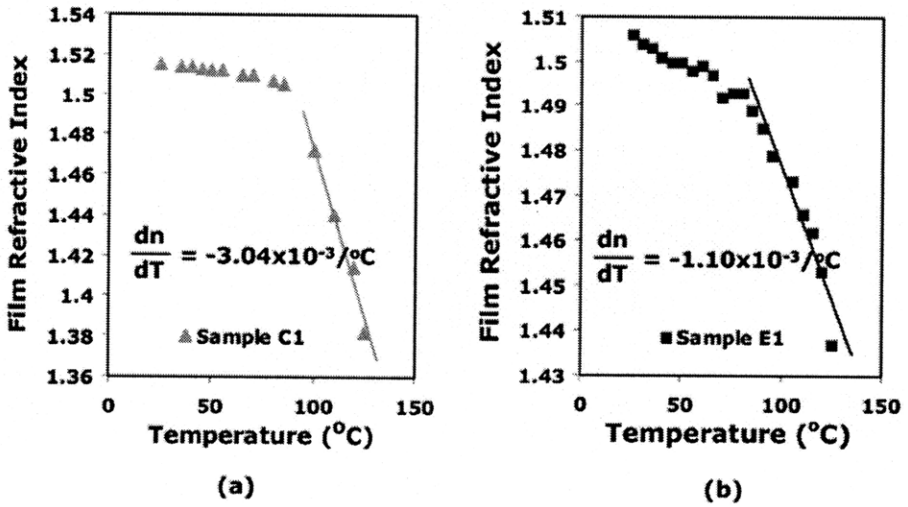

Figure 13.3. Measured temperature dependence of the refractive indices for polymer (a) C1 and (b) E1 (Figure taken from Ref. 108).

Table 13.2. Refractive indices, n_R, TO coefficients, and glass transmission temperatures, T_g, of C1 and E1.The TO coefficients are derived at high temperature regions between 100 °C and 150 °C.

DuPont polymer	Polymer class	n_R at 20 °C at 1550 nm	TO coefficient (K^{-1})	T_g (°C)
C1	Acrylate	1.52	-3.0×10^{-3}	70
E1	Acrylate	1.51	-1.1×10^{-3}	60

Because resonator's resonance wavelength is very sensitive to any effective index variation, we use racetrack resonators to demonstrate the athermal design using polymer cladding layer. The polymer coating and curing processes are done at DuPont. Polymer C1 is used with the a-Si racetrack resonators fabricated at MIT. The a-Si channel waveguide has a cross section of 700 nm × 100 nm ($w \times h$). The racetrack is 100 μm long; the bend radius is 100 μm; and the resonator-bus coupling gap is 500 nm. The effective index for the TE-mode, assuming SiO_2 top cladding layer, is calculated to be 2.13 and the confinement factor is 0.767.

With SiO_2 top cladding layer, the resonance wavelength as a function of temperature is measured and shown in Figure 13.4(a). The large fringes are Fabry-Perot resonances from the bus waveguide front and end facets. We can plot the resonance wavelength as a function of

temperature and derive the overall TO coefficient from the slope of the linear fit as shown in Figure 13.4(b). The TO coefficient is measured to be 84.73 pm/K.

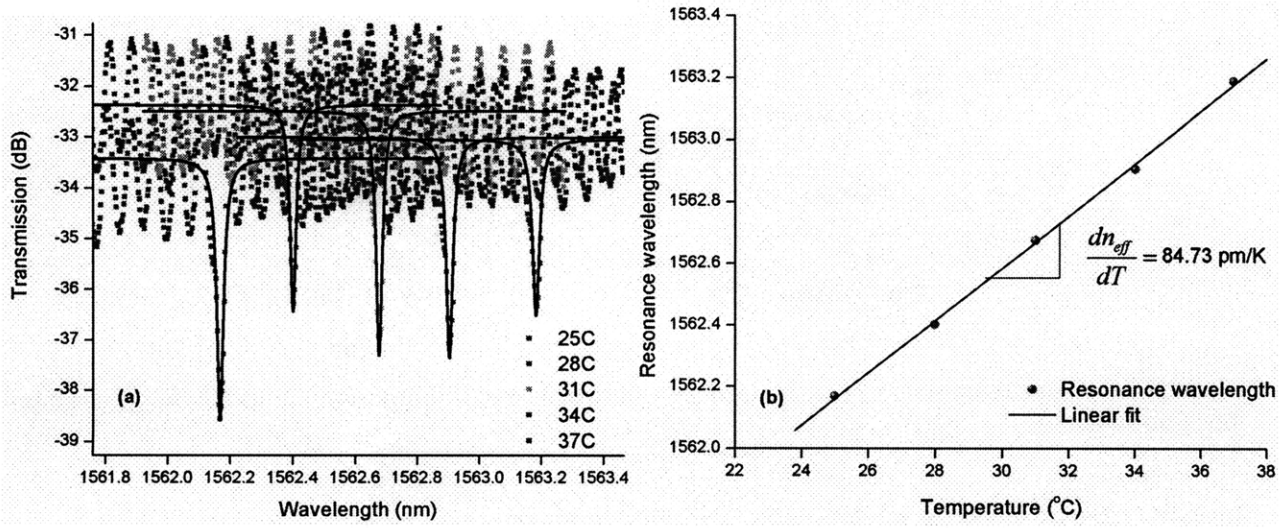

Figure 13.4. (a) Resonance wavelengths at different temperatures. The black lines are corresponding Lorentzian fits of each resonance; (b) Resonance wavelength vs. Temperature. The TO coefficient is derived to be 84.73 pm/K.

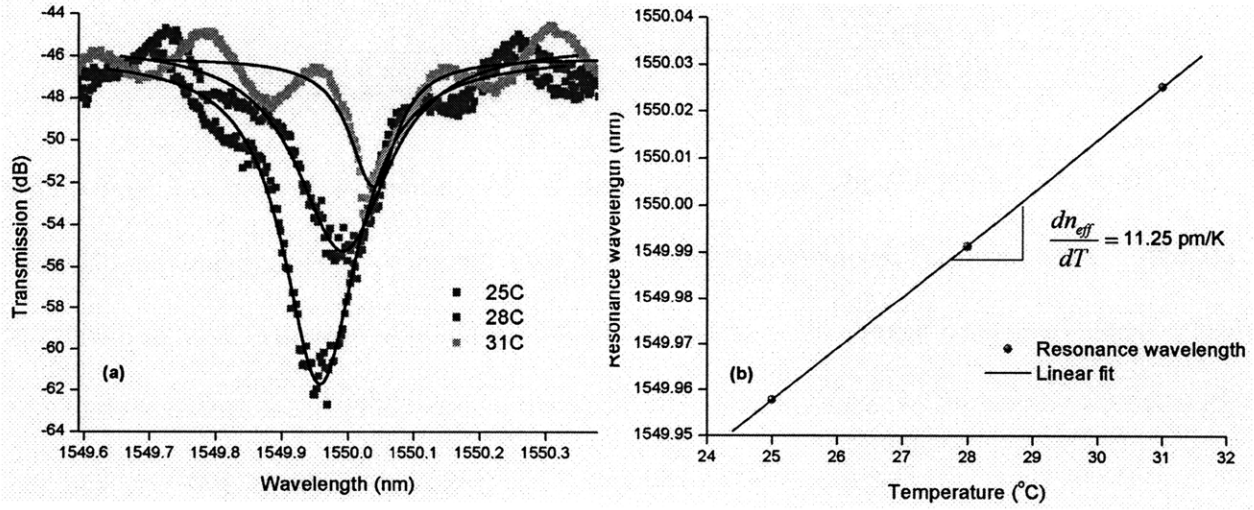

Figure 13.5. (a) Resonance wavelengths at different temperatures. The black lines are corresponding Lorentzian fits of each resonance; (b) Resonance wavelength vs. Temperature. The TO coefficient is derived to be 11.25 pm/K.

When the same racetrack resonator is cladded with polymer C1 and measured under different temperatures, the corresponding resonance spectra change as shown in Figure 13.5. We have achieved a reduced TO coefficient of 11.25 pm/K.

Noticeably, the extinction ratio of the resonance peak is affected by the index change introduced by the polymer cladding. For the straight racetrack close to the bus waveguide, the effective index is different from the rest of the more isolated resonator, the coupling between the resonator and the bus waveguide becomes temperature dependent. This can be eliminated by using ring resonators for reduced coupling length.

Because the waveguide geometry has not yet optimized for this specific polymer, we do not have zero TO coefficient. Also, the large negative TO coefficients for DuPont polymers in Table 13.2 are obtained above 100 ^{o}C beyond their glass transition temperatures, while the temperature variation measurements are done at relatively low temperatures under 50 ^{o}C, the corresponding TO coefficient should be much lower than 10^{-3} K^{-1}.

13.3. Summary

We have demonstrated a minimum TO coefficient of 11.25 pm/K in a-Si racetrack resonators and have shown the effectiveness and feasibility of using large negative TO coefficient polymer to compensate the large positive TO effect in Si channel waveguides.

(This page is intentionally left blank)

Chapter 14. Conclusions and future directions

Silicon-based optical interconnect technology, yet promising, is still in its infancy. We need to overcome many challenges before we can make silicon photonics a viable and mature technology. Among those challenges, low loss passive photonic components, such as waveguides, couplers, splitters, filters, and polarization rotators etc., are indispensable. This thesis has advanced the development of novel materials, processes, and designs of passive optical waveguides and couplers towards the goal of realizing electronic-photonic integration on silicon. The chapter-by-chapter review and future directions are summarized as follows.

14.1. Chapter-by-Chapter conclusions

In Chapter 1, I have reviewed the current challenge of increasing RC time constant in Cu interconnect technology and the benefit of using photons as information carriers on chip. Towards realizing optical interconnects on chip, this thesis work is motivated by the importance of passive photonic components, such as waveguides and couplers. Challenges in making low loss, high performance are reviewed and possible paths are identified.

In Chapter 2, I have briefly reviewed the optical waveguides materials, guiding mechanisms, different waveguide forms, and optical modes. The concepts and terminologies introduced in this chapter are essential for understanding the works in this thesis. Among all the variations an optical waveguide can have, we focus on single mode, silicon-based channel waveguides for its highest optical confinement and CMOS-compatibility.

In Chapter 3, I have briefly discussed the simulation methodologies that have been used in this thesis. FDTD is based on time-domain and it is the most accurate method for simulating EM

waves in any arbitrary structures but it is also the most time and memory consuming method. In frequency-domain, FEM is one of the methods that can be used to solve the optical modes. EME and BMP are approximated methods further from the mode solver. For many particular optical devices, they can achieve fairly high accuracy with much relaxed computation requirement compared to the FDTD. The commercial simulation packages integrate these numerical methods with convenient CAD toolkits, making the simulation easier and more efficient. However, fundamental understandings about different methods and their limitations are still required.

Chapter 4 explains the origins of optical waveguide transmission loss and provides possible paths to reduce various loss mechanisms. While bend loss, substrate leakage, top surface roughness can be prevented upon understanding them, this thesis has focused on solve the sidewall roughness scattering in silicon waveguides and bulk absorption loss in deposited amorphous silicon and silicon nitride materials. Three important causes of sidewall roughness scattering are summarized. Each can be reduced with design and process optimization. Bulk absorption in deposited amorphous silicon waveguide is due to dangling bond absorption at 1550 nm; for PECVD silicon nitride, it is the N-H bond vibration absorption centered at 1510 nm that introduces excess of loss around 1550 nm. Reducing dangling bond density in a-Si and H concentration in nitride is the key to reducing bulk absorption loss.

In Chapter 5, I have summarized the measurement techniques that have been used in this thesis. While the "paperclip" method is simple and straightforward, it requires careful sample preparation for uniform facets and consistent fiber-to-waveguide couplings that can only be guaranteed with ease using auto-alignment system. For small transmission loss coefficients below 3 dB/cm or even 1 dB/cm, it is required to have a large increment in waveguide length between adjacent waveguides in order to have large enough insertion loss different to accurately resolve the

transmission loss coefficients. The measurement is quite time consuming because multiple waveguides (> 5 with acceptable accuracy) have to be measured for each different design. Ring resonator based method is simpler and less time consuming, and yet to be accurate for even small transmission losses. Because large size resonators with long periphery length have smaller FSR, one can resolve wavelength dependency of transmission loss at each resonant wavelength given the corresponding effective index can be calculated. The measurement variation is shown to be less than 15%. The drawback of this method is that ring resonator fabrication is more complex than waveguide fabrication. Expensive and dedicated lithographic tool is required.

Chapter 6 summarizes the process development and optimization for silicon waveguide fabrications, including c-Si and a-Si. All the processes are CMOS compatible and are done in CMOS fabrication plants built for making electronics chips. Leveraging the CMOS technology is the core which silicon photonics is built on. This chapter is heavily experimental oriented, yet has some simulation works, such as the study on pattern effect for LOCOS process. By optimizing the photolithography and etch steps, we can effectively reduce the line edge roughness or sidewall roughness of silicon channel waveguides and reduce the optical transmission loss for the TE mode.

In Chapter 7, low loss, low temperature PECVE silicon nitride processes are developed for waveguide applications around 1550 nm. Although silicon nitride has low refractive index compared to silicon, it is still a very attractive waveguide material for many applications. Moreover, low loss silicon nitride can be used as hydrogen diffusion barrier as well as interlayer graded index layer to reduce silicon waveguide transmission loss. PECVD is very versatile and low cost compared to other methods. Obtain low loss, low temperature PECVD silicon nitride is the key for a-Si applications. In this chapter, three different low temperature approaches in obtaining low loss PECVD silicon nitride are discussed in details; they are: (1) via deposition chemistry. This

method can give low NH containing nitride with high SiH concentration. (2) via post-deposition UV-treatment. UV-treatment can reduce both NH and SiH bonds simultaneously. The film can be as thick as 70 nm and the total H removal percentage demonstrated is as high as 60%. However, it requires a dedicated UV chamber. (3) via post-deposition, in-situ plasma treatment. Similar to UV-treatment, this method can also reduce both NH and SiH bonds up to 90% demonstrated in this thesis. However, it is only effective for ultra-thin films with thickness less than 5 nm. The last two methods are originally developed by and are proprietary of Applied Materials Inc. The theoretical study of UV treatment process is independent work at MIT. The Monte-Carlo simulation reveals the nature of the hydrogen evolution in nitride film under UV illumination and shows consistent results with experiments.

Chapter 8 is dedicated to slot waveguides, more specially, low loss, horizontal slot waveguides. Slot waveguides have been identified as the most promising waveguide structure for realizing Er-based silicon light emission. Horizontal slot waveguide configuration is conceptually proposed and then experimentally demonstrated as the low loss slot waveguide form that can eventually realize lasing in Er-doped silicon system.

Chapter 9 summarizes most of the experimental results on waveguide transmission losses coming out of this thesis work. We have demonstrated the low loss optical transmission in single mode, c-Si channel waveguides with minimal TE mode loss of 2.7 dB/cm and TM mode loss of 0.7 dB/cm, respectively. For single mode, a-Si channel waveguides, we have achieved the lowest transmission loss of ~2.7 dB/cm for the TE-mode operation using H passivated a-Si and a thin, low loss PECVE nitride intercladding layer. We have also successfully demonstrated the damascene process for deposited a-Si channel waveguide fabrication with minimal transmission loss of ~ 2.5 dB/cm.

Chapters 10, 11, and 12 are dedicated to waveguide couplers. Low loss waveguide couplers are indispensable passive optical components that can transport optical signals among different optical devices with minimal coupling loss at the junctions. A low loss coupler is capable of overcoming the mode-size mismatch, mode-shape mismatch, mode-position mismatch, and polarization mismatch. Mode transformation is found to be ideal to happen where the mode intensity is the weakest to avoid large perturbation of optical field, thus avoiding high scattering loss. Adiabatic tapers are especially useful to transform modes without introducing scattering loss. The couplers summarized in this chapter are (1) fiber-to-waveguide couplers; (2) vertical waveguide-to-waveguide couplers; and (3) slot waveguide-based waveguide couplers and polarization rotators.

In Chapter 13, athermal design of silicon waveguide system is tentatively explored both theoretically and experimentally. In order to realize high bandwidth on-chip optical interconnect, the consensus is that employing DWDM is inevitable. However, for the large amount of narrow band filters, temperature will have a huge impact on their filter characteristics by changing the refractive index. Because actively tuning of tens of thousands of such filters would be prohibitively expensive in terms of power consumption and design space, if not impossible, passive, temperature-insensitive filters are very attractive and may be the only way to solve this problem given the fabrication can be advanced so that all the filters are tuning free as fabricated. Polymers with large negative thermo-optic (TO) coefficients can be used to compensate positive TO effect in silicon waveguides. Our preliminary experimental results shows that with polymer cladding, we can efficiently reduce the TO coefficient of a-Si racetrack resonators from ~ 85 pm/K to ~ 11 pm/K.

14.2. Future directions

14.2.1. Low loss optical waveguides and waveguide materials

In this thesis work, we have achieved consistently lower than 3 dB/cm transmission loss for the TE mode in both c-Si and a-Si single mode channel waveguides and less than 1 dB/cm for the TM-mode in c-Si waveguides. Various high performance optical couplers are also proposed and demonstrated with coupling loss of just a fraction of dB per coupler and with excellent broadband behavior between 1510 nm to 1610 nm.

Lower transmission loss in optical waveguides is desired for many applications that require extremely low loss, such as laser cavities, amplifiers, and optical buffers for slowing light.

For example, an integrated optical delay line chip would have about 10 m long coiled single mode silicon waveguides and two fiber-to-waveguide couplers. The total insertion loss should be less than 3 dB. This requires that the waveguide loss to be on the order of 1 dB/10m or 0.001 dB/cm. For c-Si waveguides with only sidewall roughness scattering loss, according to Barwicz and Haus, this corresponds to the sidewall roughness of 0.5 Å [32]. Such small transmission loss coefficient is also the key to realize Er-doped silicon-based light emitter because the potential gain coefficient of such Er system is ~ 3 dB/cm or less. Can we achieve that in the future?

Beside the techniques that we already know and we can improve on, such as dry/wet oxidation, hard mask, process optimization for photolithography and etch, hydrogen annealing may be the ultimate approach to achieve atomic flat silicon waveguide surface. It is discovered that at high temperature and in H ambient, the surface diffusivity of silicon can be greatly enhanced. H reflow of c-Si channel waveguides and shallow ridge waveguides have been demonstrated with a minimal 0.7 dB/cm loss [109,110] for TE mode operation.

As we have discussed, deposited waveguides can enable 3D photonic integration on silicon. In interconnect levels, they allow more design space and more flexibility for integration. They offer lower cost and low thermal budget too, which makes them very attractive. Beside sidewall roughness scattering mechanism similar to c-Si, a-Si and PECVE silicon nitride have bulk absorption loss. While we have learnt that hydrogen passivation can reduce the dangling bond density in a-Si, its stability is also a big concern for special applications and for integration. For example, if a MZI filter is made of hydrogenated a-Si (a-Si:H) and uses thermo-optical effect for filter tuning. Constant heating cycles above 300 ^{o}C would potentially alter the chemical composition of the a-Si:H because H out diffusion and dangling bond aggregation. Can we prevent that? For PECVE silicon nitride, the current methods of UV treatment and plasma treatment have drawbacks of either being limited by the maximal H removal percentage or being too slow to be useful for applications requiring much thicker film. Is there anything we can do to improve the process?

Incorporation of a thin silicon nitride over cladding layer around a-Si waveguide has been shown to be effective to increase its thermal stability. The reduction of the transmission loss is a combination of preserving H passivation and providing index grading. More rigorous analyses need to be done to derive the correlation among nitride thickness, H concentration, the highest temperature, and duration the whole waveguide structure can sustain before its transmission loss increases significantly. For applications with c-Si waveguides, the index grading effect of LPCVD silicon nitride over cladding layer can be studied independently. Currently, because the high optical confinement realized in those c-Si waveguides, no decisive conclusions on cladding effect can be reached. Thicker nitride or smaller waveguides should be used in the future.

For low loss, low NH containing PECVD silicon nitride using UV treatment, because we

have already had some understanding about the H evolution from the Monte Carlo model, we may think of processes to either increase the local coordination numbers for unlike groups of SiH and NH to increase the total H removal percentage, or to reduce the H rich groups, such as NH_2, possibly SiH_2 groups to allow more NH-SiH reactions.

14.2.2. Low loss optical waveguide couplers

In this thesis work, important waveguide couplers have been demonstrated for fiber-to-waveguide and waveguide-to-waveguide couplings. However, these waveguide couplers are designed solely for TE mode operations. Ideally, we would like to have polarization insensitive couplers or couplers that can change polarizations. The reason is because regular fibers do not maintain a particular polarization and the output is most likely to be a random polarization containing both TE and TM modes. If couplers only support one polarization, then one would have about 3 dB coupling loss per coupler due to the loss of the other polarization even thought for one particular polarization the coupling loss is much smaller. One possible way to achieve polarization insensitive coupling and routing is to split the polarizations, rotate one polarization to the other, and then combine them [111,112]. On the other hand, if the chip architecture is based on TE mode, meaning all the waveguides, couplers, and filters only support TE polarization, polarization maintaining fiber must be used throughout the system.

14.2.3. Athermal waveguides

Up till now, all the narrow band filters rely on some tuning mechanism to overcome the fabrication variation. The same mechanism, such as using thermo-optic effect, can be used to compensate temperature fluctuation during operation. In the future, while the process development

can guarantee the precision required to achieve tuning-free filters, athermal operation has to be passive as well. Polymer cladding has been demonstrated to be promising. With particular negative TO coefficient polymers, waveguide geometry has to be carefully designed in order to achieve the true athermal conditions. For ring resonator devices, temperature insensitive coupling is also needed in order to retain the resonance characteristics, such as the extinction ratio and bandwidth.

The past decade has been very exciting period for the development of silicon photonics. Look ahead, many great breakthroughs are on the horizon including on-chip Ge-based lasers and multi-gigahertz Ge modulator-detector links, etc. With reliable on-chip multi-wavelength laser diodes and WDM photonic channels, optical interconnects will be realized and first applied in high performance computers, likely around 2020. As processes and markets become mature, high performance, silicon-based electronic-photonic circuits or integrated modules will be adapted for more and more applications and be produced at a larger and larger scale. Eventually, optical interconnects enabled multi-core processors will become very appearing to ordinary consumers in terms of both high performance and low cost, likely around 2030. By then, we will all have computers or video game consoles with the label saying something like "Light Bridge Inside".

(This page is intentionally left blank)

References

[1] G.E. Moore, "Cramming more components onto integrated circuits," Electronics, 38(8), April 19, (1965)

[2] R. Kirchain and L.C. Kimerling, "A roadmap for nanophotonics," Nature Photon. 1, 303-305 (2007)

[3] M. Beals, J. Michel, J.F. Liu, D.H. Ahn, D. Sparacin, R. Sun, C.Y. Hong, L. C. Kimerling, A. Pomerene, D. Carothers, J. Beattie, A. Kopa, A. Apsel, M. S. Rasras, D. M. Gill, S. S. Patel, K.Y. Tu, Y. K. Chen, and A. E. White, "Process Flow Innovations for Photonic Device Integration in CMOS," Proc. SPIE Vol. 6898, 689804 (2008)

[4] M.S. Rasras, D.M. Gill, S.S. Patel, K. Tu, Y. Chen, A.E. White, A.T.S. Pomerene, D.N. Carothers, M.J. Grove, D.K. Sparacin, J. Michel, M.A. Beals, and L.C. Kimerling, "Demonstration of a Fourth-Order Pole-Zero Optical Filter Integrated Using CMOS Processes," J. Lightwave Technol. 25, 87-92 (2007)

[5] J.F. Liu, J. Michel, W. Giziewicz, D. Pan, K. Wada, D. Cannon, L.C. Kimerling, J. Chen, F.O. Ilday, F.X. Kartner, and J. Yasaitis, "High-performance, tensile-strained Ge p-i-n photodetectors on a Si platform," Appl. Phys. Lett. 87, 103501 (2005)

[6] J.F. Liu, M. Beals, A. Pomerene, S. Bernardis, R. Sun, J. Cheng, L.C. Kimerling, and J. Michel, "Waveguide-integrated, ultra-low energy consumption C-band GeSi electro-absorption modulators on Si platform," Nature Photonics, 2, 433-437 (2008)

[7] Q. Xu, B. Schmidt, S. Pradhan, and M. Lipson, "Micrometre-scale silicon electro-optic modulator," Nature 435, 325-327 (2005)

[8] K. Okamoto, "Fundamentals of Optical Waveguides," 2nd Edition, Academic Press, 2006

[9] E.A. Marcatili, "Dielectric rectangular waveguides and directional coupler for integrated optics," J. Bell Syst. Tech., 48, 2071 (1977)

[10] A. Kumar, K. Thyagarajan, and A.K. Ghatak, " Analysis of rectangular-core dielectric waveguides – An accurate perturbation approach," Opt. Lett., 8, 63 (1983)

[11] T. Tamir, "Integrated Optics," Oxford, Pergamon Press, 1975

[12] A. Taflove, "Computation Electrodynamics: The Finite-Difference Time-Domain Method," Boston, MA: Artech House, 1995.

[13] K. S. Yee, "Numerical solution of initial boundary value problems involving Maxwell's equations in isotropic media," IEEE Trans. on Antennas and Propagation, AP-14, No.3, 303 (1966)

[14] J. P. Berenger, "A perfectly matched layer for the absorption of electromagnetic-waves," J. Computational Physics, 114, 185 (1994)

[15] K. Okamoto, "Fundamentals of Optical Waveguides," 2nd Edition, Academic Press, 2006

[16] C. Yeh, K. Ha, S. B. Dong, and W. P. Brow, "Single-mode optical waveguides," Appl. Opt. 18, 1490 (1979)

[17] K. Hayata, K. Koshiba, M. Eguchi, and M. Suzuki, "Vectorial finite element method without any spurious solution for dielectric waveguiding problems using transverse magnetic field components," IEEE Trans. Microwave Theory Tech. MTT-34, 1120–1124 (1986).

[18] T. Angakaew, M. Matsuhara, and N. Kumagai, "Finite-Element. Analysis of Waveguide Modes: A Novel Approach that Eliminates. Spurious Modes," IEEE Trans. Microwave Theory Tech., MTT-35, 117 (1987)

[19] M. Koshiba, "Optical Waveguide Theory by the Finite Element Method," Tokyo, Japan/Dordrecht, The Netherlands: KTK Scientific/Kluwer Academic, 1992.

[20] J. Crank and P. Nicolson, "A practical method for numerical evaluation of solutions of partial differential equations of the heat conduction type," Proceedings of the Cambridge Philosophical Society, 43, 50 (1947)

[21] G. R. Hadley, "Transparent boundary condition for beam propagation," Opt. Lett. 16, 624-626 (1991)

[22] G. R. Hadley, "Transparent boundary condition for the beam propagation method," J. Quantum Electron., 28, 363 (1992)

[23] W. P. Huang and C. L. Xu, "Simulation of three-dimensional optical waveguides by a full-vector Beam Propagation Method," J. Quantum Electron., 29, 2639 (1993)

[24] P. Kaczmarski and P. E. Lagasse, "Bidirectional beam propagation method," Electron. Lett., 24, 675 (1988)

[25] G. R. Hadley, "Wide-angle beam propagation using Pade approximation operators," Optics Lett., 17, 1426, 1992

[26] P. Bienstman, "Rigorous and efficient modeling of wavelength scale photonic components," Doctoral Dissertation, University Gent, 2001

[27] D. F. G. Gallagher and T. P. Felici, "Eigenmode expansion methods for simulation of optical propagation in photonics: Pros and cons," Proc. SPIE 4987, 69-82 (2003).

[28] R.G. Beausoleil, J. Ahn, N. Binkert, A. Davis, D. Fattal, M. Fiorentino, N.P. Jouppi, M. McLaren, C.M. Santori, R.S. Schreiber, S.M. Spillane, D.Vantrease, and Q. Xu, "A Nanophotonic Interconnect for High-Performance Many-Core Computation," IPNRA 2008, ITUD2

[29] D. Marcuse, "Mode Conversion Caused by Surface Imperfections of a Dielectric Slab Waveguide," The Bell System Technical Journal, 48, p.3187-3215 (1969)

[30] J.P.R. Lacey and F.P. Payne, "Radiation Loss from Planar Waveguides with Random Wall Imperfections," IEEE Proc. J. Optoelectronics, 137, No.4, p.282-288 (1990)

[31] F.P. Payne and J.P.R. Lacey, "A Theoretical Analysis of Scattering Loss from Planar Optical Waveguides," IEEE Opt. Quantum Electron., 26, p.977-986 (1994)

[32] T. Barwicz and H.A. Haus "Three-Dimensional Analysis of Scattering Losses Due to Sidewall Roughness in Microphotonic Waveguides," IEEE Journal of Lightwave Technology, 23, No.9, p.2719-2732 (2005)

[33] D.L. Smith, A.S. Alimonda, C.-C. Chen, S.E. Ready, and B. Wacker, "Mechanism of SiN_xH_y Deposition from NH_3-SiH_4 Plasma," J. Electrochem. Soc., 137(2), 614 (1990)

[34] R.A. Soref and B.R. Bennett, "Electrooptical effects in silicon," IEEE J. Quantum Electron. 23, 123-129 (1987)

[35] R.A. Soref and B.R. Bennett, "Kramers–Kronig analysis of E-O switching in silicon," SPIE Integr. Opt. Circuit Eng., 704, 1986.

[36] C.A. Barrios, V.R.d. Almeida, and M. Lipson, "Low-Power-Consumption Short-Length and High Modulation-Depth Silicon Electrooptic Modulator," J. Lightwave Technol. 21, 1089 (2003)

[37] D.K. Sparacin, "Process and Design Techniques for Low Loss Integrated Silicon Photonics," Ph.D. Dissertation, MIT, 63 (2006)

[38] W. A. Gambling, H. Matsumura, and C. M. Ragdale, "Field deformation in a curved single-mode fibre," Electron. Lett. 14, 130 (1978)

[39] P. Bienstman, E. Six, M. Roelens, M. Vanwolleghem, and R. Baets, "Calculation of bending losses in dielectric waveguides using eigenmode expansion and perfectly matched layers," IEEE Photon. Technol. Lett. 14, 164–166 (2002)

[40] R. Pregla, "The method of lines for analysis of dielectric waveguide bends," J. Lightwave Technol. 14, 634–639 (1996).

[41] S. Kim and A. Gopinath, "Vector analysis of optical dielectric waveguide bends using finite-difference method," J. Lightwave Technol. 14, 2085–2092 (1996)

[42] F. Wassmann, "Modal field analysis of circularly bent singlemode fibers," J. Lightwave Technol. 17, 957–968 (1999)

[43] K. Thyagarajan, M. R. Shenoy, and A. K. Ghatak, "Accurate numerical method for the calculation of bending loss in optical waveguides using a matrix approach," Opt. Lett. 12, 296 (1987)

[44] W. Berglund and A. Gopinath, "WKBanalysis of bend losses in optical waveguides," J. Lightwave Technol. 18, 1161 (2000)

[45] R. Baets and P. E. Lagasse, "Loss calculation and design of arbitrarily curved integrated-optic waveguides," J. Opt. Soc. Am. 73, 177–182 (1983)

[46] R. T. Schermer and J. H. Cole, "Improved bend loss formula verified for optical fiber by simulation and experiment," IEEE J. Quantum Electron. 43, 899–909 (2007)

[47] B.M.A. Rahman, D.M.H. Leung, S.S.A. Obayya, and K.T.V. Grattan, "Numerical analysis of bent waveguides: bending loss, transmission loss, mode coupling, and polarization coupling," Appl. Opt. 47, 2961 (2008)

[48] G. Tittelbach, B. Richter, and W. Karthe, "Comparison of Three Transmission Methods for Integrated Optical Waveguide Propagation Loss Measurement." Pure Appl. Opt., 2, 683 (1993)

[49] P. Karminow and L. W. Stulz, "Loss in cleaved Ti-diffused LiNbO3 waveguides," Appl. Phys. Lett. 33, 62 (1978)

[50] A. Yariv, "Universal relations for coupling of optical power between micro-resonators and dielectric waveguides," Electron. Lett., 36, 321–322 (2000)

[51] G. Roelkens, P. Dumon, W. Bogaerts, D.V. Thourhout, R. Baets, "Efficient Silicon-on-Insulator Fiber Coupler Fabricated Using 248-nm-Deep UV Lithography" IEEE Photonics Technology Letters, 17(12), 2613 (2005)

[52] R. C. Jones, "New calculus for the treatment of optical systems," J. Opt. Soc. Am. 31, 488–493, (1941)

[53] Y. Sensu, A. Sekiguchi, and Y. Miyake, "Improved resolution of thick-film resist (effect of development technique)," Electronics and Communications in Japan (Part II: Electronics), 86(7), 1 – 13 (2003)

[54] L. K. Rowe, M. Elseyb, E. Postc, N. G. Tarra, A. P. Knightsb , "A CMOS-compatible rib waveguide with local oxidation of silicon isolation," Proc. SPIE, Vol. 6477, 64770L (2007)

[55] M. A. Webster, R. M. Pafchek, A. Mitchell, and T. L. Koch, "Width Dependence of Inherent TM-Mode Lateral Leakage Loss in Silicon-On-Insulator Ridge Waveguides," IEEE Photon. Technol. Lett. 19,429-431 (2007)

[56] J.H. Yi, "Silicon rich nitride for silicon based laser devices," Doctoral dissertation, MIT (2008)

[57] B. E. Deal and A. S. Grove. "General Relationship for the Thermal Oxidation of Silicon," J. Appl. Phys., 36, 3770 (1965)

[58] C. S. Rafferty. "Stress Effects in Silicon Oxidation—Simulation and Experiments," Doctoral dissertation, Stanford

University (1989)

[59] V. Senez, P. Ferreira, and B. Baccus. "Two-Dimensional Simulation of Local Oxidation of Silicon: Calibrated Viscoelastic Flow Analysis," IEEE Trans. Electron Dev., 43(5), 720–731 (1996)

[60] P. C. Andricacos, C. Uzoh, J. O. Dukovic, J. Horkans, and H. Deligianni, "Damascene copper electroplating for chip interconnections," IBM Journal of Research and Development, 42(5), 567 (1998)

[61] V. Chikarmane, K. Fischer, R. Grover, T. Ibrahim, D. Ingerly, K. Lee, C. Litteken, P. Moon, T. Mule, and S. Williams, "Process and Electrical Results for the On-die Interconnect Stack for Intel's 45nm Process Generation," Intel Technology Journal, 12(2), 2008

[62] J.F. Liu, "GeSi Photodetectors and Electro-absorption Modulators for Si Electronic-photonic Integrated Circuits," Doctoral dissertation, MIT (2007)

[63] S. Akiyama, "High Index Contrast Platform for Silicon Photonics," Ph.D. Dissertation, MIT (2004)

[64] V. Nguyen, "Efficient Power Coupling to Waveguides in High Index Contrast Systems," Ph.D. Dissertation, MIT (2005)

[65] W.A. Lanford and M.J. Rand, "The hydrogen content of plasma-deposited silicon nitride," J. Appl. Phys., 49(4), 2473 (1978)

[66] Z. Yin and F.W. Smith, "Free-energy model for bonding in amorphous covalent alloys," Phys. Rev. B, 42 (6), 3666 (1990)

[67] M. Balseanu, L.Q. Xia, V. Zubkov, M. Le, J. Lee, and H. M'Saad, "Stress Modulation of PECVD Silicon Nitride," Meet. Abstr. - Electrochem. Soc. 502, 532 (2006)

[68] Vladimir Zubkov, Mihaela Balseanu, Li-Qun Xia, and Hichem M'Saad, "Post Deposition Ultraviolet Treatment of Silicon Nitride Dielectric: Modeling and Experiment," Mater. Res. Soc. Symp. Proc., 910, 0910-A19-04 (2006)

[69] F. Bretts, A. Bienenstock, and S.R. Ovshinsky, "Radial distribution studies of amorphous Ge_xTe_{1-x} alloys," J. Non-Cryst. Solids, 4, 554 (1970)

[70] Marsaglia, G. & Zaman, A, "A new class of random number generators", Annals of Applied Probability, vol. 1, pp.462-480. (1991)

[71] D. M. Goldie and S. K. Persheyev, "Quantitative hydrogen measurements in PECVD and HWCVD a-Si:H using FTIR spectroscopy," J. Mater. Sci., 41, 5287–5291 (2006)

[72] T. Baehr-Jones, M. Hochberg, G. Wang, R. Lawson, Y. Liao, P. A. Sullivan, L. Dalton, A. K.-Y. Jen, A. Scherer, "Optical modulation and detection in slotted Silicon waveguides,",Opt. Express 13, 5216 (2005)

[73] C. A. Barrios, M. Lipson, "Electrically driven silicon resonant light emitting device based on slot-waveguide," Opt. Express 13, 10092 (2005)

[74] T. Fujisawa, M. Koshiba, "Guided Modes of Nonlinear Slot Waveguides," IEEE Photon. Technol. Lett. 8, 1530 (2006)

[75] P. Andrew Anderson, Bradley S. Schmidt and Michal Lipson, "High confinement in silicon slot waveguides with sharp bends," Opt. Express 14 9197 (2006)

[76] T. Baehr-Jones, M. Hochberg, C. Walker, and A. Scherer, "High-Q optical resonators in silicon-on-insulator-based slot waveguides," Appl. Phys. Lett. 86, 081101 (2005)

[77] N. N. Feng, J. Michel, and L C. Kimerling, "Optical field concentration in low-index waveguides," IEEE J. Quantum Electron. 42, (2006)

[78] L.A. Eldada, "Polymer integrated optics: promise versus practicality," Proceedings of SPIE 4642, Organic Photonic Materials and Devices IV, 11 (2002)

[79] T. Shoji, T. Tsuchizawa, T. Watanabe, K. Yamada, and H. Morita, "Low loss mode size converter from 0.3pm square Si wire waveguides to single mode fibers," ELECTRONICS LETTERS, 38(25), 1669 (2002)

[80] S. Itabashi, H. Fukuda, T. Tsuchizawa, T. Watanabe, J. Takahashi, T. Shoji, and K. Yamada, "Silicon wire waveguide fabrication and microphotonics devices," OFC 2005, OFL1

[81] Vilson R. Almeida, Roberto R. Panepucci, and Michal Lipson, "Nanotaper for compact mode conversion," OPTICS LETTERS, 28(15), (2003)

[82] A. Sure, T. Dillon, J. Murakowski, C. Lin, D. Pustai, and D. Prather, "Fabrication and characterization of three-dimensional silicon tapers," Opt. Express 11, 3555 (2003)

[83] G. Masanovic, G. Reed, W. Headley, B. Timotijevic, V. Passaro, R. Atta, G. Ensell, and A. Evans, "A high efficiency input/output coupler for small silicon photonic devices," Opt. Express 13, 7374 (2005)

[84] M.M. Spuhler, B.J. Offrein, G.L. Bona, R. Germann, I. Massarek, and D. Erni, "A Very Short Planar Silica Spot-Size Converter Using a Nonperiodic Segmented Waveguide," Journal Of Lightwave Technology, 16(9), 1680 (1998)

[85] B. Luyssaert, P. Vandersteegen, D. Taillaert, P. Dumon, "A Compact Photonic Horizontal Spot-Size Converter Realized in Silicon-on-Insulator," IEEE Photonics Technology Letters, 17(1), 73 (2005)

[86] Andre Delage, Siegfried Janz, Dan X. Xu, Dan Dalacu, Boris Lamontagne, and Alexei L. Bogdanov, Graded-index coupler for microphotonic SOI waveguides, Proceedings of SPIE, 5577, 204 (2004)

[87] C. Manolatou, "Passive Components for Dense Optical Integration Based on High Index-Contrast," MIT PhD Dissertation (2001)

[88] V.Nguyet, "Efficient Power Coupling to Waveguides in High Index Contrast Systems," MIT PhD Disseratation (2005)

[89] V. Nguyen, T. Montalbo, C. Manolatou, A. Agarwal, C.Y. Hong, J. Yasaitis, L.C. Kimerling, and J. Michel, "Silicon-based highly-efficient fiber-to-waveguide coupler for high index contrast systems," Appl. Phys. Lett. 88, 081112 (2006)

[90] J.F. Liu, M. Beals, A. Pomerene, S. Bernardis, R. Sun, J. Cheng, L.C. Kimerling, and J. Michel, "Waveguide-integrated, ultra-low energy consumption C-band GeSi electro-absorption modulators on Si platform," Nature Photonics, 2, 433-437, (2008)

[91] J.F. Liu, J. Michel, W. Giziewicz, D. Pan, K. Wada, D. Cannon, L. C. Kimerling, J. Chen, F. O. Ilday, F. X. Kartner, and J. Yasaitis, "High-performance, tensile-strained Ge p-i-n photodetectors on a Si platform," Appl. Phys. Lett. 87, 103501 (2005)

[92] D. Ahn, C.Y. Hong, J. Liu, W. Giziewicz, M. Beals, L.C. Kimerling, J. Michel, J. Chen, and F.X. Kärtner, "High performance, waveguide integrated Ge photodetectors," Opt. Express 15, 3916-3921 (2007)

[93] D. Cannon, J.F. Liu, Y. Ishikawa, K. Wada, D.T. Danielson, S. Jongthammanurak, J. Michel, and L.C.

Kimerling, "Tensile strained epitaxial Ge films on Si(100) substrates with potential application in L-band telecommunications," Appl. Phys. Lett., 84, 906-908 (2004)

[94] B. E. A. Saleh and M. C. Teich, Fundamentals of Photonics (P266, John Wiley & Sons, Inc., 1991)

[95] H. A. Haus, Wave and Fields in Optoelectronics (P218, Prentice-Hall, Inc., Englewood Cliffs, NJ, 1984)

[96] Y. Shani, C. H. Henry, R. C. Kistler, R. F. Kazarinov, and K. J. Orlowsky, "Integrated optic adiabatic polarization splitter on silicon," Appl. Phys. Lett. 56, 120 (1990)

[97] A. Yariv and X. Sun, "Supermode Si/III-V hybrid lasers, optical amplifiers, and modulators: A proposal and analysis," Opt. Express 15, 9147 (2007)

[98] M. Beals, J. Michel, J. Liu, D. Ahn, D. K. Sparacin, R. Sun, C-Y Hong, L. C. Kimerling, A. Pomerene, D. Carothers, J. Beattie, A. Kopa, A. Apsel, M. S. Rasras, D. M. Gill, S. S. Patel, K. Y. Tu, Y-K Chen, and A. E. White, "Process Flow Innovations for Photonic Device Integration in CMOS," Proc. SPIE 6898, 689804 (2008).

[99] D. K. Sparacin, R. Sun, A. Agarwal, M. Beals, J. Michel, L. C. Kimerling, T. Conway, A. Pomerene, D. Carothers, M. Grove, D. M. Gill, M. S. Rasras, S. S. Patel, and A. E. White, "Low-loss amorphous silicon channel waveguides for integrated photonics," Proceedings of 3rd IEEE International Conference on Group IV Photonics, 255-257, 2006.

[100] J.F. Liu, D. Pan, S. Jongthammanurak, D. Ahn, C.Y. Hong, M. Beals, L.C. Kimerling, and J. Michel, "Waveguide-Integrated Ge p-i-n Photodetectors on SOI Platform," 3rd IEEE International Conference on Group IV Photonics,2006, 173

[101] Beam propagation simulator, BeamPROP software, Rsoft-Design Inc., http://www.rsoftinc.com/products/component_design/BeamPROP

[102] "Photonic Materials, Devices and Systems – Nanostructures Technology, Research and Applications" RLE (Research Laboratory of Electronics at MIT) Progress Report (2001)

[103] C. Angulo Barrios, M. Lipson, "Electrically driven silicon resonant light emitting device based on slot-waveguide", Opt. Exp., 13 (25), 10092, (2005).

[104] M. R. Watts and H. A. Haus, "Integrated mode-evolution-based polarization rotators," Opt. Lett., 29 (2), 138 (2005).

[105] Y. Kokubun, N. Funato, and M. Takizawa, "Athermal waveguides for temperature-independent lightwave devices," IEEE Photonics Technology Letters, 5(11), 1297 (1993)

[106] N. Ooba, Y. Hibino, Y. Inoue, and A. Sugita, "Athermal silica-based arrayed-waveguide grating multiplexer using bimetal plate temperature compensator," Electron. Lett., 36(21), 1800 (2000)

[107] W.N. Ye and R. Sun, unpublished work at MIT

[108] W.N. Ye, J. Michel, L.C. Kimerling, and L. Eldada, "Polymer-cladded athermal high-index-contrast waveguides," Proc. SPIC, 6897, 68970S (2008)

[109] M.C.M. Lee and M.C. Wu, "Thermal annealing in hydrogen for 3-D profile transformation on silicon-on-insulator and sidewall roughness reduction", Journal of Microelectromechanical Systems. 15(2), 338-343 (2006)

[110] M.A. Webster, R.M. Pafchek, A. Mitchell, T.L. Koch, "Width Dependence of Inherent TM-Mode Lateral Leakage Loss in Silicon-On-Insulator Ridge Waveguides," Photonics Technology Letters, IEEE 19(6), 429-431 (2007)

[111] D. Taillaert, H. Chong, P. Borel, L. Frandsen, R. De La Rue, and R. Baets, "A compact two-dimensional grating coupler used as a polarization splitter," IEEE Photon Technol. Lett. 15(9), 1249–1251 (2003)

[112] H. Fukuda, K. Yamada, T. Tsuchizawa, T. Watanabe, H. Shinojima, and S. Itabashi, "Silicon photonic circuit with polarization diversity," Opt. Express 16, 4872-4880 (2008)